Department of Pure and Applied Chemistry

The Low-Temperature Formation
of
Mixed-Metal Oxides

Thomas Wai Sing Yip

MSci (Hons)

September 2011

For submission to the University of Strathclyde

for the degree of Doctor of Philosophy

Declaration of Authenticity and Author's Rights

This thesis is the result of the author's original research. It has been composed by the author and has not been previously submitted for examination which has led to the award of a degree.

The copyright of this thesis belongs to the author under the terms of the United Kingdom Copyright Acts as qualified by University of Strathclyde Regulation 3.50. Due acknowledgement must always be made of the use of any material contained in, or derived from, this thesis.

Signed:

Date:

Abstract

This thesis describes a new route to lithium molybdate, Li_2MoO_4, which involves grinding together $LiOH\cdot H_2O$ and MoO_3 in air at room temperature. X-ray powder diffraction data show that the formation of highly crystalline Li_2MoO_4 is largely complete after 10 min, and that this product crystallises with the phenacite structure-type. This structure is the same as that derived from an X-ray diffraction study of a single crystal of Li_2MoO_4 grown from aqueous solution [$R\overline{3}$; a = 14.3178(14) Å, c = 9.5757(9) Å]. Differential scanning calorimetric measurements show that the reaction between the solid reagents proceeds spontaneously, even at sub-ambient temperatures, and is driven by the liberation of water from the lattice of $LiOH\cdot H_2O$. In this manner, Li_2MoO_4 is prepared as mono-disperse particles, which are smaller and more regularly shaped than those yielded by other synthetic methods.

This reaction has been developed further to provide a new route to the lithium ion exchange of a series of protonated Ruddlesden-Popper layered perovskites ($HLaTiO_4$, $H_2SrTa_2O_7$ and $H_2La_2Ti_3O_{10}$), with a controlled proton and lithium content. This involves grinding a stoichiometric quantity of $LiOH\cdot H_2O$ with each of the solid acids. X-ray powder diffraction data show that the reactions leading to $H_{1-x}Li_xLaTiO_4$ [$P4/nmm$; $x \geq 0.1$] and $HLiSrTa_2O_7$ [$Ama2$] are complete after 5 d, whilst those leading to $H_{2-2x}Li_{2x}La_2Ti_3O_{10}$ [$I4/mmm$; $x \geq 0.125$] are complete after 53 min. Neutron powder diffraction data of the intermediate members of the

$H_{1-x}Li_xLaTiO_4$ series indicate that the interlayer cations are disordered and remain on the 16*k* (H^+) and 2*b* (Li^+) sites identified in the end-member phases.

The exchanged phases could be modified by dehydration at 360-480 °C to give new defective layered perovskites: $\square_{1-x}Li_xLaTiO_{4[(1-x)/2]}$ ($0.5 \leq x \leq 0.9$), $\square LiSrTa_2O_{6.5}$ and $\square LiLa_2Ti_3O_{9.5}$. AC impedance spectroscopy measurements indicate that these samples demonstrate a lower total ionic conductivity than that of the respective lithium end-members.

Acknowledgements

A number of people need to be thanked for their contribution towards the completion of thesis, but to none more greatly than my supervisor, Dr Edmund Cussen, to whom I shall forever be indebted for his support and guidance. I would also like to thank him for having convinced me to relocate with him from my undergraduate grounds at Nottingham, for this move has proven to be enriching both personally and academically.

I also thank the key collaborators in this work, Dr Claire Wilson and Dr Donald MacLaren, for collecting and analysing the single-crystal X-ray diffraction and electron microscopy data, respectively. I would also like to thank Mr Jim Morrow for his assistance not only with various analytical techniques, but also for his unrivalled knowledge of all things swage-lock and his assistance on the two occasions that our lab was relocated. Thanks must also be given to Dr John Liggat for his assistance with differential scanning calorimetry, Dr Paul Edwards for his help in collecting scanning electron micrographs, Dr Emmanual Suard for her assistance with neutron diffraction, Mr Bob Fabian for his help in constructing the AC impedance rig and Dr Fiona Coomer for her assistance in proof reading this thesis.

I also feel it highly appropriate to thank my senior school chemistry teacher, Mr Amir Walji, to whom I must thank for instilling within me a love for chemistry and for helping me make the leap to degree level chemistry. I would also like to

make an honourable mention to Prof. Duncan Gregory with whom I undertook an undergraduate summer project in solid-state synthesis; the experiences and impressions gained from working with his group strongly helped to shape the path that has led me to this point in my life.

Finally, I would like to thank my parents, Peter and Susan, for their unwavering support in my longer than anticipated sojourn in academia, Derek Anderson for keeping a roof over my head whilst I wrote up this thesis, and Peter Lawrence who helped me to maintain a working level of sanity in the last months of writing.

Contents

1 Introduction

1.1 Crystalline Solids

A classical description of a ceramic is that of an inorganic, non-metallic solid constituted of an ordered array of ions where, other than for thermal vibration, the motion of an ion from a lattice position is restricted by the crystal structure.[1] A simplistic interpretation of a crystalline material may therefore be that of an array of immovable ions. From this description, ceramic materials can be easily understood to be both hard and rigid. The mobility of ions in a ceramic can be compared with that in a vitrified material or glass. A glass is formed as an inorganic product of fusion which has been supercooled below its fusion temperature, T_f, to a rigid condition without crystallising, and so, this product retains much of the liquid-like structure of the melt.[1, 2] The motion of ions in a glass is impeded by the high viscosity of the disordered material, and below a critical temperature designated as the glass transition, T_g, is restricted to be infinitesimally small, as illustrated in Figure 1.1. Glasses may therefore be considered kinetically stable or in a state of metastable equilibrium.

The poor mobility of ions in solids can be anecdotally demonstrated through the myth surrounding the flow of glass in panes of stained glass windows commonly found in medieval cathedrals from the 10th century onwards. The apparent

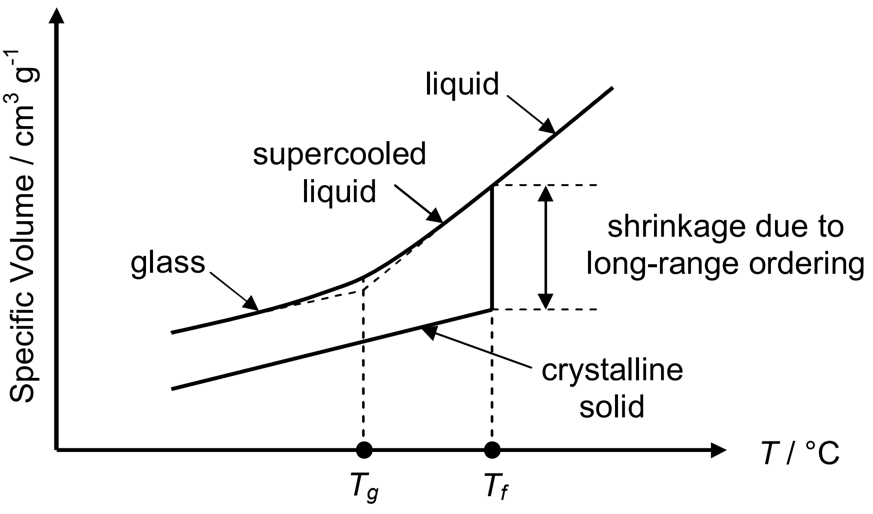

Figure 1.1 Changes in specific volume for both a crystalline solid and a glass on cooling from a high-temperature melt through the fusion temperature, T_f, and the glass transition temperature, T_g.[1]

thickening of these panes of glass at the bottom of the window has commonly been accredited to the slow motion of ions over many centuries. However, a study by Zanotto *et al.*, which involved extrapolating the Arrhenius-dependence followed by germanium oxide glass to approximate that of glass in general, indicated that a significant change in dimension would be observed only after 10^{23} years,[3, 4] *i.e.* a period of time which is several orders of magnitude longer than the expected lifetime of our universe.[5]

Nevertheless, the ions in solids can be coerced into motion over more meaningful and useful time-scales by heating the material to higher temperatures. These temperatures are often in excess of 1000 °C, and are used to provide sufficient energy to simultaneously break the large number of bonds in the material and to overcome the energy barrier to ion migration. This enhancement in ionic mobility can be observed in real terms when a ceramic tube that is unsupported at its mid-section is heated over several weeks. During this period, a ceramic will gradually deform under the action of gravity, indicating that the ions have sufficient kinetic energy to migrate and thus relieve strains in the tube body.

1.2 Synthesis of Crystalline Solids

1.2.1 Conventional Solid-state Synthesis

The motion of ions in a solid can be quantified in terms of ionic conductivity, σ_i, which is defined as the inverse of resistivity, ρ.[1] A typical ionic solid such as sodium chloride has a room-temperature ionic conductivity of the order of *ca.* 10^{-8} S cm^{-1}.[6] Increasing the temperature of this salt leads to an enhancement in ionic conductivity that reaches a value of *ca.* 10^{-5} S cm^{-1} immediately below its melting point. Upon reaching a molten state, the ionic conductivity increases abruptly to a value of *ca.* 1 S cm^{-1} that is typical of salt solutions at room temperature. Therefore, by thermally activating ion migration, mass transport can be effective over the course of days. It is in this way that the entropically-driven mixing of cations, from a mixture of solid reagents, has been traditionally exploited to drive the formation of higher-order compounds. Indeed, this synthetic approach has been employed in the manufacture of ceramics and glass-ceramic composites for several millennia, with evidence of the first pottery ware dating as far back as 16000 BC from the Hunan province of China.[7] However, the basis of this technology has remained largely the same to this day, and involves firing kaolinite-rich clay, *i.e.* kaolin, at temperatures in excess of 1100 °C to form mullite. This refractory material is responsible for the useful mechanical properties inherent to pottery. For historical reasons,[8] the chemical formula of mullite is generally given as $Al_6Si_2O_{13}$, or alternatively as $3Al_2O_3{\cdot}2SiO_2$. This is in spite of the material forming part of a solid-solution that can range from $2Al_2O_3{\cdot}SiO_2$ to $3Al_2O_3{\cdot}2SiO_2$.

On heating kaolinite, $Al_2Si_2O_5(OH)_4$, up to the synthesis temperature of mullite, a number of transformations are observed.[9, 10] The first transformation occurs at *ca.* 550 °C, where dehydration of the structure, as given by:

$$Al_2Si_2O_5(OH)_4 \rightarrow Al_2Si_2O_7 + 2H_2O, \qquad (1.1)$$

results in the amorphous phase metakaolin, $Al_2Si_2O_7$. On increasing the temperature further to 950-1000 °C, metakaolin undergoes phase separation according to the equation:

$$2Al_2Si_2O_7 \rightarrow Al_4\square_2Si_3O_{12} + SiO_2, \qquad (1.2)$$

to give a defective spinel-type structure, $Al_4\square_2Si_3O_{12}$, and amorphous SiO_2. A further and final increase in temperature to 1075 °C and above produces mullite, $Al_6Si_2O_{13}$, and further SiO_2, as given by:

$$3Al_4\square_2Si_3O_{12} \rightarrow 2Al_6Si_2O_{13} + 5SiO_2. \qquad (1.3)$$

Despite being first characterised from a geological specimen in the early 20th century,[11, 12] mullite has aided the endeavours of many an alchemist and chemist since the late Middle Ages.[13] At this time, potters from the Hesse region of Germany discovered that heating kaolin to temperatures in excess of 1100 °C resulted in a fired product that was exceptionally resilient against thermal and mechanical stresses. Vessels with such properties were highly desired by both alchemists and metallurgists of the time, and so the method of their manufacture was never published, making Hessian crucibles world-renowned. These properties have since been determined to result from sintering of particles of mullite, which exhibit a needle-like morphology.

The application of this high-temperature approach to solid-state synthesis in modern chemistry has proven to be highly successful and continues to be technologically important, but is achieved at a considerable cost in energy, and with poor control afforded to particle growth. These limitations have therefore led to a number of alternative synthetic routes being explored.

1.2.2 Alternative Synthetic Approaches

1.2.2.1 Precipitation

A wet-chemistry approach, such as precipitation from solution, is often adopted to take advantage of the greater control afforded to nucleation and crystal growth in the solution phase, to yield discrete and interestingly-shaped particles of a target product. This approach may alternatively be used to prepare a precursor to a target phase, which is then calcined, at a temperature that is often lower than that employed in the corresponding high-temperature route, to give the target product. This has been demonstrated for a variety of molybdates containing either lithium or a transition metal, and each case involved the room-temperature mixing of ammonium heptamolybdate with lithium hydroxide[14] or a transition-metal nitrate,[15] respectively, in aqueous media. The resulting precipitates constituted either the target product, as in the case of lithium molybdate, or otherwise a hydrated phase that was subsequently heat treated at 400 °C in order to yield the dehydrated ABO_4 product. In the case of lithium molybdate, the influence of factors such as solution concentration, magnetic stirring and acoustic agitation on nucleation and crystal growth were also investigated. These effects were found to lead to appreciable differences in both the size and the morphology of the precipitates formed. Scheelite-type ABO_4 molybdates and tungstates containing alkaline earth metals or lead have also been prepared in solution, to yield similarly discrete particles with a narrow size distribution. These precipitates were formed *via* simple metathesis reactions that proceeded from the room-temperature mixing of a metal chloride with sodium molybdate or sodium tungstate, in aqueous media.[16]

1.2.2.2 Sol-gel and Related Processes

A more advanced approach to size and morphological control of particle formation is embodied in the sol-gel technique.[17] This wet-chemistry approach brings the reagent ions into intimate contact with one another in a precursor phase that is formed through hydrolysis and condensation reactions. These reactions lead to the growth of clusters (*via* a base catalysed reaction) or polymeric chains (*via* an acid catalysed reaction), and when the connectivity between these units spans the vessel, a gel is formed, as demonstrated by an elastic response to stress. At this point the gel is still interpenetrated by the solvent which will contain many clusters or chains that have yet to become attached to the network. With time, these dispersed clusters and polymeric chains will also undergo condensation reactions in order to cross-link with the surrounding network, and so, increase the viscosity of the gel, as illustrated in Figure 1.2. The solvent is then allowed to evaporate, and the resultant xerogel calcined at a relatively low temperature to yield the target product.

The synthesis of metal oxides *via* sol-gel processing has traditionally been limited by the availability of a small number of metal-alkoxide precursors, *e.g.* Ti, Zr, Hf, V, Nb, Ta, Mo and W. However, an alkoxide-free variation of the traditional sol-gel method,

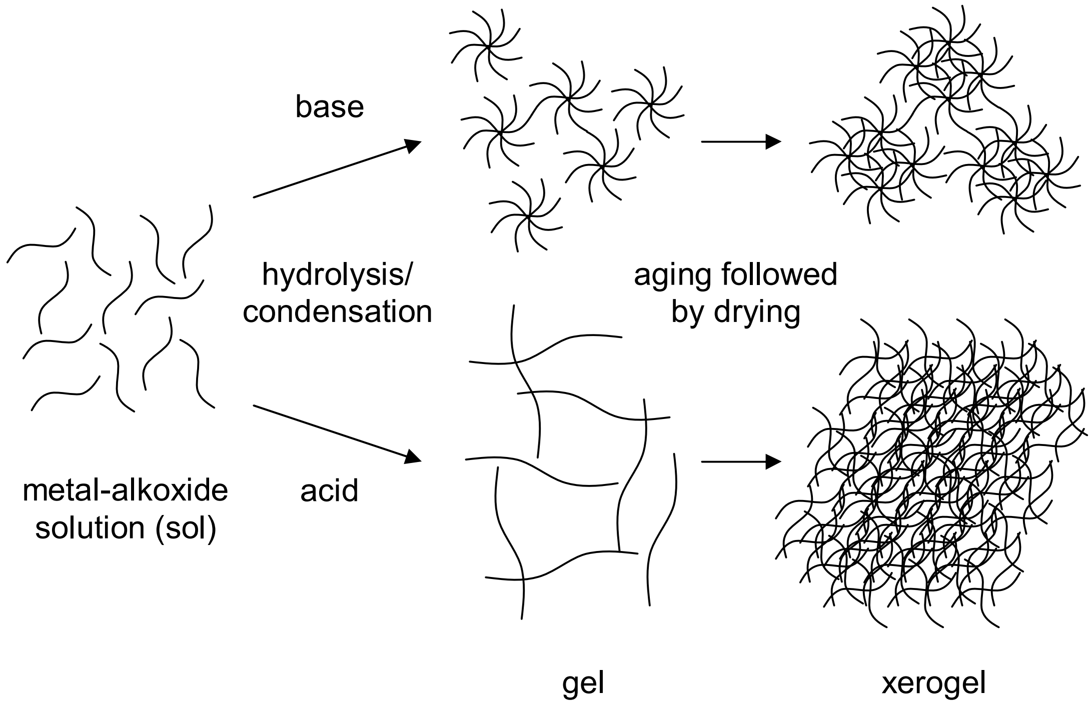

Figure 1.2 Schematic of the sol-gel process, showing the formation of a xerogel from either base- or acid-catalysed network formation between metal alkoxides.

designated the “epoxide addition method”,[18] employs, instead, a mixture of hydrated metal chlorides and an epoxide. The epoxide acts as a proton scavenger and similarly facilitates the hydrolysis and condensation reactions that are necessary to form a gel network. During epoxidation, the irreversible ring-opening reaction effectively removes a proton from solution, and thus increases the pH of the solution. This rise in pH leads to the growth of an open network of inhomogeneous, nanometre-sized particles. It has also been noted that whilst divalent species do not readily form gel networks using this method, due to the poor acidity of the aquo ligands relative to those coordinated to metals of higher valence, they can be incorporated by higher valent species that do form gel networks, such as the lanthanides. This has been demonstrated for a doped lanthanum manganite perovskite, $La_{0.85}Sr_{0.15}MnO_3$,[18] and involved the room-temperature gelation of a sol formed from a mixture of hydrated metal chlorides and propylene oxide in methanolic solution and subsequent purification and drying steps carried out at ambient temperature. The resultant mesoporous xerogel was then calcined at 700 °C in order to decompose the intermediate hydroxide, chloride and oxychloride compounds and yield nanocrystalline particles of $La_{0.85}Sr_{0.15}MnO_3$. These particles exhibited a narrow size distribution and remained discrete despite undergoing heat treatment at 700 °C. This, the authors suggested, may be related to the porous nature of the as prepared xerogel precursor, which, due to the open structure and poor inter-particle contact, is likely to hinder particle agglomeration as a result of sintering.

Another common variation of the sol-gel method is the Pechini method,[19] which is based on the polyesterification of an α-hydroxy carboxylic acid, such as citric acid, with a diol, such as ethylene glycol, in order to form a gel network. This method has been successfully employed in the synthesis of a lanthanum cobaltate perovskite, $LaCoO_3$,[19] and involved the addition of an aqueous solution containing citric acid, cobalt carbonate and lanthanum nitrate to ethylene glycol at 90 °C. This mixture was stirred for 3 hr in order to allow for polyesterification and evaporation of excess water. The resulting viscous solution was then heat treated at 400 °C to decompose the organic precursor phases, and the resultant solid calcined at 600 °C to yield sub-micron particles of $LaCoO_3$ with a narrow size distribution.

1.2.2.3 Mechanical Synthesis

Wet-chemistry techniques often lead to the formation of precursor phases, and so, simultaneously have the effect of reducing the diffusion path length between the reagent ions. This is readily demonstrated by the use of lower temperatures during the calcination step, relative to the conventional high-temperature preparations. An alternative means of reducing the synthesis temperature can be sought through ball-milling a suitable mixture of crystalline reagents. By repeatedly subjecting a mixture of solid reagents to a combination of attritive and compressive forces, the overall size of the crystallites is reduced, typically to sub-micron dimensions,[20] whilst the concentration of crystal defects is increased. The latter often leads to the formation of an amorphous layer that encapsulates each crystallite, and it is the mixing of these amorphous regions through further collisions that can lead to nucleation and crystal growth of the target phase. Therefore, mechanical activation can sometimes lead directly to the formation of a target phase, *i.e.* without the formation of transitional phases that are typically associated with conventional high-temperature syntheses, albeit in a poorly crystalline state. This has been demonstrated for a number of lead-based perovskites such as $Pb(Mg_{1/3}Nb_{2/3})O_3$ and $Pb(Zr_{0.52}Ti_{0.48})O_3$,[21] and a series of lanthanum molybdates that include $La_2Mo_2O_7$, $La_2Mo_2O_9$ and $La_7Mo_7O_{30}$.[22, 23] In the case of $La_7Mo_7O_{30}$, this involved ball-milling a stoichiometric mixture of lanthanum oxide and molybdenum trioxide at room temperature for 12 hr using a tungsten carbide vial and ball set. During this reaction, molybdenum is partially reduced through contact with the tungsten carbide surfaces to give poorly crystalline

$La_7Mo_7O_{30}$. The crystallinity of this material could subsequently be improved by heat treating the sample at 800 °C under secondary vacuum. In other cases, subsequent thermal treatment has been employed to additionally improve the purity of a ball-milled sample, but at a temperature that is significantly lower than that employed in the corresponding high-temperature route. This has been demonstrated for the electrode material $LiMn_2O_4$,[24] whose preparation as a single-phase sample was achieved by firing the impure ball-milled sample at 700 °C. This can be compared with the significantly higher firing temperature of 900 °C that is used in the conventional high-temperature preparation of this material.

1.2.2.4 Self-propagating High-temperature Synthesis

Other more exotic synthetic approaches have employed high-energy starting materials in order to access pathways that lead to strongly exothermic reactions. These reactions occur in the solid state and are typically driven by metathesis or combustion. Solid-state metathesis reactions typically involve the reaction of one or more metal chlorides with an alkali metal oxide, and exploit the high lattice energy associated with the formation of the salt by-product to drive the reaction. This has been demonstrated for a series of lanthanide chromate and lanthanide iron oxides, $LnMO_3$ (Ln = La, Pr, Nd, Sm, Eu, Gd, Dy, Ho, Er or Yb; M = Cr or Fe),[25] and involves the same intimate mixing of the reagent powders as carried out in the conventional high-temperature preparations of these materials, but differs in that the exothermicity of the reaction reduces considerably the temperature of heat treatment from 1200 °C to 800 °C.[26]

If a metathesis reaction is sufficiently exothermic, the reagent mixture can be initiated from a point source, using a hot filament or naked flame, and lead to a self-propagating high-temperature reaction.[27] These reactions can rapidly reach temperatures in excess of 2000 °C, and run to completion within seconds. A number of simple binary oxides have been prepared in this way.[28-30] In the case of combustion synthesis, the reagent mixture can be ignited instead, and similarly leads to a high-temperature reaction front that propagates through the sample in a self-sustaining manner, as illustrated by the advancement of a solid flame over the surface of a reacting pellet in Figure 1.3. This has been demonstrated for a number of sodium-substituted lanthanum manganites, $La_{1-x}Na_xMnO_3$ ($x = 0 - 0.4$),[28] alkaline earth substituted lanthanum manganites $La_{1-x}A_xMO_3$ (A = Ca or Sr; $x = 0 - 0.4$),[29] and a series of lanthanide chromites, LnCrO$_3$.[26] In the case of $La_{0.6}Ca_{0.4}MnO_3$,[29] this involved pelleting a mixture of lanthanum oxide, manganese metal, calcium oxide, and sodium perchlorate, and subsequently igniting the pellet using a naked flame. The reaction between these reagents was driven by the exothermic oxidation of the manganese metal by oxygen, and so the presence of solid sodium perchlorate was deliberately chosen to act as an internal oxidising agent that provided a source of oxygen. This reaction proceeded to self-heat to a maximum temperature of 1900 °C and ran to completion within a period of *ca.* 35 s.

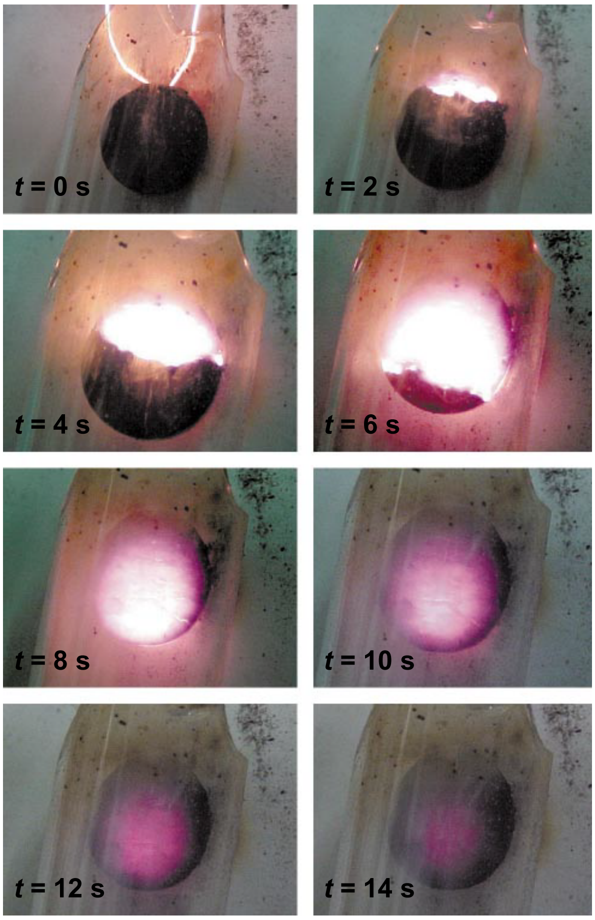

Figure 1.3 Outline of a combustion-type self-propagating high-temperature reaction from the point of ignition, during which the propagation of a high-temperature reaction front over the surface of the pellet can be observed.[30] These photographs were collected at two second intervals.

It is suggested by the authors that during this time, the sodium chloride by-product melts and acts as an internal wetting agent, allowing for enhanced mass transport of the reactants, before ultimately evaporating from the sample.

Self-heating high-temperature reactions can be similarly initiated using microwaves.[31] This method of heating exploits the interaction of microwaves with dielectric materials, and can lead to rapid internal or volumetric heating of a sample to temperatures in excess of 1200 °C. Consequently, microwaves can also be employed to rapidly synthesise materials. However, for the purpose of self-heating high-temperature synthesis, microwaves are employed instead to achieve ignition at the centre of the sample, such that the high-temperature front propagates radially outwards to the sample surface. This can help to sustain the propagation of the high-temperature front in weakly exothermic reactions, as well as influence the development of the microstructure of the product.

1.3 Direct Reaction between Solids at Room Temperature

This thesis reports the discovery of an unusual reaction that provides both a rapid and an efficient route to preparing discrete particles of lithium molybdate with a narrow size distribution. This reaction occurs between crystalline lithium hydroxide monohydrate and molybdenum trioxide, and proceeds upon contact between these two solids at room temperature. This reaction has been developed further to give an unusual method for replacing the protons in protonated Ruddlesden-Popper type layered perovskites with lithium cations, with stoichiometric control of the proton and lithium content.

1.4 References

1. A. R. West, *Basic Solid State Chemistry*, 2nd edn., John Wiley & Sons, Inc., Chichester, 2005.
2. W. H. Zachariasen, *J. Am. Chem. Soc.*, 1932, **54**, 3841-3851.
3. E. D. Zanotto, *Am. J. Phys.*, 1998, **66**, 392-395.
4. E. D. Zanotto and K. G. Prabhat, *Am. J. Phys.*, 1999, **67**, 260-262.
5. E. Komatsu, K. M. Smith, J. Dunkley, C. L. Bennett, B. Gold, G. Hinshaw, N. Jarosik, D. Larson, M. R. Nolta, L. Page, D. N. Spergel, M. Halpern, R. S. Hill, A. Kogut, M. Limon, S. S. Meyer, N. Odegard, G. S. Tucker, J. L. Weiland, E. Wollack and E. L. Wright, *Astrophys. J., Suppl. Ser.*, 2011, **192**, 18.
6. S. Hull, *Rep. Prog. Phys.*, 2004, **67**, 1233-1314.
7. E. Boaretto, X. Wu, J. Yuan, O. Bar-Yosef, V. Chu, Y. Pan, K. Liu, D. Cohen, T. Jiao, S. Li, H. Gu, P. Goldberg and S. Weiner, *Proc. Natl. Acad. Sci. U.S.A.*, 2009, **106**, 9595-9600.
8. W. E. Cameron, *Nature*, 1976, **264**, 736 - 738.
9. G. W. Brindley and M. Nakahira, *J. Am. Ceram. Soc.*, 1959, **42**, 319-324.
10. W. M. Carty and U. Senapati, *J. Am. Ceram. Soc.*, 1998, **81**, 3-20.
11. N. L. Bowen and J. W. Greig, *J. Am. Ceram. Soc.*, 1924, **7**, 238-254.
12. N. L. Bowen, J. W. Greig and E. G. Ziess, *J. Wash. Acad. Sci.*, 1924, **14**, 183-191.

13. M. Martinón-Torres, T. Rehren and I. C. Freestone, *Nature*, 2006, **444**, 437-438.

14. M. Inagaki, Y. Nishikawa and M. Sakai, *J. Eur. Ceram. Soc.*, 1992, **10**, 123-128.

15. C. Peng, L. Gao, S. Yang and J. Sun, *Chem. Commun.*, 2008, 5601-5603.

16. V. Thangadurai, C. Knittlmayer and W. Weppner, *Mater. Sci. Eng., B*, 2004, **106**, 228-233.

17. C. J. Brinker and G. W. Scherer, *Sol-Gel Science: The Physics and Chemistry of Sol-Gel Processing*, Academic Press, Inc., San Diego, 1990.

18. C. N. Chervin, B. J. Clapsaddle, H. W. Chiu, A. E. Gash, J. H. Satcher Jr. and S. M. Kauzlarich, *Chem. Mater.*, 2006, **18**, 1928-1937.

19. S. Ivanova, A. Senyshyn, E. Zhecheva, K. Tenchev, V. Nikolov, R. Stoyanova and H. Fuess, *J. Alloys Compd.*, 2009, **480**, 279-285.

20. M. A. Meyers, A. Mishra and D. J. Benson, *Prog. Mater Sci.*, 2006, **51**, 427-556.

21. J. Wang, J. M. Xue, D. M. Wan and B. K. Gan, *J. Solid State Chem.*, 2000, **154**, 321-328.

22. P. Lacorre and R. Retoux, *J. Solid State Chem.*, 1997, **132**, 443-446.

23. F. Goutenoire, R. Retoux, E. Suard and P. Lacorre, *J. Solid State Chem.*, 1999, **142**, 228-235.

24. W. T. Jeong, J. H. Joo and K. S. Lee, *J. Alloys Compd.*, 2003, **358**, 294-301.

25. I. P. Parkin, A. V. Komarov and Q. Fang, *Polyhedron*, 1996, **15**, 3117-3121.

26. M. V. Kuznetsov and I. P. Parkin, *Polyhedron*, 1998, **17**, 4443-4450.

27. I. P. Parkin, *Transition Met. Chem.*, 2002, **27**, 569-573.

28. M. V. Kuznetsov, I. P. Parkin, D. J. Caruana and Y. G. Morozov, *Mendeleev Commun.*, 2006, **16**, 36-38.

29. M. V. Kuznetsov, I. P. Parkin, D. J. Caruana and Y. G. Morozov, *J. Mater. Chem.*, 2004, **14**, 1377-1382.

30. I. P. Parkin, Q. A. Pankhurst, L. Affleck, M. D. Aguas and M. V. Kuznetsov, *J. Mater. Chem.*, 2001, **11**, 193-199.

31. J.-H. Peng, J. Binner and S. Bradshaw, *Mater. Sci. Technol.*, 2002, **18**, 1419-1427.

2 Literature Review

The compounds investigated in this thesis relate to lithium molybdate and a series of Ruddlesden-Popper type layered perovskites. This chapter presents an overview of lithium molybdate and related structures, as well as of layered perovskites and their reactivity.

2.1 Lithium Molybdate and Related Structures

2.1.1 Lithium Molybdate

Lithium molybdate, Li_2MoO_4, is primarily used as an additive to inhibit corrosion in industrial refrigeration systems,[1] but has been shown to be an effective catalyst for the oxidation of both methane[2] and methanol.[3] The material has also been shown to be a potential candidate as a scintillation detector for rare nuclear processes.[4] Lithium molybdate crystallises in the space group $R\overline{3}$ with the phenacite structure-type,[5, 6] and is constituted of approximately regular LiO_4 and MoO_4 tetrahedra that are connected by trigonally coordinated oxide anions in a corner-sharing network. These tetrahedral units are distributed in a fully ordered manner such that each MoO_4 unit is connected to eight LiO_4 units, whilst each LiO_4 unit is connected to a combination of four LiO_4 and four MoO_4 units, as illustrated in Figure 2.1.

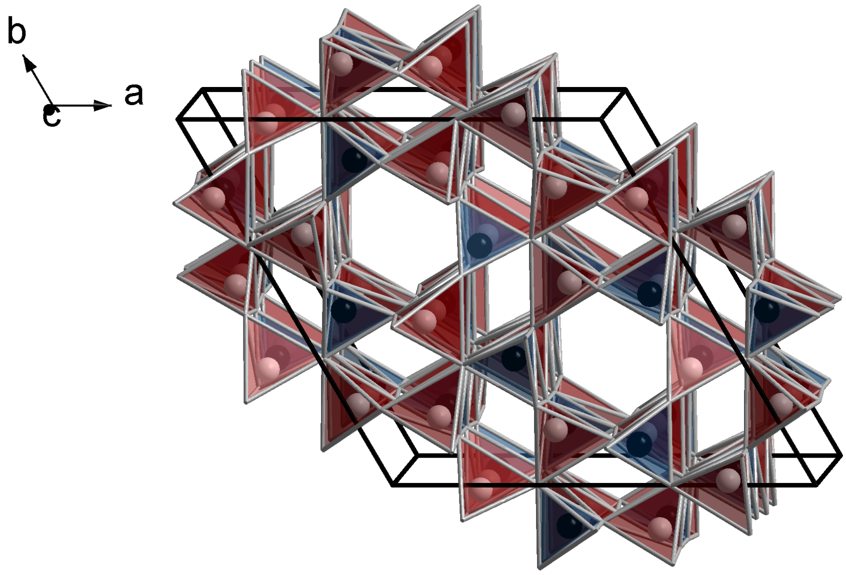

Figure 2.1 Crystal structure of Li_2MoO_4[5, 6] showing the arrangement of the MoO_4 (blue) and LiO_4 (red) tetrahedra.

2.1.2 Lithium Tungstate

Under ambient conditions, lithium tungstate, Li_2WO_4 I, is isostructural with lithium molybdate.[5] However, unlike the molybdate analogue, the tungstate undergoes a number of structural transformations under non-ambient conditions of either temperature or pressure, or both, to give three polymorphs: Li_2WO_4 II,[7] Li_2WO_4 III[8] and Li_2WO_4 IV.[9] Li_2WO_4 II crystallises in the space group $I4_1/amd$,[7] and is related to the spinel-type structure. The oxide anions form a face-centred cubic array in which the tungsten cations and one equivalent of lithium cations, Li(2), occupy octahedral oxide environments, whilst the remaining equivalent of lithium cations, Li(1), occupies a tetrahedral oxide environment. The $Li(2)O_6$ units form a edge-sharing network, as illustrated in Figure 2.2(i), around which the WO_6 and $Li(1)O_4$ units are connected *via* edge-sharing and corner-sharing, respectively. The distribution of the tungsten and Li(2) cations gives rise to a combination of W_4O_{16} tetramers (formed by edge-sharing) and Li_4O_{12} tetramers (formed by corner-sharing), as illustrated in Figure 2.2(ii).

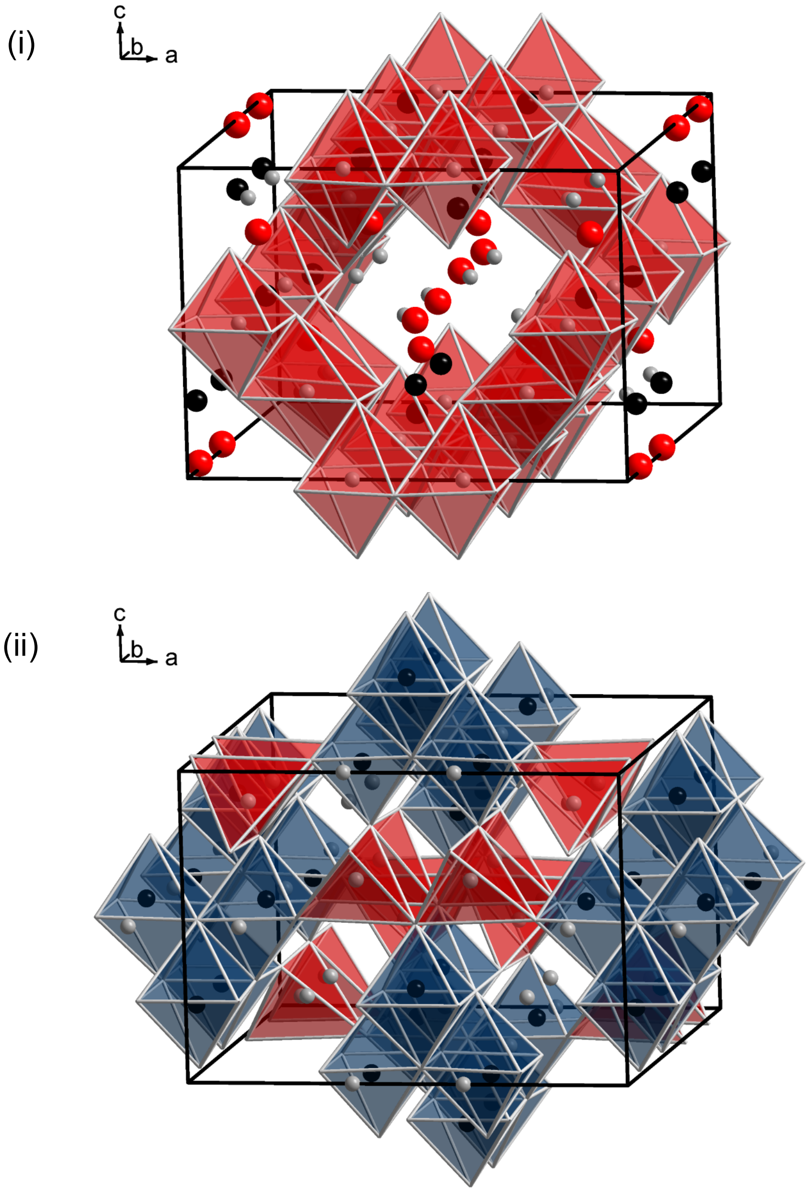

Figure 2.2 Crystal structures of Li_2WO_4 II[7] showing the arrangements of (i) the $Li(2)O_6$ (red) octahedra, and (ii) the $Li(1)O_4$ (red) and WO_6 (blue) polyhedra.

The second polymorph, Li_2WO_4 III, crystallises in the space group *Pnnm*,[8] and consists of a hexagonal close-packed array of oxide anions in which the tungsten cations occupy octahedral oxide environments. The distribution of the tungsten cations gives rise to edge-sharing W_4O_{16} tetramers, as illustrated in Figure 2.3, similarly to Li_2WO_4 II. However, this cluster differs from the W_4O_{16} tetramer reported for Li_2WO_4 II in that the four tungsten cations adopt a co-planar arrangement that is parallel to the (100) plane. The positions of the lithium cations were unable to be located in this study, but it has been suggested by the authors of this study that these cations probably occupy the vacant octahedral interstices so as to form a continuous, three-dimensional framework structure.

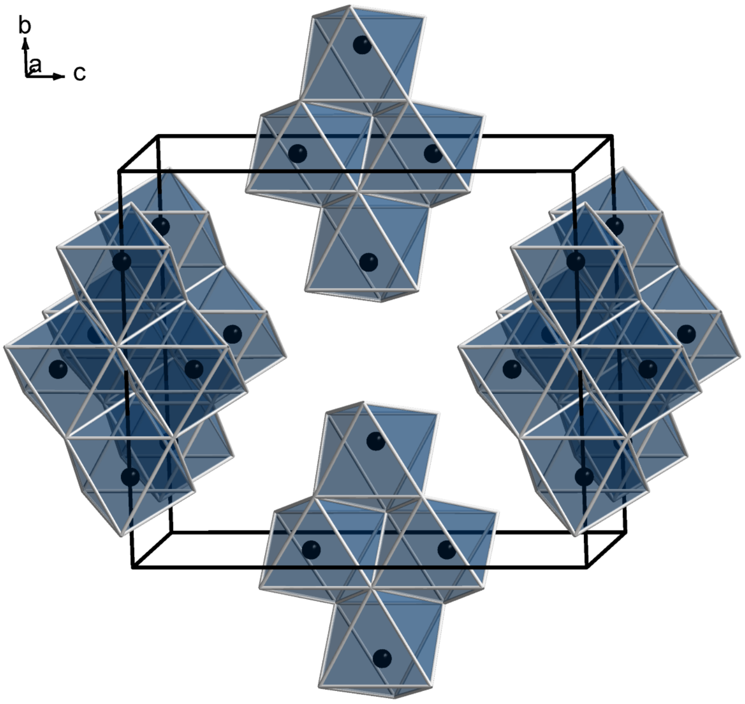

Figure 2.3 Crystal structure of Li_2WO_4 III[8] showing the arrangement of the WO_6 (blue) tetrahedra. The positions of the lithium cations are unknown, but it has been suggested[8] that these cations occupy the vacant octahedral interstices in between the edge-sharing W_4O_{16} tetramers.

The densest lithium tungstate polymorph, Li_2WO_4 IV, crystallises in the space group $C12/c1$,[9] and is related to the wolframite structure-type. The structure of Li_2WO_4 IV is similar to that of Li_2WO_4 III in that the former also consists of a hexagonal close-packed array of oxide anions in which the lithium and tungsten cations occupy octahedral oxide environments. However, the distribution of these cations differs considerably from that reported for Li_2WO_4 III, and gives rise to alternating layers of LiO_6 and WO_6 octahedra along the [100] direction, as illustrated in Figure 2.4; these layers are connected to one another by both face- and corner-sharing. The LiO_6 layers consist of an edge-sharing net of LiO_6 octahedra, whilst the WO_6 layers consist of chains of edge-sharing WO_6 octahedra that zig-zag parallel to (100) plane in the [001] direction.

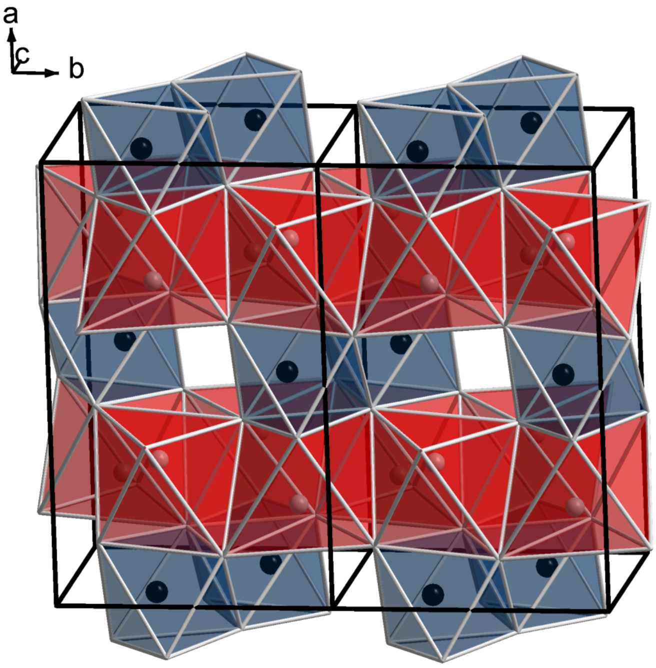

Figure 2.4 Crystal structure of Li_2WO_4 IV[9] showing the arrangement of the LiO_6 (red) and WO_6 (blue) octahedra.

2.1.3 Hydrated Lithium Tungstate

Whilst lithium molybdate is not known to exist in any hydrous form, Li_2WO_4 I readily transforms to $Li_2WO_4 \cdot {}^4\!/_7\, H_2O$ under a hydrated atmosphere.[10] The structure of this hydrated phase is described in the space group $P\overline{4}3m$,[11] and differs considerably from that of the anhydrous phase in that the tungsten cations occupy two different oxide environments: as isolated WO_4 tetrahedra on the edges of the unit cell, and as WO_6 octahedra that form an edge-sharing tetramer, as illustrated in Figure 2.5. The latter encapsulates a lithium cation, and so, gives rise to a lithium-tungsten separation of 2.075 Å, which is very short considering that the average lithium oxide

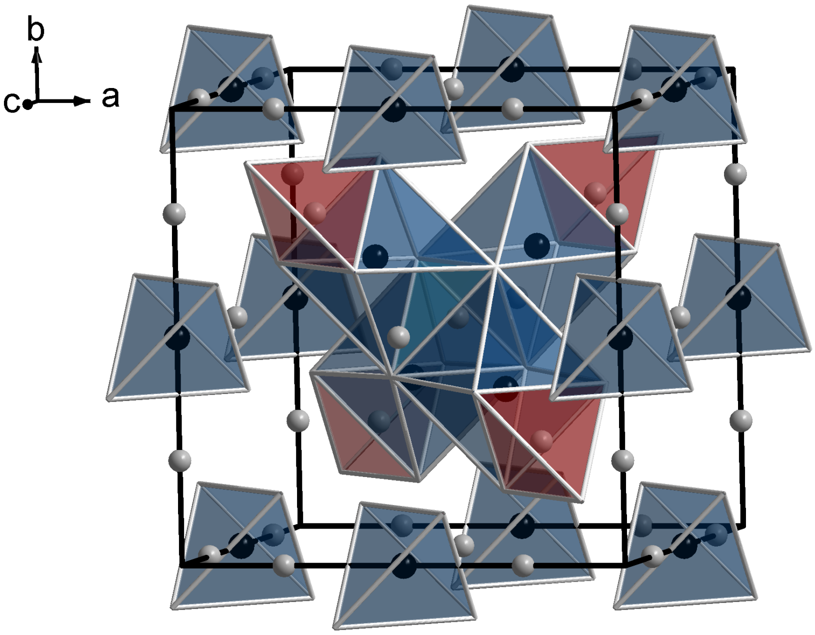

Figure 2.5 Crystal structure of $Li_2WO_4 \cdot {}^4\!/_7\, H_2O$[11] showing the arrangement of the tungsten oxide polyhedra (blue) and selected LiO_4 tetrahedra (red). The remaining lithium oxide tetrahedra are not shown for clarity, but the corresponding Li^+ cations are indicated by a grey sphere.

separation is 1.968 Å.[12] Accordingly, the tungsten cations located in these 6-coordinate sites are displaced away from the central lithium cation to reflect the strong intercationic repulsions. Interestingly, lithium occupies three other crystallographically distinct sites, all in tetrahedral oxide coordination. One of these LiO_4 units also shares a face with a WO_6 unit, and gives rise to an even shorter intercation separation of 1.528 Å. However, given these non-physical intercation separations and the fact that the scattering intensity from lithium cations cannot be confidently assigned on the basis of laboratory X-ray diffraction data, it is likely that the structure of $Li_2WO_4 \cdot \frac{4}{7} H_2O$ was incorrectly determined.

2.1.4 Sodium Molybdate: Anhydrous and Dihydrate

Both sodium molybdate, Na_2MoO_4, and the corresponding dihydrate, $Na_2MoO_4{\cdot}2H_2O$, feature isolated MoO_4 units that are connected to the surrounding lattice by corner-sharing oxide anions, similarly to lithium molybdate. However, sodium molybdate crystallises with the normal spinel-type structure, as described in the space group $Fd\overline{3}m$,[13] and so the surrounding lattice is composed, instead, of an edge-sharing network of approximately regular NaO_6 octahedra, where each oxide anion in the MoO_4 unit is coordinated to a combination of three Na sites and one Mo site, as illustrated in Figure 2.6.

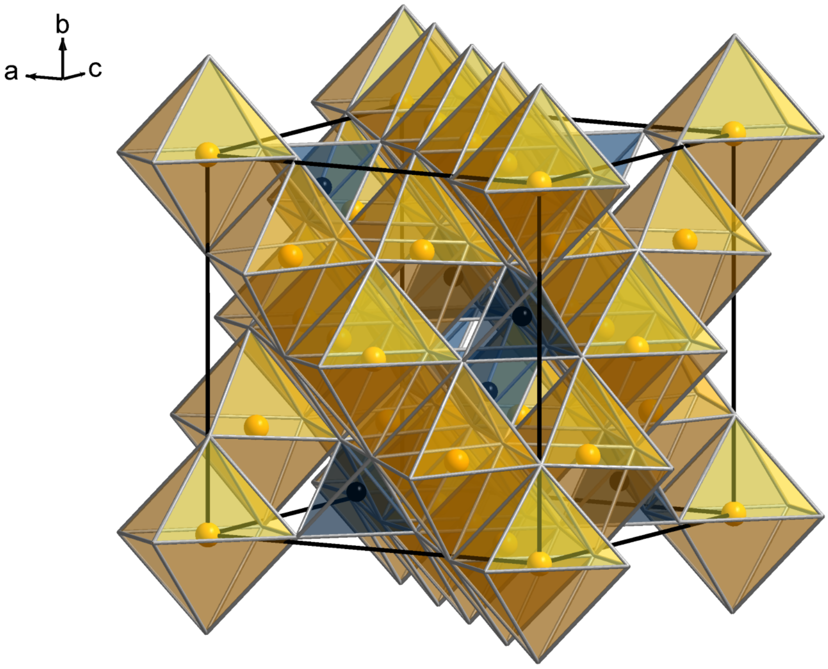

Figure 2.6 Crystal structure of Na_2MoO_4[13] showing the arrangement of the MoO_4 (blue) and NaO_6 (orange) polyhedra.

By contrast, the hydrous form of sodium molybdate crystallises with the wolframite structure-type, as described in the space group *Pbca*,[14] and can be considered to be built-up from alternate layers of isolated MoO_4 units and water of crystallisation, as illustrated in Figure 2.7. These layers are held together by two crystallographically distinct sodium oxide polyhedra: an approximately regular NaO_6 octahedron, and a highly distorted NaO_5 trigonal bipyramid. Each of these sodium sites is surrounded by two oxide anions that are associated with water of crystallisation, whilst the remaining oxide anions are shared with neighbouring MoO_4 tetrahedra.

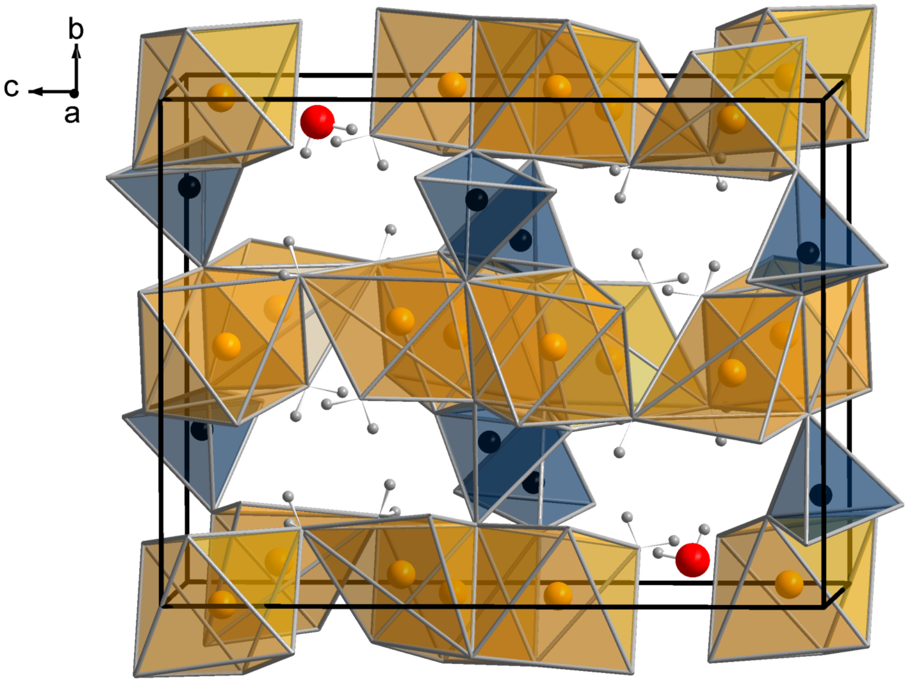

Figure 2.7 Crystal structure of $Na_2MoO_4{\cdot}2H_2O$[14] showing the arrangement of the MoO_4 (blue) and the sodium oxide (orange) polyhedra. Protons and oxide anions associated with water of crystallisation are indicated by grey and red spheres respectively.

2.1.5 Li*RE*$(MoO_4)_2$ and Na_5*RE*$(MoO_4)_4$

Other compounds that are related to lithium molybdate through the presence of isolated MoO_4 tetrahedra include a series of lithium rare earth double molybdates, Li*RE*$(MoO_4)_2$ (*RE* = Ce, Nd or Y),[6, 15] and the sodium yttrium analogue $NaY(MoO_4)_2$.[16] These compounds are isomorphous and crystallise with a scheelite-type ($CaWO_4$)[17] structure, as described in the space group $I4_1/a$. In the case of $NaY(MoO_4)_2$, the sodium and yttrium cations are disordered over the 8-coordinate site (the Ca site in $CaWO_4$), and give rise to an edge-sharing network of $(Na/Y)O_8$ polyhedra. The MoO_4 units are connected to this network by corner-sharing *via* trigonally coordinated oxide anions, such that each oxide anion is coordinated to a combination of one Mo site and two disordered Na/Y sites, as illustrated in Figure 2.8. By comparison, each oxide anion in the isostructural compound $SrMoO_4$ is trigonally coordinated to one Mo site and two Sr sites.[18]

A series of molybdates with the formula Na_5*RE*$(MoO_4)_4$ (*RE* = La, Tb, Lu or Y)[16, 19-21] adopt a structure that is related to, but more complex than, scheelite. For the corresponding sodium yttrium molybdate, $Na_5Y(MoO_4)_4$, this structure can be derived from that of the double molybdate by increasing the ratio of sodium to yttrium cations that are distributed over the 8-coordinate sites, and then ordering these cations such that every fifth site is occupied by yttrium, whilst the remaining sites adapt to accommodate sodium in a highly distorted octahedral geometry, as

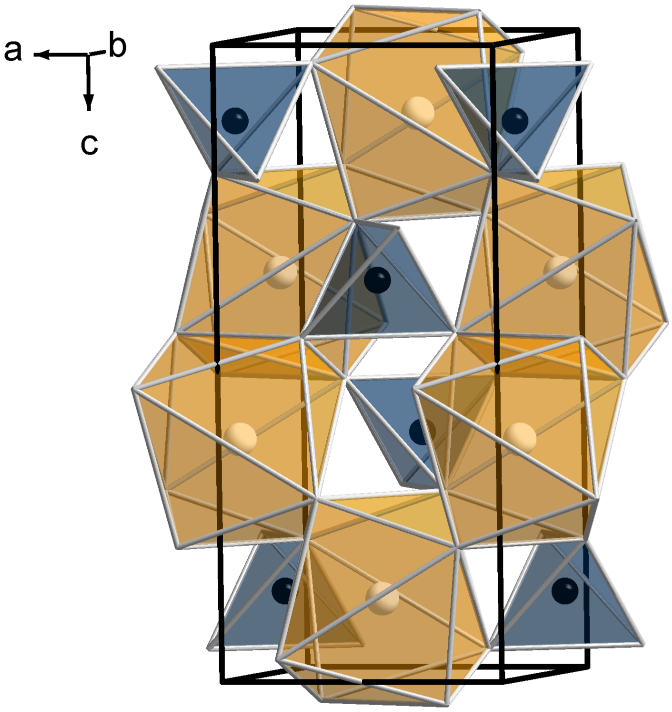

Figure 2.8 Crystal structure of $NaY(MoO_4)_2$[16] showing the arrangement of the MoO_4 (blue) and $(Na/Y)O_8$ (orange) polyhedra.

illustrated in Figure 2.9(i). An additional, crystallographically distinct, sodium site is also present in the structure of $Na_5Y(MoO_4)_4$, and can be derived by replacing every fifth molybdenum in the double-molybdate structure with sodium. However, these sodium cations are coordinated by oxide anions that are shared with the neighbouring MoO_4 tetrahedra, and so, whilst the MoO_4 units remain isolated, each NaO_4 unit is connected, instead, to four MoO_4 units, as illustrated in Figure 2.9(ii).

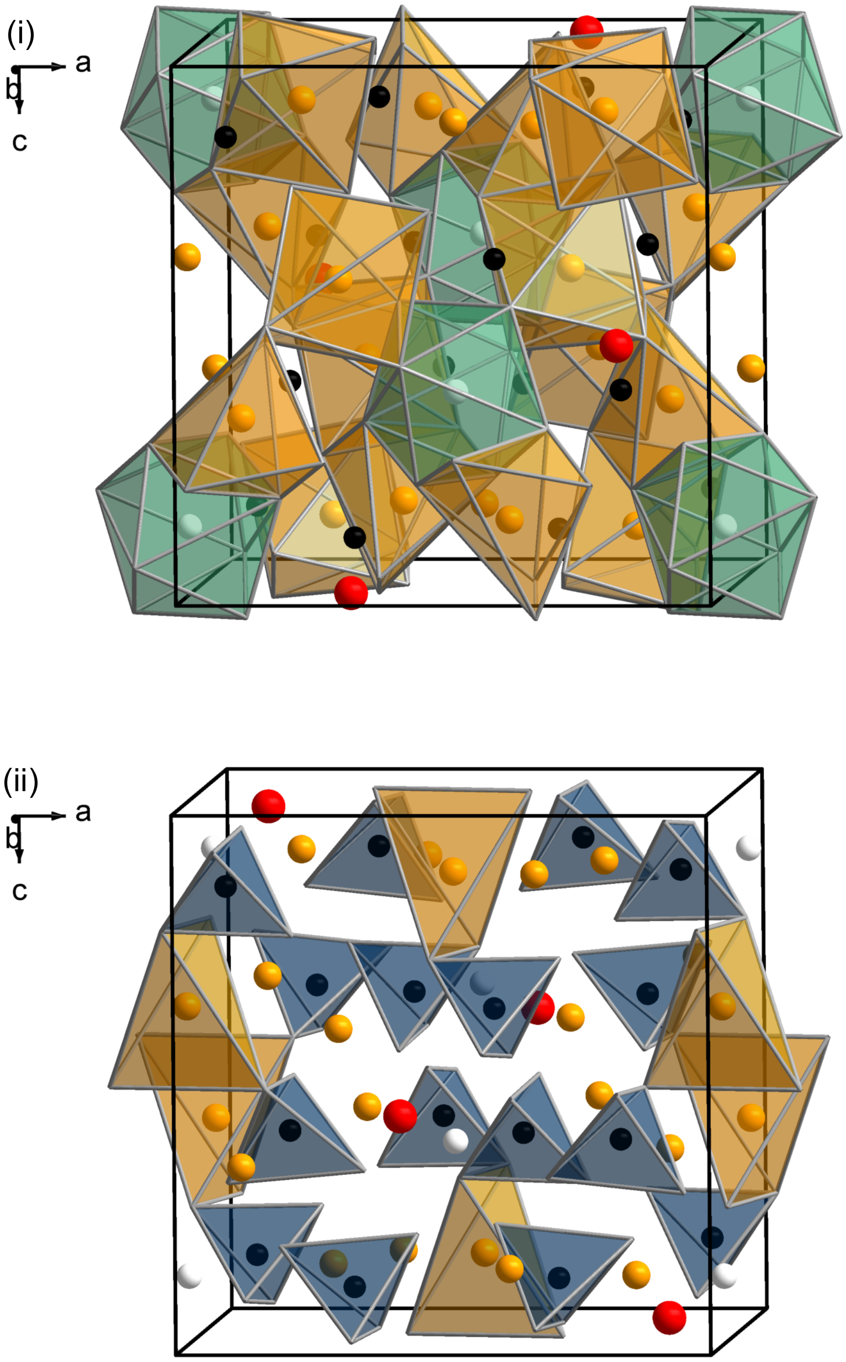

Figure 2.9 Crystal structures of $Na_5Y(MoO_4)_4$[16] showing the arrangements of (i) the YO_8 (green) and NaO_6 (orange) polyhedra, and (ii) the MoO_4 (blue) and NaO_4 (orange) tetrahedra.

The α-polymorph of $LiLa(MoO_4)_2$, whilst chemically related to the other lithium rare earth double molybdates, is not isostructural, and represents, instead, an orthorhombic modification that differs significantly from the structure of scheelite. This structure was reported by Klevtsova almost 40 years ago,[22] and describes the molybdenum cations as being equally distributed over two crystallographically distinct 4-coordinate sites with tetrahedral geometries; the former being approximately regular, and the latter being slightly distorted, as illustrated in Figure 2.10. These MoO_4 units remain isolated from one another, similarly to Li*RE*$(MoO_4)_2$ (*RE* = Ce, Nd or Y).

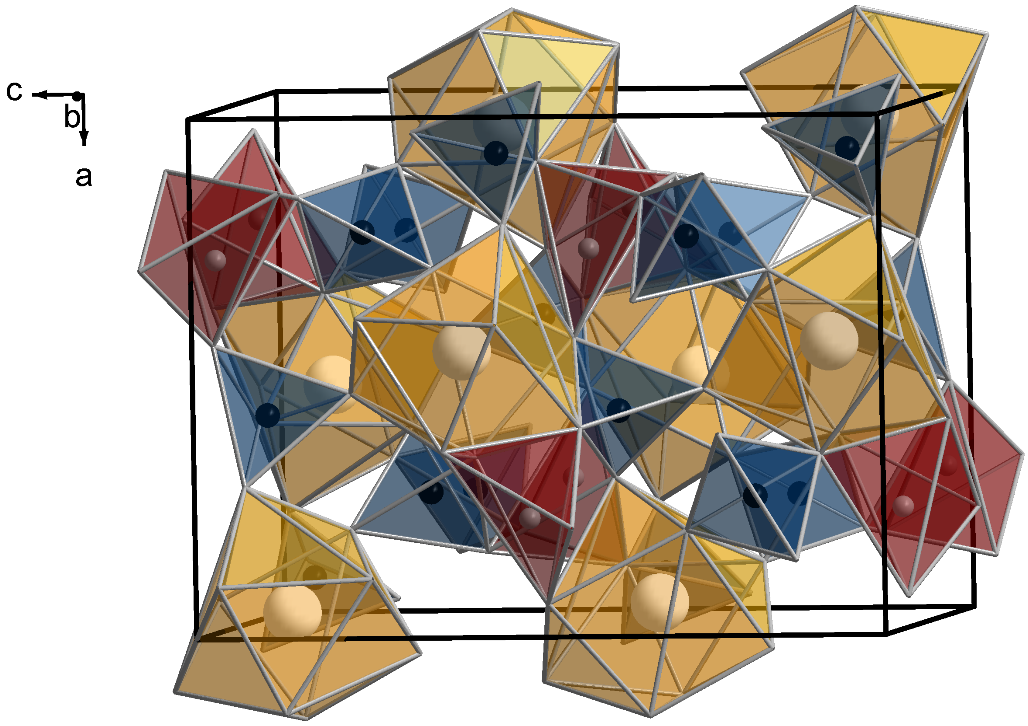

Figure 2.10 Crystal structure of α-$LiLa(MoO_4)_2$[22] showing the arrangement of the MoO_4 (blue), LaO_9 (orange) and LiO_5 (red) polyhedra.

However, here the resemblance to the scheelite-type structure ends, since the rare earth cation no longer occupies an 8-coordinate site that gives rise to a framework of edge-sharing $RE\mathrm{O}_8$ polyhedra. The study by Klevtsova found that lanthanum occupies a 9-coordinate site instead, such that pairs of LaO_9 polyhedra share a common edge to give isolated, dimeric units. Consequently, the framework of α-$\mathrm{LiLa(MoO_4)_2}$ is comprised of $\mathrm{Mo(1)O_4}$, $\mathrm{Mo(2)O_4}$ and $\mathrm{La_2O_{16}}$ units, where the first $\mathrm{MoO_4}$ unit is connected to four $\mathrm{La_2O_{16}}$ units through common apices, and the second $\mathrm{MoO_4}$ unit is connected to three $\mathrm{La_2O_{16}}$ units; two through common apices and the third through a common edge. The lithium cations are connected to this molybdenum and lanthanum framework by both corner-sharing and edge-sharing, and occupy an unusual, 5-coordinate site with a highly distorted trigonal-bipyramidal geometry.

2.1.6 Cerium Niobate

Cerium niobate, $\mathrm{CeNbO_4}$, crystallises with the fergusonite-type structure, as described in the space group $I2_1/a$,[23] and is a monoclinic distortion of the scheelite structure. This modification retains the lanthanide cation on an 8-coordinate site, which gives rise to an edge-sharing network of $\mathrm{CeO_8}$ polyhedra. Interestingly, however, the niobium cation occupies a 6-coordinate site with an unusual coordination geometry, as illustrated in Figure 2.11. This coordination environment is derived from the

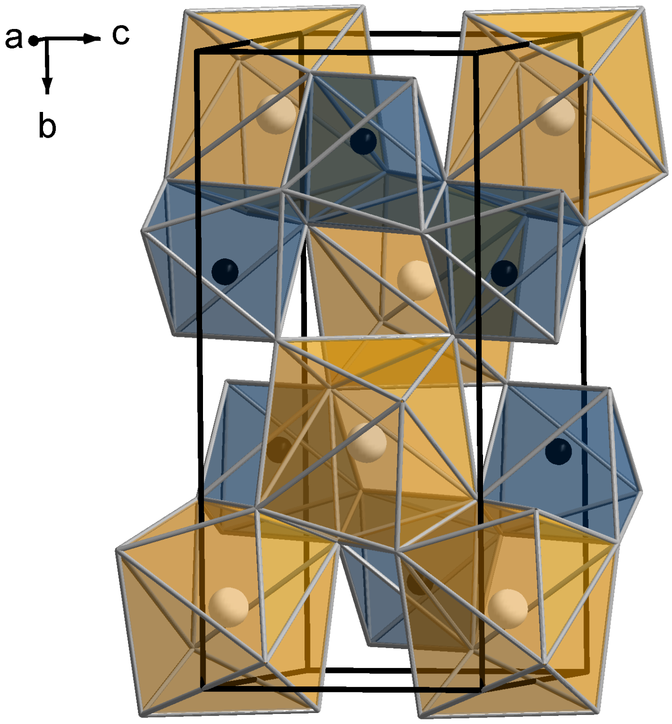

Figure 2.11 Crystal structure of $CeNbO_4$[23] showing the arrangement of the NbO_6 (blue) and CeO_8 (orange) polyhedra.

niobium cation being surrounded by eight oxide anions in an arrangement that can be described as two interpenetrating tetrahedra, *i.e.* with additional oxide anions capping each of the faces of a normal tetrahedron. However, two of these Nb-O distances are too long to be considered involved in bonding, and so, give rise to an unusual 6-coordinate geometry. Consequently, these CeO_8 and NbO_6 polyhedra are connected by both corner-sharing and edge-sharing *via* two crystallographically distinct oxide anions: one that is coordinated to two Nb sites and another that is trigonally coordinated to a combination of one Nb site and two Ce sites.

2.2 Structure and Reactivity of Layered Perovskites

2.2.1 Introduction

Layered perovskite compounds are derivatives of the ideal ABX_3 perovskite structure,[24] where A is a large cation such as an alkaline earth metal, B is a smaller cation such as a transition metal, and X is an anion such as oxide. Of these, the most investigated are three homologous series of compounds whose arrangement of perovskite layers ($A_{n-1}B_nX_{3n+1}$) occurs parallel to the (001) planes. These compounds belong to the Ruddlesden-Popper series, $A'_2[A_{n-1}B_nX_{3n+1}]$,[25, 26] the Dion-Jacobson series, $A'[A_{n-1}B_nX_{3n+1}]$,[27, 28] and the Aurivillius series, $(Bi_2O_2)[A_{n-1}B_nX_{3n+1}]$.[29, 30] The structures of these compounds are built-up of n layers of a corner-sharing framework of BX_6 octahedra, in which A-site cations are located in the 12-fold cuboctahedral interstitial sites. These perovskite layers are then interleaved with A'-site cations or bismuth-oxide intergrowths, as illustrated in Figure 2.12.

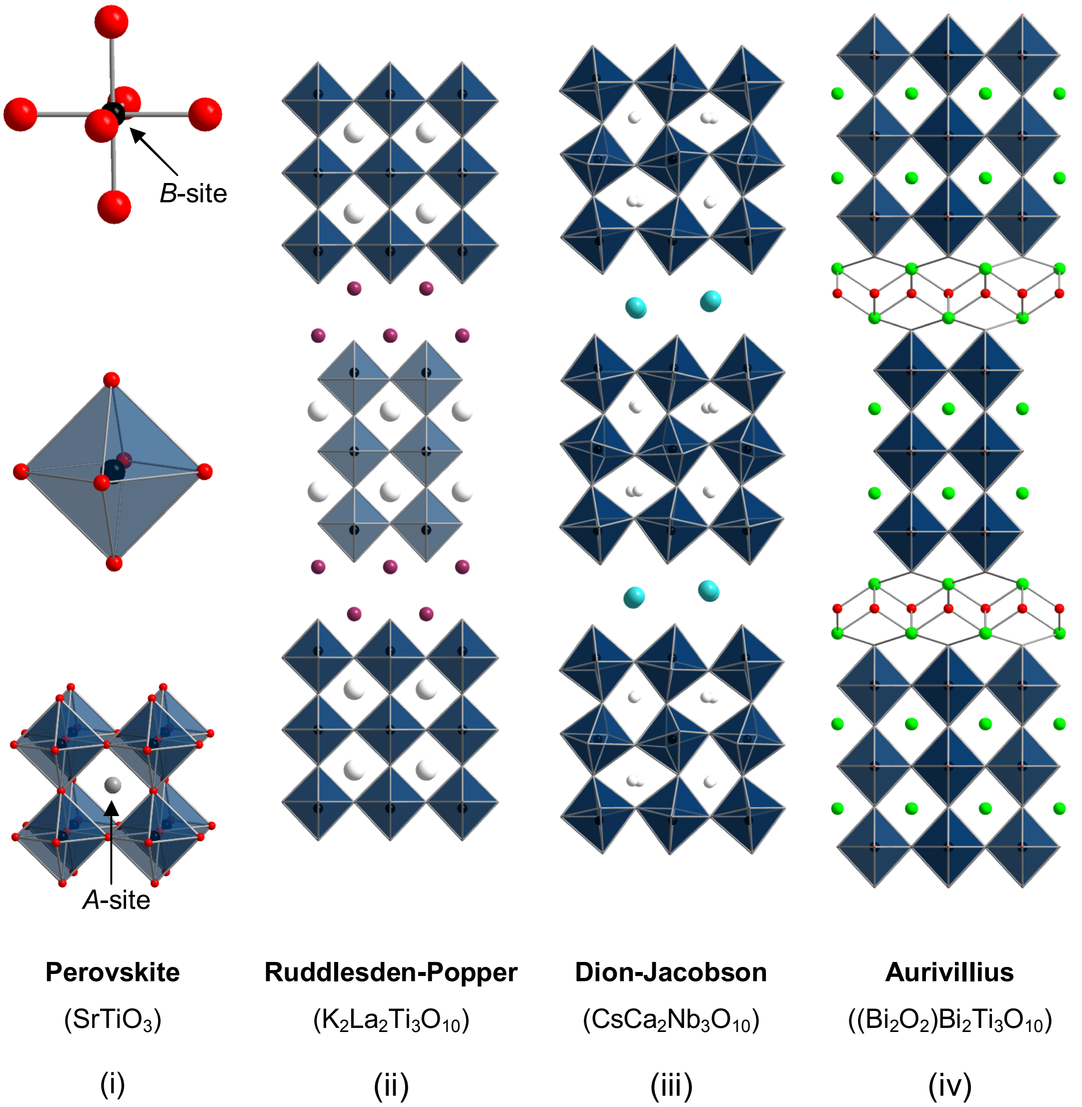

Perovskite ($SrTiO_3$) (i)

Ruddlesden-Popper ($K_2La_2Ti_3O_{10}$) (ii)

Dion-Jacobson ($CsCa_2Nb_3O_{10}$) (iii)

Aurivillius ($(Bi_2O_2)Bi_2Ti_3O_{10}$) (iv)

Figure 2.12 Crystal structures of (i) perovskite ($SrTiO_3$),[31] together with the (ii) Ruddlesden-Popper ($K_2La_2Ti_3O_{10}$),[32] (iii) Dion-Jacobson ($CsCa_2Nb_3O_{10}$),[33] and (iv) Aurivillius ($(Bi_2O_2)Bi_2Ti_3O_{10}$)[30] layered derivatives. The perovskite layers in these compounds are interleaved with layers of alkali metal *A′*-site cations or $(Bi_2O_2)^{2+}$ intergrowths. Sr^{2+}, K^+, La^{3+}, Cs^+, Ca^{2+}, Bi^{3+} and O^{2-} ions are represented by grey, purple, white, turquoise, white, green and red spheres, respectively, whilst TiO_6 and NbO_6 octahedra are indicated by blue units.

2.2.2 Ruddlesden-Popper Compounds, $A'_2[A_{n-1}B_nX_{3n+1}]$

The Ruddlesden-Popper family of layered perovskites represents a homologous series of compounds given by the general formula $A'_2[A_{n-1}B_nX_{3n+1}]$, where $n = \infty$ corresponds to the ideal ABX_3 perovskite structure. The structures of these layered compounds can be derived from the ABX_3 perovskite structure *via* a crystallographic shear along the (001) plane to give an integral framework of corner-sharing BX_6 octahedra on one face, and a similar framework with missing apical oxide anions on the opposing face. This anion deficiency is compensated for by interleaving a single AX unit between the sheared layers, which both restores the integrity of the BX_6 octahedra and offsets the adjacent perovskite layers by ½**a**+½**b**, as illustrated in Figure 2.12(ii). This offset results in the apical anions of the BX_6 octahedra lying directly above or below an A-site cation in the interlayer region, and so, gives rise to two sheets of metal oxide which can be considered to have a distorted rock-salt type structure. Consequently, the A-site cations in the interlayer region can be described as occupying a crystallographically distinct site, A', of 9-fold coordination, whilst the A-site cations within the perovskite layer remain in the ideal A-site of 12-fold coordination.

The $n = 1$ - 3 homologues of the Ruddlesden-Popper series have been prepared for a variety of metal-oxide compositions.[24] Higher-order homologues in this series have yet to be produced as single phases *via* traditional high-temperature solid-state routes. However, by using pulsed-laser deposition, the layer-by-layer growth of metastable, thin-film heterostructures can be carried out. This has been demonstrated for a number of $n = 4 - 6$ compounds.[34, 35]

The $n = 1$ compounds of the general formula A'_2BX_4 represent the end member of this homologous series, and, in the absence of octahedral tilting, crystallise with the K_2NiF_4 structure-type, as described in the space group *I*4/*mmm*. Single-layered Ruddlesden-Popper compounds exist for a large number of compositions, and have been shown to exhibit cation ordering at both the *A'*- and *B*-sites. In the case of the Na*RE*TiO_4 (*RE* = La, Pr, Nd, Sm, Eu, Gd, Y or Lu) series of compounds,[36-38] which are described by the formula $A'_2[BX_4]$, the structure adopts an unusual ordering of the *A'*-site cations, where the sodium and rare earth cations alternate between the perovskite layers, as illustrated in Figure 2.13. This ordering reduces the symmetry of the La-, Pr- and Nd-containing compounds to *P*4/*nmm*. For the smaller rare earth analogues, this ordering is coupled with tilting of the TiO_6 octahedra, such that these structures can be described, instead, in the orthorhombic space group *Pbcm*.

The ordering of the *A'*-site cations in the Na*RE*TiO_4 series of compounds has been attributed to the large difference in charge between the sodium and rare earth cations. This charge imbalance is compensated for by a displacement of the titanium cations towards the sodium rock-salt layer. In the case of the $n = 3$ homologues, this displacement is observed only for the outer layers of BX_6 octahedra, and so the *B*-site cations in the centre of the perovskite layer remain undistorted. This distortion of the BX_6 octahedra is a very common feature of both Ruddlesden-Popper and Dion-Jacobson compounds that exhibit *A'*-site ($n = 1$) or *A'*- and *A*-site ($n > 1$) ordering.[24]

By contrast, the TiO_6 polyhedra in the archetypal Ruddlesden-Popper compounds Sr_2TiO_4 (n = 1)[25] and $Sr_3Ti_2O_7$ (n = 2)[26] exhibit an almost regular octahedral geometry.

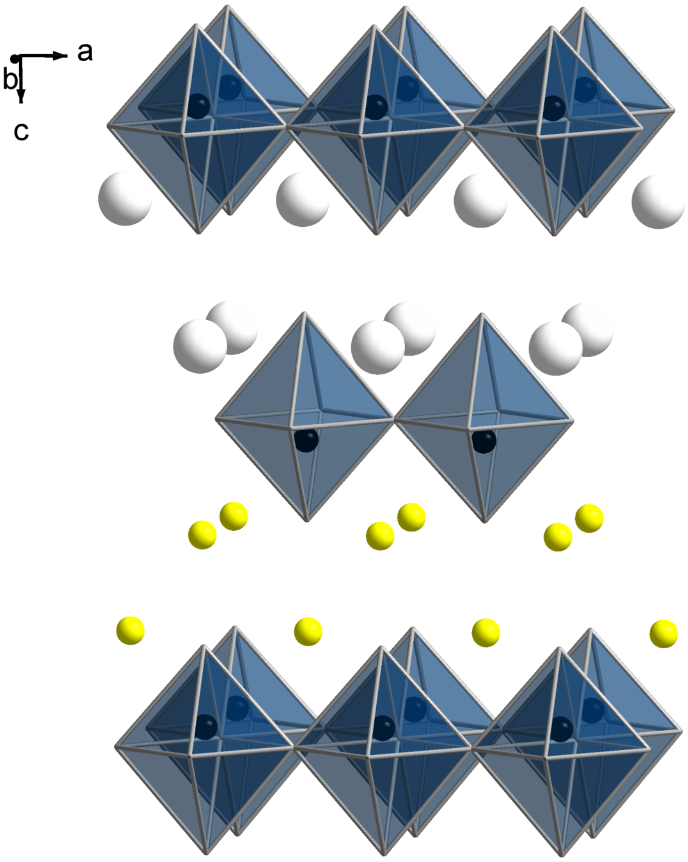

Figure 2.13 Crystal structure of the Ruddlesden-Popper layered perovskite $NaLaTiO_4$,[36-38] illustrating the *A′*-site ordering of Na^+ (yellow spheres) and La^{3+} (white spheres) cations between single-layer thick sheets of corner-sharing TiO_6 octahedra (blue units) .

2.2.2.1 Lithium- and Proton-containing Derivatives of the Ruddlesden-Popper Compounds

Lithium cations are too small to occupy the 9-coordinate site that is usually associated with *A′*-site cations in the aristotypical Ruddlesden-Popper structure, and inhabit, instead, a more suitably sized, 4-coordinate site with an unusual, flattened tetrahedral geometry, as illustrated for the case of $Li_2SrTa_2O_7$ in Figure 2.14. These units form an edge-sharing network of LiO_4 tetrahedra in the interlayer, and so, can be considered to be related to both the Ruddlesden-Popper and Dion-Jacobson structure-types. The formation of a derivative structure such as this has been ascribed to the small ionic radius of the lithium cation, and has been confirmed by neutron diffraction studies of the $n = 2$ compounds $Li_2SrTa_2O_7$[39] and $Li_2La_{2/3}Ta_2O_7$.[40]

In the case of $Li_2SrTa_2O_7$, rows of TaO_6 octahedra along the [001] direction exhibit an equal tilt in opposite directions relative to non-tilted octahedra in an *I*4/*mmm* compound such as $K_2SrTa_2O_7$.[41] This tilting reduces the symmetry of the structure to *Cmcm*. Tilting of these TaO_6 octahedra also gives rise to a cooperative distortion of the LiO_4 tetrahedra, such that a fifth neighbouring oxide anion is brought to within a distance of *ca.* 2.4 Å of the lithium site. Therefore, the coordination of the lithium cation could be considered as intermediate between tetrahedral and square pyramidal. It has been shown that with heating, the tilting of these TaO_6 octahedra progressively decreases until, at 230 °C, the structure of $Li_2SrTa_2O_7$ can be described in the aristotypical *I*4/*mmm* space group.

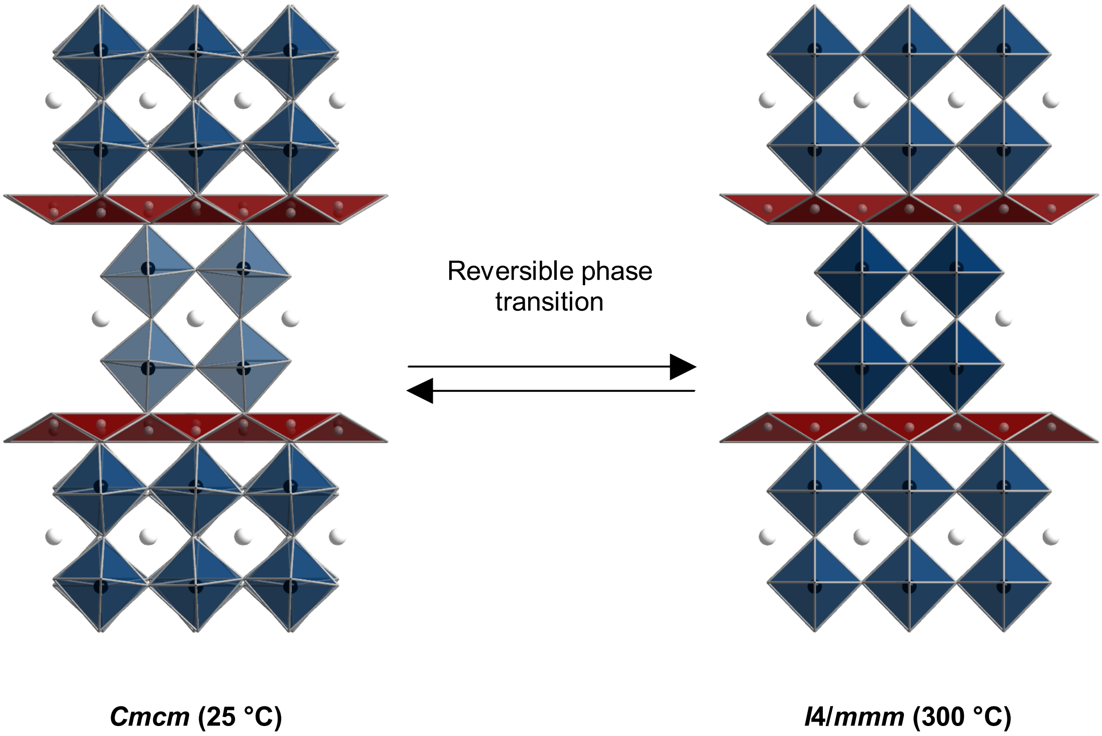

Figure 2.14 Crystal structures of $Li_2SrTa_2O_7$ at room temperature and 300 °C.[39] At room temperature, the structure exhibits equal tilting of the TaO_6 octahedra in opposite directions along the [001] direction. Sr^{2+} cations are represented by white spheres, whilst LiO_4 and TiO_6 polyhedra are indicated by red and blue units, respectively.

It has also been noted that the reduced interlayer separation in these lithium-containing compounds prevents the insertion of water.[32, 42] For example, the $n = 3$ lithium lanthanum titanate $Li_2La_2Ti_3O_{10}$ exhibits an interlayer separation of *ca.* 1.2 Å, as illustrated in Figure 2.15, and does not absorb water even in the event of being washed and left to dry at room temperature. By contrast, the potassium analogue exhibits a larger interlayer separation of *ca.* 2.8 Å, and as such, readily hydrates at room temperature to give $K_2La_2Ti_3O_{10}\cdot 2H_2O$.[32]

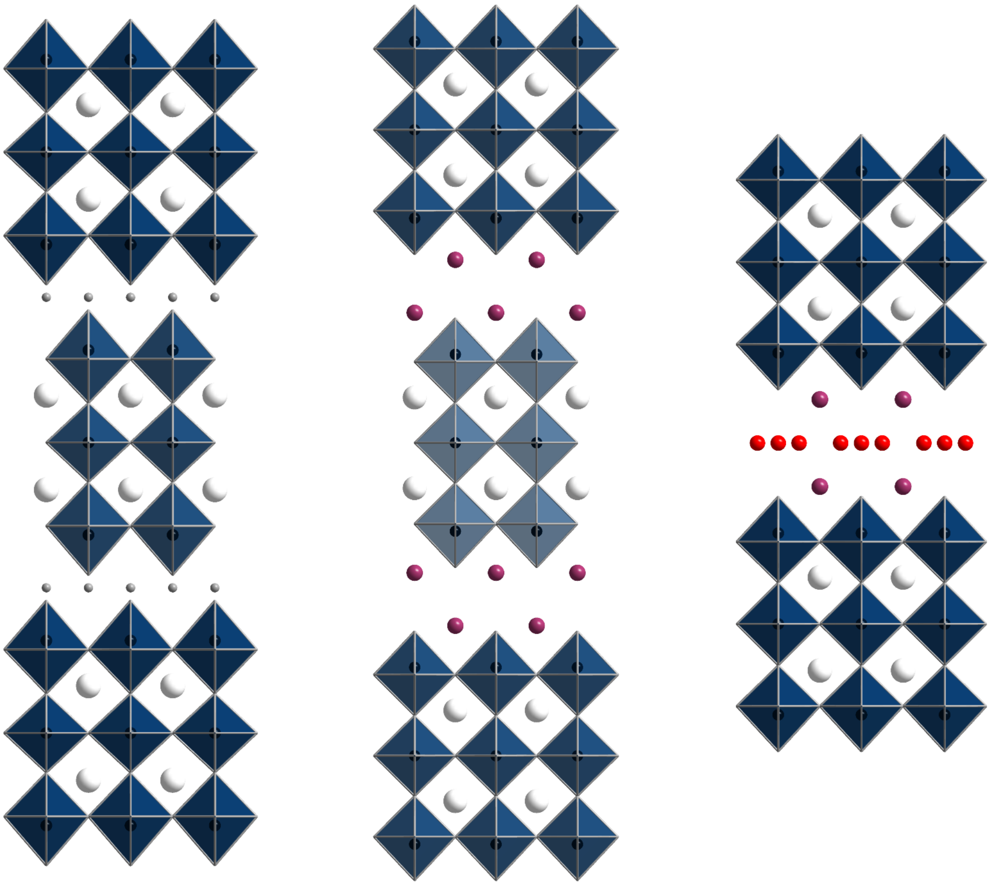

$Li_2La_2Ti_3O_{10}$ (i)

$K_2La_2Ti_3O_{10}$ (ii)

$K_2La_2Ti_3O_{10} \cdot 2H_2O$ (iii)

Figure 2.15 Crystal structures of (i) $Li_2La_2Ti_3O_{10}$, (ii) $K_2La_2Ti_3O_{10}$, and (iii) $K_2La_2Ti_3O_{10} \cdot 2H_2O$,[32] where the disordered position of intercalated water is indicated by its oxide position (red spheres). Alkali metal and lanthanum cations are represented by grey and white spheres respectively, whilst TiO_6 octahedra are indicated by blue units.

The alkali metal interlayer cations in both the Ruddlesden-Popper and Dion-Jacobson series of compounds can typically be replaced with protons *via* ion exchange in dilute acid at room temperature or 60 °C.[43] This low-temperature approach allows the exchanged phases to retain the structure of the parent host lattice, and so the lattice parameter along the stacking direction can readily be determined. However, to date, only the $n = 1$ compounds H*Ln*TiO_4 (*Ln* = La or Nd) have been satisfactorily characterised, by means of Rietveld analysis of neutron powder diffraction data.[44, 45] The structures of both these compounds can be described in the same space group, *P*4/*nmm*, as that of the Na*Ln*TiO_4 precursor,[37] but differ from the parent phase in that the proton is disordered over a large number of equivalent positions about an apical oxide anion in the interlayer, as illustrated in Figure 2.16. In contrast to these tetragonal phases, the structure of $NaYTiO_4$ crystallises in the orthorhombic space group *Pbcm*.[37] The replacement of the sodium cations in $NaYTiO_4$ with protons was reported by Nishimoto *et al.* to reduce the symmetry of the structure to $P2_1/c$.[45] This study was similarly conducted on the basis of neutron powder diffraction data, and although moving to a lower symmetry space group accounted better for the possible peak splitting, the overall fit remained unconvincing with significant intensity mismatches present throughout the entire *d*-space range.

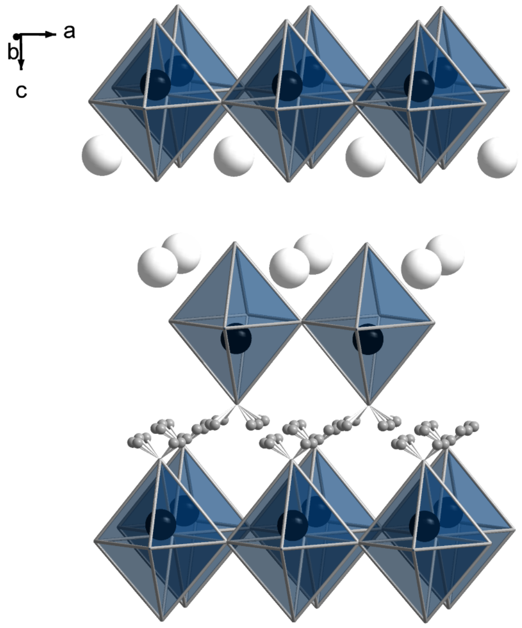

Figure 2.16 Crystal structure of $HLaTiO_4$,[44] illustrating the positionally disordered coordination environment of the protons. H^+ and La^{3+} cations are represented by grey and white spheres respectively, whilst TiO_6 octahedra are indicated by blue units.

For these $n = 1$ compounds, hydrogen bonding over the interlayer region between the protons and the apical oxide anions of the TiO_6 octahedra is sufficiently strong to result in a regular stacking sequence. This situation can be contrasted with the $n = 2$ series of compounds $H_2SrM_2O_7$ (M = Ta or Nb)[46] and the $n = 3$ compound $H_2La_2Ti_3O_{10}$,[47] where attempts to characterise these compounds by Rietveld analysis have failed due to a combination of low-resolution diffraction data and non-uniform peak broadening. The latter has been ascribed to weak hydrogen bonding interactions that can result in misalignments between adjacent perovskite layers, *i.e.* stacking faults.[48]

2.2.3 Dion-Jacobson Compounds, $A'[A_{n-1}B_nX_{3n+1}]$

The structures of the Dion-Jacobson series of layered perovskites are built-up from the same $A_{n-1}B_nX_{3n+1}$ perovskite layers that are observed in the Ruddlesden-Popper series of compounds, but differ in that the *A'*- and *A*-site cations are exclusively ordered over the interlayer region and the perovskite layer, respectively, with the former present in only half of the available interlayer sites. Furthermore, in addition to being staggered, the relative arrangement of adjacent perovskite layers can also become partially staggered, or eclipsed; this is dependent upon the size of the *A'*-site cation. For example, when the *A'*-site is occupied by a small cation such as lithium or sodium, the adjacent perovskite layers exhibit an offset of ½**a**+½**b**. However, substitution of a larger cation such as potassium leads to only a partial offset of ½**a**, whilst substitution of an even larger cation such as rubidium or caesium leads to no offset in the *ab* plane. Consequently, the coordination of the *A'*-site cation varies with ionic radius, and increases from 4-coordinate with tetrahedral geometry for both lithium and sodium, to 6-coordinate with trigonal-prismatic geometry for potassium, and to 8-coordinate with cubic geometry for both rubidium and caesium,[24] as illustrated in Figure 2.17. The tetrahedral geometry adopted by sodium is atypical, but is prevalent among Dion-Jacobson type layered perovskites, including $NaLaNb_2O_7$,[49] α-$NaCa_2Nb_3O_{10}$,[27] and $NaCa_2NaNb_4O_{13}$.[50]

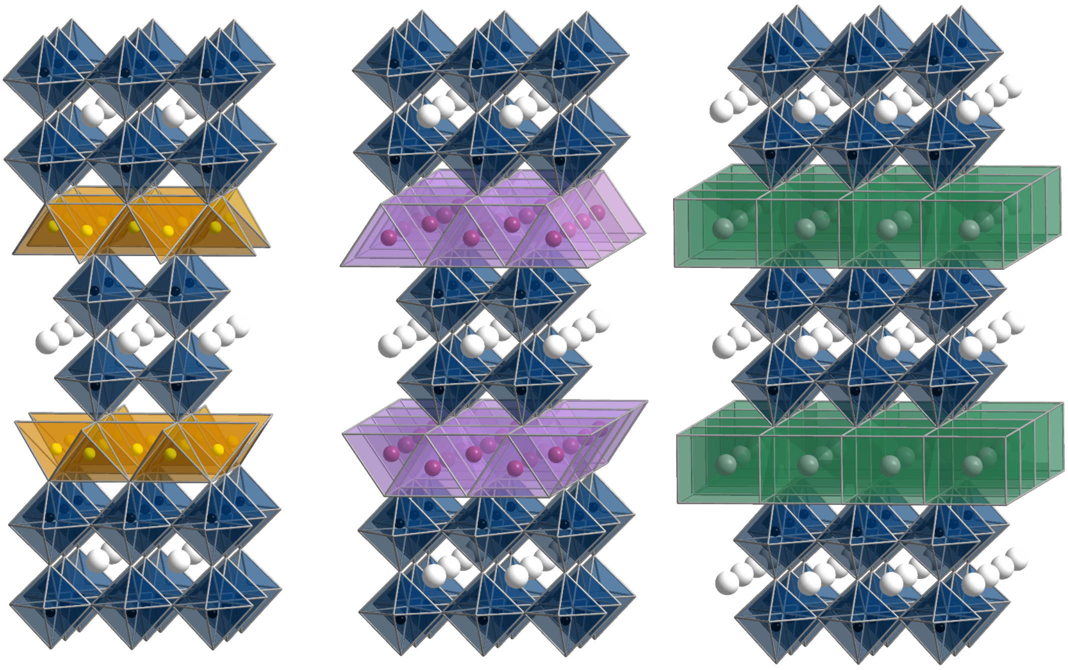

$NaLaNb_2O_7$

Na^+ in tetrahedral coordination

Perovskite layers offset by ½**a**+½**b**

(i)

$KLaNb_2O_7$

K^+ in trigonal-prismatic coordination

Perovskite layers offset by ½**a**

(ii)

$CsLaNb_2O_7$

Cs^+ in cubic coordination

Perovskite layers show no offset

(iii)

Figure 2.17 Crystal structures of a number of $n = 2$ Dion-Jacobson layered perovskites, (i) $NaLaNb_2O_7$,[49] (ii) $KLaNb_2O_7$,[49] and (iii) $CsLaNb_2O_7$,[51] illustrating the differences in both the coordination of the *A*′-site cation and the relative arrangements of adjacent perovskite layers with increasing cation size.

The opportunity for adjacent perovskite layers to become eclipsed in the Dion-Jacobson structure, and not in the related Ruddlesden-Popper structure, has been ascribed to the lower charge density in the interlayer region. From this, it can be reasoned that that the electrostatic interactions that hold together the layers of perovskite and *A′*-site cations are relatively weak in the Dion-Jacobson structure.

The $n = 2$ to $n = 7$ homologues of the Dion-Jacobson series have been prepared for a number of metal-oxide compositions.[24] Solid solutions involving either of the *A*-sites or the *B*-site have also been demonstrated. However, cation ordering at the *B*-site has only been demonstrated for a limited number of compositions that involve a combination of titanium and either niobium or tantalum. In the case of $CsCaLaTiNb_2O_{10}$, this ordering is unusual in that the structure is stabilised with a asymmetric distribution of the two cations: Cs-($Ti_{0.15}Nb_{0.85}$)-($Ti_{0.70}Nb_{0.30}$)-($Ti_{0.15}Nb_{0.85}$)-Cs.[52]

In the absence of tilting of the BX_6 octahedra and displacements of the *A′*-site cations, these structures can be described in either a body-centred (Li and Na) or a primitive (Rb and Cs) tetragonal space group. However, if the *A′*-site is occupied by potassium, the structure can be described, instead, in an orthorhombic space group.

2.2.4 Aurivillius Compounds, $(Bi_2O_2)[A_{n-1}B_nX_{3n+1}]$

The Aurivillius family of layered perovskites can be characterised by the same $A_{n-1}B_nX_{3n+1}$ perovskite layers that are observed in the Ruddlesden-Popper and the Dion-Jacobson families of compounds, but also, more distinctly, by an intergrowth of $(Bi_2O_2)^{2+}$ layers. These layers are constituted of bismuth cations that alternate above and below a square-planar net of oxide anions to give two sheets of BiO_4 square pyramids that are contiguous with one another, as illustrated in Figure 2.18.

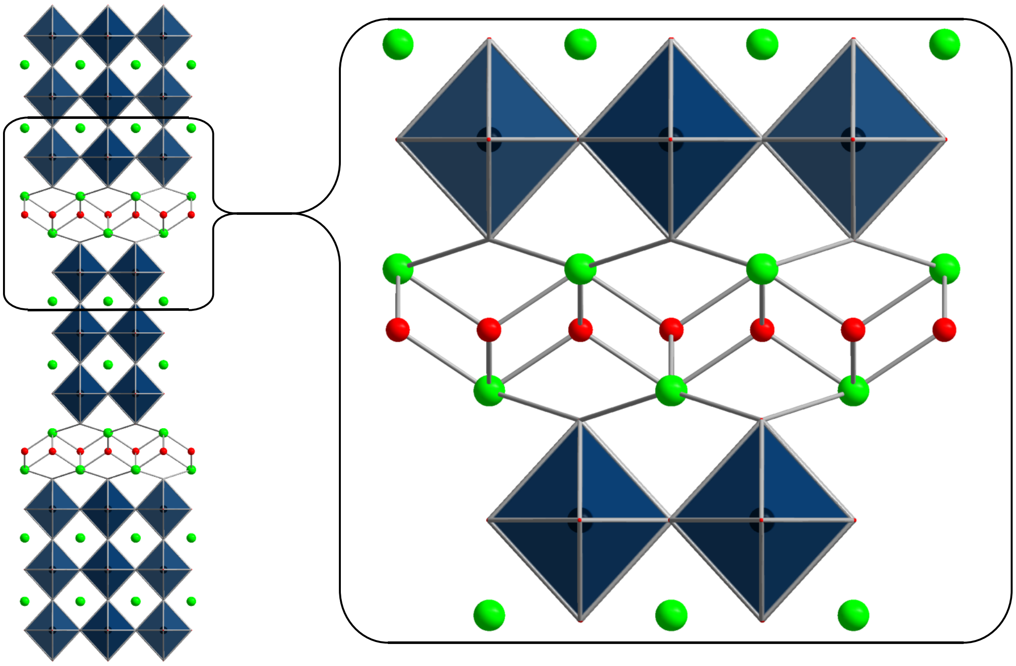

Figure 2.18 Crystal structure of the $n = 3$ Aurivillius layered perovskite $(Bi_2O_2)Bi_2Ti_3O_{10}$.[30] The inset illustrates the unusual structure of the $(Bi_2O_2)^{2+}$ layers, which give rise to highly distorted BiO_8 square-antiprisms. Bi^{3+} and O^{2-} ions are represented by green and red spheres respectively, whilst TiO_6 octahedra are indicated by blue units.

This $(Bi_2O_2)^{2+}$ layer is connected to the adjacent perovskite layers by weak bonding between the bismuth $6s^2$ lone pair and four nearest neighbour apical oxide anions in the perovskite layer, to give BiO_8 square antiprisms.

The $n = 1 - 5$ homologues of the Aurivillius series have been prepared for a wide variety of metal-oxide compositions.[24] Solid solutions involving the A-site or the B-site, or both, have also been demonstrated.[24] However, complete cation ordering at the B-site has only been demonstrated in the case of the $n = 3$ compound $Bi_2Sr_2Nb_2MnO_{12-\delta}$,[53] where the manganese cations order into the central layer. A number of different cations can also be substituted onto the bismuth site in the $(Bi_2O_2)^{2+}$ layer, including lead, thallium, tellurium, antimony and tin, and this is typically accompanied by considerable disorder between the A-sites in the perovskite layer and the bismuth sites in the $(Bi_2O_2)^{2+}$ layer.

X-ray powder diffraction data typically reveal an orthorhombic *Fmmm* structure for these compounds, as was initially reported by Aurivillius.[29, 30] However, subsequent studies have shown that this in fact represents an average structure, and that the majority of these compounds adopt other orthorhombic or monoclinic structures. This has been demonstrated for the archetypal Aurivillius compound $(Bi_2O_2)Bi_2Ti_3O_{10}$, which has been shown to be more accurately described by a commensurate modulation of a monoclinic $B1a1$ structure.[54]

Interestingly, the Aurivillius compounds can also form mixed-layered structures, *i.e.* structures composed of two different thicknesses of perovskite layer. This has been demonstrated for $Bi_7Ti_4NbO_{21}$,[55] which is composed of double-layer perovskite slabs corresponding to the $n = 2$ compound Bi_3TiNbO_9, and triple-layer perovskite slabs corresponding to the $n = 3$ compound $Bi_4Ti_3O_{12}$. Therefore, the resulting compound exhibits the stacking sequence BPPBPPP (B = $(Bi_2O_2)^{2+}$ layer, P = perovskite layer), the pattern of which has been observed using high-resolution transmission electron microscopy.[56]

2.2.5 Ion-exchange Reactions

The replacement of alkali metal interlayer cations in both the Ruddlesden-Popper and Dion-Jacobson families of compounds has been widely demonstrated by ion-exchange reactions,[24] and typically involves reaction of the layered perovskite with a salt at relatively low temperatures.[43] For example, the $n = 1$ Ruddlesden-Popper compounds $NaLnTiO_4$ (Ln = La or Eu) can be exchanged in molten salts such as $LiNO_3$ or $AgNO_3$ at 250-300 °C to give $LiLnTiO_4$ and $AgLnTiO_4$.[42] A similar reactivity can be seen for the $n = 2$ Dion-Jacobson compound $KLaNb_2O_7$,[49] which can be exchanged in $LiNO_3$ or $NaNO_3$ to give $LiLaNb_2O_7$ and $NaLaNb_2O_7$. It is also possible to carry out ion-exchange reactions on triple-layer perovskites such as the Ruddlesden-Popper compound $Na_2La_2Ti_3O_{10}$ and the Dion-Jacobson compound $RbCa_2Ta_3O_{10}$, which can be similarly exchanged in $LiNO_3$ or $NaNO_3$ to give $Li_2La_2Ti_3O_{10}$[32] or $ACa_2Ta_3O_{10}$ (A = Li or Na).[57] By comparison, the archetypal Ruddlesden-Popper compounds Sr_2TiO_4 ($n = 1$), $Sr_3Ti_2O_7$ ($n = 2$) and $Sr_4Ti_3O_{10}$ ($n = 3$), do not undergo ion exchange.

The alkali metal interlayer cations in the Ruddlesden-Popper structure can also be replaced by divalent alkaline earth or transition metal species, but when this occurs, a significantly lower exchange efficiency of 70-85 % is typically achieved.[58] This has been demonstrated for $NaLaTiO_4$, which can be exchanged in molten MCl_2 (M = Co, Cu or Zn) to give a new series of compounds, $M^{II}_{0.5}LaTiO_4$,[59] that represent a hybrid of the Ruddlesden-Popper and Dion-Jacobson structure-types. In some cases, this ion exchange is accompanied by a lateral shift of ½**a**+½**b** in the relative arrangement of the perovskite layers, which is dependent upon the method of ion exchange employed. For example, $NaEuTiO_4$ can be exchanged in molten $Ca(NO_3)_2$ to give $Ca_{0.43}Na_{0.15}EuTiO_4$,[60] whose structure retains the staggered arrangement of the perovskite layers in the $NaEuTiO_4$ parent phase. However, performing the ion exchange in an aqueous solution of $Ca(NO_3)_2$ results, instead, in an eclipsed arrangement of the perovskite layers that flank the alkaline earth interlayer,[61] as illustrated in Figure 2.19. This phenomenon, the authors suggest, arises from the intercalation of water molecules, which can sufficiently expand the alkaline earth interlayer to afford lateral mobility between the perovskite layers.

Divalent ion exchange has also been demonstrated for the $n = 3$ Ruddlesden-Popper compound $K_2Eu_2Ti_3O_{10}$, which can be exchanged in an aqueous solution of a nitrate salt, $M^{II}(NO_3)_2$ (M = Ni, Cu or Zn), to give a corresponding series of Dion-Jacobson compounds $MEu_2Ti_3O_{10}$,[58] in which the perovskite layers are eclipsed. In the case of $ZnEu_2Ti_3O_{10}$, this member can also be prepared by exchange in molten $ZnCl_2$, and, similarly to the preparation of $Ca_{0.43}Na_{0.15}EuTiO_4$, retains the staggered arrangement of the perovskite layers in the parent phase.

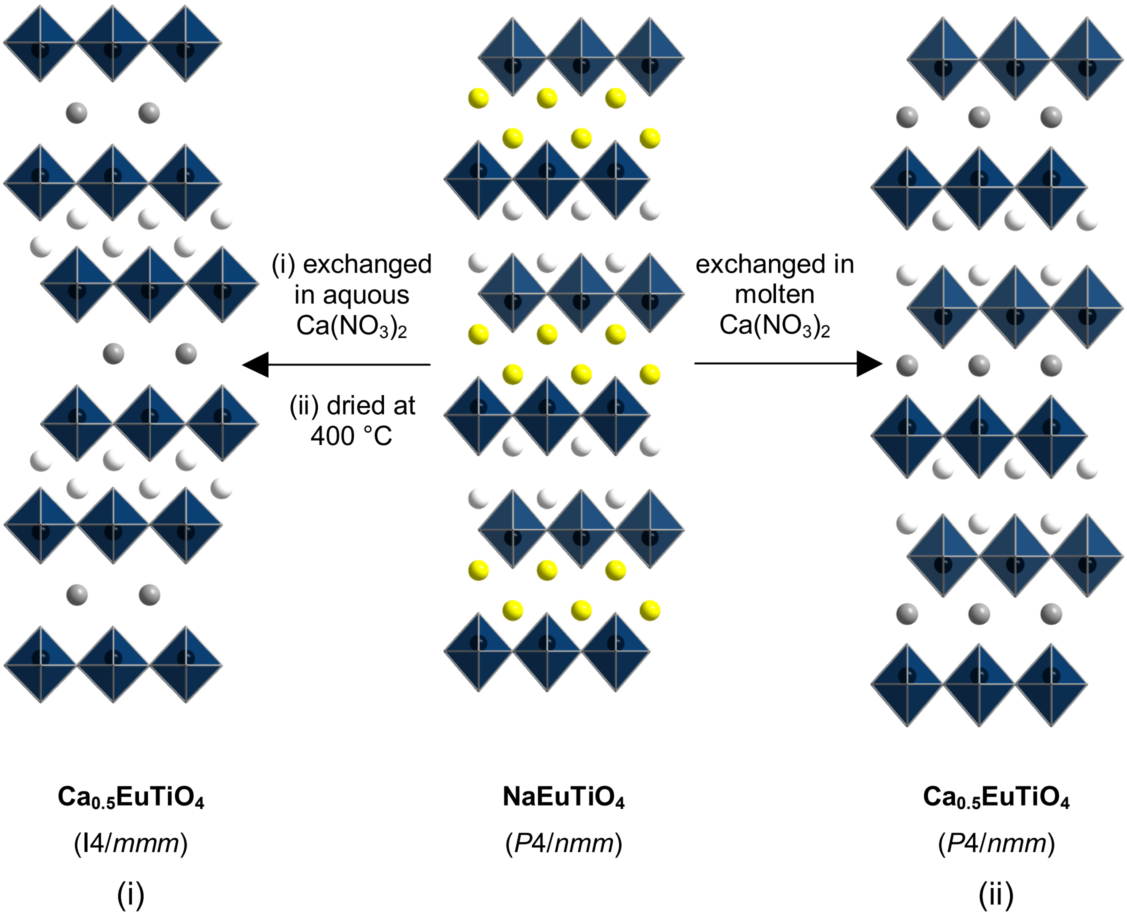

Figure 2.19 A schematic diagram of the proposed transformations of $NaEuTiO_4$ to $Ca_{0.5}EuTiO_4$, illustrating (i) the eclipsed arrangement adopted by the perovskite layers that flank the alkaline earth interlayer when the exchange is performed in aqueous solution,[61] and (ii) the staggered arrangement that is retained when the exchange is performed in molten salt.[60] Na^+, Ca^{2+} and Eu^{3+} cations are represented by yellow, grey and white spheres, respectively, whilst TiO_6 octahedra are indicated by blue units.

Ion-exchange reactions can also be used to prepare the protonated forms of layered perovskites,[43] and generally involve stirring the layered perovskite in dilute acid. For example, $NaRETiO_4$ (RE = La, Nd, Sm, Gd and Y) can be exchanged using 0.1 mol dm^{-3} of nitric acid at room temperature to give a corresponding series of solid acids, H*RE*TiO$_4$.[62] Many other Ruddlesden-Popper phases, including $H_2SrM_2O_7$ (M = Nb or Ta)[46] and $H_2La_2Ti_3O_{10}$,[47] and equally numerous Dion-Jacobson phases, including $HLaNb_2O_7$[49] and $HCa_2Nb_3O_{10}$,[63] have been prepared in a similar manner. In regards to the Aurivillius series of compounds, it has been shown in a number of cases that the bismuth-oxide sheet can be selectively leached from the interlayer using acid, and replaced with protons.[64-66] In the case of the n = 3 compound $(Bi_2O_2)[Sr_2NaNb_3O_{10}]$,[64] this involves reaction with 6 mol dm^{-3} of hydrochloric acid at room temperature to give the compound $H_{1.8}[Bi_{0.2}Sr_{0.8}NaNb_3O_{10}]$, whose c lattice parameter (14.3 Å) is comparable to that of the structurally related Dion-Jacobson phase $HCa_2Nb_3O_{10}$ (14.37 Å).[63]

The ion-exchange reactions described thus far have involved the replacement of the alkali metal interlayer cations with smaller cations. The replacement of interlayer cations with larger cations is rarely seen for ion-exchange reactions that involve single atomic species, and has been demonstrated only for the preparation of K*Ln*TiO$_4$ from a solid acid.[67] Here, H*Ln*TiO$_4$ (*Ln* = La, Nd, Sm, Eu, Gd or Dy) can be exchanged with aqueous potassium hydroxide at 60 °C to give hydrated $KLnTiO_4{\cdot}xH_2O$ phases that can subsequently be heated at 500 °C to give a corresponding series of anhydrous layered perovskites, K*Ln*TiO$_4$. By contrast, a number of varied examples exist where the alkali-metal interlayer cations are replaced with larger cationic structural units. For example, pairs of sodium cations in $NaLaTiO_4$ can be replaced with a vanadyl cationic unit, $(VO)^{2+}$, through reaction with aqueous $VOSO_4$ at 50-65 °C to give the compound $Na_{0.10}(VO)_{0.45}LaTiO_4$.[68] A more unusual intergrowth of $(CuX)^+$ (X = Cl or Br) layers has been shown to replace the potassium cations in $KLaNb_2O_7$, and involves reaction with molten CuX_2 (X = Cl or Br) at 325 °C to give the new layered perovskites $(CuX)LaNb_2O_7$.[69] Here, the interlayer region is constituted of an ordered net of copper and halide ions, where the copper centres coordinate to the apical oxide anions of the NbO_6 octahedra and the coplanar halide anions to give an edge-sharing layer of CuO_2X_4 octahedra, as illustrated in Figure 2.20. A more recent analysis of the structure by Kodenkandath *et al.* used neutron diffraction data,[70] and determined that the positions of the chloride anions are in fact disordered over four positions, which was not indicated by their previous X-ray diffraction study.

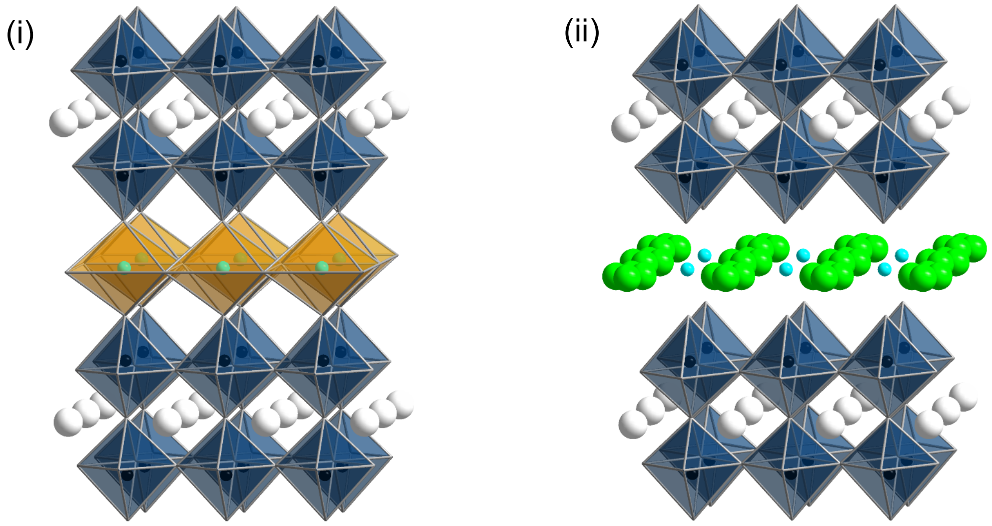

Figure 2.20 Crystal structure of $(CuCl)LaNb_2O_7$ determined from (i) X-ray[69] and (ii) neutron[70] diffraction data, illustrating the edge-sharing layer of CuO_2Cl_4 octahedra (orange) that are interleaved with the perovskite layers (blue) *via* corner-sharing apical oxide anions. The structure derived from the neutron diffraction study shows that the chloride anions are in fact disordered over four positions. Cu^+, Cl^- and La^{3+} ions are represented by turquoise, green and white spheres respectively, whilst TiO_6 octahedra are indicated by blue units.

The protons in protonated layered perovskites can also be replaced with even larger, organic-based cationic units. For example, reaction with bulky organic bases such as tetrabutylammonium hydroxide ($TBA^+ OH^-$), $[(C_4H_9)_4N][OH]$, can give compounds such as $TBA_xH_{1-x}Ca_2Nb_3O_{10}$.[71] However, in these instances, very often even before complete exchange has occurred, the accompanying increase in the interlayer distance allows solvent molecules to intercalate into the interlayer, which causes these regions to swell to the point of delamination.[72] The resulting suspension contains, amongst other things, negatively charged perovskite sheets that can be self-assembled into monolayer-thin films using cationic substrates. This approach has been used to form thin-film heterostructures that contain complex stacking sequences.[43]

2.2.6 More Complex Topochemical Transformations

In addition to ion-exchange reactions, the reactivity of the interlayer region can also lead to more complex transformations of the Ruddlesden-Popper and Dion-Jacobson series of compounds. These topochemical processes involve dehydration or reduction, and can be used to convert a layered perovskite into either a higher-order homologue or a three-dimensional perovskite. For example, the $HLnTiO_4$ (Ln = La, Nd, Sm or Gd) series of compounds undergo topochemical dehydration when heat treated at 480-500 °C for *ca.* 15 min to give the corresponding series of $n = 2$ Ruddlesden-Popper compounds $Ln_2\square Ti_2O_7$.[73] This process involves the removal of both the interlayer protons and the equivalent of one row of apical oxide anions as water, and results in the collapse of the interlayer to give vacant *A*-sites in the newly bridged perovskite layer, as illustrated in Figure 2.21. This topochemical transformation arises from the unique ordering of the protons and lanthanide cations in the $n = 1$ compound, and so the dehydration of higher-order Ruddlesden-Popper homologues leads, instead, to the formation of *A*-site deficient, three-dimensional perovskites. This has been demonstrated for a number of $n = 2$ protonated

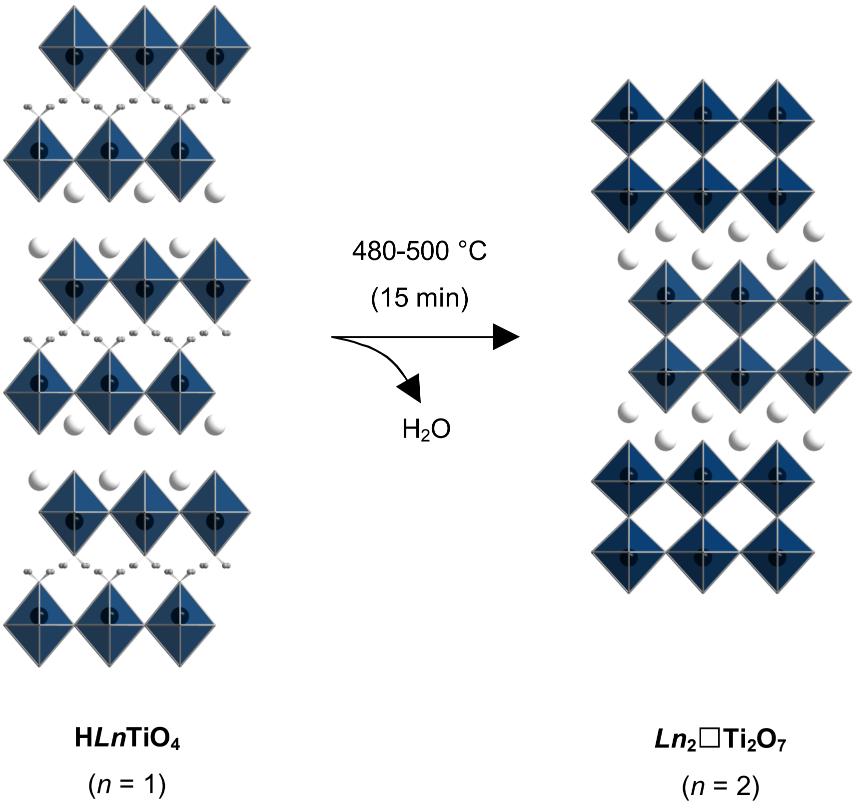

Figure 2.21 A schematic diagram illustrating the proposed topochemical dehydration of the $n = 1$ compound H*Ln*TiO$_4$ (*Ln* = La, Nd, Sm or Gd) to give the *A*-site deficient, $n = 2$ Ruddlesden-Popper compounds $Ln_2\square Ti_2O_7$.[73] H^+ and Ln^{3+} cations are represented by grey and white spheres respectively, whilst TiO_6 octahedra are indicated by blue units.

Ruddlesden-Popper compounds, including $H_2SrTa_2O_7$[46] and $H_2SrTa_{1.6}Nb_{0.4}O_7$,[74] as well as for a number of $n = 3$ compounds, including $H_2Sr_{1.5}Nb_3O_{10}$[46] and $H_2SrLaTi_2TaO_{10}$.[75] In each of these cases, the dehydrated product exhibits disordering of the occupied and vacant *A*-sites.

However, in the case of $H_2Ln_2Ti_3O_{10}$ (Ln = La, Nd, Sm or Gd), these materials undergo topochemical dehydration at 400 °C to give, instead, an intermediate series of anion-deficient layered phases $\square_2Ln_2Ti_3O_9$.[76, 77] It is only with heating at a higher temperature of 900-1000 °C that the La- and Nd-containing compounds transform to the *A*-site deficient, three-dimensional perovskites $\square_{1/3}Ln_{2/3}TiO_3$,[47, 77] where the *A*-site cations are disordered amongst the available interstitial sites in the perovskite lattice, as illustrated in Figure 2.22. By contrast, heating the dehydrated Sm- and Gd-containing compounds at 950 °C leads, instead, to the pyrochlores $Ln_2Ti_2O_7$.[47]

In contrast to protonated Ruddlesden-Popper compounds, protonated Dion-Jacobson compounds contain only half the number of protons that are required to remove a row of apical oxide anions, and so, do not form analogous, three-dimensional phases upon dehydration of the interlayer region. In the case of $HCa_2Nb_3O_{10}$, it has been suggested that dehydration of the interlayer region leads to the partially dehydrated phase $Ca_4Nb_6O_{19}$, where only half of the interlayer has topochemically collapsed to give a buckled arrangement between the perovskite layers.[78]

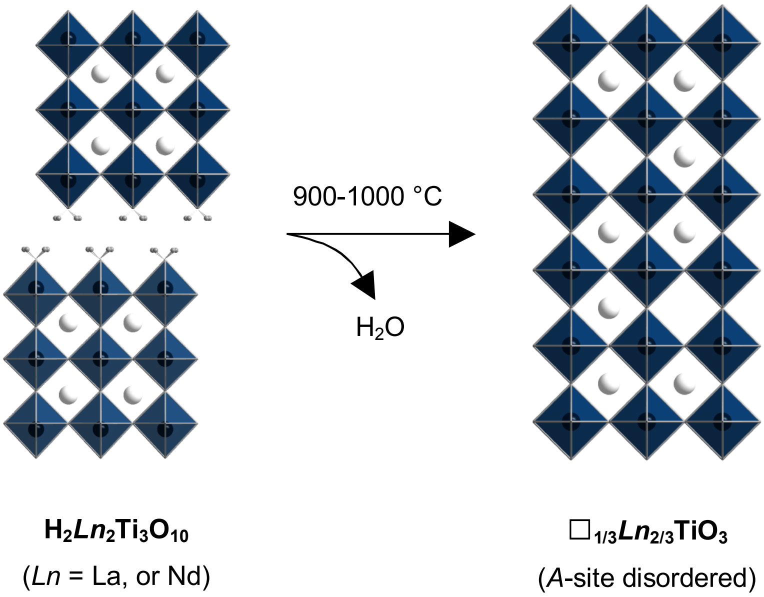

Figure 2.22 A schematic diagram illustrating the proposed topochemical dehydration of the $n = 3$ compounds $H_2Ln_2Ti_3O_{10}$ (Ln = La or Nd) to give the A-site deficient, three-dimensional perovskites $\square_{1/3}Ln_{2/3}TiO_3$.[47] Lanthanide cations are represented by white spheres, whilst TiO_6 octahedra are indicated by blue units.

The transformation of Dion-Jacobson compounds into three-dimensional perovskites can be similarly achieved by topochemical reduction. However, in contrast to topochemical dehydration, this process exploits the reduction of an A- or B-site cation under a hydrogen atmosphere to remove the equivalent of one row of apical oxide anions from the interlayer region as water. This approach inherently leads to the formation of non-defective, three-dimensional perovskites since bridging of the perovskite layers necessitates that the interlayer A'-site cations be encased in the newly formed cuboctahedral interstitial sites, as illustrated in Figure 2.23. This has been demonstrated for a number of Dion-Jacobson compounds, including

$A\mathrm{Eu^{III}}_2\mathrm{Ti_3O_{10}}$ (A = Ca or Sr) and $A\mathrm{Eu^{III}}_2\mathrm{Ti_2NbO_{10}}$ (A = Li or Na),[58] and involves heating the compounds under hydrogen atmosphere to give the series $A\mathrm{Eu^{II}}_2\mathrm{Ti_3O_9}$ (A = Ca or Sr), where the A-site cations retain the ordering of the parent phase, and $A\mathrm{Eu^{II}}_2\mathrm{Ti_2NbO_9}$ (A = Li or Na), where the A-site cations are disordered. It is noted that in each of these series of compounds there is at least one reducible species present, but additional experiments by Schaak *et al.*[58] have indicated that the reduction of the $\mathrm{Eu^{3+}}$ cation occurs much more readily than either the $\mathrm{Ti^{4+}}$ or the $\mathrm{Nb^{5+}}$ cations.

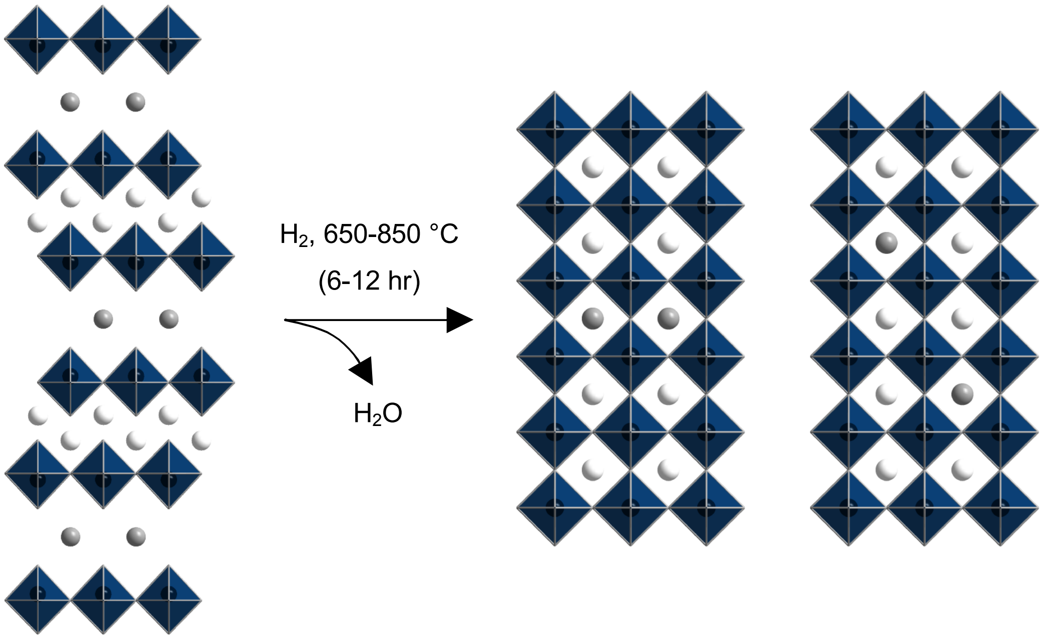

$A\mathrm{Eu^{III}}_2M_3\mathrm{O_{10}}$
(M = Ti/Nb)
(A = Li, Na, Ca or Sr)

$A\mathrm{Eu^{II}}_2\mathrm{Ti_3O_9}$
(A = Ca or Sr)
(A-site ordered)

$A\mathrm{Eu^{II}}_2\mathrm{Ti_2NbO_9}$
(A = Li or Na)
(A-site disordered)

Figure 2.23 A schematic diagram illustrating the proposed topochemical reduction of $A\mathrm{Eu^{III}}_2M_3\mathrm{O_{10}}$ to give the three-dimensional perovskites $A\mathrm{Eu^{II}}_2M_3\mathrm{O_9}$.[58] A and Eu cations are represented by grey and white spheres respectively, whilst $M\mathrm{O_6}$ octahedra are indicated by blue units.

Topochemical reduction can be similarly employed to transform $n = 1$ Ruddlesden-Popper compounds into non-defective, $n = 2$ layered perovskites. However, since bridging of the perovskite layers necessitates that the proportion of interlayer A'-site cations be halved, these monovalent cations must first be replaced by divalent species in order to form a hybrid Ruddlesden-Popper/Dion-Jacobson compound; this has been discussed previously in this section with respect to the formation of $Ca_{0.5}Eu^{III}TiO_4$. The topochemical reduction of a hybrid compound such as $Ca_{0.5}Eu^{III}TiO_4$ can be carried out by heating the material at 625 °C for 30 min under a hydrogen atmosphere to give the non-defective, $n = 2$ Dion-Jacobson compound $CaEu^{II}{}_2Ti_2O_7$,[61] as illustrated in Figure 2.24. It is noted that, similarly to other topochemical transformations, there is only a short window of duration in which the $CaEu^{II}{}_2Ti_2O_7$ product can be stabilised during heating. These short reaction times are necessary to isolate the topochemical products, and attest to the metastable nature of these compounds.

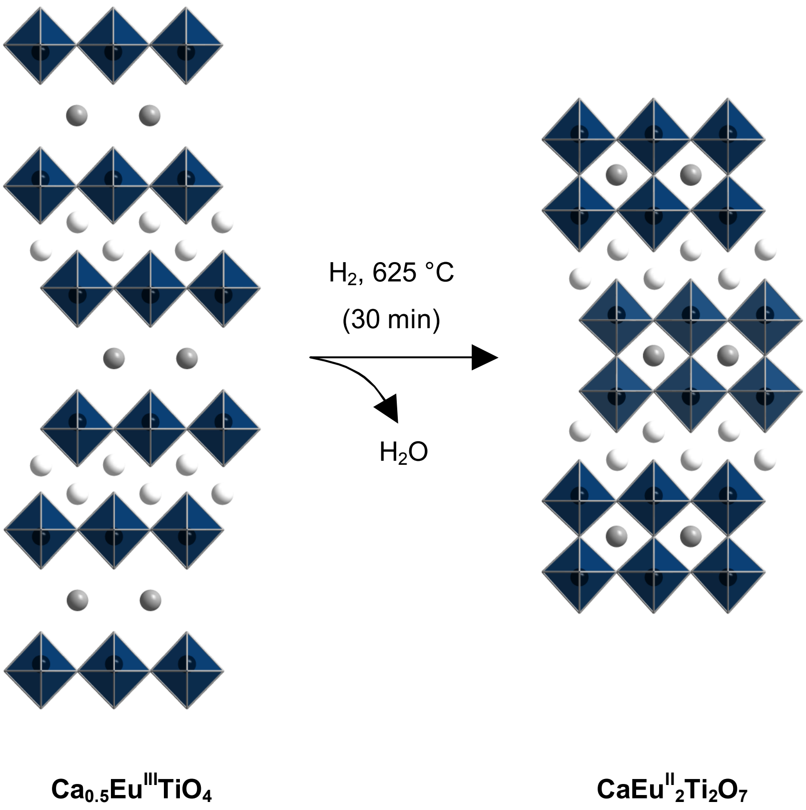

Figure 2.24 A schematic diagram illustrating the proposed topochemical reduction of $Ca_{0.5}Eu^{III}TiO_4$ to give the non-defective, $n = 2$ Dion-Jacobson compound $CaEu^{II}_2Ti_2O_7$.[61] Ca^{2+} and Eu cations are represented by grey and white spheres respectively, whilst TiO_6 octahedra are indicated by blue units.

2.3 References

1. V. S. Sastri, *Corrosion Inhibitors: Principles and Applications*, John Wiley & Sons, Ltd, Chichester, 2001.
2. A. Erdöhelyi, K. Fodor, R. Németh, A. Hancz and A. Oszkó, *J. Catal.*, 2001, **199**, 328-337.
3. A. Erdöhelyi, A. Hancz, M. Tóth and É. Novák, *Catal. Today*, 2004, **91-92**, 117-120.
4. O. P. Barinova, F. A. Danevich, V. Y. Degoda, S. V. Kirsanova, V. M. Kudovbenko, S. Pirro and V. I. Tretyak, *Nucl. Instrum. Methods Phys. Res. A*, 2010, **613**, 54-57.
5. W. H. Zachariasen and H. A. Plettinger, *Acta Cryst.*, 1961, **14**, 229-230
6. U. Kolitsch, *Z. Kristallogr.*, 2001, **216**, 449-454.
7. H. Horiuchi, N. Morimoto and S. Yamaoka, *J. Solid State Chem.*, 1979, **30**, 129-135.
8. K. A. Wilhelmi, K. Waltersson and P. Löfgren, *Acta Cryst.*, 1977, **C6**, 219-223.
9. H. Horiuchi, N. Morimoto and S. Yamaoka, *J. Solid State Chem.*, 1980, **33**, 115-119.
10. A. H. Yahaya and A. K. Arof, *Mater. Sci. Eng., B*, 1995, **34**, 7-11.
11. A. Hüllen, *Berichte der Bunsengesellschaft für physikalische Chemie*, 1966, **70**, 598-606.
12. R. D. Shannon, *Acta Cryst.*, 1976, **A32**, 751-767.

13. K. G. Bramnik and H. Ehrenberg, *Z. Anorg. Allg. Chem.*, 2004, **630**, 1336-1341.

14. F. Capitelli, M. D. Selim and K. K. Mukherjea, *Asian J. Chem.*, 2006, **18**, 2856-2860.

15. A. N. Ergorova, A. A. Maier, N. N. Nevskii and M. V. Provotorov, *Inorg. Mater.*, 1982, **18**, 1763-1766.

16. N. J. Stedman, A. K. Cheetham and P. D. Battle, *J. Mater. Chem.*, 1994, **4**, 707-711.

17. A. Zalkin and D. H. Templeton, *J. Chem. Phys.*, 1964, **40**, 501-504.

18. E. Gürmen, E. Daniels and J. S. King, *J. Chem. Phys.*, 1971, **55**, 1093-1097.

19. V. A. Efremov, V. K. Trunov and T. A. Berezina, *Sov. Phys. Crystallogr.*, 1982, **27**, 77-81.

20. V. A. Efremov, T. A. Berezina, I. M. Averina and V. K. Trunov, *Sov. Phys. Crystallogr.*, 1980, **25**, 146.

21. R. F. Klevtsova, L. A. Glinskaya, L. P. Kozeeva and P. V. Klevtsov, *Sov. Phys. Crystallogr.*, 1973, **17**, 672-676.

22. R. F. Klevtsova, *Sov. Phys. Crystallogr.*, 1975, **20**, 456-458.

23. A. Santoro, M. Marezio, R. S. Roth and D. Minor, *J. Solid State Chem.*, 1980, **35**, 167-175.

24. R. H. Mitchell, *Perovskites: Modern and Ancient*, Almaz Press Inc., Thunder Bay, 2002.

25. S. N. Ruddlesden and P. Popper, *Acta Cryst.*, 1957, **10**, 538-539.

26. S. N. Ruddlesden and P. Popper, *Acta Cryst.*, 1958, **11**, 54-55.

27. M. Dion, M. Ganne and M. Tournoux, *Mater. Res. Bull.*, 1981, **16**, 1429-1435.

28. A. J. Jacobson, J. W. Johnson and J. T. Lewandowski, *Inorg. Chem.*, 1985, **24**, 3727-3729.

29. B. Aurivillius, *Ark. Kemi*, 1949, **1**, 463-480.

30. B. Aurivillius, *Ark. Kemi*, 1949, **1**, 499-512.

31. V. M. Goldschmidt, *Skr. Nor. Vidensk.-Akad., [Kl.] 1: Mat.-Naturvidensk. Kl.*, 1927, 1-156.

32. K. Toda, J. Watanabe and M. Sato, *Mater. Res. Bull.*, 1996, **31**, 1427-1435.

33. M. Dion, M. Ganne, M. Tournoux and J. Ravez, *Rev. Chim. Miner.*, 1984, **21**, 92-103.

34. L. Yan, H. J. Niu, C. A. Bridges, P. A. Marshall, J. Hadermann, G. van Tendeloo, P. R. Chalker and M. J. Rosseinsky, *Angew. Chem. Int. Ed.*, 2007, **46**, 4539-4542.

35. L. Yan, H. J. Niu, G. V. Duong, M. R. Suchomel, J. Bacsa, P. R. Chalker, J. Hadermann, G. van Tendeloo and M. J. Rosseinsky, *Chem. Sci.*, 2011, **2**, 261-272.

36. G. Blasse, *J. Inorg. Nucl. Chem.*, 1968, **30**, 656-658.

37. K. Toda, Y. Kameo, S. Kurita and M. Sato, *J. Alloys Compd.*, 1996, **234**, 19-25.

38. S.-H. Byeon, K. Park and M. Itoh, *J. Solid State Chem.*, 1996, **121**, 430-436.

39. T. Pagnier, N. Rosman, C. Galven, E. Suard, J.-L. Fourquet, F. L. Berre and M.-P. Crosnier-Lopez, *J. Solid State Chem.*, 2009, **182**, 317–326.

40. F. Le Berre, M.-P. Crosnier-Lopez, Y. Laligant, E. Suard, O. Bohnke, J. Emery and J. L. Fourquet, *J. Mater. Chem.*, 2004, **14**, 3558-3565.

41. M.-P. Crosnier-Lopez, F. Le Berre and J.-L. Fourquet, *J. Mater. Chem.*, 2001, **11**, 1146-1151.

42. K. Toda, S. Kurita and M. Sato, *J. Ceram. Soc. Jpn.*, 1996, **104**, 140-142.

43. R. E. Schaak and T. E. Mallouk, *Chem. Mater.*, 2002, **14**, 1455-1471.

44. S. Nishimoto, M. Matsuda, S. Harjo, A. Hoshikawa, T. Kamiyama, T. Ishigaki and M. Miyake, *J. Eur. Ceram. Soc.*, 2006, **26**, 725-729.

45. S. Nishimoto, M. Matsuda, S. Harjo, A. Hoshikawa, T. Kamiyama, T. Ishigaki and M. Miyake, *J. Solid State Chem.*, 2006, **179**, 1892-1897.

46. N. S. P. Bhuvanesh, M.-P. Crosnier-Lopez, H. Duroy and J.-L. Fourquet, *J. Mater. Chem.*, 2000, **10**, 1685-1692.

47. J. Gopalakrishnan and V. Bhat, *Inorg. Chem.*, 1987, **26**, 4299-4301.

48. M.-P. Crosnier-Lopez and J.-L. Fourquet, *Solid State Sci.*, 2005, **7**, 530-538.

49. M. Sato, J. Abo, T. Jin and M. Ohta, *J. Alloys Compd.*, 1993, **192**, 81-83.

50. M. Sato, Y. Kono and T. Jin, *J. Ceram. Soc. Jpn.*, 1993, **101**, 980-984.

51. N. Kumada, N. Kinomura and A. W. Sleight, *Acta Cryst.*, 1996, **C52**, 1063-1065

52. Y.-S. Hong, S.-J. Kim, S.-J. Kim and J.-H. Choy, *J. Mater. Chem.*, 2000, **10**, 1209-1214.

53. W. J. Yu, Y. I. Kim, D. H. Ha, J. H. Lee, Y. K. Park, S. Seong and N. H. Hur, *Solid State Commun.*, 1999, **111**, 705-709.

54. A. D. Rae, J. G. Thompson, R. L. Withers and A. C. Willis, *Acta Cryst.*, 1990, **B46**, 474-487.

55. T. Kikuchi, A. Watanabe and K. Uchida, *Mater. Res. Bull.*, 1977, **12**, 299-304.

56. S. Horiuchi, T. Kikuchi and M. Goto, *Acta Cryst.*, 1977, **A33**, 701-703.

57. K. Toda, M. Takahashi, T. Teranishi, Z.-G. Ye, M. Sato and Y. Hinatsu, *J. Mater. Chem.*, 1999, **9**, 799-803.

58. R. E. Schaak and T. E. Mallouk, *J. Am. Chem. Soc.*, 2000, **122**, 2798-2803.

59. S. Y. Kim, J.-M. Oh, J.-C. Park and S.-H. Byeon, *Chem. Mater.*, 2002, **14**, 1643-1648.

60. R. A. McIntyre, A. U. Falster, S. Li, W. B. Simmons, Jr., C. J. O'Connor and J. B. Wiley, *J. Am. Chem. Soc.*, 1998, **120**, 217-218.

61. R. E. Schaak, E. N. Guidry and T. E. Mallouk, *Chem. Commun.*, 2001, 853-854.

62. S.-H. Byeon, J.-J. Yoon and S.-O. Lee, *J. Solid State Chem.*, 1996, **127**, 119-122.

63. A. J. Jacobson, J. T. Lewandowski and J. W. Johnson, *J. Less-Common Met.*, 1986, **116**, 137-147.

64. W. Sugimoto, M. Shirata, Y. Sugahara and K. Kuroda, *J. Am. Chem. Soc.*, 1999, **121**, 11601-11602.

65. Y. Tsunoda, M. Shirata, W. Sugimoto, Z. Liu, O. Terasaki, K. Kuroda and Y. Sugahara, *Inorg. Chem.*, 2001, **40**, 5768-5771.

66. W. Sugimoto, M. Shirata, K. Kuroda and Y. Sugahara, *Chem. Mater.*, 2002, **14**, 2946-2952.

67. R. E. Schaak and T. E. Mallouk, *J. Solid State Chem.*, 2001, **161**, 225-232.

68. D. Neiner, V. Golub and J. B. Wiley, *Mater. Res. Bull.*, 2004, **39**, 1385–1392.

69. T. A. Kodenkandath, J. N. Lalena, W. L. Zhou, E. E. Carpenter, C. Sangregorio, A. U. Falster, W. B. Simmons, Jr., C. J. O'Connor and J. B. Wiley, *J. Am. Chem. Soc.*, 1999, **121**, 10743-10746.

70. G. Caruntu, T. A. Kodenkandath and J. B. Wiley, *Mater. Res. Bull.*, 2002, **37**, 593-598.

71. A. J. Jacobson, J. W. Johnson and J. T. Lewandowski, *Mater. Res. Bull.*, 1987, **22**, 45-51.

72. R. E. Schaak and T. E. Mallouk, *Chem. Mater.*, 2000, **12**, 2513-2516.

73. V. Thangadurai, G. N. Subbanna and J. Gopalakrishnan, *Chem. Commun.*, 1998, 1299-1300.

74. P. J. Ollivier and T. E. Mallouk, *Chem. Mater.*, 1998, **10**, 2585-2587.

75. R. E. Schaak and T. E. Mallouk, *J. Solid State Chem.*, 2000, **155**, 46-54.

76. V. Thangadurai, A. K. Shukla and J. Gopalakrishnan, *Solid State Ionics*, 1994, **73**, 9-14.

77. M. Richard, L. Brohan and M. Tournoux, *J. Solid State Chem.*, 1994, **112**, 345-354.

78. M. Fang, C. H. Kim and T. E. Mallouk, *Chem. Mater.*, 1999, **11**, 1519-1525.

3 Theory and Experimental Techniques

3.1 Diffraction by Crystalline Solids

The periodic arrangement of atoms in a crystalline solid can behave like a three-dimensional diffraction grating when irradiated with certain types of radiation.[1] This is similar in principle to the interference phenomenon demonstrated by Young's "double-slit" experiment,[2] where visible light is passed through two parallel slits, creating two sources of coherent light that subsequently interfere with one another. This interference pattern is evidenced on a receiving screen, and will exhibit regions of low intensity and regions of high intensity which arise from the destructive and constructive interference, respectively, of the two wave fronts of light. If we instead consider a series of rows of point scatterers, *i.e.* atoms, that interact elastically with the incoming radiation, then these atoms will under specific geometric conditions act as secondary light sources, and so, interference will occur between the emergent wave fronts. These conditions, with reference to the two parallel planes of atoms in Figure 3.1, specify that wave B must travel a whole number of wavelengths further than wave A for constructive interference to occur. This relationship is embodied in Bragg's Law,[3] as given by:

$$n\lambda = 2d\sin\theta, \tag{3.1}$$

where n is the diffraction order (which must be an integral number), λ is the wavelength (Å) of the incident and diffracted beams, d is the interplanar spacing (Å) and θ is the scattering angle (°).

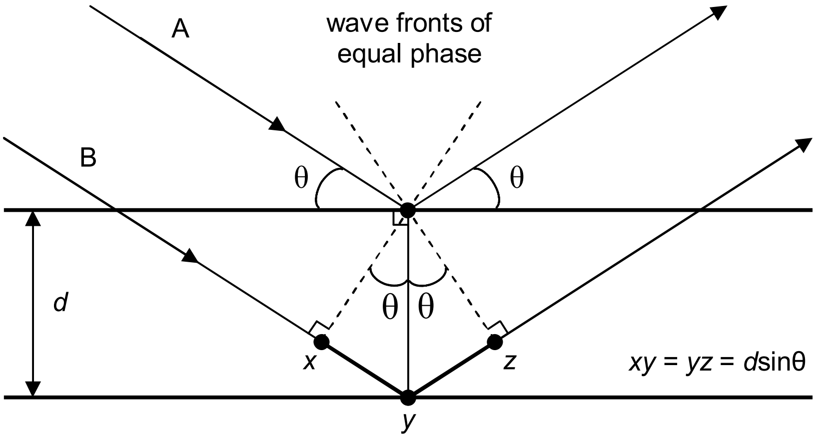

Figure 3.1 Scattering of waves A and B at a scattering angle, θ, between two parallel planes of atoms separated by an interplanar spacing, *d*. The path difference between waves A and B is indicated by *xyz*.

When the Bragg condition is satisfied, the waves A and B are in phase and constructive interference occurs, resulting in a diffracted beam. Outside this regime, the waves are out of phase and destructive interference occurs, resulting in a diffracted beam of reduced intensity. However, if wave B is out of phase with wave A by exactly half a wavelength, then complete destructive interference occurs, resulting in the absence of a diffracted beam.

3.1.1 Unit Cells and Bravais Lattices

The atoms in a crystal have a periodic arrangement.[1] The nomenclature used to describe this periodicity can be more easily understood by first considering the simplified case of a periodic pattern in two-dimensional space. This pattern can be represented by the combination of a grid and a motif of atoms. The latter can be situated at or near the intersections of the grid, as illustrated in Figure 3.2. This grid is more commonly termed the *lattice* and the intersections of the grid are called *lattice points*.[1] Each of these lattice points are related by translational symmetry and have identical environments. The smallest repeating unit of this lattice defines the *unit cell*, which can be classified as either *primitive*, where only a sum total of one lattice point is located within the unit cell, or *centred*, where multiple lattice points are located within the unit cell.[1] Therefore, in a crystal, the centring of a three-dimensional unit cell can occur at the centre of each of the faces (*face-centred*), at the centre of each face in a pair of opposing faces (*base-centred*), or at the centre of the cell (*body-centred*). Base-centred unit cells can be further classified as *A*-, *B*- or *C*-centred, where the additional lattice points lie in the plane bound by the two remaining axes. The combination of these four lattice types with the seven crystal

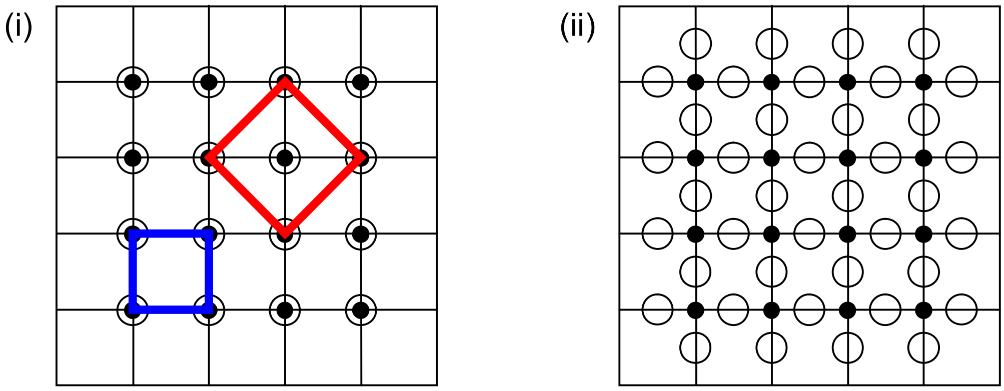

Figure 3.2 Schematic diagrams of a two-dimensional lattice showing a motif of atoms (empty circles) located (i) at or (ii) near the lattice points (filled circles). (i) additionally shows a *primitive* unit cell (blue) and a *centred* unit cell (red).

systems, the latter defined by the translational symmetry of the lattice, leads to 14 *unique* permutations called Bravais lattices,[1] as summarised in Table 3.1; this excludes combinations that violate symmetry considerations or that can be described by a smaller unit cell. For example, in the structure of sodium chloride, as illustrated in Figure 3.3, the unit cell is described as face-centred cubic, where the lattice points of the unit cell coincide with the positions of the chloride anions.

Table 3.1 The fourteen Bravais lattices and the seven crystal systems from which they are derived.[1]

Crystal system	Unit cell shape	Bravais lattice
Cubic	$a = b = c,\ \alpha = \beta = \gamma = 90°$	*P*, *F*, *I*
Tetragonal	$a = b \neq c,\ \alpha = \beta = \gamma = 90°$	*P*, *I*
Orthorhombic	$a \neq b \neq c,\ \alpha = \beta = \gamma = 90°$	*P*, *F*, *I*, *A*/*B*/*C*
Hexagonal	$a = b \neq c,\ \alpha = \beta = 90°,\ \gamma = 120°$	*P*
Trigonal*	$a = b = c,\ \alpha = \beta = \gamma \neq 90°$	*P*
	$a = b \neq c,\ \alpha = \beta = 90°,\ \gamma = 120°$	*R*
Monoclinic	$a \neq b \neq c,\ \alpha = \gamma = 90°,\ \beta \neq 90°$	*P*, *C*
Triclinic	$a \neq b \neq c,\ \alpha \neq \beta \neq \gamma \neq 90°$	*P*

* A primitive rhombohedral lattice (*P*) can also be described using a rhombohedrally centred hexagonal lattice (*R*) that is three times larger.

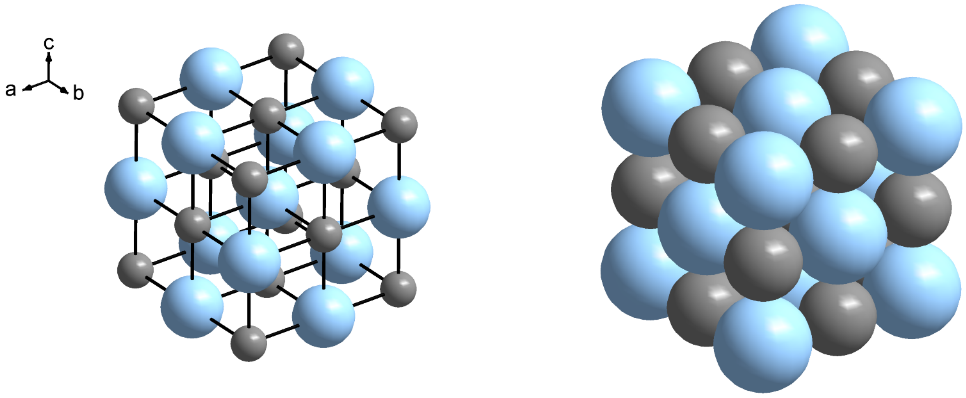

Figure 3.3 Face-centred cubic structure of sodium chloride.[4] Na^+ and Cl^- ions are represented by grey and blue spheres respectively.

3.1.2 Lattice Planes and Directions, and Systematic Absences

A lattice plane is an imaginary construct that defines a plane that is coincident with a lattice point located on one or more of the crystallographic axes, as illustrated in Figure 3.4. There are therefore many different crystallographic planes that can arise from the three-dimensional arrangement of atoms in a crystal. These lattice planes intercept the unit cell edges at fractional parts or at infinity, and so, can be expressed on the basis of the unit cell vectors **a**, **b** and **c**. The reciprocals of these fractional coordinates define three indices, h, k, and l, which are termed Miller indices,[1] and are written in parentheses as (hkl) when used to describe a specific crystallographic plane. A specific crystallographic direction can be defined, instead, by expressing the fractional coordinates as a ratio of whole numbers to give the indices u, v and w,[1] which

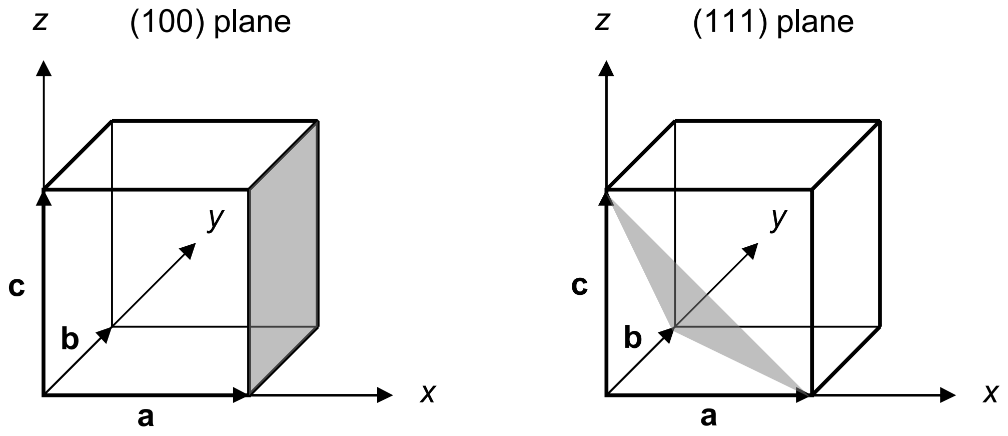

Figure 3.4 (100) and (111) lattice planes illustrated for a unit cell of cubic symmetry.

are written in parentheses as [*uvw*]. Families of planes and directions can be denoted by the use of curly brackets, *e.g.* {100}, and angle brackets, *e.g.* <100>, respectively. The spacing between adjacent (*hkl*) planes is designated by d_{hkl}. For a cubic system, the interplanar spacing is related to the unit cell parameter, a_0, by the following relationship:

$$\frac{1}{d_{hkl}} = \left(\frac{h^2 + k^2 + l^2}{a_0^2}\right)^{1/2}.^{1} \tag{3.2}$$

The substitution of equation (3.2) into the Bragg equation then gives:

$$\sin^2\theta = \frac{\lambda^2}{4{a_0}^2}\left(h^2 + k^2 + l^2\right). \tag{3.3}$$

Therefore, it can be seen that the positions of these reflections are dependent only on the identity of the Bravais lattice and the unit cell dimensions, and not on the unit cell contents. If a single phase is present, the indexing of a diffraction pattern should be consistent and give rise to a single set of lattice parameters. The form of equation (3.2) becomes more complex when the symmetry of the lattice is reduced to yield similar relationships for the other six crystal systems.

The translational symmetry operations that contribute towards the overall symmetry of a crystal, *i.e.* the Bravais lattice and the translational components of screw axes and glide planes, are readily apparent since certain groups of (*hkl*) reflections will be systematically absent. Systematic absences occur when atoms in one plane scatter exactly out of phase with atoms in another, resulting in destructive interference.[1]

Consequently, a number of reflection conditions may be evaluated for, that will help in identifying the crystal symmetry. For example, each centred lattice type should yield a class of reflections that conform to the conditions summarised in Table 3.2.[1]

Table 3.2 Reflection conditions for the five lattice types.[1]

Lattice type	Reflection condition
P (primitive)	None
I (body-centred)	$h + k + l = 2n$
F (face-centred)	h, k, l either all odd or all even
A, B, C (base-centred)	(A) $k + l = 2n$ (B) $h + l = 2n$ (C) $h + k = 2n$
R (rhombohedrally centred hexagonal cell)	(obverse) $-h + k + l = 3n$ (reverse) $h + k + l = 3n$

3.1.3 Space Groups

The relative intensities of (hkl) reflections depend on the interactions between the atomic structure and the incoming radiation, but also on the relative positions of the atoms in the structure. The symmetry within a crystal can be described through the combination of 32 crystallographic point groups, *i.e.* rotations, reflections and roto-inversions, with the translational elements of centring, screw axes and glide planes. This leads to the classification of 230 space groups that describe all possible permutations of symmetry within a crystal.[5]

3.2 X-ray Diffraction

X-rays are useful for probing the internal structure of crystalline materials because they have wavelengths that are similar in magnitude to the interatomic separations of a crystal (*ca.* 2 Å), and are sufficiently energetic to penetrate solids, *i.e.* bulk sensitive.[6]

X-ray radiation of the type Cu K_α is generated when a stream of electrons is accelerated through *ca.* 40 kV and bombards a copper target.[6] Only a small proportion (*ca.* 1%) of the energy of the incident electron beam is converted into X-rays, and so the target anode must be cooled with water. The incident electrons are produced by heating a tungsten filament, and have enough energy to ionise a core electron from the copper K (1*s*) level. The resultant hole state is filled by an electron dropping from the $L_{2,3}$ (2*p*) level to the K level, and the energy liberated as X-ray radiation, as illustrated in Figure 3.5.

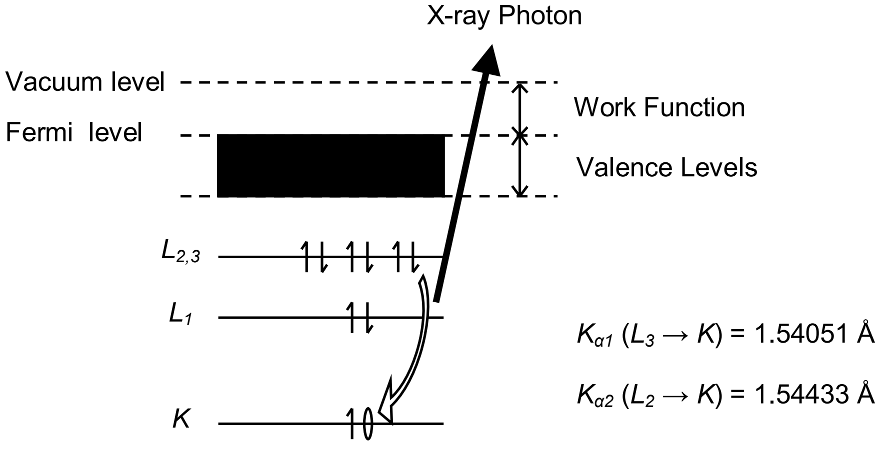

Figure 3.5 Energy level diagram of X-ray emission.[6]

The resulting Cu K_α radiation contains both $K_{\alpha 1}$ and $K_{\alpha 2}$ wavelength radiations due to the two possible spin states in the $L_{2,3}$ level. X-ray radiation is also given off by other transitions, such as K_β radiation ($3p \rightarrow 1s$; $\lambda = 1.3922$ Å) and Bremsstrahlung radiation, the latter of which is sometimes referred to as white radiation and is characterised by a continuous distribution of X-rays. However, only K_α radiation is used in diffraction experiments because of its characteristic and more intense nature. To obtain a monochromatic source of K_α radiation, a filter made from nickel foil can be used to absorb the K_β radiation and the majority of the white radiation, leaving an almost monochromatic beam of K_α radiation.[6] This is because the energy required to ionise a nickel 1*s* electron corresponds to 1.488 Å, which lies between the energies of K_α radiation and K_β radiation. Alternatively, a single crystal called a monochromator may be used to diffract radiation of a certain wavelength, *i.e.* $K_{\alpha 1}$ radiation, which can then go on to interact with the sample.[6]

When X-rays interact with an atom in a sample, the varying electric field of the X-ray beam perturbs the electrons surrounding the atom, causing them to vibrate. The oscillating electrons then act as secondary point sources of X-rays that are in phase, or coherent, with the incident X-ray beam. However, the intensity of the scattered radiation decreases as the angle between the incident beam and diffracted beam, 2θ, increases.[6] To illustrate this, consider an atom with two electrons, where an incident beam of X-rays comprising waves A and B are scattered by the electrons at an angle 2θ from the direction of incidence, as illustrated in Figure 3.6. These electrons are separated by very short distances within the atom, such that the path difference

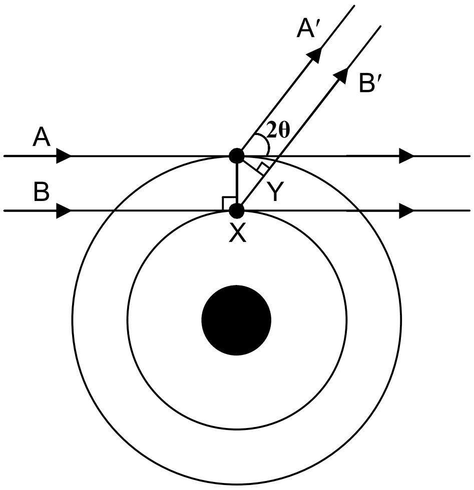

Figure 3.6 An incident beam of X-rays, waves A and B, being scattered by the electrons in an atom to give the diffracted waves A′ and B′.[6] The path difference between the incident and diffracted waves is indicated by the distance XY.

between the scattered beams A′ and B′, is only slightly less than the wavelength of Cu K_α radiation, resulting in only partial destructive interference. However, as the angle 2θ increases, the path difference between waves A′ and B′ will gradually increase, and will result in a scattered beam of reduced intensity. Consequently, the X-rays scattered by the electron cloud surrounding an atom will interfere and give rise to a fall-off in the scattered intensity as a function of the angle 2θ. This behaviour is described by the scattering amplitude, or form factor, f_x, of an atom and is theoretically derived from wave function theory.[6] This form factor can be related to both the angle and wavelength, as illustrated in Figure 3.7, and at $\sin\theta/\lambda = 0$ increases as a function of atomic number, or, more specifically, the number of electrons associated with that atom. Consequently, X-rays are relatively insensitive to light atomic species such as hydrogen and lithium, especially when in the presence of significantly heavier elements.

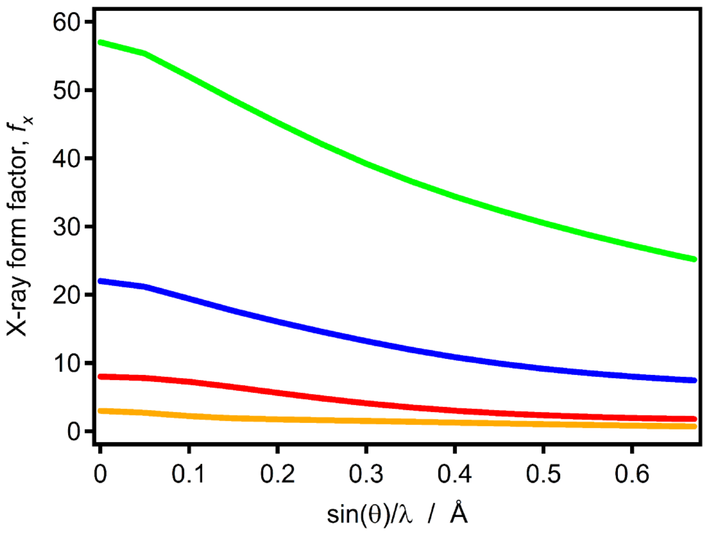

Figure 3.7 Angular fall off of the X-ray form factor, f_x, for Li (orange line), O (red line), Ti (blue line) and La (green line).[7] When sinθ/λ = 0, f_x corresponds to the atomic number of the element. Range of sinθ/λ has been shown for Cu K_α radiation.

The use of unpolarised sources of X-rays, *i.e.* typical laboratory sources, also causes the intensity, I, of the scattered beam to reduce as a function of angle, as described by the Thomson equation[1]:

$$I = \frac{1}{2}\left(1 + \cos^2 2\theta\right). \tag{3.4}$$

X-rays polarised perpendicular to the plane of scattering would give rise to a zero reduction in intensity, and so, this attenuation arises from the incident X-rays having an in-plane component to their polarisation and reaches a maximum when 2θ = 90°.

3.2.1 X-ray Single Crystal Diffraction

In X-ray single crystal diffraction, intensity data are collected using an area charge coupled device (CCD) detector on a frame-by-frame basis as the crystal is rotated about three axes. The intensity of (*hkl*) diffraction spots, or reciprocal lattice nodes,[8] can therefore be constituted from a series of images that are sequentially separated by a small angle. In this way, the majority of reciprocal space within the limiting sphere can be made to cross the sphere of reflection, and thus brought to satisfy the Bragg condition.[8] By using these intensity data together with the indexing that they provide, the relative positions of the atoms can be approximated using structure solution methods,[8] such as the Patterson method or Direct Methods, and subsequently refined by least-squares minimisation routines that are collected in programmes such as SHELX.[9]

3.2.2 X-ray Powder Diffraction

In contrast to a single crystal, a powder sample contains many crystals or assemblages of smaller crystals, which are randomly orientated with respect to one another.[1] Consequently, when a polycrystalline sample is irradiated with X-rays, there will be a certain proportion of crystals whose (*hkl*) planes will both satisfy the Bragg condition and lie in all possible rotational positions about the axis of the incident beam. Thus, a reflection originating from a (*hkl*) plane will be observed in all possible reflection positions about the incident axis, and together, these reflections form the surface of a cone of diffracted radiation,[1] as illustrated in Figure 3.8. Therefore, in order to carry out a crystallographic study of a polycrystalline material, the intensity arising from each of these diffraction cones must be measured.

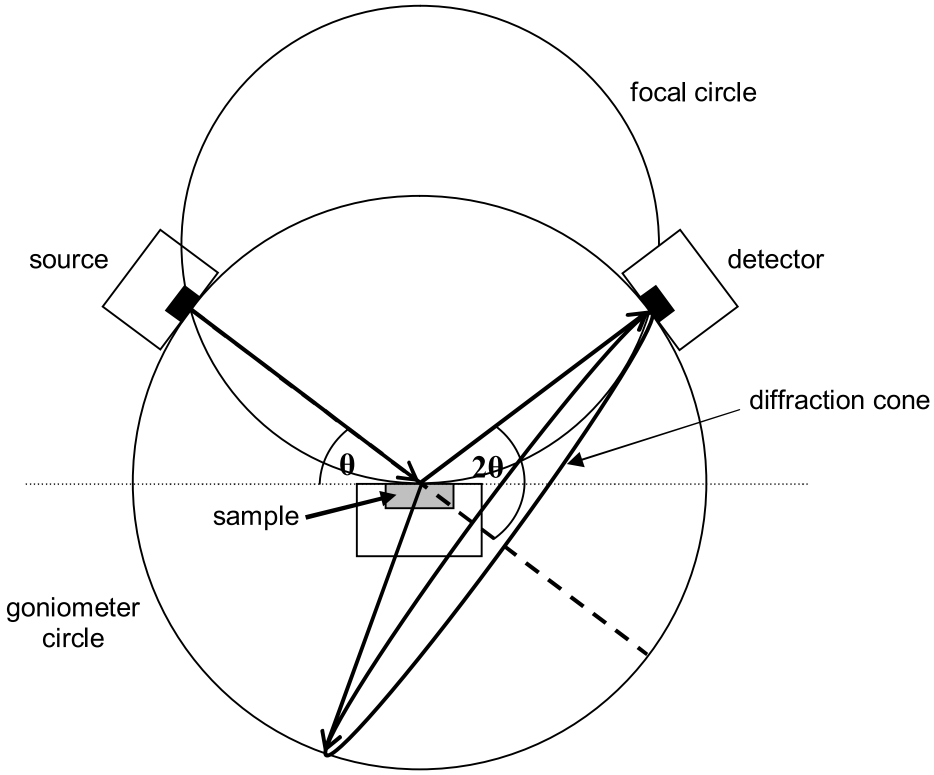

Figure 3.8 Schematic of a polycrystalline sample undergoing diffraction on a powder diffractometer operating in θ-2θ Bragg-Brentano geometry.[1]

Traditionally, these cones have been measured all at once *via* the exposure of photographic film as part of the Debye-Scherrer method.[1] However, it is now more convenient to use a diffractometer which samples the intensity of a diffraction cone using a 1-dimensional (scintillation) or 2-dimensional (CCD) detector; as each crystal plane is brought into the reflection condition *via* the precise motion of the goniometer, the intensity from a fraction of the diffraction cone will be measured as a function of angle 2θ.[1] The data analysed in this thesis were collected using a Siemens D500 powder X-ray diffractometer operating in θ-2θ Bragg-Brentano geometry and equipped with a nickel foil filter, a graphite monochromator and a scintillation-type detector.

It is clear that intensity data can be more straightforwardly obtained using the powder approach, but because the (*hkl*) planes are randomly orientated throughout the sample, those with the same *d*-spacing will diffract at the same Bragg angle. The resulting overlap of symmetry-equivalent reflections means that a significant quantity of crystallographic information is merged. The structural characterisation of a polycrystalline sample is further complicated by the partial overlap of neighbouring peaks due to finite peak widths. Consequently, powder data do not usually yield enough information with which to perform a complete structure determination. However, with some prior knowledge of the crystal structure, it is possible to simultaneously model and deconvolute these peaks using a least-squares minimisation approach called Rietveld analysis,[10] as will be discussed in section 3.4.

3.3 Neutron Diffraction

Neutron diffraction can serve as a complementary technique to X-ray diffraction because, unlike for X-rays, the variation in the neutron scattering length of an atom, or more specifically an atomic nucleus, does not follow a straightforward linear dependence with atomic number,[11] as illustrated in Figure 3.9. Consequently, neutron scattering can provide excellent contrast between adjacent atoms in the periodic table. Furthermore, light atomic species such as hydrogen and lithium, which interact weakly with X-rays, can make a significant contribution to the neutron diffraction pattern.

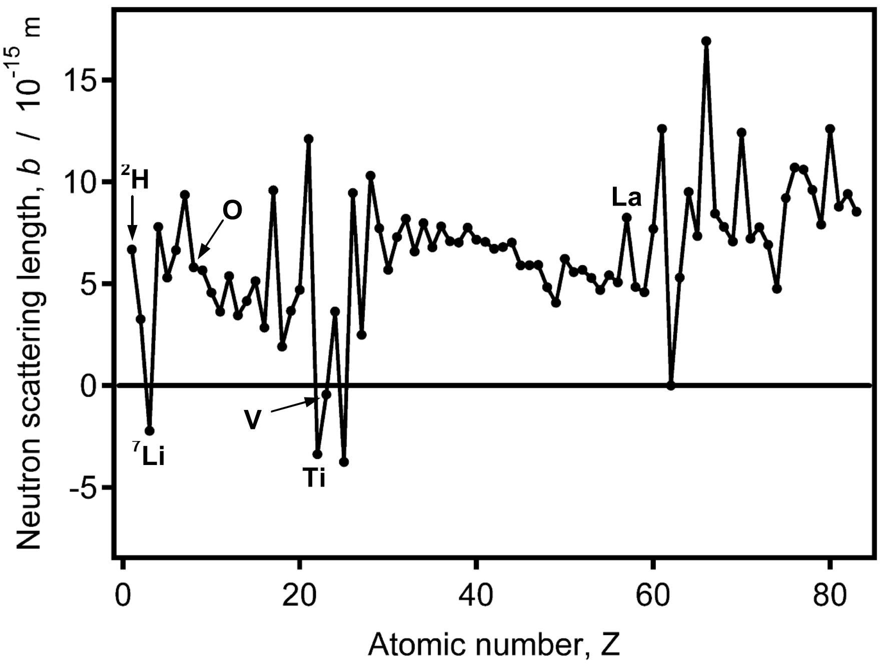

Figure 3.9 Irregular variation in neutron scattering length, *b*, as a function of atomic number.[11]

Neutrons are typically generated from nuclear reactors or spallation sources,[12] but in either case yield hot neutrons that are unsuitably high in energy to probe the internal structure of crystalline materials. In order to take advantage of the wave nature of these particles, the energy of these neutrons must first be moderated to lower temperatures. This is achieved through scattering interactions with a medium such as heavy water to produce *thermal neutrons*,[12] *i.e.* neutrons that possess a lower kinetic energy. The kinetic energy of these neutrons follows a Maxwellian distribution, and can be related to the temperature of the moderating medium using:

$$\frac{1}{2}mv^2 = \frac{3}{2}k_BT,\ [12] \tag{3.5}$$

where m is the mass of a neutron (1.675×10^{-27} kg), v is the velocity of a neutron (m s^{-1}), k_B is the Boltzmann constant (1.381×10^{-23} J K^{-1}) and T is the temperature of the moderator (K). The wavelength of a neutron, λ (Å), is related to its velocity by the de Broglie relationship,[12] as given by:

$$\lambda = \frac{h}{mv}. \tag{3.6}$$

where h is the Planck constant (6.626×10^{-34} kg m^2 s^{-1}). Substitution of the de Broglie relationship into equation (3.5) then gives:

$$\lambda^2 = \frac{h^2}{2mk_BT}. \tag{3.7}$$

This shows that a neutron moderated to 373 K has a mean wavelength of 1.595 Å, which is comparable to the wavelength of Cu K_α radiation. A monochromatic beam of neutrons at this wavelength can subsequently be obtained using a (335) germanium crystal monochromator, as used on the instrument D2B at the Institut Laue-Langevin in Grenoble.[13]

The scattering length of an atomic nucleus (*ca.* 10^{-15} m) is considerably smaller than the wavelength of an incident neutron (*ca.* 10^{-10} m). The probability of an interaction occurring between an incident neutron and the nucleus of an atom in a target sample is correspondingly very low, with the neutron scattering cross-section, σ (barn), defined as:

$$\sigma = 4\pi b^2,^{12} \tag{3.8}$$

where *b* is the neutron scattering length of the target element (10^{-15} m) and the unit of 1 barn is equivalent to 10^{-28} m^2. A consequence of this low scattering cross-section is that the scattering amplitude of an atom does not fall off with angle 2θ as it does for X-rays. However, the relatively weak interaction between neutrons and atomic nuclei necessitates the irradiation of larger, multi-gram samples. Indeed, the penetrative power of neutrons is so great that elements such as vanadium, which has a scattering length very close to zero, can be used in the fabrication of bulky sample environments, such as cryostats and high pressure cells, as well as sample containers.

3.4 Rietveld Analysis

By understanding how radiation is scattered by atoms in a crystal, we can begin to mathematically describe the outcomes of a diffraction experiment. All that is further required is a description of the unit cell and the relative positions of its contents. The summation of the scattering amplitude of all the atoms contributing to a specific (*hkl*) plane within the unit cell can then be carried out. This sum is designated the structure factor, F_{hkl}^{calc}.[10] For an atom, *j*, with site occupancy, *N*, and form factor, *f*, at the fractional coordinates, *x, y, z*, the calculated intensity of the diffracted beam, I_{hkl}^{calc}, is proportional to $\left(F_{hkl}^{calc}\right)^2$, as given by:

$$I_{hkl}^{calc} \propto \left(F_{hkl}^{calc}\right)^2 = \left[\sum_j N_j f_j e^{2\pi i\left(hx_j+ky_j+lz_j\right)} e^{\frac{-8\pi^2 U_{iso}\sin^2\theta}{\lambda^2}}\right]^2 ,^{10} \qquad (3.9)$$

where U_{iso} denotes the isotropic root-mean-square displacement of an atom that arises from either thermal motion or random static disorder, or both. Consequently, the intensity associated with an isolated Bragg reflection can be compared with the square of a calculated structure factor, *i.e.* an intensity generated from a proposed model of the crystal structure. However, the peaks observed in a powder diffraction pattern are typically a sum of a number of overlapping reflections. There are also a number of other contributing factors that must be taken into consideration when modelling the profile of a peak, such as instrumental factors and specimen characteristics. These factors are all encompassed in equation (3.10) which calculates the intensity, y_c, at the i^{th} step in a powder diffraction pattern, as given by:

$$y_{ci} = s\sum_{hkl} L_{hkl}\left(F_{hkl}^{calc}\right)^2 \phi\left(2\theta_i - 2\theta_{hkl}\right)P_{hkl}A + y_{bi}\ ,^{10} \qquad (3.10)$$

where s is the scale factor, L_{hkl} contains the Lorentz, polarisation and multiplicity factors, ϕ is the reflection profile function, θ_i is the position of the i^{th} peak, θ_{hkl} is the position of the i^{th} peak corrected for the zero-point error of the diffractometer, P_{hkl} is the preferred orientation function, A is the absorption factor, and y_{bi} is the background intensity at the i^{th} step defined by a background function.

In order to obtain accurate intensities from an observed powder pattern, the background and profile functions must both be well approximated through modelling. For the analyses carried out in this thesis the background was modelled using a shifted Chebyschev function,[14] which consists of a sum of polynomials, whilst the profiles were modelled using a pseudo-Voigt function described by

Thomson, Cox and Hastings.[15] A pseudo-Voigt function, pV, is a linear combination of Gaussian, G, and Lorentzian, L, functions as given by:

$$pV = \eta L + (1-\eta)G\,,^{16} \tag{3.11}$$

where η denotes the mixing parameter and ranges between zero and unity. The full width at half-maximum (FWHM) of the Gaussian component of the peak shape, Γ_g, is given by:

$$\Gamma_g = \sqrt{(8\ln 2)\sigma^2}\,,^{16} \tag{3.12}$$

and is proportional to σ which varies as a function of the Bragg angle 2θ according to:

$$\sigma^2 = U\tan^2\theta + V\tan\theta + W + \frac{P}{\cos^2\theta}.^{16} \tag{3.13}$$

The coefficients U, V, W and P can be refined, with the final term $P/\cos^2\theta$ representing crystallite size (Scherrer) broadening. By comparison, the Lorentzian contribution, γ, varies as a function of the Bragg angle according to:

$$\gamma = \frac{X + X_e\cos\phi}{\cos\theta} + (Y + Y_e\cos\phi + \gamma_L d^2)\tan\theta\,,^{16} \tag{3.14}$$

where the first term describes crystallite size (Scherrer) broadening, and the second term describes microstrain broadening. The coefficients X, X_e, Y, Y_e and γ_L can also be refined, where X_e and Y_e arise from anisotropic broadening, and γ_L denotes an empirical extension to the anisotropic contribution to microstrain.

Given this comprehensive description of the diffraction experiment, the objective then is to simultaneously refine all these parameters using a least-squares approach. This serves to iteratively minimise the calculated intensity, y_{ci}, against the observed intensity, y_i, over the whole diffraction pattern. Consequently, deconvolution of both partially and completely overlapping peaks can be carried out, allowing for valuable information contained in these profiles to be recovered.

The problem with overlapping peaks was first addressed by Rietveld almost half a century ago,[17] and it is due to the combination of the successful implementation and free distribution of this code that this method is now referred to as Rietveld analysis. This procedure is now routinely used in the analysis of powder diffraction data to determine the crystal structure that provides the best fit to the observed data.[10, 18] For the analyses carried out in this thesis, the GSAS suite of programs[16] was used to perform these calculations.

The quantity minimised in these least-squares refinements is the residual, S_y,[16] as given by:

$$S_y = \sum_i w_i (y_i - y_{ci})^2 , \tag{3.15}$$

where w_i is a weighting term equal to $1/y_i$. This weighting is used to determine how much each observation in the diffraction pattern influences the estimated parameters, since each i^{th} data point will be associated with different degrees of variability over the combinations of parameters being refined. Residual or R factors, provide a measure of the fit on a cycle-by-cycle basis, and so, gauge the agreement between the observed pattern and the calculated pattern during refinement. The indices given by equations (3.16) and (3.17) are just two of many that have been developed,[16] as given by:

$$R_{wp} = \left(\frac{\sum w_i (y_i - y_{ci})^2}{\sum w_i (y_i)^2} \right)^{1/2} \tag{3.16}$$

$$R_p = \frac{\sum | y_i - y_{ci} |}{\sum y_i} \tag{3.17}$$

An improvement in the fit between the observed pattern and the calculated pattern would be indicated by consecutively smaller values of R. R_{wp} is considered to be the most meaningful residual factor, since the numerator is the residual being minimised, and therefore most comparable to the progress of the refinement. Another commonly referenced index for representing how well the fitted model accounts for the data is the goodness-of-fit indicator, χ^2,[16] as given by:

$$\chi^2 = \left(\frac{\sum_i w_i (y_i - y_{ci})^2}{N - P + C} \right)^{1/2} = \left(\frac{R_{wp}}{R_e} \right)^2, \tag{3.18}$$

where N is the number of observations observed, P is the number of parameters refined, C is the number of constraints applied, and R_e is the expected R index for R_{wp}, given by:

$$R_e = \left(\frac{(N - P + C)}{\sum w_i (y_i)^2} \right)^{1/2} .^{16} \tag{3.19}$$

An improvement in the goodness-of-fit would be indicated by consecutive values of χ^2 approaching unity. However, a value of χ^2 less than unity may imply a high value of R_e, which, in turn, would most likely indicate that the data were not collected over a long enough time period. Alternatively, the value of R_{wp} may be low; this can arise from the presence of a high background, which increases the value of the denominator, or the observation of a low number of peaks. The latter can lead to a low value of R_{wp} since a background varying slowly as a function of angle 2θ can be more satisfactorily modelled than a series of Bragg peaks.

3.5 Bond Valence Sum (BVS) Analysis

Bond valence parameters relate bond valences to bond distances and have been derived for a large number of bonds.[19] The derivation of these element specific, bond valence parameters involved the systematic analysis of many well determined crystal structures to develop a consistent scheme upon which to draw general comparisons. Given this limitation, the scheme does not account for structures exhibiting disorder, partial occupancies or ambiguous atomic valences.

The calculated bond valence, v_{ij}, between atoms i and j, is described as a unique function of the bond distance, d_{ij}, by the empirical expression:

$$v_{ij} = e^{\left(\frac{R_{ij}-d_{ij}}{b}\right)},^{19} \qquad (3.20)$$

where R_{ij} is the bond valence parameter between atoms i and j, and b is a constant which takes the value of 0.37 Å. The sum of all the calculated bond valences around an atom i should then, for a structure exhibiting regular bonding environments, approximately equal the formal valence of atom i, V_i, as given by:

$$\sum_j v_{ij} = V_i \,. \qquad (3.21)$$

3.6 Scanning Electron Microscopy (SEM)

A scanning electron microscope accelerates a finely focused beam of electrons onto a target sample, resulting in the emission of electrons (secondary electrons, Auger and back-scattered electrons), X-rays, light (cathodoluminesense) and heat (phonons).[20] The detection of secondary electrons from this array of signals is used for the purpose of imaging,[20] and yields contrast images of the sample surface with superb depth of field. Modern scanning electron microscopes are capable of imaging with a spatial resolution of 1.5 - 10 nm for well prepared and highly electrically conductive samples. The particle morphologies of the polycrystalline materials synthesised herein were examined using a FEI Sirion 200 scanning electron microscope operating under a vacuum of *ca.* 10^{-8} bar.

The electrons that constitute the incident beam are typically generated by thermionic emission from a tungsten filament, which are then accelerated through a potential of 5 kV by an anode. The resulting electron beam is focused by magnetic lenses which reduce the focal spot of the beam to a few nanometres. A pair of scanning coils is then used to deflect the focussed beam so as to scan over a rectangular area of the sample surface in a raster fashion. The interaction between the incident electron beam and the target sample occurs within a finite, pear-shaped volume that can extend as far as five micrometres beneath the sample surface. However, the emission of secondary electrons originates from within a depth of just a few nanometres, and is highly localised to the region illuminated by the focussed beam, as illustrated in Figure 3.10. These secondary electrons are accelerated toward a scintillator-photomultiplier detector, and the resulting signal contributes to a two-dimensional intensity distribution that constitutes the image seen in an electron micrograph.

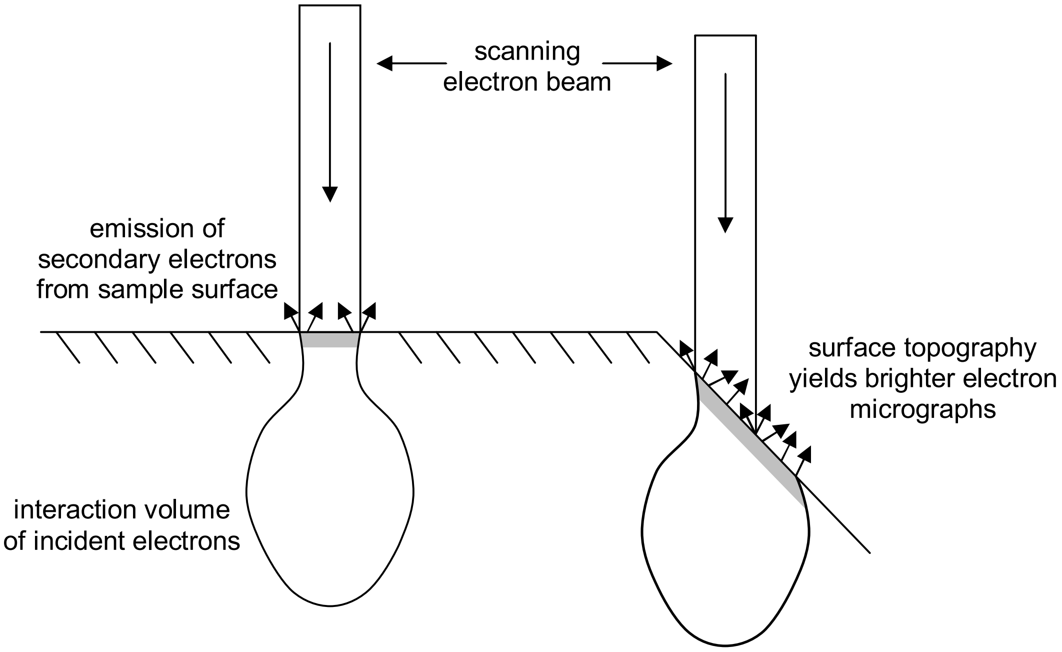

Figure 3.10 Interaction of a scanning electron microscope beam with the surface of a sample. Secondary electrons can only escape from within a depth of a few nanometres of the surface.

The contrast exhibited by an electron micrograph is dependent upon the number of secondary electrons that reach the detector. If the electron beam is incident perpendicular to a flat surface then the interacting volume is symmetric about the axis of the beam. However, if the angle of incidence increases, the interacting volume will be shallower on one side of the beam, allowing a greater number of secondary electrons to be generated. Consequently, sloping surfaces will appear brighter than horizontal surfaces. The ability to image the surface topography of the sample in this manner provides the electron micrograph with a depth of field.

3.7 Transmission Electron Microscopy (TEM)

A transmission electron microscope accelerates a finely focussed beam of electrons onto a target sample in a similar fashion to that of a scanning electron microscope.[20] However, the energy of this beam (*ca.* 100 kV) is significantly higher than that employed for the purposes of SEM, and information about the interactions between the incident electrons and the sample is instead provided by the transmitted beam. Using this approach, both a contrast image and an electron diffraction pattern of a selected area of the sample can be viewed interchangeably;[20] if the back focal plane of the objective lens is focussed on the detector, then a diffraction pattern will be observed, whereas if the front focal plane is in focus, a contrast image is instead observed. The ability to probe the local structure with atomic resolution lends this technique to the study of structural defects. However, care must be taken when interpreting these images as the features observed will be dominated by heavy atoms, and will have arisen from the superposition of all atoms projected along the beam direction.

By orientating a sample at high magnification, an area of a crystallite that satisfactorily transmits electrons can be selected for electron diffraction. In this way, single crystal domains within a crystallite can often be studied. However, the scattering of electrons by atoms originates from both nuclear as well electronic scattering, such that the interaction of electrons with atoms is several million times greater than that of X-rays with atoms.[21] This large increase in scattering efficiency means that electrons can be scattered by a number of different (*hkl*) planes before being transmitted to the detector, which modifies considerably the intensity distributions. The difficulty in interpreting these intensities means that the analysis of electron diffraction data cannot be carried out in the same way as for X-ray diffraction data collected from a single crystal, and instead requires a much more intensive, wave-mechanical treatment of the data.[20]

3.8 Thermogravimetric Analysis (TGA)

A thermogravimetric analyser provides a quantitative measure of the change in mass of a sample as a function of time or temperature.[22] This technique can be used to follow processes such as desorption, dehydration, decomposition, oxidation and reduction, allowing for the thermal stability of a material to be evaluated.[22] Experiments in this thesis were carried out using a Perkin Elmer TGA 7 thermogravimetric analyser.

In a typical experiment, a sample of mass of 5 - 40 mg is contained in a platinum pan and is suspended from the internal balance of the TGA using a hang-down wire, as illustrated in Figure 3.11. The sample is then enclosed within a furnace in which the flow of a selected gas can be precisely controlled. During heating, this gas will also have a role in purging volatised species from the furnace chamber, which can either be analysed using a complementary technique such as mass spectrometry, or vented as exhaust gas.

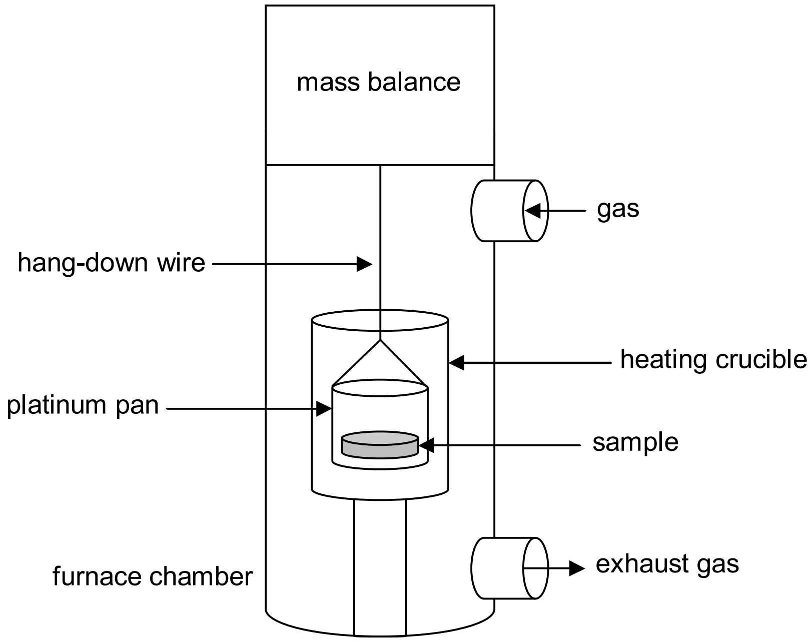

Figure 3.11 Schematic of a thermogravimetric analyser.

3.9 Differential Scanning Calorimetry (DSC)

A differential scanning calorimeter determines the heat required to maintain a sample and a reference at the same heating rate as a function of time or temperature.[22] The temperatures and heat flows are measured in a controlled environment, allowing for information about the physical and chemical properties of the sample to be analysed.[22] The progress of the reaction between lithium hydroxide monohydrate and molybdenum trioxide, as discussed in Chapter 4, was followed using a TA Instruments Q1000 DSC equipped with a refrigerated cooling system.

In a typical experiment, a sample of mass *ca.* 10 mg is contained within an aluminium pan, and this, together with an empty reference pan, is enclosed within a calorimetric cell. The temperatures of the sample and reference are maintained to be the same using separate heating elements, as shown in Figure 3.12. The difference in power

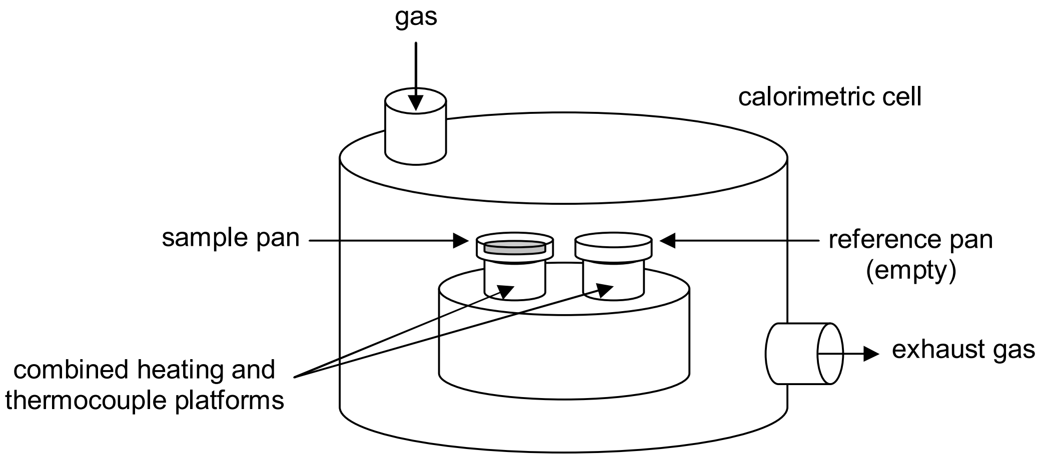

Figure 3.12 Schematic of a differential scanning calorimeter.

supplied to each element necessary to maintain a constant heating rate is then used to quantify the heat flow to or from the sample, *Q*/*t*; the heat, *Q* (J), supplied per unit time, *t* (s).

Differential scanning calorimetry is typically conducted under the constant pressure of a controlled flow of a selected gas. Under this condition, the definition of enthalpy, *H* (J), given by:

$$H = U + pV,^{23} \tag{3.22}$$

where U is internal energy (J), p is pressure (Pa) and V is volume (m^3), can be simplified. The differentiation of equation (3.22) is first performed to give:

$$dH = dU + pdV + Vdp\,. \tag{3.23}$$

Since any change in internal energy is given by:

$$dU = dQ - pdV,^{23} \tag{3.24}$$

where dQ is the infinitesimal amount of energy added to the system by heating and pdV is the infinitesimal amount of energy transferred to the environment in the form of mechanical (pressure-volume) work, the substitution of equation (3.24) into equation (3.23) can be carried out to give:

$$dH = dQ + Vdp\,. \tag{3.25}$$

Therefore, under constant pressure, equation (3.25) can be simplified to:

$$\left(\frac{dQ}{dt}\right)_p \approx \frac{dH}{dt}, \tag{3.26}$$

such that the change in the heat supplied is approximately equivalent to a change in enthalpy. The difference in heat flow between the sample and reference can then be given by:

$$\Delta\frac{dH}{dt} = \left(\frac{dH}{dt}\right)_{reference} - \left(\frac{dH}{dt}\right)_{sample}. \tag{3.27}$$

Typically, peaks arising from positive differences in heat flow correspond to exothermic events such as crystallisation, whilst those arising from negative differences correspond to endothermic events such as melting. However, there is no universal convention to the signage of heat flow.[22]

The enthalpy change of a process can be determined by taking the integral of the corresponding peak above the base line.[22] Assuming that the heat capacity of the reference is constant over the temperature range covered by this peak, it follows that the enthalpy change associated with the reference will cancel out, thus giving:

$$\int\left(\frac{dH}{dt}\right)_{sample} dt = \Delta H_{sample}. \tag{3.28}$$

3.10 AC Impedance Spectroscopy

AC impedance spectroscopy is a general term for the measurement of various electrical responses of materials in the bulk or at an interface, or both, using AC current methods.[24] The experiments conducted in this thesis were collected in terms of the impedance response in the frequency domain, and were used to study the transport properties of a range of polycrystalline materials. These data were collected using a Solartron 1260 frequency response analyser, and analysed using the ZView3 (version 3.20) software.

In its most common form, AC impedance spectroscopy involves applying an AC voltage, V, as a function of angular frequency, ω, across a sample:

$$V = V_0 e^{i\omega t},^{24} \qquad (3.29)$$

where V_0 is the magnitude of the voltage (V), $\omega = 2\pi f$ (rad s^{-1}), f is frequency (s^{-1}) and t is time (s). This results in the flow of an alternating current, I, through the sample:

$$I = I_0 e^{i(\omega t + \Phi)},^{24} \qquad (3.30)$$

that is of the same frequency as the voltage, but whose phase is rotated by an angle, Φ. Accordingly, the impedance of the sample, Z, also consists of real and imaginary parts that belong to the resistive and capacitive components respectively, of the electrical response. This can be expressed using Ohm's Law as:

$$Z = \frac{V_0}{I_0} e^{-i\Phi} = |Z| e^{-i\Phi} = |Z| \cos\Phi - i|Z| \sin\Phi = Z' - iZ'',^{24} \quad (3.31)$$

which, in turn, can be represented as a complex-plane plot, as illustrated in Figure 3.13. Therefore, when *Φ* = 0, the voltage and current are in phase, and so the impedance response corresponds to that of a resistor, *R*:

$$Z_R = R.^{24} \quad (3.32)$$

Conversely, when *Φ* = -90°, there is no real component, and so the impedance response corresponds to that of a capacitor, *C*:

$$Z_C = \frac{1}{i\omega C}.^{24} \quad (3.33)$$

In a typical experiment, a pelleted sample is attached with platinum electrodes and positioned in a furnace in which the flow of a selected gas can be controlled. This pellet is then arranged in an electrical circuit with a frequency response analyser, which measures the current and voltage responses of the sample as a function of

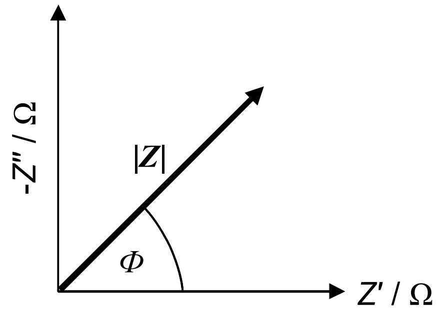

Figure 3.13 Complex-plane plot of the imaginary component, *Z''*, plotted against the real component, *Z'*, of the impedance response. *Φ* is the rotation in phase of the current output with respect to the voltage input.

frequency. These measurements are conducted with the sample under thermal equilibrium, and are repeated for a range of temperatures. For each of these temperatures, the impedance response is represented in the form of a complex-plane plot, as illustrated in Figure 3.14 for idealised ionic conduction in a polycrystalline sample. This impedance profile can be correlated with the microstructure of a polycrystalline sample, where the semicircle at high frequency corresponds to intragrain conduction, the semicircle at lower frequency corresponds to intergrain conduction, and the tail-like contribution at low frequency corresponds to the storage of charge at the interface between the sample and electrode.[24] These features can, in turn, be modelled on the basis of circuit components,[24] where each of the semicircles can be fitted using a parallel combination of a resistor and a capacitor.

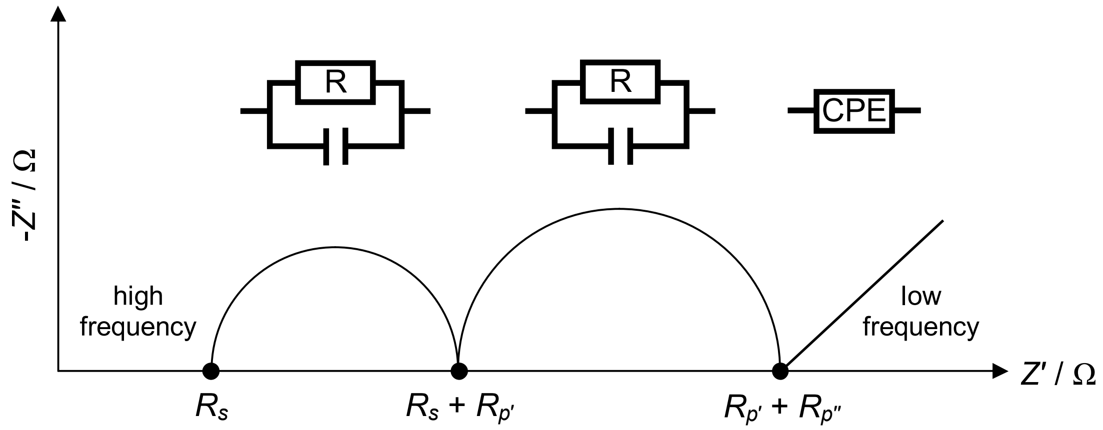

Figure 3.14 Complex-plane plot for idealised ionic conduction in a polycrystalline sample, where the imaginary component, Z'', is plotted against the real component, Z', of the impedance response. The equivalent series resistance and the polarised resistance are denoted by R_s and R_p respectively. Each feature contributing to the impedance profile corresponds to a component of the sample-electrode system, and can be modelled on the basis of circuit components, as indicated above each feature.

In the case of the first semicircle, this model is given by:

$$Z = R_s + \frac{R_p}{1+\omega^2 R_p^2 C^2} - \frac{i\omega R_p^2 C}{1+\omega^2 R_p^2 C^2}, ^{24} \tag{3.34}$$

where R_s is the equivalent series resistance of the circuit components outwith the sample (Ω), R_p is the resistance arising from the sample (Ω), and C is the capacitance arising from the sample (F). Therefore, in the limiting case at high frequency, both the real and imaginary terms relating to the impedance of the sample disappear to give:

$$Z = R_s, \tag{3.35}$$

which corresponds to the semicircular intercept on the real axis at high frequency. As the frequency tends to zero, equation (3.34) will instead simplify to give:

$$Z = R_s + R_p, \tag{3.36}$$

which corresponds to the semicircular intercept on the real axis at lower frequency. In practice, arcs that are partially or completely overlapping and that are depressed below the real axis are more commonly observed. The latter represents non-ideal behaviour, and can be accounted for by using a constant phase element (CPE) in place of a capacitor.[24] The impedance of a constant phase element is defined as:

$$Z_{CPE} = \frac{1}{(i\omega)^P B}, ^{24} \tag{3.37}$$

where P is a constant ($0 \leq P \leq 1$) and B is the non-ideal capacitance (F). Therefore, when $P = 1$, Z_{CPE} corresponds to the impedance of an ideal capacitor, Z_C. The tail-like contribution at low frequency can similarly be modelled using a constant phase element, by adding this component in series to the first two RC or RCPE components.[24]

In order to determine the total ionic conductivity of a sample, σ_{total} (S cm^{-1}), at a temperature, T (K), the total resistance, R_{total} (Ω), derived from the semicircles in the complex-plane plot must first be corrected for the electrode-material contact area, A (cm^2), and the pellet thickness, l (cm), using the equation:

$$\rho = \frac{R_{total} A}{l},^{6} \qquad (3.38)$$

to give the value of the resistivity, ρ (Ω cm). The total ionic conductivity is then given by taking the reciprocal of the resistivity:

$$\sigma_{total} = \frac{1}{\rho}.^{6} \qquad (3.39)$$

Ionic conductivity is usually an activated process,[6] and so the total ionic conductivities derived from impedance data collected over a range of temperatures may be expressed using the Arrhenius relationship,[6] as given by:

$$\sigma_{total} = Ae^{\frac{-E_a}{k_B T}}, \qquad (3.40)$$

where A is a pre-exponential factor, E_a is the activation energy (J), and k_B is the Boltzmann constant (1.380 J K^{-1}).

By performing impedance measurements under various conditions of temperature and atmosphere, and correlating their effect to the response of the sample, the influence of microstructure on the conductivity of a polycrystalline solid can be investigated.

3.11 References

1. B. D. Cullity and S. R. Stock, *Elements of X-Ray Diffraction*, 3rd edn., Prentice Hall, 2001.
2. T. Young, *Philos. Trans.*, 1804, **94**, 1-16.
3. W. L. Bragg, *Proc. Camb. Philol. Soc.*, 1913, **17**, 43-57.
4. W. H. Bragg and W. L. Bragg, *Proc. R. Soc. Lond. A*, 1913, **88**, 428-428.
5. C. Hammond, *The Basics of Crystallography and Diffraction*, 2nd edn., Oxford University Press, New York, 2001.
6. A. R. West, *Basic Solid State Chemistry*, 2nd edn., John Wiley & Sons, Inc., Chichester, 2005.
7. J. A. Ibers and W. C. Hamilton, *International Tables for X-ray Crystallography, Volume IV*, Kynoch Press, Birmingham, 1974.
8. C. Giacovazzo (Ed.), H. L. Monaco, G. Artioli, D. Viterbo, M. Milanesio, G. Ferraris, G. Gilli, P. Gilli, G. Zanotti and M. Catti, *Fundamentals of Crystallography*, 3rd edn., Oxford University Press, New York, 2011.
9. G. M. Sheldrick, *Acta Cryst.*, 2008, **A64**, 112-122.
10. R. A. Young, ed., *The Rietveld Method*, Oxford University Press, Oxford, 1996.
11. A.-J. Dianoux and G. Lander, *Institut Laue-Langevin: Neutron Data Booklet*, 2nd edn., OCP Science, Philadelphia, 2003.
12. G. L. Squires, *Introduction to the Theory of Thermal Neutron Scattering*, Dover Publications, Inc., Mineola, New York, 1996.

13. E. Suard and A. Hewat, *Neutron News*, 2001, **12**, 30-33.

14. M. Abramowitz and I. A. Stegun, *Handbook of Mathematical Functions with Formulas, Graphs, and Mathematical Tables*, 9th edn., Dover Publications, Inc., New York, 1972.

15. P. Thompson, D. E. Cox and J. B. Hastings, *J. Appl. Crystallogr.*, 1987, **20**, 79-83.

16. A. C. Larson and R. B. Von Dreele, *General Structure Analysis System (GSAS)*, Los Alamos National Laboratory Report LAUR 86-748, 2004.

17. H. M. Rietveld, *J. Appl. Crystallogr.*, 1969, **2**, 65-71.

18. L. B. McCusker, R. B. Von Dreele, D. E. Cox, D. Louër and P. Scardi, *J. Appl. Crystallogr.*, 1999, **32**, 36-50.

19. N. E. Brese and M. O'Keeffe, *Acta Cryst.*, 1991, **B47**, 192-197.

20. D. Brandon and W. D. Kaplan, *Microstructural Characterisation of Materials*, 2nd edn., John Wiley & Sons, Ltd., Chichester, 2008.

21. C. G. Shull and E. O. Wollan, *Science*, 1948, **108**, 69-75.

22. P. J. Haines, *Principles of Thermal Analysis and Calorimetry*, Royal Society of Chemistry, Cambridge, 2002.

23. P. W. Atkins and J. de Paula, *Atkins' Physical Chemistry*, 7th edn., Oxford University Press, Oxford, 2002.

24. E. Barsoukov and J. R. Macdonald, *Impedance Spectroscopy: Theory, Experiment and Applications*, 2nd edn., John Wiley & Sons, Inc., Hoboken, New Jersey, 2005.

4 Direct Room-temperature Preparation of Li_2MoO_4 from Crystalline $LiOH\cdot H_2O$ and MoO_3

4.1 Introduction

Complex metal oxides are conventionally prepared by heating stoichiometric combinations of binary salts at high temperature.[1] These temperatures are often in excess of 1000 °C, and are used to meet two of the basic requirements for reaction between solids: to provide sufficient energy to simultaneously break the large number of bonds in the crystalline reagents and to overcome the energy barrier to ion migration. By thermally activating ion migration, mass transport can be effective over the course of days, during which time the entropically driven mixing of cations is exploited to drive the formation of higher-order compounds.

This high-temperature approach often allows compounds to be prepared in a straightforward manner, but at a considerable energy cost and with poor control afforded to particle growth. In addition to these failings, the use of high temperatures can also introduce complications where reagents show significant volatility at these high temperatures. This is particularly problematic in the preparation of some lithium-containing compounds.[2] The limitations of synthesis at high temperature have led to a number of alternative synthetic approaches being explored, as previously discussed in Chapter 2.

This chapter describes another such alternative synthetic route that relates to the preparation of lithium molybdate, Li_2MoO_4. Polycrystalline samples of lithium molybdate can be readily prepared by high-temperature solid-state reaction,[3] to give fused, monolithic particles. Smaller, mono-disperse particles of lithium molybdate, which are more suited for industrial applications, have been prepared following a multi-step synthesis that involves precipitation from ethanolic solution.[4] By contrast, this new and unusual route to lithium molybdate proceeds from solid reagents at room temperature, and is thus more environmentally sound than either of the above methods. This one-step reaction occurs spontaneously using readily available starting materials, and yields relatively uniform, micrometre-sized particles. The driving force behind this reaction has been investigated using calorimetry. An investigation into the applicability of this reaction as a synthetic route is also reported. In addition, given that fast-ion conduction is exhibited in closely related phases,[5, 6] the transport properties of lithium molybdate have been evaluated by AC impedance spectroscopy.

Lithium molybdate crystallises in the space group $R\bar{3}$ with the phenacite (Be_2SiO_4)[7] structure-type, as first suggested by Zachariasen and Plettinger almost 50 years ago,[8] and consists of isolated $(MoO_4)^{2-}$ tetrahedra that are connected by charge balancing lithium cations. A number of reports have suggested modifications of the structure of lithium molybdate with trigonal[9] and orthorhombic[3] symmetries, however, these studies have been contradicted.[4, 10] Of particular interest was the report of the trigonal modification in the space group $P3_2$, since the implications of a chiral space group is of considerable importance in determining the physical properties of lithium molybdate. In order to resolve this ambiguity, a redetermination of the crystal structure of lithium molybdate is also presented.

4.2 Experimental

4.2.1 Synthesis of Li_2MoO_4

Lithium molybdate was prepared following four different synthetic routes. The samples yielded from these preparations will be referred to as samples **A**, **B**, **C** and **D**. The reagents used in these preparations were supplied by Alfa Aesar in purities in excess of 99 %, and were used in stoichiometric quantities.

Sample **A** was prepared using lithium hydroxide monohydrate (1.829 g, 43.59 mmol), $LiOH{\cdot}H_2O$, and molybdenum trioxide (3.137 g, 21.79 mmol), MoO_3, which were ground together under ambient conditions for *ca.* 1 min using an agate mortar and pestle. This procedure led to the formation of a paste that dried at room temperature after *ca.* 1 hr, leaving a layer of product on the surface of the mortar that was then dislodged and ground to a fine powder. The preparation of sample **B** brought the same reagents, as finely ground powders, into intimate contact with one another with minimal agitation. This was achieved by mixing the reagents by stirring, and then gently compacting the resulting mixture using the pestle and mortar. The third sample, **C**, was prepared following a previously reported high-temperature solid-state route.[3] This synthesis proceeded by heating a pelleted mixture of lithium carbonate (1.478 g, 20.00 mmol) and molybdenum trioxide (2.879 g, 20.00 mmol) in a furnace at 600 °C for 6 hr, *via* a 1 °C min^{-1} ramp from room temperature. The sample was then ground and pressed into a pellet, and heated at 600 °C for a further 7 hr *via* the same heating regime. Sample **D** was prepared by grinding crystals of lithium molybdate to give a fine polycrystalline material. These crystals were grown by dissolving lithium hydroxide monohydrate (4.196 g, 100.0 mmol) and molybdenum trioxide (7.197 g, 50.00 mmol) in 25 mL of deionised water at room temperature. This solution was then heated in an open flask at 30 °C for 18 hr, after which time the majority of the solvent had evaporated and crystals were visible. The resulting crystals were collected by vacuum filtration, washed with water, and allowed to dry at room temperature in air.

X-ray powder diffraction was used to follow the progress of the reaction between lithium hydroxide monohydrate and molybdenum trioxide. This experiment was carried out by grinding the reagents together for *ca.* 1 min to yield a paste, in the same manner to that giving sample **A**. The resulting paste was then mounted on a sample holder, and a series of X-ray powder diffraction measurements were performed. Diffraction data were collected over the range $15.00 \leq 2\theta \leq 39.99°$, using a step size of 0.03° 2θ and a count time of 0.5 s $step^{-1}$.

Differential scanning calorimetry was additionally used to follow the progress of the reaction between lithium hydroxide monohydrate (3.2 mg, 76 μmol) and molybdenum trioxide (5.5 mg, 38 μmol), under a dynamic atmosphere of dry air. These reagents were both finely ground and placed separately into the halves of a partitioned aluminium pan at room temperature. This temporary partition, which was made of card, was used to keep the reagents separate as they were cooled to -80 °C and equilibrated at this temperature. Once the reagents had reached thermal equilibrium, the cell was opened and the partition was carefully removed whilst the pan remained *in situ*. The reagents were then mixed for 10 s using a steel pin before the cell was closed again. In the course of opening and closing the cell to mix the reagents, the temperature of the aluminium pan did not exceed -60 °C. The mixture was then re-equilibrated to -80 °C before being heated to 200 °C at a rate of 1 °C min^{-1}, where it was held for 5 min. The resulting crystalline solid was analysed by X-ray powder diffraction. Additional calorimetric measurements incorporating temperature cycling, isotherms and different heating rates were also employed to further investigate the observed transitions.

The role of water in the preparation of sample **A** was investigated by performing a reaction using anhydrous lithium hydroxide (0.599 g, 25.0 mmol) and molybdenum trioxide (1.799 g, 12.50 mmol). These reagents were ground together under ambient conditions for 10 min, and, in contrast to the preparation of sample **A**, remained friable. This mixture was then left to stand in an open-top vial that was exposed to ambient atmosphere. X-ray powder diffraction was used to follow the progress of the reaction over the course of several months.

The versatility of the reaction used to prepare samples **A** and **B** was explored by substituting (i) lithium hydroxide monohydrate with sodium hydroxide monohydrate and (ii) molybdenum trioxide with tungsten trioxide, in separate experiments. Each set of starting materials [$NaOH{\cdot}H_2O$ (1.829 g, 43.59 mmol) and MoO_3 (3.137 g, 21.79 mmol); $LiOH{\cdot}H_2O$ (3.137 g, 21.79 mmol) and WO_3 (3.137 g, 21.79 mmol)] were ground together in stoichiometric quantities under ambient conditions for 20 min. X-ray powder diffraction was then used to identify the products of each of these reactions.

4.2.2 Characterisation of Lithium Molybdate

Crystals of lithium molybdate suitable for X-ray structure analysis were grown by dissolving 2.3 g of sample **A** in 20 mL of freshly boiled deionised water at *ca.* 70 °C. This solution was boiled in an open flask for 10 min, after which time small crystals were visible. At this point, the solution was removed from the heat and allowed to cool to room temperature. Single-crystal X-ray diffraction data were collected from a colourless columnar crystal of dimensions $0.30 \times 0.10 \times 0.10$ mm^3. These data were collected and analysed by Dr Claire Wilson. Details of the data collection are given in Table 4.1.

In order to identify the presence of lithium molybdate in samples **A**, **B**, **C** and **D**, X-ray powder diffraction data suitable for Rietveld analysis were collected from each of these samples over the range $10 \leq 2\theta \leq 80°$. The structural model derived from the single-crystal X-ray diffraction study of lithium molybdate was then refined against each of these powder diffraction data sets.

The size and morphology of the particles comprising samples **A**, **B**, **C** and **D** were evaluated by scanning electron microscopy. The microstructure of sample **A** was additionally evaluated on the bulk scale, using nitrogen adsorption/desorption measurements at 77 K. This experiment involved degassing approximately 0.45 g of sample **A** at temperatures of up to 100 °C for 4 hr whilst under a reduced pressure of 10 μmHg. This degassed sample was transferred to the surface area analyser, where the free-space volume of the sample chamber was determined at 77 K. The molar quantity of nitrogen adsorbed or desorbed by the sample was then measured on increasing or decreasing, respectively, the relative pressure over the range $0.3 \leq P/P_0 \leq 1.0$.

The presence of guest species in the structure of lithium molybdate was evaluated with respect to the thermal stability of the bulk sample using thermogravimetric measurements. The thermal stability of samples **A** and **B** were investigated under a dynamic atmosphere of dry helium, whereby approximately 10 - 20 mg of sample was equilibrated at 50 °C for 5 min before being heated up to 500 °C at a rate of 10 °C min^{-1}.

The mobility of ions in the structure of lithium molybdate was evaluated by AC impedance spectroscopy in air. Approximately 0.27 g of sample **A** was pressed under a load of 3 tonnes to give a 10 mm diameter cylindrical pellet approximately 1.4 mm thick. This pellet was attached with two platinum electrodes and loaded into a sample holder. The pellet was then sintered at 600 °C in air for 3 d, *via* a 2.5 °C min^{-1} ramp from room temperature. After this period of sintering, impedance data were collected over the range $0.2 \leq f \leq 10^6$ Hz at isothermal points on cooling the sample from 600 °C to 250 °C.

4.3 Results

4.3.1 The Structure of Li_2MoO_4

The structure of lithium molybdate was solved from single-crystal X-ray diffraction data in the space group $R\overline{3}$ (a = 14.3178(14) Å and c = 9.5757(9) Å), with no reflections that violated the systematic absences hkl: h-k+l = 3n and 00l: l = 3n associated with this space group. This starting structural model was refined by full-matrix least-squares against F^2, with positional and anisotropic atomic displacement parameters refined for all atoms. The final refinement of 65 variables using 867 unique reflections converged at $R(F) = 0.016$ and $wR(F^2) = 0.036$ with $S = 1.259$. Difference Fourier calculations based on this model show that the highest peak is 0.39 e Å^{-3}, whilst the deepest hole is -0.38 e Å^{-3}, indicating that there is no residual electron density of chemical significance. This final structural model provides a good fit to the observed data, as shown by the fit parameters and electron density analysis, and is in agreement with the structure determination by Kolitsch.[10] Details of the data collection, solution and refinement are given in Table 4.1, whilst the refined crystal structure is illustrated in Figure 4.1. The atomic parameters are given in Table 4.2, and selected interatomic distances are listed in Table 4.3.

Table 4.1 Experimental details of the crystallographic characterisation of a single crystal of Li_2MoO_4

Crystal data	
Chemical formula	Li_2MoO_4
Formula weight (M_r) / g mol^{-1}	173.82
Cell setting	Trigonal
Space group	$R\bar{3}$
T / K	150(2)
a / Å	14.3178(14)
c / Å	9.5757(9)
V / Å^3	1700.0(2)
Z	18
D_c / Mg m^{-3}	3.056
Radiation type	Mo K_α
μ / mm^{-1}	3.319
Crystal form	Columnar
Colour	Colourless
Crystal size / mm	0.30 × 0.10 × 0.10
Data collection	
Data collection method	ω
Absorption correction	Multi-scan[a]
T_{min}	0.536
T_{max}	0.718
No. of (measured, independent, observed) reflections	(3533, 867, 858)
Criterion for observation	$I > 2\sigma(I)$
R_{int}	0.026
θ_{max} / °	27.46
Refinement	
$R(F)$, $wR(F^2)$, S	0.016, 0.036, 1.259
No. of reflections	867
No. of parameters	65
Weighting scheme[b]	$w = 1 / [\sigma^2(F_o^2) + (0.0163P)^2 + 2.0800P]$
$(\Delta / \sigma)_{\text{max}}$	0.001
$\Delta\rho_{\text{max}}$, $\Delta\rho_{\text{min}}$ / e Å^{-3}	0.39, -0.38

[a] Based on symmetry-related measurements

[b] $P = (F_o^2 + 2F_c^2) / 3$

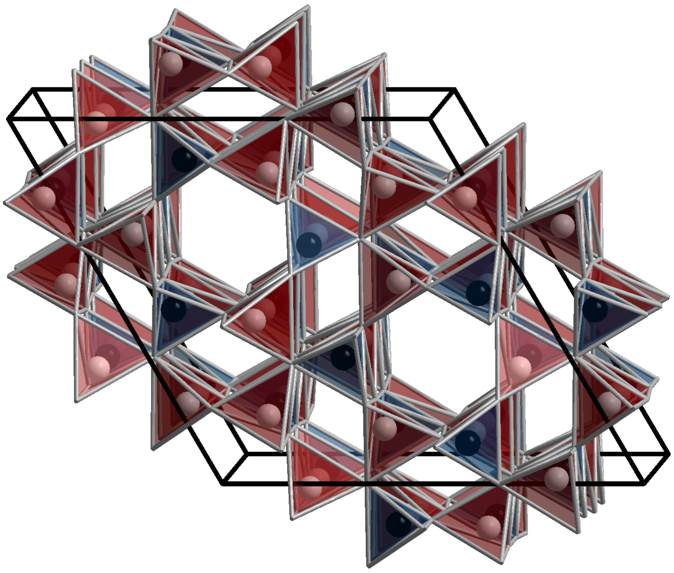

Figure 4.1 The crystal structure of Li_2MoO_4 derived from least-squares refinement against single-crystal X-ray diffraction data collected at 150 K. The lithium (white spheres) and molybdenum (black spheres) cations are tetrahedrally coordinated to oxide anions. These tetrahedral units are connected by trigonally coordinated oxide anions in a corner-sharing network, and in such a manner that a fully ordered distribution of metal cations is generated.

Table 4.2 Structural parameters for Li_2MoO_4 derived from least-squares refinement against single-crystal X-ray diffraction data collected at 150 K

Atom	*Site*	*x*	*y*	*z*	U_{eq} / Å^2
Mo	18*f*	0.647338(13)	0.118283(13)	0.08391(2)	0.00836(8)
Li1	18*f*	0.4550(3)	0.1411(3)	0.2472(4)	0.0136(8)
Li2	18*f*	0.8560(3)	0.3091(3)	-0.0816(4)	0.0138(8)
O1	18*f*	0.66476(11)	0.00505(11)	0.0847(2)	0.0117(3)
O2	18*f*	0.57914(11)	0.11951(11)	0.2369(2)	0.0122(3)
O3	18*f*	0.77690(12)	0.23377(12)	0.0835(2)	0.0130(3)
O4	18*f*	0.57780(11)	0.11881(11)	-0.0686(2)	0.0122(3)

Table 4.3 Selected interatomic distances (Å) derived from least-squares refinement against single-crystal X-ray diffraction data collected at 150 K

Li1–O1	1.95601(4)	Li2–O1	1.95297(4)	Mo–O1	1.76214(3)
–O2	1.95617(4)	–O3	1.93330(3)	–O2	1.76815(3)
–O2	1.99820(4)	–O4	1.99760(4)	–O3	1.76586(3)
–O3	1.95360(3)	–O4	1.98304(4)	–O4	1.77266(3)
‹ Li1–O ›	1.966	‹ Li2–O ›	1.968	‹ Mo–O ›	1.767

X-ray powder diffraction data collected from sample **A** could be indexed on the basis of a unit cell (a ~ 14.3 Å, c ~ 9.6 Å) of symmetry $R\overline{3}$, and two additional weak Bragg peaks arising from the presence of molybdenum trioxide and an unidentified third phase. The description of this unit cell is consistent with the structural model derived from the single-crystal X-ray diffraction study of lithium molybdate, suggesting that reaction (4.1) had occurred.

$$2LiOH{\cdot}H_2O + MoO_3 \rightarrow Li_2MoO_4 + 3H_2O \qquad (4.1)$$

This model was fitted against the data collected from sample **A** with a total of 15 parameters refined, including background terms, phase fractions, a diffractometer zero-point error, lattice parameters and profile coefficients. The refined lattice parameters resulting from this fit were *ca.* 0.02 Å longer than those determined from the single-crystal study. These increases reflect the thermal expansion of lithium molybdate on heating from 150 K to 293 K, *i.e.* the temperatures employed in the single-crystal and powder diffraction experiments, respectively. Trial refinements that allowed the non-lithium atomic parameters to vary did not significantly improve the quality of the fit, and so the final refinement used the atomic coordinates derived from the single-crystal X-ray diffraction study and isotropic atomic displacement parameters that were fixed at 0.01 $Å^2$ for all atoms. The molybdenum trioxide impurity was modelled as a minor secondary phase in the final refinement, from which a content of approximately 1 wt. % was determined. The final fit obtained to the data collected from sample **A** is shown in Figure 4.29, where it is compared with a theoretical X-ray powder diffraction pattern of the single-crystal structure of lithium molybdate.

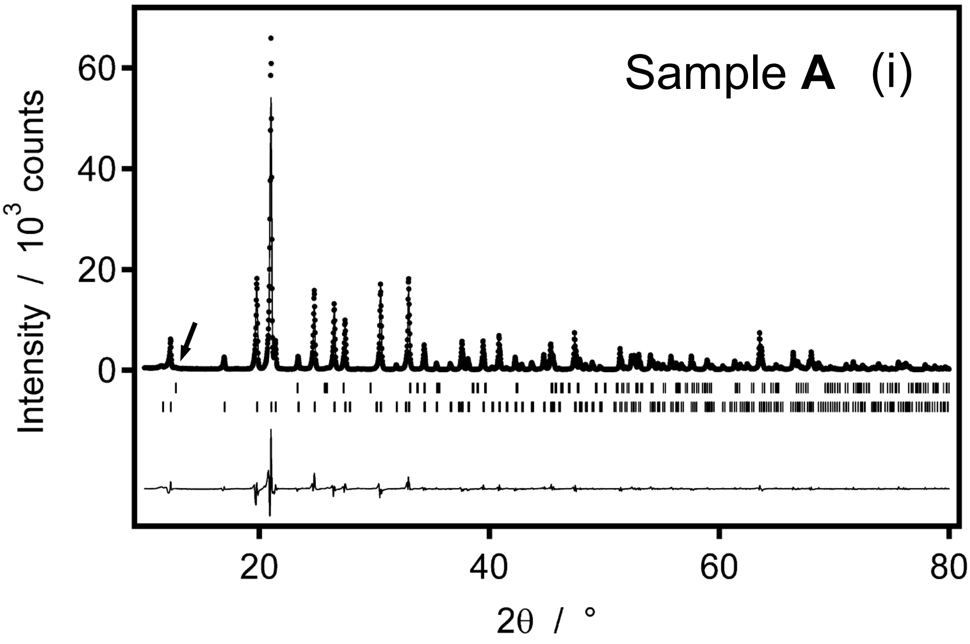

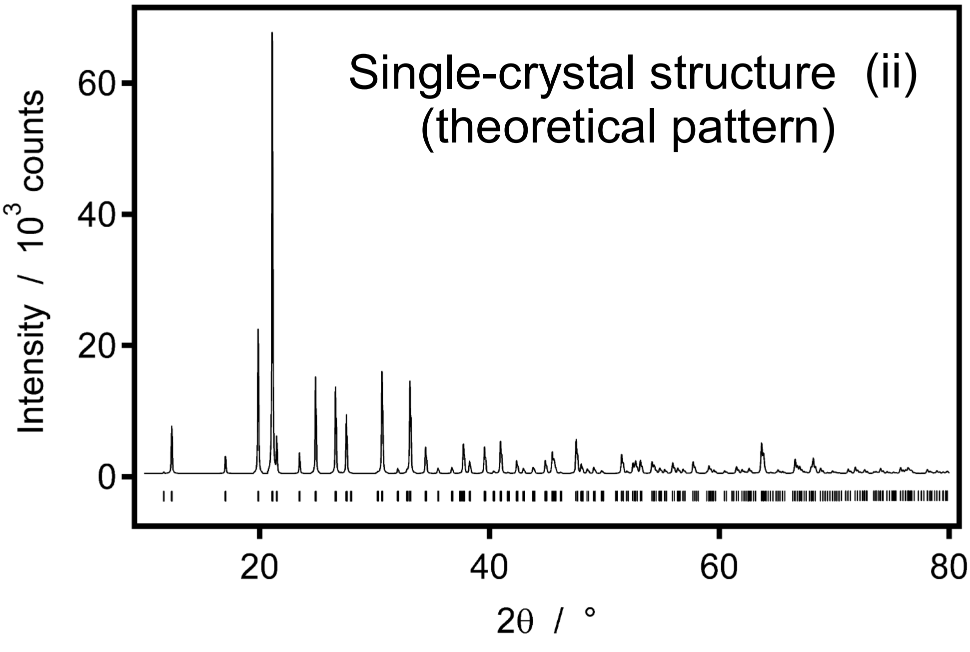

Figure 4.2 (i) Observed (dots), calculated (top line) and difference (bottom line) X-ray powder diffraction patterns for sample **A**. (ii) Theoretical (line) X-ray powder diffraction of the single-crystal structure of Li_2MoO_4. The vertical bars indicate the allowed Bragg reflection positions for Li_2MoO_4. Sample **A** contains a small quantity of MoO_3 (0.0037(8) wt. %), and the most intense peak arising from this phase is indicated with an arrow. In (i), an additional upper set of vertical bars indicate the allowed Bragg reflection positions for MoO_3.

X-ray powder diffraction data collected from samples **B**, **C** and **D** were fitted in a similar manner. A comparison of these fits showed no significant variation in either of the lattice parameters between the four differently prepared samples of lithium molybdate.

4.3.2 Time-dependent Study of $2LiOH{\cdot}H_2O + MoO_3$

A series of X-ray powder diffraction patterns collected from a 2:1 mixture of lithium hydroxide monohydrate and molybdenum trioxide after the reagents were introduced and ground together for 1 min are shown in Figure 4.3. Data collected within the first

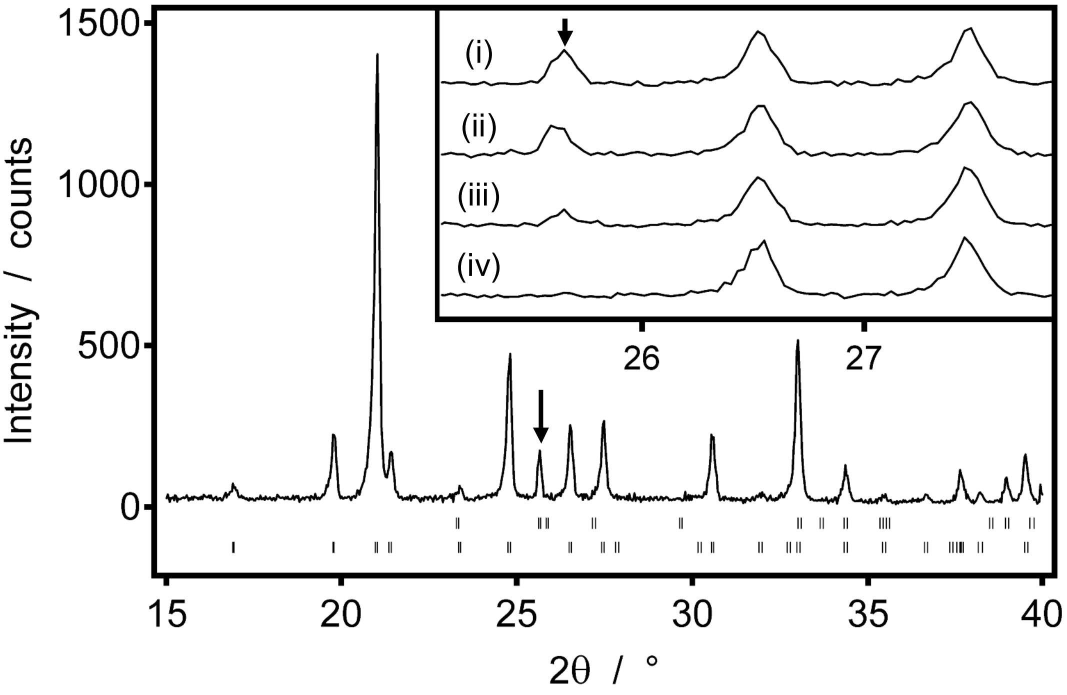

Figure 4.3 Observed X-ray powder diffraction pattern collected from a 2:1 mixture of $LiOH{\cdot}H_2O$ and MoO_3 after the reagents were introduced and ground together for 1 min. The inset shows data collected in the *ca.* 40 min period following grinding: (i) after 10 min, (ii) after 20 min, (iii) after 30 min, and (iv) after 40 min. The upper and lower vertical bars indicate the allowed Bragg reflection positions for MoO_3 and Li_2MoO_4 respectively. The most intense reflection due to MoO_3 is indicated with an arrow. In (i), MoO_3 is present as a 0.014(7) wt. % minority phase.

10 min show that lithium molybdate constitutes ≥ 99 wt. % of the sample, demonstrating that the reagents undergo rapid reaction when ground together at room temperature. Subsequent data sets show that the fraction of molybdenum trioxide steadily decreases with time. After 40 min, the diffraction pattern resembles the data collected from sample **A**. An examination of the widths of the Bragg peaks between this material and the other four samples of lithium molybdate revealed no significant variation, indicating that reaction (4.1) produces lithium molybdate in a highly crystalline state, rather than by slow ageing of an amorphous intermediate.

4.3.3 Reactivity between Anhydrous Reagents

X-ray powder diffraction data were collected from a 2:1 mixture of anhydrous lithium hydroxide and molybdenum trioxide over the course of several months. Data collected 1 d after the reagents were introduced and ground together show that lithium molybdate constituted 12 wt. % of the sample, demonstrating that anhydrous lithium hydroxide does not undergo facile reaction with molybdenum trioxide. This implies that the water of crystallisation in lithium hydroxide monohydrate plays a vital role in the rapidity of reaction (4.1). Data collected from the same sample after five months of standing in ambient atmosphere show that lithium molybdate constituted 44 wt. % of the sample, and had remained a minority phase.

4.3.4 Differential Scanning Calorimetry (DSC)

Calorimetric data collected from a 2:1 mixture of $LiOH{\cdot}H_2O$ and MoO_3 after the reagents were introduced and mixed *in situ* at -80 °C are shown in Figure 4.4. Data collected on heating to 200 °C, at a rate of 1 °C min^{-1}, clearly show an exotherm followed by an endotherm as the sample is heated through 0 °C, and a second, larger endotherm in the temperature range $26 \leq T \leq 49$ °C. Cooling the sample from a temperature above these transitions, 200 °C, and heating through the same temperature range again showed that these three transitions are irreversible.

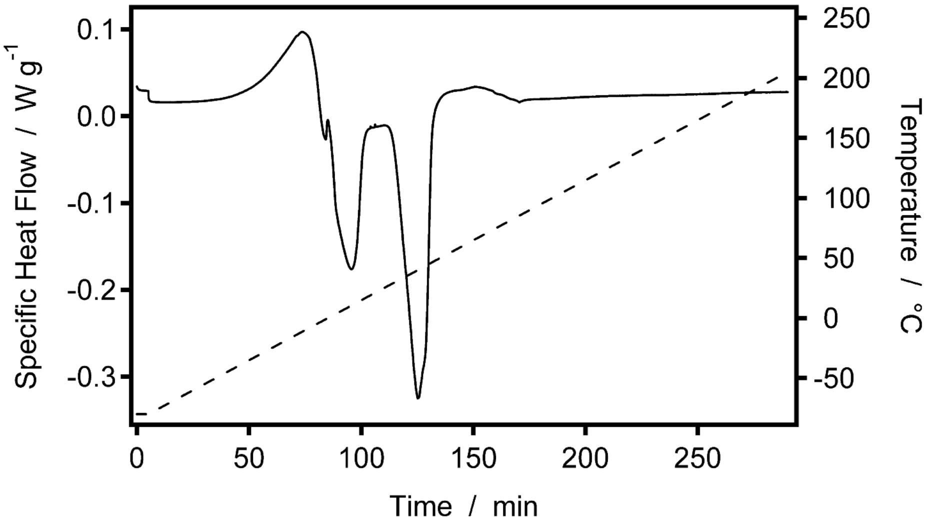

Figure 4.4 Calorimetric data collected on heating a 2:1 mixture of $LiOH{\cdot}H_2O$ and MoO_3 from -80 °C to 200 °C at a rate of 1 °C min^{-1} under a dynamic atmosphere of dry air. The reagents were introduced and mixed *in situ* at -80 °C. The specific heat flow is indicated by a continuous line, with exothermic and endothermic processes indicated by positive and negative heat flows respectively. The temperature is indicated by a dashed line.

As sample **A** was prepared at room temperature, it follows that either one or both of the transitions observed below this temperature arise as a result of reaction between the reagents. The relationship between these two transitions was investigated by introducing an isothermal period after the initiation of the exotherm at around 3 °C. This measurement is shown in Figure 4.5 and shows that the two processes could not be separated, *i.e.* once the exothermic process is initiated, the endothermic process will subsequently occur.

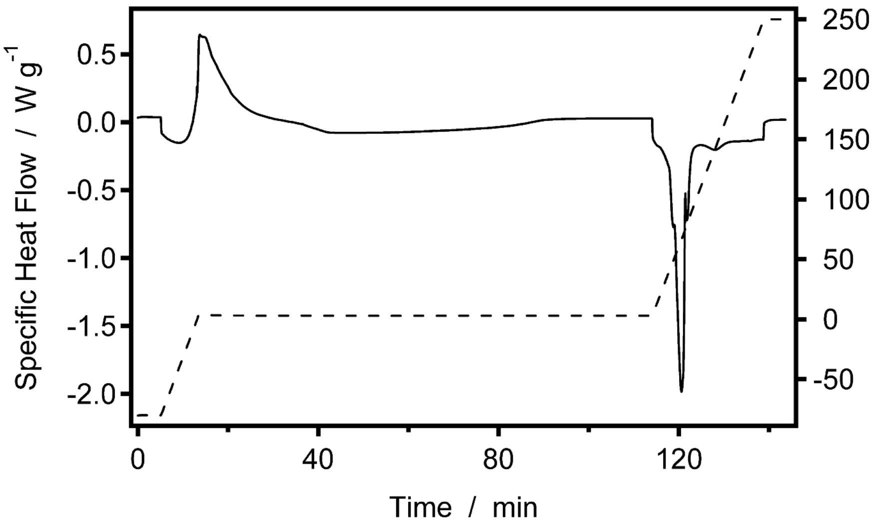

Figure 4.5 Calorimetric data collected on heating a 2:1 mixture of $LiOH \cdot H_2O$ and MoO_3 from -80 °C to 250 °C. The sample was heated at a rate of 5 °C min^{-1} to 3 °C. This temperature was maintained for a period of 100 min and then increased to 250 °C at 5 °C min^{-1}. The specific heat flow is indicated by a continuous line, with exothermic and endothermic processes indicated by positive and negative heat flows respectively. The temperature is indicated by a dashed line.

Given that reaction (4.1) produces anhydrous lithium molybdate, the water by-product of this reaction must inevitably be vaporised within the temperature range studied, $-80 \leq T \leq 200$ °C. This process could be unambiguously assigned to the large endotherm occurring over the temperature range $26 \leq T \leq 49$ °C, since this is the only feature of significance between room temperature and 200 °C. However, X-ray powder diffraction data collected from the material resulting from these DSC measurements show that a small quantity of MoO_3 remains unreacted; this suggests that the straightforward mixing of the reagents at -80 °C by stirring does not provide a sufficiently homogenous mixture for complete reaction to occur. The presence of unreacted MoO_3 implies that a stoichiometric equivalent amount of LiOH was also present.

In order to assess the contributions of these unreacted starting materials to the calorimetric profiles, the thermal behaviour of MoO_3 and $LiOH \cdot H_2O$ were investigated separately. Calorimetric data collected from $LiOH \cdot H_2O$ show that this material gives rise to a significant endotherm at around 45 °C, as shown in Figure 4.6(i). Thermogravimetric data collected from the same material show that a significant mass loss occurs at this temperature, which is commensurate with the evaporation of one mole of water per formula unit. By contrast, MoO_3 shows no significant thermal behaviour on heating over the same temperature range, as shown in Figure 4.6(ii). Incomplete reaction between $LiOH \cdot H_2O$ and MoO_3 will therefore introduce an enthalpic contribution to the final endotherm, from unreacted $LiOH \cdot H_2O$. This prevents the extent of reaction (4.1) from being quantified from these measurements.

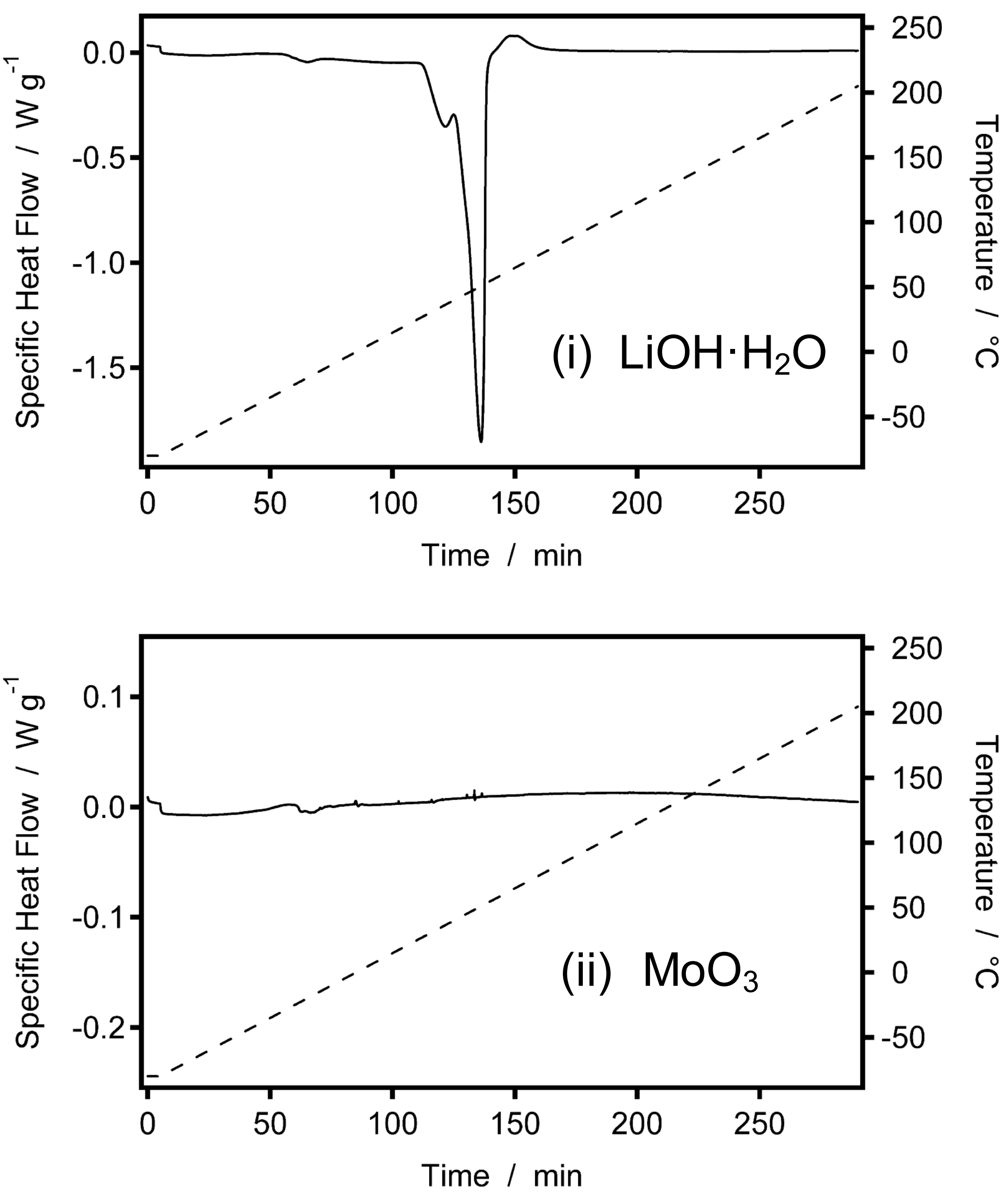

Figure 4.6 Calorimetric data collected from (i) LiOH·H_2O and (ii) MoO_3 heated from -80 °C to 200 °C at 1 °C min^{-1} under a dynamic atmosphere of dry air. The specific heat flow is indicated by a continuous line, with exothermic and endothermic processes indicated by positive and negative heat flows respectively. The temperature is indicated by a dashed line.

4.3.5 Thermogravimetric Analysis (TGA)

Thermogravimetric data collected from samples **A** and **B** both show a mass loss of approximately 1 wt. %, as illustrated for sample **A** in Figure 4.7. A mass loss of 1 wt. % is commensurate with the evaporation of 0.1 moles of water per formula unit. This negligible quantity supports the structure derived from the X-ray diffraction study of lithium molybdate, which showed that the channels in this structure are empty.

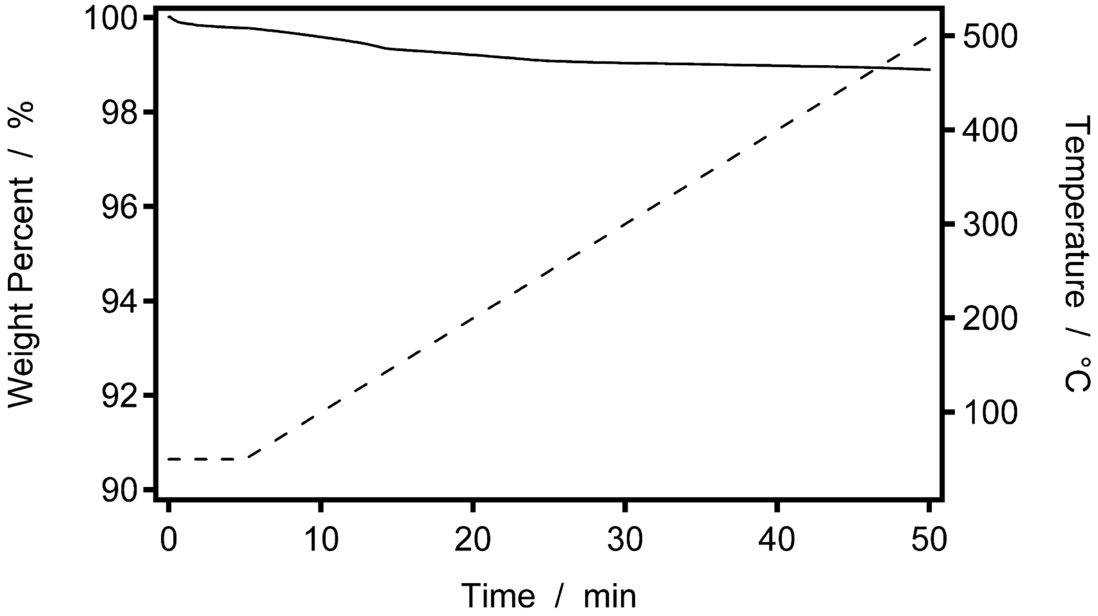

Figure 4.7 Thermogravimetric data collected on heating sample **A** from room temperature to 500 °C under a dynamic atmosphere of dry helium. The mass of sample **A** is represented by a continuous line, whilst the temperature is indicated by a dashed line.

4.3.6 Surface Area Analysis

Nitrogen adsorption/desorption isotherms collected from sample **A** are shown in Figure 4.8. Both these isotherms exhibit the characteristics of a Type II isotherm,[11] where a small uptake in nitrogen at low relative pressure, corresponding to monolayer adsorption, is followed by a larger uptake of nitrogen at higher relative pressure, which arises from multilayer adsorption. This adsorption/desorption behaviour is typified by the physisorption of gases by finely divided, macroporous or non-porous materials.[12]

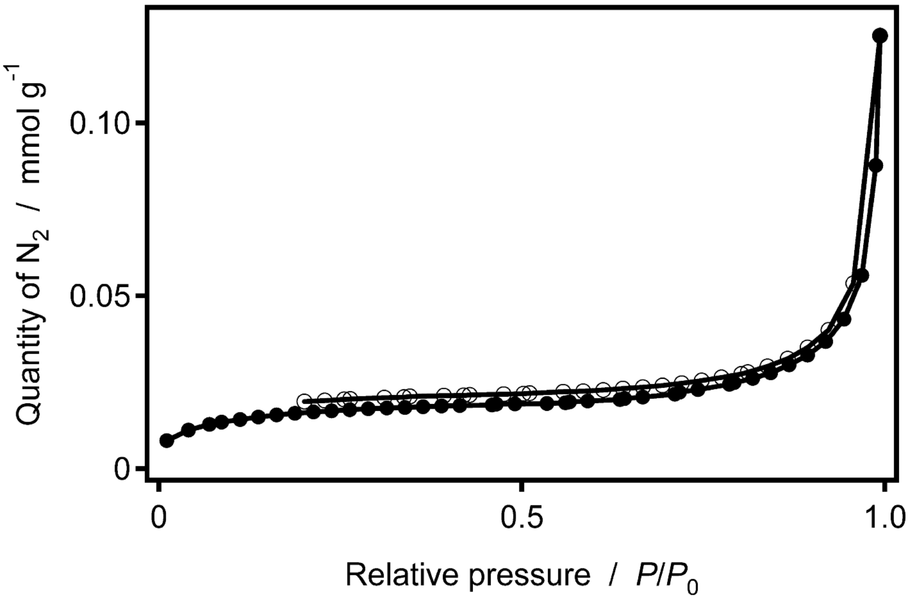

Figure 4.8 Nitrogen adsorption (filled circles) and desorption (open circles) isotherm data collected from sample **A** on increasing and decreasing, respectively, the relative pressure at 77 K.

The adsorption isotherm data collected from sample **A** could be modelled using BET theory,[13] with the adsorption of up to a monolayer of nitrogen identified over the relative pressure range $0.07 \leq P/P_0 \leq 0.16$, as illustrated in Figure 4.9. This fit indicates that sample **A** has a specific surface area of 1.351(4) m^2 g^{-1}, which is representative of a polycrystalline, non-porous material.

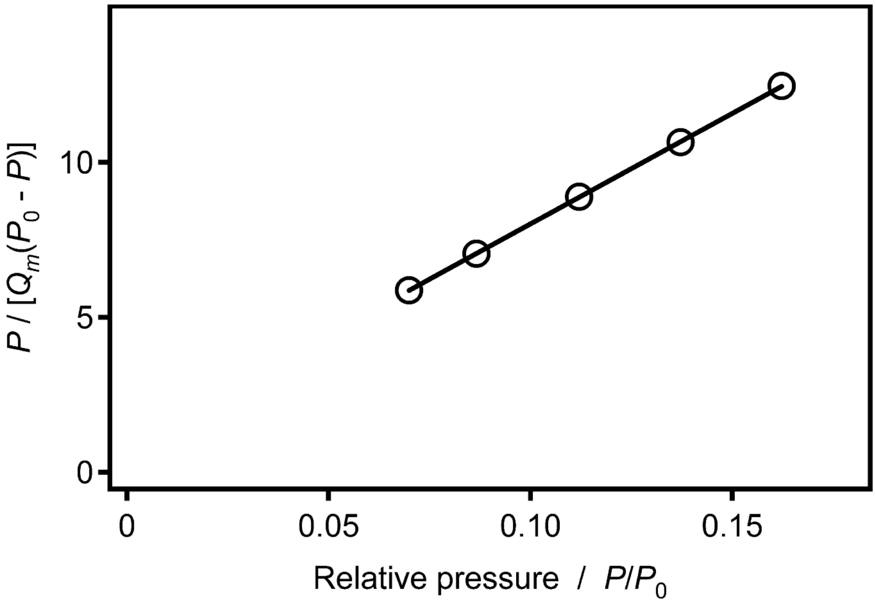

Figure 4.9 BET transform of adsorption isotherm data collected at 77 K, where the solid line indicates a linear fit to the transformed isotherm data. The quantity of nitrogen adsorbed to give monolayer coverage, Q_m, is equal to $1/(s+i)$, where s is the slope and i is the y-intercept.

4.3.7 Scanning Electron Microscopy (SEM)

Scanning electron micrographs recorded from each of the four samples of lithium molybdate are shown in Figure 4.10, and show considerable variations in particle morphology and particle size. Samples **A** and **B**, made by direct reaction between the crystalline reagents at room temperature, each exhibit a relatively narrow distribution of particle sizes that range between 0.3 - 3 μm, for Sample **A**, and 0.1 - 12 μm, for Sample **B**. Sample **A** was prepared by grinding the reagents together until a paste was formed; this approach produces a regular distribution of smooth, columnar particles with an aspect ratio of approximately 4:1. Performing the same reaction with minimal agitation of the reaction mixture, so as not to form a paste (preparation of sample **B**), produces particles with morphologies similar to those of sample **A**, but with a wider distribution of sizes, and a larger mean size. Both of these preparations lead to a considerably more homogeneous sample than recrystallisation from solution (sample **C**), which yields particles that range in size from 0.1 - 80 μm. In even greater contrast, lithium molybdate prepared by conventional solid-state reaction at 600 °C (sample **D**) yields monolithic blocks of fused material that are several hundreds of micrometres in size.

Scanning electron micrographs were also recorded from the materials used to prepare samples **A** and **B**. These micrographs are shown in Figure 4.11, and show that the reagents and products have considerably different particle morphologies and particle sizes.

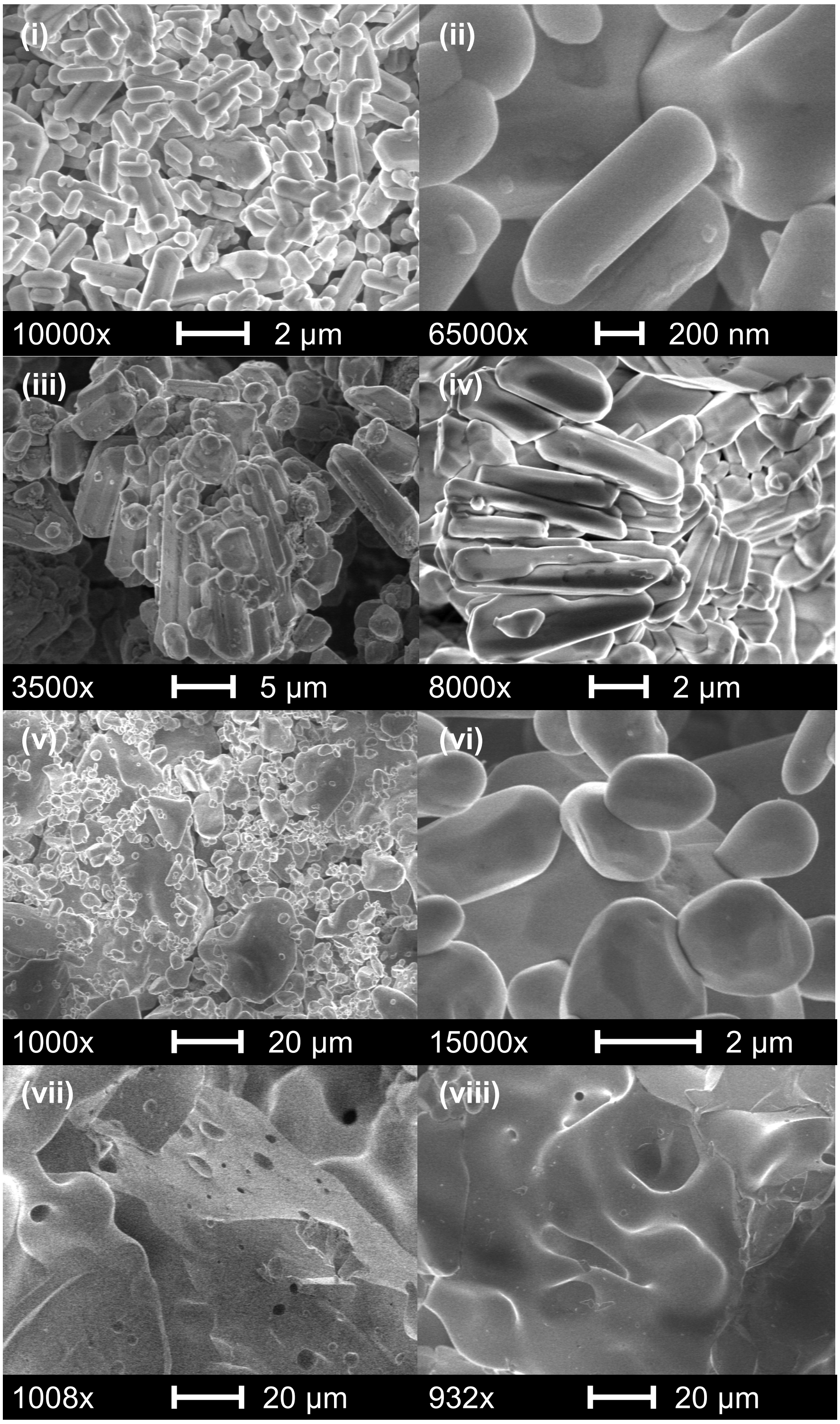

Figure 4.10 Scanning electron micrographs of Li_2MoO_4 recorded from (i) and (ii) sample **A**, (iii) and (iv) sample **B**, (v) and (vi) sample **C**, and (vii) and (viii) sample **D**.

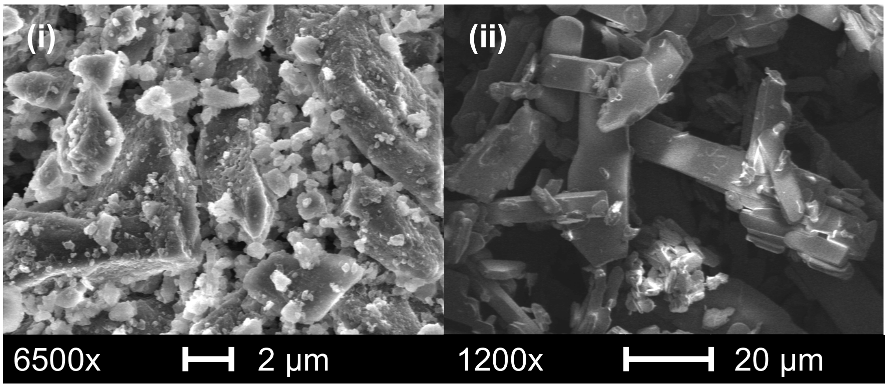

Figure 4.11 Scanning electron micrographs recorded from (i) $LiOH{\cdot}H_2O$ and (ii) MoO_3. These materials were used to prepare samples **A** and **B**.

4.3.8 AC Impedance Spectroscopy

AC impedance data collected over the temperature range $250 \leq T \leq 550$ °C from a sintered pellet of sample **A** show a semicircular arc that could be fitted using an equivalent circuit model. This model consisted of a resistor (R) arranged in parallel with a constant phase element (CPE). At $T \geq 400$ °C, a tail-like contribution is additionally observed at low frequency, as illustrated in Figure 4.12. This tail-like contribution could be modelled by adding a constant phase element in series to the equivalent circuit, and is attributed to ion-blocking at the electrode interface.

The conductivity of Li_2MoO_4 was derived from these impedance data using the equivalent circuit model described above. The temperature dependence of this conductivity behaviour was modelled using a modified Arrhenius equation, as given by $\sigma_{total}T = Ae^{\frac{-E_a}{k_BT}}$; this can be compared with the unmodified equation in section 3.10. This dependence is illustrated in Figure 4.13,

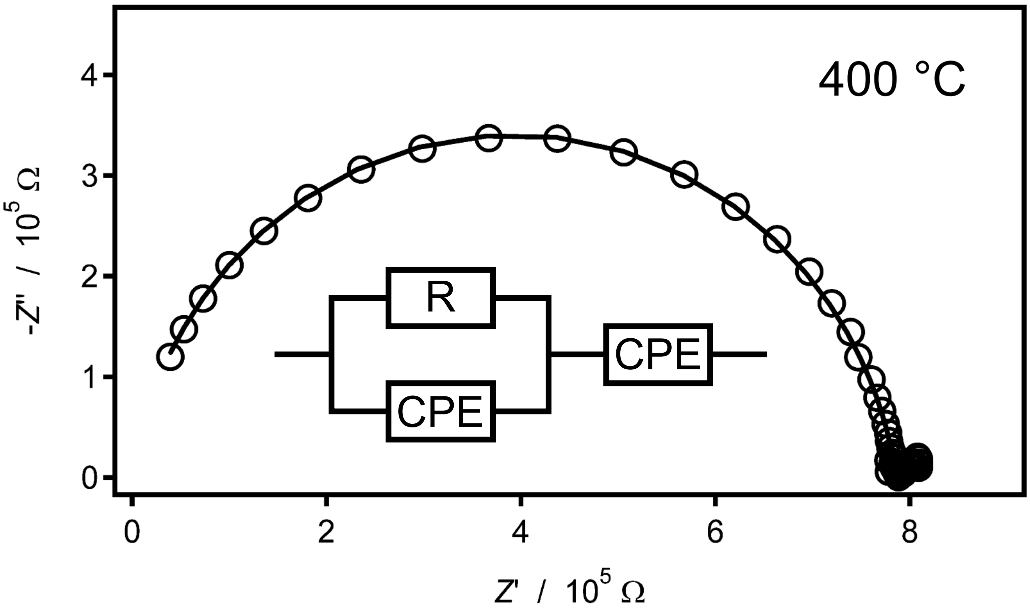

Figure 4.12 A complex-plane representation of AC impedance data collected from a sintered pellet of sample **A** at 400 °C. The conductivity of Li_2MoO_4 was derived from AC impedance data using the equivalent circuit shown. The AC impedance data and equivalent circuit fit are represented by circles and a continuous line respectively.

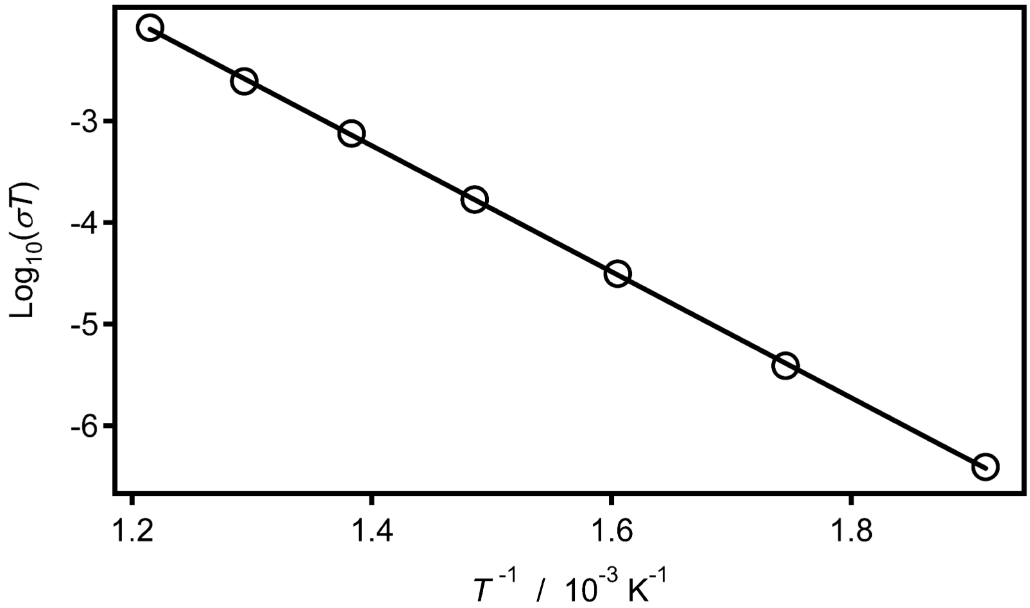

Figure 4.13 An Arrhenius plot of conductivity data collected over the temperature range $250 \leq T \leq 550$ °C from a sintered pellet of sample **A**. The conductivity data and Arrhenius fit are represented by circles and a continuous line respectively.

and indicated an activation energy of 1.23(2) eV over the temperature range $250 \leq T \leq 550$ °C. A conductivity of 2.5×10^{-7} S cm^{-1} was derived from data collected at 400 °C, which, together with the activation energy, suggest that Li_2MoO_4 is a poor ionic conductor at room temperature.

4.3.9 Reactivity of Heavy Metal Analogues

The reagents $NaOH{\cdot}H_2O$ and MoO_3 were ground together under ambient conditions for 30 min, and, in contrast to the preparation of sample **A**, did not form a paste. X-ray powder diffraction data collected *ca.* 1 hr after these reagents were introduced and ground together are shown in Figure 4.14. These diffraction data could be largely indexed on the basis of an orthorhombic cell (a = 8.4847(4) Å, b = 10.5713(5) Å and c = 13.8369(7) Å) of symmetry *Pbca*, and could subsequently be fitted using the structural model reported for $Na_2MoO_4{\cdot}2H_2O$.[14] Taking these observations together, it can be concluded that reaction (4.2) had occurred.

$$2NaOH{\cdot}H_2O + MoO_3 \rightarrow Na_2MoO_4{\cdot}2H_2O + H_2O \qquad (4.2)$$

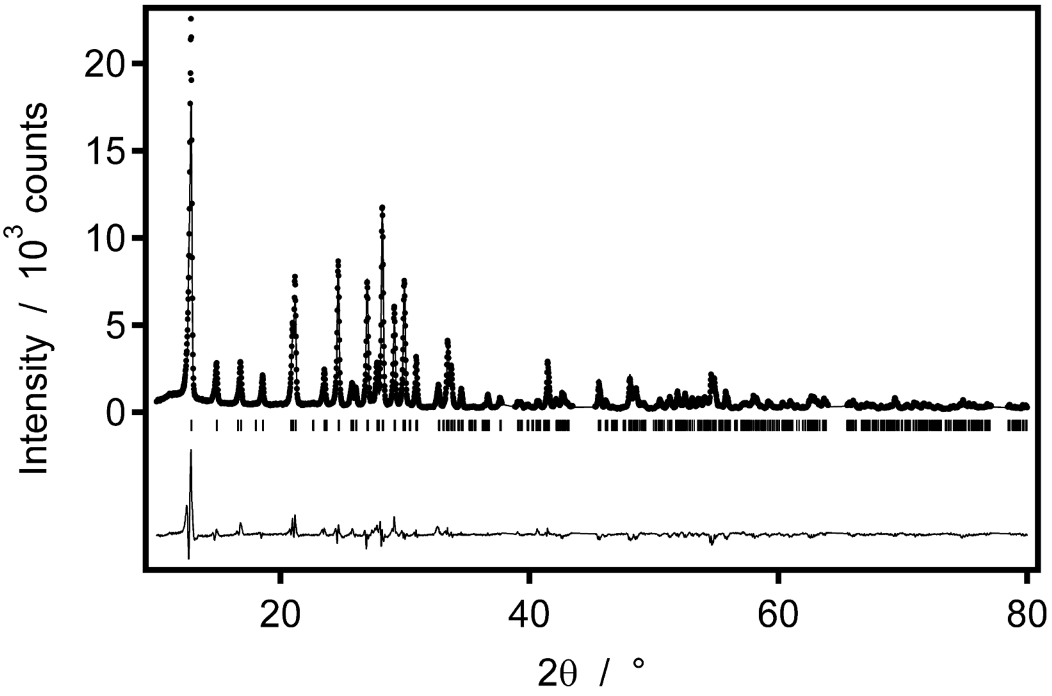

Figure 4.14 Observed (dots), calculated (top line) and difference (bottom line) X-ray powder diffraction patterns collected from a 2:1 mixture of $NaOH·H_2O$ and MoO_3. The vertical bars indicate the allowed Bragg reflection positions for $Na_2MoO_4·2H_2O$. Excluded regions correspond to peaks arising from the aluminium sample holder.

The grinding together of the reagents $LiOH·H_2O$ and WO_3 also did not lead to the formation of a paste. However, in contrast to the preparation of $Na_2MoO_4·2H_2O$, this sample could be identified from X-ray powder diffraction data as a mixture predominantly composed of Li_2WO_4[8] and unreacted WO_3,[15, 16] as shown in Figure 4.15. This sample was left to stand for a week in ambient atmosphere, after which time diffraction data were collected from the sample, showing the presence of several additional peaks. These peaks could be indexed on the basis of a cubic cell

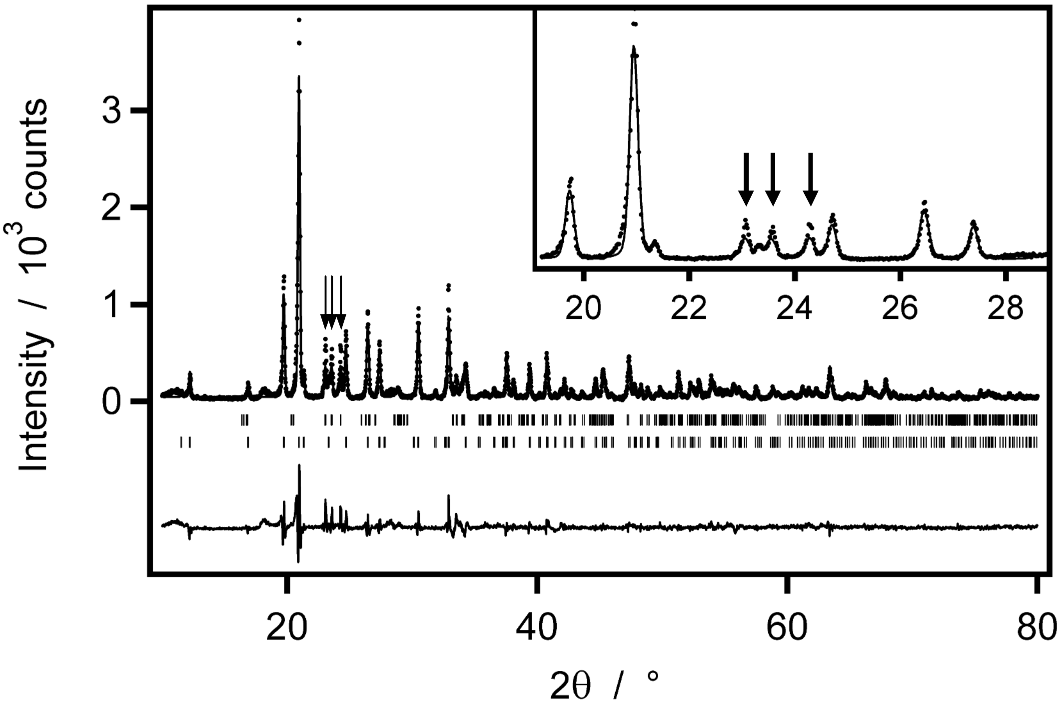

Figure 4.15 Observed (dots), calculated (top line) and difference (bottom line) X-ray powder diffraction patterns collected from a 2:1 mixture of $LiOH{\cdot}H_2O$ and WO_3. The inset highlights the presence of unreacted WO_3 reagent. The upper and lower vertical bars indicate the allowed Bragg reflection positions for WO_3 and Li_2WO_4 respectively. The most intense reflections due to WO_3 are indicated with arrows.

of dimensions *a* ~ 8.3 Å, which is consistent with the structural model reported for $Li_2WO_4{\cdot}\frac{4}{7}H_2O$, as described in the space group $P\bar{4}3m$.[17] An excess quantity of $LiOH{\cdot}H_2O$ (10 wt. %) was then ground with this sample, resulting in the sample changing in colour from pale yellow to white. Diffraction data collected from this mixture showed that the addition of excess $LiOH{\cdot}H_2O$ had resulted in further reaction of WO_3 and promoted the formation of $Li_2WO_4{\cdot}\frac{4}{7}H_2O$. In an attempt to obtain a single, crystalline phase, an additional 5 wt. % of $LiOH{\cdot}H_2O$ was ground with the sample on two further occasions, resulting in a total addition of 20 wt. % excess of $LiOH \cdot H_2O$. At this point, the diffraction data collected from the sample could be indexed on the basis of a cubic cell of dimensions a = 8.3173(2) Å, and one additional weak Bragg peak that could not be identified. However, fitting the diffraction data using the model reported for $Li_2WO_4 \cdot \frac{4}{7} H_2O$ resulted in a number of intensity mismatches, as shown in Figure 4.16. Allowing the atomic positions to refine against these data did not lead to a significant improvement in the quality of the fit.

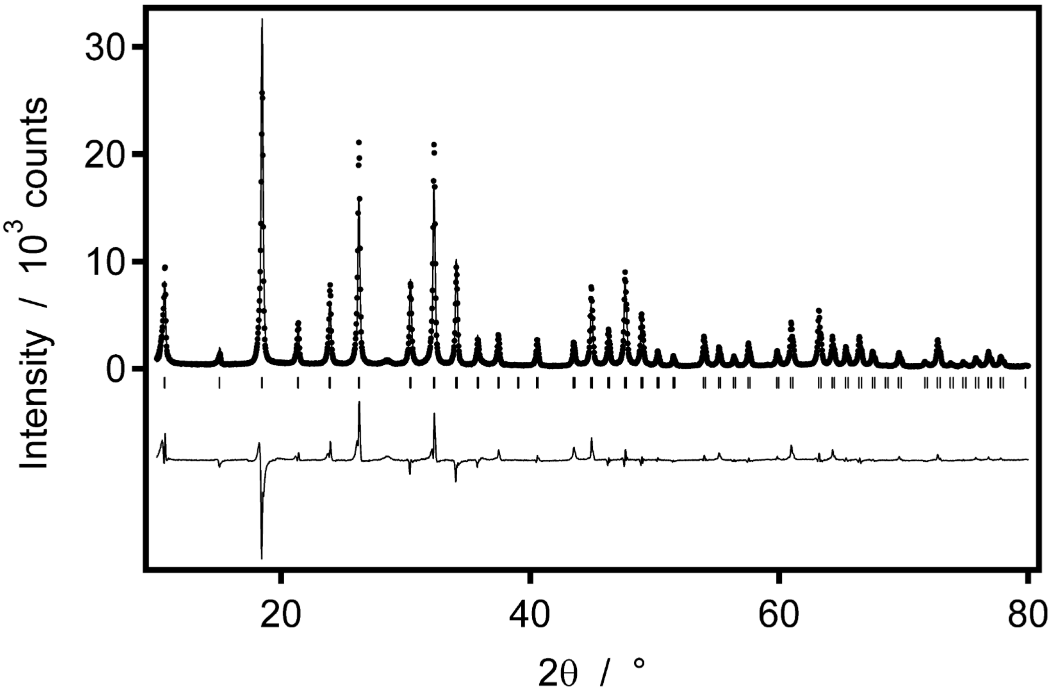

Figure 4.16 Observed (dots), calculated (top line) and difference (bottom line) X-ray powder diffraction patterns collected from a 2:1 mixture of $LiOH \cdot H_2O$ and WO_3 that was further reacted with a total excess of 20 wt. % of $LiOH \cdot H_2O$. The vertical bars indicate the allowed Bragg reflection positions for a cubic cell in the space group $P\bar{4}3m$.

4.4 Discussion

The X-ray single-crystal diffraction study of lithium molybdate indicated that the crystal structure is best described in the space group $R\overline{3}$, as previously suggested by Zachariasen and Plettinger,[8] and more recently reported by Kolitsch.[10] In a study by Sharma and Choudhary,[3] an orthorhombic unit cell was instead proposed, but this is incompatible with the single-crystal diffraction data. A further study, by Barinova *et al.*,[9] suggested a hexagonal unit cell of symmetry $P3_2$, on the basis of which the X-ray powder diffraction data presented in the current study could also be indexed. This is permissible since the hexagonally set $R\overline{3}$ cell has the same dimensions as the $P3_2$ cell, and so both these cells must share the same peak positions. However, the rhombohedral centring of the $R\overline{3}$ cell means that this hexagonally set cell can be equally well described using a smaller, primitive rhombohedral cell ($a = b = c$ and $\alpha = \beta = \gamma \neq 90°$) that is ⅓ of the volume. This primitive rhombohedral cell is distinguished from the primitive hexagonal $P3_2$ cell by the systematic absence of ⅔ of the allowed Bragg reflection positions. Modelling the powder diffraction data with the reported $P3_2$ structural model leads to a large number of reflection positions that are associated with zero Bragg intensity. Nevertheless, the $P3_2$ model is equally capable of fitting the observed data.

A comparative study of the $R\overline{3}$[10] and $P3_2$[9] structures reveals that both these structures are built up from units of LiO_4 and MoO_4 tetrahedra that are connected by trigonally coordinated oxide anions into a corner-sharing network. These tetrahedral units are distributed in a fully ordered manner such that each MoO_4 unit is connected to eight LiO_4 units, whilst each LiO_4 unit is connected to a combination of four LiO_4 and four MoO_4 units. Consequently, the differences between these two structures are small, and arise largely as a result of variable displacements in the oxide anion sublattice, as shown in Figure 4.17. However, given the higher symmetry of the metal cation sublattice, there exists no obvious driver that would account for a distortion of the metal oxide tetrahedra, and thus give a lower symmetry polymorph. By also taking into consideration the many redundant Bragg reflection positions generated by the space group $P3_2$, it is much more likely that the previous assignment of $P3_2$ symmetry to the structure of lithium molybdate was an

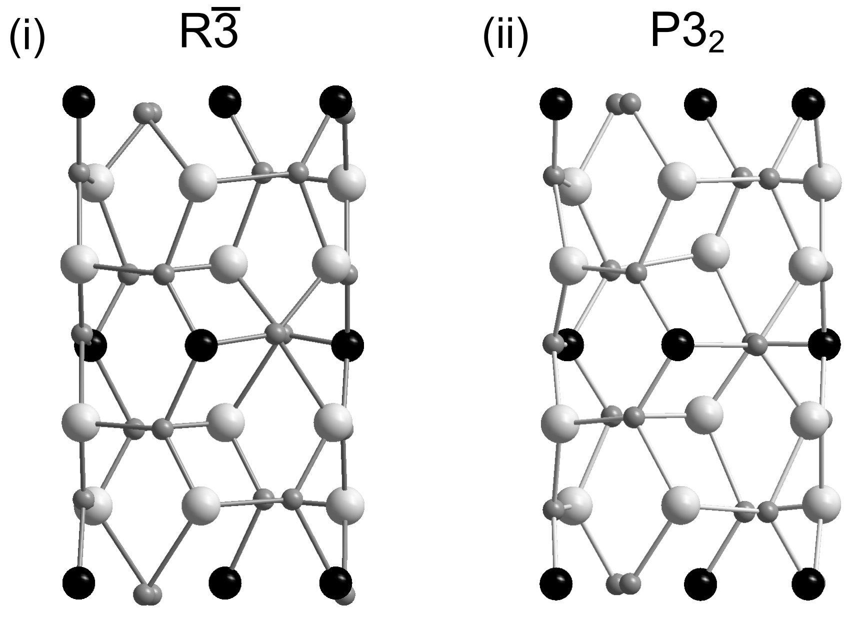

Figure 4.17 The crystal structure of Li_2MoO_4 described in (i) the space group $R\overline{3}$ [10] and (ii) the space group $P3_2$.[9] The lithium (light grey spheres) and molybdenum (black spheres) cations are tetrahedrally coordinated to oxide anions (dark grey spheres).

underestimate of the $R\overline{3}$ symmetry. X-ray powder diffraction data collected from each of the four polycrystalline samples of lithium molybdate, which were prepared following a variety of synthetic routes, can be fitted using the $R\overline{3}$ structural model derived from the single-crystal diffraction study.

Samples of Li_2MoO_4 were prepared by high-temperature reaction and recrystallisation from aqueous solution, as well as by an unconventional method involving the direct reaction between $LiOH \cdot H_2O$ and MoO_3 at room temperature. Individually, these solid reagents are stable at room temperature, but, when briefly mixed by grinding, rapidly produce highly crystalline Li_2MoO_4, with complete conversion of the reagents observed in less than 50 min. This unusual synthesis produces a significant quantity of water per mole of MoO_3, which, if intimately combined with the solid components of the reaction mixture, leads to the formation of a paste that then dries to give sample **A**. However, by using finely ground reagents, brief stirring followed by gentle compaction is also adequate to produce both a highly pure and a highly crystalline sample of lithium molybdate, sample **B**. By contrast, the reaction between LiOH and MoO_3, following extensive grinding, proceeds very slowly under ambient conditions, and remains incomplete after several months of standing. This suggests that the reaction between these two materials occurs indirectly and instead proceeds *via* LiOH scavenging water from the surrounding atmosphere; thus enabling the formation of the hydrated material that can then undergo direct reaction with MoO_3. An alternative route that involves LiOH reacting with atmospheric CO_2 to produce Li_2CO_3 and H_2O is unlikely to contribute to the formation of Li_2MoO_4 as the carbonate is only slightly soluble in water.[18]

The diffusion of ions in the solid state at room temperature is usually too slow to allow a reaction to be observed, and so it is noteworthy that highly crystalline Li_2MoO_4 can be readily formed at room temperature. The introduction of mechanical energy *via* high-energy ball milling has, in rare cases, resulted in the formation of crystalline ternary compounds from binary reagents.[19-21] By contrast, the preparation of sample **B** used a minimal amount of energy to mix the reagents, and so it is unlikely that the process of mixing these reagents is capable of driving the formation of lithium molybdate. In order to determine whether this reaction will proceed in the absence of mechanical work, the reagents must be mixed whilst their reaction with one another is inhibited. The formation of a paste in the preparation of sample **A** together with the slow rate of reaction between LiOH and MoO_3 suggest that the presence of water is crucial to the reaction proceeding at room temperature. Therefore, by mixing the reagents at -80 °C, *i.e.* at well below the freezing point of water, the absence of liquid water will be ensured, and so the reaction should not be initiated on mixing.

The design of the calorimetric experiment allowed mechanical energy in the form of stirring to be applied to the reagents at -80 °C. In a subsequent step, the temperature of the mixture was steadily increased, in which way the reaction between the interspersed reagents is initiated. On heating the mixture from -80 °C to room temperature, the mixture gives rise to only two significant thermal responses: an exothermic event which is immediately followed by an endothermic event. Given that the preparation of samples **A** and **B** show that Li_2MoO_4 is produced at room temperature, and that no other significant transitions arise from either the reagents or the products below this temperature, these two transitions must represent the reaction between $LiOH{\cdot}H_2O$ and MoO_3. Moreover, these data show that it is possible to produce Li_2MoO_4 in the absence of mechanical work, indicating that reaction (4.1) occurs spontaneously upon contact between the reagents.

The difference in energy between these two calorimetric transitions gives a measure of the overall enthalpy change of the reaction, and so, provides an insight into the thermodynamic drivers behind the reaction. It is noted that, due to incomplete reaction, the enthalpies of the processes associated with each of these transitions cannot be absolutely quantified. However, the relative integrated energies of these transitions show unambiguously that the reaction is associated with a positive change in enthalpy. As the reaction proceeds spontaneously in the forward direction, it follows that the change in Gibbs energy must be negative, and so, this unfavourable change in enthalpy must be more than compensated by a positive change in the entropy of the reaction. Given also that the majority of atoms in the crystalline reagents go on to form water, this gain in entropy must be dominated by the additional degrees of freedom afforded to each of these atoms in the liquid phase. It can therefore be inferred that the reaction is driven by the liberation of water from the lattice of $LiOH{\cdot}H_2O$.

Scanning electron microscopy shows that the particles in **A** and **B** bear no resemblance in either morphology or size to particles of either of the reagents. This suggests that the formation of Li_2MoO_4 involves crystallisation from a liquid phase. This, in turn, implies that both reagent lattices are destroyed, which, given the presence of water of crystallisation, will lead to the formation of a highly concentrated aqueous solution. The lattice of $LiOH{\cdot}H_2O$ contains pairs of edge-sharing LiO_4 tetrahedra, which are arranged in corner-sharing rows, whereas the lattice of MoO_3 is built up of layers of edge-sharing MoO_6 octahedra, as illustrated in Figure 4.18. These crystal structures show that the reagents have a considerably different atom connectivity compared to the lattice of Li_2MoO_4. This indicates that the destruction of the reagent lattices is a necessary step in order for Li_2MoO_4 to be formed at room temperature; the degree of bond-breaking and bond-making required to arrive at the product structure would be energetically unfeasible in the solid state at this temperature. Furthermore, as the mobility of ions is considerably higher in the

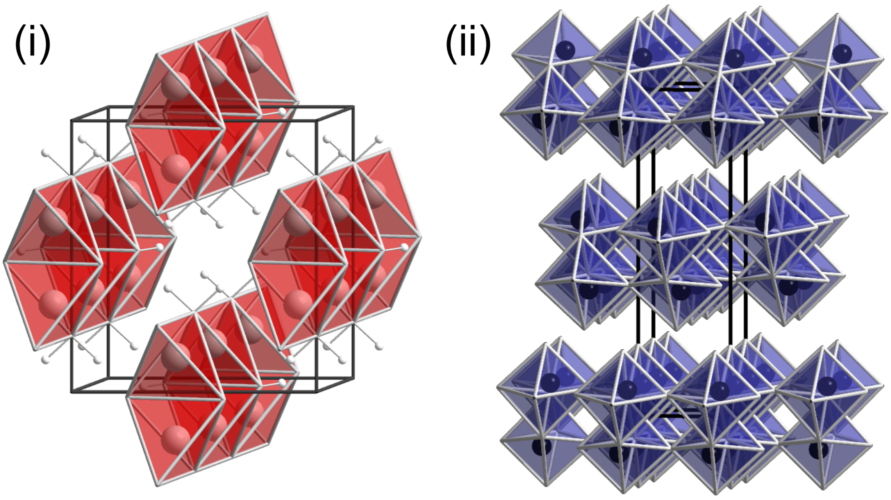

Figure 4.18 The crystal structures of (i) $LiOH{\cdot}H_2O$[22] (ii) and MoO_3.[23] H^+, Li^+ and Mo^{6+} cations are represented by white, grey and black spheres respectively. Oxide coordination is indicated by shaded polyhedra.

liquid phase than in the solid phase, the intervention of liberated water in the formation of Li_2MoO_4 is likely to also account for the observed rapidity of the reaction. Therefore, although this reaction is initiated by contact between solid reagents, and produces a solid product, it should not be considered a reaction that is carried out in the solid state. In this respect, the reaction is similar to a number of solid-solid organic reactions that proceed *via* the formation of a liquid melt.[24]

In addition to playing an important role in the thermodynamics of the reaction, it is clear from the above considerations that water is intimately involved in the formation of Li_2MoO_4. This water is liberated from the lattice of $LiOH \cdot H_2O$ upon contact with MoO_3, resulting in a residual equivalent of LiOH. As MoO_3 is insoluble in water, but readily dissolves in alkali,[25] LiOH must dissolve in the liberated water in order for MoO_3 to also enter into solution. This implies that if the surface layers of $LiOH \cdot H_2O$ at the interface between the two reagents liquefy and form an alkaline boundary layer, this layer will be sufficiently basic to dissolve the surface layers of MoO_3 to give a local, highly concentrated solution of Li^+ and $(MoO_4)^{2-}$.[26] This could lead to the nucleation and crystal growth of Li_2MoO_4 within the interfacial region between the two reagents. This crystallisation of Li_2MoO_4 will render the aqueous solution undersaturated, and thus facilitate further dissolution of the reagent particles. However, due to the relatively dense structure of Li_2MoO_4, and the highly constrained nature of the coordination environments of Li^+ and Mo^{6+}, the crystallised phase is likely to prohibit the facile transfer of cations. This is supported by the AC impedance spectroscopy study of a sintered pellet of sample **A**, which determined

Li_2MoO_4 to be a poor ionic conductor, even at temperatures of up to 550 °C. The formation of product between the two reagents could therefore form a barrier to mass transport and impede the reaction. This implies that particle growth may be governed by a mechanism that is self-limiting.

The particles in samples **A** and **B** are smaller and more regularly shaped than particles produced by either recrystallisation from aqueous solution or high-temperature reaction. These differences in particle size and particle morphology are consistent with the direct room-temperature reaction following a self-limiting particle-growth mechanism. However, a comparison of the particles in sample **A** with those in sample **B** reveals that larger and less regularly shaped particles are grown when the reagents are mixed with minimal agitation, *i.e.* the preparation of sample **B**. These additional observations show that particle growth is not self-limited, but is instead limited by kinetic considerations: a greater number of instances of nucleation arise in the preparation of sample **A**, as the reactive interfaces are continuously renewed by grinding (reaction proceeds rapidly), whereas crystal growth is allowed to progress further in the preparation of sample **B**, as the mixture of reagents is disturbed less during the course of the reaction (reaction proceeds more slowly).

It is clear that these kinetic limitations strongly influence the morphology and size of the particles grown. A study by Inagaki *et al.* has previously shown that rod-shaped particles of Li_2MoO_4 can be precipitated from ethanolic solution.[4] The morphology and size of these particles were manipulated by adjusting the concentrations of the various components added to the ethanolic precipitation medium, and the manner and rate of stirring. By careful tuning of the precipitation conditions, a minimum particle size of *ca.* 0.8 × 0.8 × 4 μm could be obtained. By contrast, the direct reaction between $LiOH \cdot H_2O$ and MoO_3 at room temperature yields smaller particles, and provides a considerably more rapid route to Li_2MoO_4 without the use of solvents and heating, or the need for post-synthetic separation of the product. It is also noteworthy that the small and regularly shaped particles obtained from this facile reaction are well suited for industrial processing; for example, for either catalytic[27] or mechanical[28] applications. Furthermore, this reaction is sufficiently general to permit the substitution of either $NaOH \cdot H_2O$ or WO_3 to give the hydrated materials $Na_2MoO_4 \cdot 2H_2O$ and $Li_2WO_4 \cdot \frac{4}{7} H_2O$ respectively. These reactions suggest that this synthetic approach may be amenable to the stabilisation of other crystal structures.

4.5 Conclusions

$LiOH \cdot H_2O$ and MoO_3 undergo direct reaction with one another at room temperature to give highly crystalline lithium molybdate. This spontaneous reaction proceeds to completion within minutes, and is driven by the gain in entropy associated with the liberation of water from the lattice of $LiOH \cdot H_2O$. The morphology and size of the particles produced suggest that this reaction is not topotactic in nature, but instead involves localised dissolution of the reagents. The rapidity of this reaction severely limits crystal growth, and leads to the production of relatively uniform, micrometre-sized particles. A limited degree of morphological control can be exerted by grinding the reagents together, as opposed to mixing the reagents using the minimum input of mechanical work. In this way, crystal growth is constrained to a further extent to give smaller and more regularly shaped particles.

It is noteworthy that the reaction between $LiOH \cdot H_2O$ and MoO_3 is facilitated by common chemical phenomena such as the release of water of crystallisation, and the dissolution of crystalline solids in water/alkali. This reactivity is different when either starting material is substituted with larger metal cation analogues, and instead proceeds to give hydrated products. Additionally, in the case of $LiOH \cdot H_2O$ and WO_3, the reaction does not proceed as one step, and leads to the stabilisation of a structure that is significantly more complex than anticipated. These results suggest that other ternary or higher-order compounds may be easily accessible *via* direct reaction between crystalline reagents at room temperature.

4.6 Publications

Some of the work described in this chapter has been published as T.W.S. Yip, E.J. Cussen and C. Wilson, *Dalton Trans.*, 2010, **39**, 411-417, DOI: 10.1039/b908266b.

4.7 References

1. C. N. R. Rao and J. Gopalakrishnan, *New Directions in Solid State Chemistry*, 2nd edn., Cambridge University Press, Cambridge, 1997.
2. E. J. Cussen and T. W. S. Yip, *J. Solid State Chem.*, 2007, **180**, 1832-1839.
3. S. Sharma and R. N. P. Choudhary, *J. Mater. Sci. Lett.*, 1999, **18**, 669-672.
4. M. Inagaki, Y. Nishikawa and M. Sakai, *J. Eur. Ceram. Soc.*, 1992, **10**, 123-128.
5. L. Sebastian, Y. Piffard, A. K. Shukla, F. Taulelle and J. Gopalakrishnan, *J. Mater. Chem.*, 2003, **13**, 1797-1802.
6. *US Pat.*, 6 346 348, 2002.
7. W. L. Bragg, *Proc. R. Soc. Lond. A*, 1927, **113**, 642-657.
8. W. H. Zachariasen and H. A. Plettinger, *Acta Cryst.*, 1961, **14**, 229-230
9. A. V. Barinova, R. K. Rastsvetaeva, Y. V. Nekrasov and D. Y. Pushcharovskii, *Doklady Chemistry*, 2001, **376**, 16-19.
10. U. Kolitsch, *Z. Kristallogr.*, 2001, **216**, 449-454.
11. K. S. W. Sing, D. H. Everett, R. A. W. Haul, L. Moscou, R. A. Pierotti, J. Rouquerol and T. Siemieniewska, *Pure Appl. Chem.*, 1985, **57**, 603-619.
12. K. S. W. Sing, *J. Porous Mater.*, 1995, **2**, 5-8.
13. S. Brunauer, P. H. Emmett and E. Teller, *J. Am. Chem. Soc.*, 1938, **60**, 309-319.
14. K. Matsumoto, A. Kobayashi and Y. Sasaki, *Bull. Chem. Soc. Jpn.*, 1975, **48**, 1009-1013.

15. S. Tanisaki, *J. Phys. Soc. Jpn.*, 1960, **15**, 566-573.

16. S. Tanisaki, *J. Phys. Soc. Jpn.*, 1960, **15**, 573-581.

17. A. Hüllen, *Berichte der Bunsengesellschaft für physikalische Chemie*, 1966, **70**, 598-606.

18. *CRC Handbook of Chemistry & Physics*, 90th edn., CRC Press, 2010.

19. P. Lacorre and R. Retoux, *J. Solid State Chem.*, 1997, **132**, 443-446.

20. F. Goutenoire, R. Retoux, E. Suard and P. Lacorre, *J. Solid State Chem.*, 1999, **142**, 228-235.

21. J. Wang, J. M. Xue, D. M. Wan and B. K. Gan, *J. Solid State Chem.*, 2000, **154**, 321-328.

22. N. W. Alcock, *Acta Cryst.*, 1971, **B27**, 1682-1683.

23. H. Braekken, *Z. Kristallogr.*, 1931, **78**, 484-489.

24. G. Rothenberg, A. P. Downie, C. L. Raston and J. L. Scott, *J. Am. Chem. Soc.*, 2001, **123**, 8701-8708.

25. N. N. Greenwood and A. Earnshaw, *Chemistry of the Elements*, 2nd edn., Butterworth-Heinemann, Oxford, 1997.

26. J. F. W. Mosselmans, P. F. Schofield, J. M. Charnock, C. D. Garner, R. A. D. Pattrick and D. J. Vaughan, *Chem. Geol.*, 1996, **127**, 339-350.

27. A. Erdöhelyi, K. Fodor, R. Németh, A. Hancz and A. Oszkó, *J. Catal.*, 2001, **199**, 328-337.

28. V. S. Sastri, *Corrosion Inhibitors: Principles and Applications*, John Wiley & Sons, Ltd, Chichester, 2001.

5 Quantitative Li^+ Ion Exchange of $HLaTiO_4$ at Room Temperature using Crystalline $LiOH\cdot H_2O$

5.1 Introduction

The desire for a more environmentally sustainable future is driving the development of a number of important technologies, including rechargeable batteries[1] and fuel cells,[2] that rely on the mobility of ions in continuous framework solids. Compositionally complex solids, such as these, have traditionally been prepared by heating stoichiometric combinations of binary salts at high temperature.[3] These temperatures are often in excess of 1000 °C, and are used to provide the energy necessary to simultaneously break the large number of bonds in the crystalline reagents and overcome the energy barrier to ion migration. However, the use of thermally harsh conditions to achieve mass transport typically means that only the most thermodynamically stable product will result. In order to address this limitation, low-temperature processes, typically occurring below 500 °C, have been employed to manipulate the structures of these high-temperature products, with examples dating back as far as the mid-1970s.[4] These soft-chemical processes facilitate the modification of a subset of ions, most often of a layered phase, whilst the rest of the ions remain immobile and maintain the integrity of the structure. Moreover, these low-temperature approaches offer access to unusual materials that are either thermodynamically or kinetically unstable under the high-temperature synthetic conditions traditionally employed in the solid state.

A number of low-temperature modifications have been reported for the Ruddlesden-Popper family of layered perovskites.[5] These phases are comprised of a variable thickness (n = 1, 2, 3… ∞) of perovskite that are separated by layers of rock-salt structure.[6] The layers of corner-sharing TiO_6 octahedra adopt a staggered arrangement with respect to one another, and so the interlayer cations are accommodated in nine-coordinate environments. In the case of $NaLaTiO_4$, the layers of perovskite are separated by an unusual ordering of these cations, which alternate between the layers; this ordering is unique to the single-layer variant, and is driven by the differences in size and charge between the cation species. The sodium cations can be replaced with other monovalent cations by chemically treating the material in a dilute acid, such as HNO_3 (to give $HLaTiO_4$),[7] or alternatively in a molten salt, such as $LiNO_3$ (to give $LiLaTiO_4$)[8] or $ZnCl_2$ (to give the defective phase $Zn_{0.5}\square_{0.5}LaTiO_4$).[9] These ion-exchange reactions all employ an excess of cations in order to drive the exchange. However, this reliance on a cation excess provides little or no control over the extent of exchange, and typically leads to the fully exchanged material.

In this chapter we present a new approach to Li^+ ion exchange of the protonated Ruddlesden-Popper phase $HLaTiO_4$, using stoichiometric amounts of $LiOH{\cdot}H_2O$. By grinding these two solids together at room temperature, protons are quantitatively replaced with lithium cations to give the new solid-solution series $H_{1-x}Li_xLaTiO_4$. The structures of these ion exchanged phases have been analysed by neutron powder diffraction in order to elucidate the positions of the interlayer cations. In addition, the lithium-rich members of this series of compounds can be modified by dehydration to give a subsequent series of defective layered perovskites, $\square_{1-x}Li_xLaTiO_{4-[(1-x)/2]}$, which have been analysed by X-ray powder diffraction. These defective phases presumably contain a mixture of lithium cations and vacant sites, and thus bear strong similarities with the fast lithium-conducting perovskites, $Li_{3x}La_{2/3-x}TiO_3$.[10, 11] In light of these similarities, the transport properties of these defective phases have been analysed by AC impedance spectroscopy in order to evaluate their potential as fast-ion conductors.

5.2 Experimental

The $n = 1$ Ruddlesden-Popper compound $NaLaTiO_4$ was prepared using conventional ceramic methods: an excess of sodium carbonate (1.386 g + 40 wt. %, 13.07 mmol + 40 mol %) and stoichiometric quantities of dried lanthanum oxide (4.259 g, 13.07 mmol) and titanium(III) oxide (1.879 g, 13.07 mmol) were ground together for 30 min, pressed into pellets, and heated in a furnace at 800 °C for 12 hr, *via* a 1 °C min^{-1} ramp from room temperature. This sample was ground with a further 40 wt. % excess of sodium carbonate and heated at 950 °C for 24 hr, *via* a 2.5 °C min^{-1} ramp from 700 °C. Excess sodium carbonate was then removed by washing the sample with 200 mL of water. The washed sample was dried at 120 °C in air for 1 hr.

The solid acid, $HLaTiO_4$, was prepared by suspending (6.502 g, 23.75 mmol) of $NaLaTiO_4$ in 475 mL of nitric acid (*ca.* 0.1 mol dm^{-3}, H^+ in 2-fold excess). This suspension was stirred at room temperature for *ca.* 2 d in ambient atmosphere. The exchanged product was then filtered under vacuum and washed with 200 mL of water before being dried at 120 °C in air for 1 hr. The deuterated analogue, $DLaTiO_4$, was prepared, instead, by suspending $NaLaTiO_4$ in deuterated nitric acid whilst under N_2 atmosphere. The deuterated product was then filtered under vacuum and washed with 200 mL of D_2O before being dried at 120 °C for 1 hr, all the while exposed to ambient atmosphere.

The replacement of protons or deuterium cations with lithium cations in ALaTiO$_4$ (A = H or D) was carried out by grinding the solid acid with stoichiometric quantities of isotopically-enriched $LiOH{\cdot}H_2O$ ($^7Li > 99$ %) under ambient conditions.

These reagents (*ca.* 1 g) were ground together for 30 min using a pestle and mortar, and underwent a marked reduction in friability that was largely recovered on completion of grinding. This mixture was then left to stand in an open-top vial for *ca.* 2 d in ambient atmosphere. Multigram samples suitable for neutron powder diffraction experiments were prepared by combining several of the $DLaTiO_4$-derived batches of lithium-exchanged product.

The structures of $HLaTiO_4$, $DLaTiO_4$ and the two corresponding series of lithium-exchanged phases were preliminarily analysed by X-ray powder diffraction using a Siemens D500 diffractometer in Bragg-Brentano geometry. These data were collected under ambient conditions using Cu K_α radiation over the range $2 \leq 2\theta \leq 100°$. In order to elucidate the positions of the hydrogen and lithium cations, both $DLaTiO_4$ and the $DLaTiO_4$-derived series of lithium-exchanged compounds were subsequently analysed by neutron powder diffraction. Neutron powder diffraction data were collected using the constant wavelength diffractometer D2B at the Institut Laue-Langevin, Grenoble. Samples were studied under ambient conditions and at 5 K using radiation of wavelengths 1.593 Å and 2.398 Å in the range $2 \leq 2\theta \leq 150°$. Due to the set-up of the instrument D2B,[12] the longer wavelength radiation was allowed to vary in Rietveld refinements that were carried out simultaneously against data collected at both wavelengths.

X-ray powder diffraction was used to follow the progress of the reaction between $LiOH \cdot H_2O$ and $HLaTiO_4$ over the course of several weeks. This experiment was carried out by grinding the reagents together for *ca.* 20 min. The resulting mixture was then mounted on a sample holder, and a series of X-ray powder diffraction measurements were performed. Diffraction data were collected over the range $10 \leq 2\theta \leq 60°$, using a step size of 0.04° 2θ and a count time of 0.8 s step^{-1}.

The thermal stabilities of $HLaTiO_4$ and the lithium-exchanged phases were evaluated using a Perkin Elmer TGA 7 thermal gravimetric analyser. These measurements were carried out under a dynamic atmosphere of dry helium, whereby approximately 30 mg of sample was equilibrated at 38 °C for 5 min before being heated to temperatures of up to 800 °C. Additional experiments involving both the protonated and lithium-exchanged phases being heated in air and then analysed by X-ray powder diffraction were also employed; these experiments were used to correlate the losses in mass to changes in structure.

The $NaLaTiO_4$ precursor, the reagents, and the lithium-exchanged samples were examined using an FEI Sirion 200 scanning electron microscope. The lithium-exchanged material was more closely examined using an FEI Tecnai F20 transmission electron microscope.

The transport properties of the dehydrated phases were investigated by AC impedance spectroscopy using a Solartron SI 1260 frequency response analyser. These experiments were carried out by pressing approximately 0.4 g of the as made lithium-exchanged sample under a load of 3 tonnes to give a 10 mm diameter cylindrical pellet approximately 2 mm thick. This pellet was attached to two platinum electrodes and heated from room temperature to temperatures of up to 600 °C in air. AC impedance data were then collected over the range $0.2 \leq f \leq 10^6$ Hz on both heating and cooling the sample over this temperature range. Additional data were collected with the pellet contained in dynamic atmospheres of dry N_2, wet N_2 and dry O_2.

5.3 Results

5.3.1 Reaction between $HLaTiO_4$ and $LiOH·H_2O$

X-ray powder diffraction data collected from a sample of $HLaTiO_4$ ground with one equivalent of $LiOH·H_2O$ showed that the layered structure of $HLaTiO_4$ had been retained, and that the lattice parameters had undergone a significant change to the values reported for $LiLaTiO_4$.[13] These observations suggest that protons had been replaced with lithium cations in a quantitative manner. Given that grinding an equimolar mixture of $HLaTiO_4$ and $LiOH·H_2O$ appeared to result in ion exchange, this process was repeated using sub-stoichiometric quantities of $LiOH·H_2O$, as described by reaction (5.1).

$$HLaTiO_4 + x^7LiOH·H_2O \rightarrow H_{1-x}Li_xLaTiO_4 + (2x)H_2O \qquad (5.1)$$

The samples afforded by these reactions yielded X-ray powder diffraction patterns that could be indexed using the same space group, *P*4/*nmm*, as that of both $HLaTiO_4$ and $LiLaTiO_4$. These indexings gave rise to a smooth evolution in lattice parameters between the end-member compounds. However, X-rays are relatively insensitive to both protons and lithium cations, and so, in order to probe for these cations, a neutron powder diffraction study of the deuterated analogues of this series of compounds was performed.

Neutron powder diffraction data collected from $DLaTiO_4$ were fitted using the literature model[14] in the centrosymmetric setting of the space group *P*4/*nmm*. Preliminary analyses showed that the sample contained protons rather than deuterium cations, with a refined site occupancy of 0.119(1) H and 0.006(1) D. Due to the negligible refined quantity of deuterium cations, these data suggest that the neutron samples had undergone isotopic exchange with atmospheric moisture, and were subsequently fitted using exclusively protons on this site. The positions and displacements of all the atoms were then allowed to refine. This refinement proceeded to convergence using isotropic displacement parameters to give the fit parameters $R_{wp} = 4.39$, $\chi^2 = 8.863$. The application of anisotropic displacement parameters to model all non-hydrogen atoms led to a small improvement in the quality of fit ($R_{wp} = 4.16$, $\chi^2 = 7.973$). However, treating the data collected from the lithium-exchanged samples in a similar manner resulted in non-positive definite anisotropic displacement parameters. Consequently, an isotropic description of the atomic displacement parameters was employed to describe the structure of $HLaTiO_4$.

The above refinement against the $HLaTiO_4$ data set accounts for protons in 16 partially ($\frac{1}{8}$) occupied general positions that are adjacent to the apical oxide anions within the interlayer region. Given that there are two formula units per unit cell, this model implies that the protons are statistically distributed over eight positions around each of these oxide anions, as illustrated in Figure 5.1. In an attempt to localise the hydrogen position, a trial refinement was undertaken to model the data in the space group *P*4/*n*. The reduced symmetry of this sub group leads to the 16 general positions, as described in *P*4/*nmm*, being split into two equally sized populations, and so, allows for partial ordering of the protons. The positions and atomic displacement parameters of all the atoms in this model were fixed at the values determined from the refinement in *P*4/*nmm*. The occupancies of the two hydrogen sites were then refined within the constraints of the stoichiometry, and resulted in an unstable refinement. Consequently, the final structural model of $HLaTiO_4$ was described in the space group *P*4/*nmm*. This model provides a good fit to the observed data, as shown in Figure 5.2.

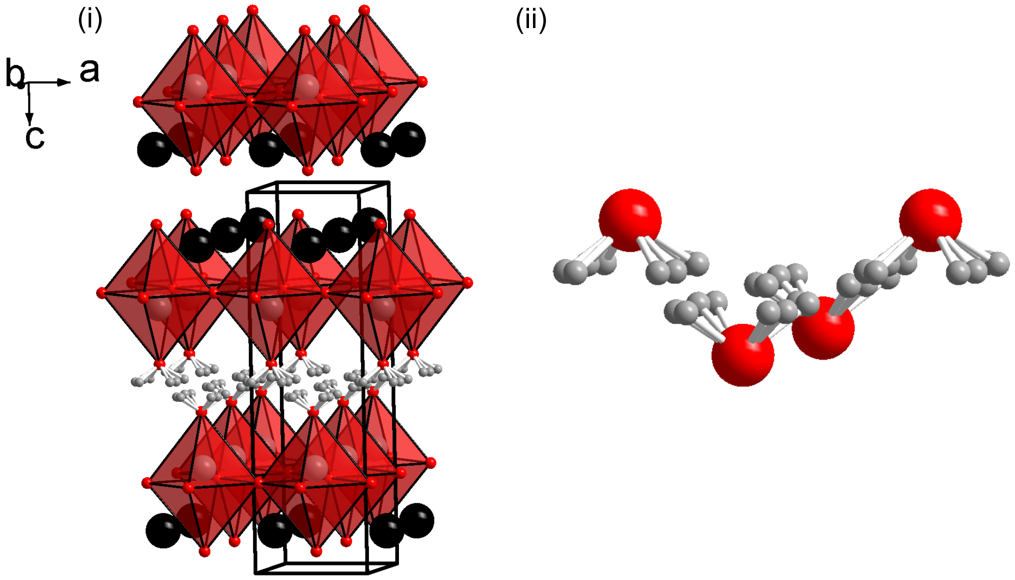

Figure 5.1 (i) Crystal structure of $HLaTiO_4$ derived from least-squares refinement against neutron powder diffraction data. H^+ and La^{3+} cations are represented by grey and black spheres respectively, whilst TiO_6 octahedra are indicated by red units. (ii) Expanded view of the interlayer region showing proton disordered over all possible positions of the 16 *K* site.

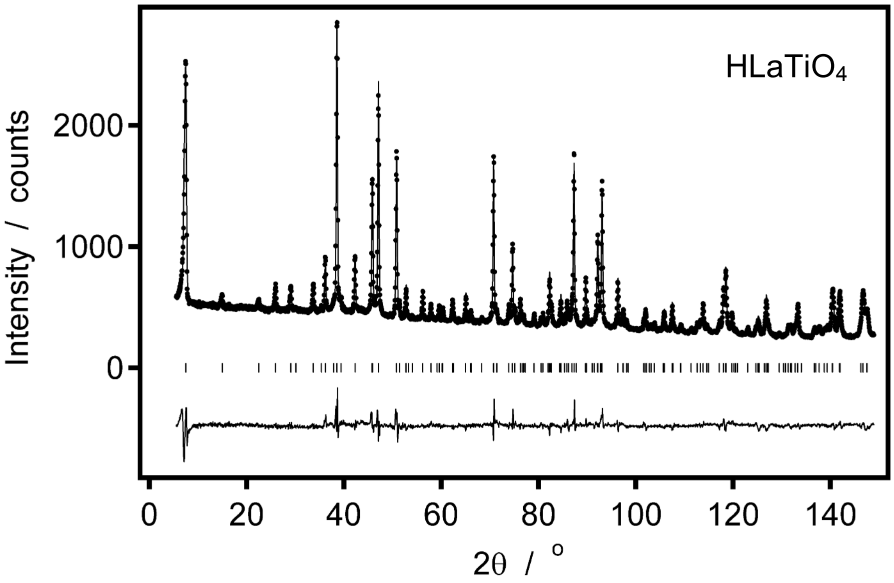

Figure 5.2 Observed (dots), calculated (top line) and difference (bottom line) neutron powder diffraction patterns for $HLaTiO_4$. The vertical bars indicate the allowed Bragg reflection positions for $HLaTiO_4$.

Neutron powder diffraction data collected from the $x = 1$ sample were preliminarily fitted using a lithium-deficient structural model, *i.e.* $[LaTiO_4]^-$. The low angle (001) reflection in this data set exhibited a highly asymmetric peak shape, and so, was excluded from this refinement. A difference Fourier calculation was then carried out, which showed only a single, chemically significant difference in the scattering density; this indicated the presence of ^7Li at (¼, ¾, ½). The model of the $[LaTiO_4]^-$ sublattice was subsequently modified to include lithium on this site, as illustrated in Figure 5.3. In addition, close inspection of the diffraction pattern revealed very weak contributions from the vanadium sample holder, and a small quantity of lithium carbonate that was not detectable in the X-ray diffraction pattern. Both these minor phases were included in the refinement. A full refinement of this model against the neutron diffraction data was carried out using isotropic atomic displacement parameters, and resulted in the fit parameters $R_{wp} = 4.53$, $\chi^2 = 7.238$. This model provides a good fit to the observed data, as shown in Figure 5.4.

Neutron powder diffraction data collected from the intermediate $x = 0.5$ sample could be fitted in a similar manner to data collected from $LiLaTiO_4$, with the addition of protons on the crystallographic site identified in $HLaTiO_4$ and the H/Li content adjusted to reflect the anticipated target stoichiometry. This refinement was carried out simultaneously against neutron diffraction data collected using radiation of wavelengths 1.593 Å and 2.398 Å. The (001) reflection exhibited a highly asymmetric peak shape and was excluded from both these data sets, as similarly

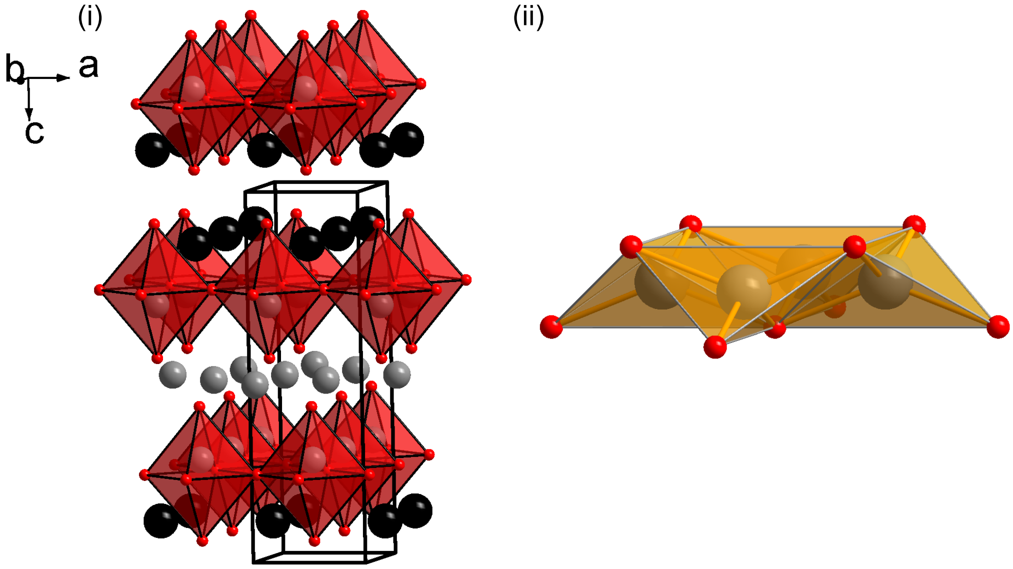

Figure 5.3 (i) Crystal structure of $LiLaTiO_4$ derived from least-squares refinement against neutron powder diffraction data. Li^+ and La^{3+} cations are represented by grey and black spheres respectively, whilst TiO_6 octahedra are indicated by red units. (ii) Expanded view of the interlayer region showing the flattened tetrahedral geometry of the LiO_4 coordination environment.

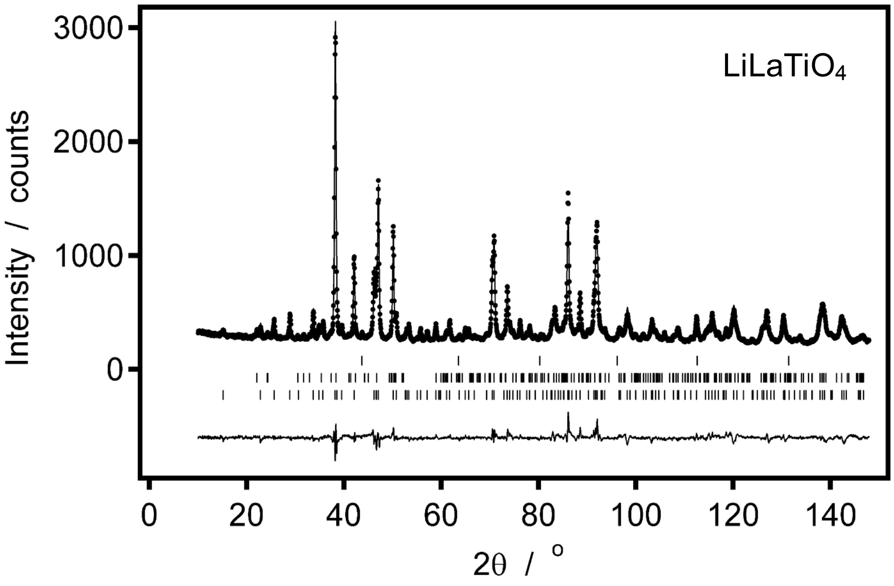

Figure 5.4 Observed (dots), calculated (top line) and difference (bottom line) neutron powder diffraction patterns for $LiLaTiO_4$. The upper, middle and lower sets of vertical bars indicate the allowed Bragg reflection positions for vanadium (sample holder), Li_2CO_3 and $LiLaTiO_4$, respectively. The sample contains Li_2CO_3 as a 0.0133(7) wt. % minority phase.

carried out in the analysis of the lithium end-member data set. The positions of all the non-hydrogen and non-lithium species as well as the isotropic displacement parameters of all the atoms, readily refined to convergence to give the fit parameters $R_{wp} = 4.47$, $\chi^2 = 3.776$. Similar analyses were carried out on neutron data collected from the $x = 0.1$, 0.25, 0.75 and 0.9 samples, and in all cases resulted in good agreement between the observed and calculated diffraction patterns. However, attempts to refine the hydrogen position in these H/Li-containing models led to unstable refinements, presumably due to the low occupancy of this site. Consequently, the position of hydrogen was fixed at the coordinates (0.387, 0.068, 0.4869), and the corresponding displacement parameter constrained to a value 1.5 times larger than that of the adjacent oxide anion; the latter reflects the considerably smaller mass of proton compared to that of the oxide anion. In addition, for compounds containing low site occupancies of lithium, it was necessary to fix the lithium displacement parameter at a physically reasonable value of 0.012 Å^2.

In order to gauge the sensitivity of the above models to the H/Li content, the site occupancies of hydrogen (16*k* site) and lithium (2*b* site) were allowed to refine independently of each other. In the case of the intermediate series member, sample $x = 0.5$, this showed that the data were representative of a partially exchanged sample of $HLaTiO_4$ containing equimolar quantities of hydrogen and lithium; $H_{0.45(2)}Li_{0.53(3)}LaTiO_4$ ($R_{wp} = 4.48$, $\chi^2 = 3.787$). Similar unconstrained refinement of the hydrogen and lithium site occupancies of all the compounds in the series gave good agreement with the target stoichiometries, as shown in Figure 5.5. The

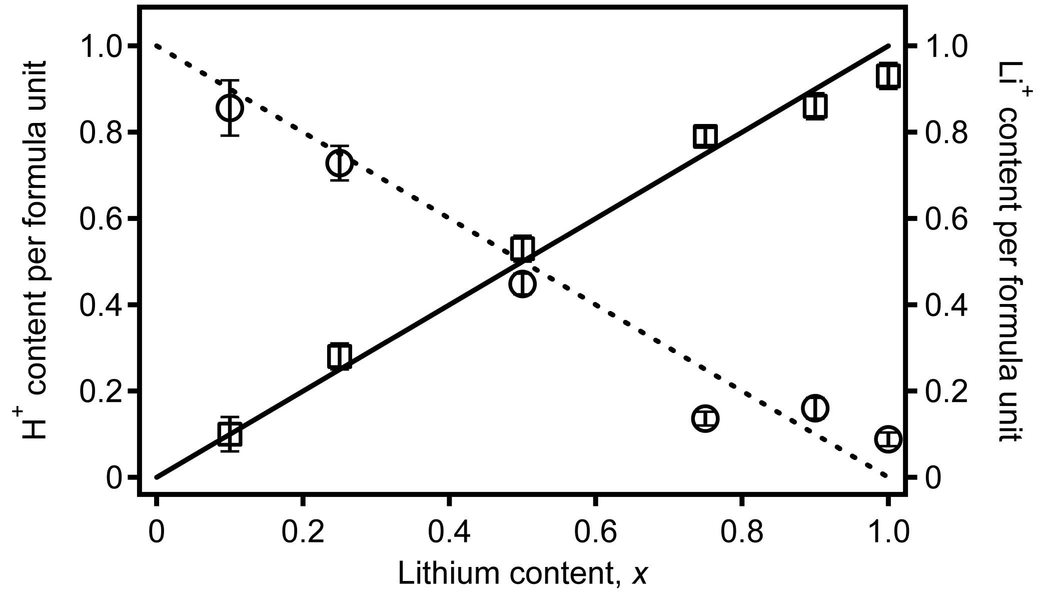

Figure 5.5 Hydrogen (circles) and lithium (squares) contents per formula unit for the $H_{1-x}Li_xLaTiO_4$ phases derived from least-squares refinement against neutron powder diffraction data. The dashed and solid lines represent the anticipated content of hydrogen and lithium, respectively.

hydrogen and lithium site occupancies were subsequently left fixed in accordance with the reaction stoichiometry. The final fit and structural parameters of all of the data sets in the series are presented in Tables 5.1 - 5.3, whilst selected bond distances and bond angles are listed in Tables 5.4 - 5.5. The changes in the unit cell parameters are illustrated in Figure 5.6. The fits to the x = 0.1, 0.25, 0.75 and 0.9 data sets are shown in Figures 5.7 - 5.9.

Table 5.1 Fit parameters for the $\mathrm{H_{1-\mathit{x}}Li_{\mathit{x}}LaTiO_4}$ series of compounds derived from least-squares refinement against neutron powder diffraction data

Compound	**a / Å**	**c / Å**	**V / Å^3**	R_{wp} **/ %**	χ^2	**Variables**
$\mathrm{HLaTiO_4}$	3.72006(5)	12.2914(3)	170.099(6)	4.39	8.863	30
$\mathrm{H_{0.9}Li_{0.1}LaTiO_4}$	3.7230(2)	12.280(2)	170.20(3)	3.42	3.553	34
$\mathrm{H_{0.75}Li_{0.25}LaTiO_4}$	3.7379(2)	12.279(2)	171.56(3)	3.10	4.378	30
$\mathrm{H_{0.5}Li_{0.5}LaTiO_4}$ *	3.75083(14)	12.2161(7)	171.86(2)	4.48	3.792	40
$\mathrm{H_{0.5}Li_{0.5}LaTiO_4}$ (5 K)	3.74442(13)	12.2036(7)	171.10(2)	3.83	3.991	29
$\mathrm{H_{0.25}Li_{0.75}LaTiO_4}$	3.75834(9)	12.1513(5)	171.638(11)	3.59	5.970	27
$\mathrm{H_{0.1}Li_{0.9}LaTiO_4}$	3.76123(9)	12.1116(5)	171.341(11)	3.97	5.815	28
$\mathrm{LiLaTiO_4}$	3.76411(8)	12.0747(4)	171.081(9)	4.47	7.046	27

* Simultaneous refinement against 1.593 Å and 2.39766(14) Å wavelength data sets

Table 5.2 Structural parameters for the $\mathrm{H_{1-\mathit{x}}Li_{\mathit{x}}LaTiO_4}$ series of compounds derived from least-squares refinement against neutron powder diffraction data

Compound	**La 2*c* (¼, ¼, *z*)**	**Ti 2*c* (¼, ¼, *z*)**	**O1 4*f* (¾, ¼, *z*)**	**O2 2*c* (¼, ¼, *z*)**	**O3 2*c* (¼, ¼, *z*)**
$\mathrm{HLaTiO_4}$	0.8811(2)	0.2957(4)	0.7428(2)	0.4442(3)	0.0782(2)
$\mathrm{H_{0.9}Li_{0.1}LaTiO_4}$	0.8842(5)	0.3047(9)	0.7438(5)	0.4448(7)	0.0741(6)
$\mathrm{H_{0.75}Li_{0.25}LaTiO_4}$	0.8822(4)	0.2981(6)	0.7451(4)	0.4410(5)	0.0799(4)
$\mathrm{H_{0.5}Li_{0.5}LaTiO_4}$	0.8814(2)	0.2966(4)	0.7445(2)	0.4401(3)	0.0794(2)
$\mathrm{H_{0.5}Li_{0.5}LaTiO_4}$ (5 K)	0.8821(3)	0.2949(5)	0.7452(2)	0.4425(3)	0.0794(3)
$\mathrm{H_{0.25}Li_{0.75}LaTiO_4}$	0.8809(2)	0.2950(3)	0.7431(2)	0.4409(2)	0.0792(2)
$\mathrm{H_{0.1}Li_{0.9}LaTiO_4}$	0.8802(2)	0.2965(3)	0.7427(2)	0.4412(2)	0.0801(2)
$\mathrm{LiLaTiO_4}$	0.8802(2)	0.2978(3)	0.7425(2)	0.4414(2)	0.0799(2)

Atomic coordinates of proton and lithium: H 16 *K* (0.387(9), 0.068(9), 0.4869(12)); Li 2*b* (¼, ¾, ½)
Atomic coordinates of proton were derived from full refinement of the $\mathrm{HLaTiO_4}$ parent phase, and were adopted in the refinement of all other proton-containing phases.

Table 5.3 Atomic displacement parameters, $100U_{iso}$ (Å^2), for the $\mathrm{H_{1-\mathit{x}}Li_{\mathit{x}}LaTiO_4}$ series of compounds derived from least-squares refinement against neutron powder diffraction data

Compound	**H 16*k* ***	**Li 2*b***	**La 2*c***	**Ti 2*c***	**O1 4*f***	**O2 2*c***	**O3 2*c***
$\mathrm{HLaTiO_4}$	5.4(6)	n/a	0.72(4)	0.79(9)	0.75(4)	2.51(8)	0.75(6)
$\mathrm{H_{0.9}Li_{0.1}LaTiO_4}$	5.6(3)	1.2	1.61(10)	3.1(3)	1.29(9)	3.8(2)	2.0(2)
$\mathrm{H_{0.75}Li_{0.25}LaTiO_4}$	1.9(2)	1.2	0.99(9)	0.4(2)	0.57(8)	1.26(14)	0.37(11)
$\mathrm{H_{0.5}Li_{0.5}LaTiO_4}$	2.63(13)	2.2(4)	1.23(6)	1.08(13)	0.94(5)	1.75(9)	1.12(8)
$\mathrm{H_{0.5}Li_{0.5}LaTiO_4}$ (5 K)	2.13(15)	1.0(4)	1.18(7)	1.1(2)	0.35(5)	1.42(10)	0.34(8)
$\mathrm{H_{0.25}Li_{0.75}LaTiO_4}$	1.63(9)	1.2(2)	0.51(4)	0.29(8)	0.36(4)	1.08(6)	0.66(6)
$\mathrm{H_{0.1}Li_{0.9}LaTiO_4}$	1.68(9)	1.7(2)	0.41(4)	0.18(9)	0.39(4)	1.12(6)	0.64(6)
$\mathrm{LiLaTiO_4}$	n/a	2.0(2)	0.80(4)	0.28(8)	0.69(4)	1.06(5)	1.04(6)

* Constrained atomic displacement parameter: $100U_{iso}(\mathrm{H}) = 1.5 \times 100U_{iso}(\mathrm{O2})$

Table 5.4 Selected bond distances (Å) for the H^+/Li^+ and La^{3+} interlayers derived from least-squares refinement against neutron powder diffraction data

Compound	**8 × H-O2***	**8 × H-O2$^{\neq}$**	**4 × Li-O2**	**4 × La-O1**	**La-O3**	**4 × La-O3**
$HLaTiO_4$	0.997(14)	1.984(13)		2.519(2)	2.423(3)	2.6778(7)
$H_{0.9}Li_{0.1}LaTiO_4$	0.993(5)	1.983(4)	1.981(3)	2.537(5)	2.332(9)	2.682(2)
$H_{0.75}Li_{0.25}LaTiO_4$	1.021(3)	2.009(3)	2.005(2)	2.515(4)	2.427(6)	2.6839(14)
$H_{0.5}Li_{0.5}LaTiO_4$	1.023(2)	2.018(2)	2.0131(13)	2.513(2)	2.419(4)	2.6949(7)
$H_{0.5}Li_{0.5}LaTiO_4$ (5 K)	1.011(2)	2.002(2)	1.9995(14)	2.509(3)	2.409(4)	2.6891(8)
$H_{0.25}Li_{0.75}LaTiO_4$	1.0222(14)	2.0146(11)	2.0115(9)	2.517(2)	2.409(3)	2.7015(5)
$H_{0.1}Li_{0.9}LaTiO_4$	1.020(2)	2.0132(12)	2.0109(10)	2.512(2)	2.421(3)	2.7028(5)
$LiLaTiO_4$			2.0108(9)	2.511(2)	2.412(3)	2.7049(5)

* Proton-oxide separation immediately about the apical oxide position, *i.e.* a hydroxyl group.

$^{\neq}$ Proton-oxide separation that spans the interlayer region, *i.e.* a hydrogen bond.

Table 5.5 Selected bond distances (Å), bond angles (°) and interlayer distances (Å) for the perovskite layer derived from least-squares refinement against neutron powder diffraction data

Compound	**4 × Ti-O1**	**Ti-O2**	**Ti-O3**	**O1-Ti-O1**	**O1-Ti-O2**	**$O2_z \cdots O2_z$**
$HLaTiO_4$	1.9195(12)	1.825(6)	2.674(5)	86.50(6)	104.30(13)	1.372(7)
$H_{0.9}Li_{0.1}LaTiO_4$	1.955(4)	1.72(2)	2.83(2)	84.7(2)	107.8(3)	1.36(2)
$H_{0.75}Li_{0.25}LaTiO_4$	1.943(2)	1.755(11)	2.679(9)	85.72(12)	105.8(2)	1.449(13)
$H_{0.5}Li_{0.5}LaTiO_4$	1.9416(13)	1.753(6)	2.653(5)	86.16(7)	105.00(14)	1.463(7)
$H_{0.5}Li_{0.5}LaTiO_4$ (5 K)	1.935(2)	1.801(8)	2.629(6)	86.33(9)	104.7(2)	1.36(5)
$H_{0.25}Li_{0.75}LaTiO_4$	1.9353(10)	1.774(5)	2.622(4)	86.72(6)	103.83(12)	1.436(5)
$H_{0.1}Li_{0.9}LaTiO_4$	1.9397(11)	1.753(5)	2.621(5)	86.56(6)	104.18(13)	1.424(5)
$LiLaTiO_4$	1.9439(11)	1.733(5)	2.631(5)	86.41(6)	104.50(13)	1.415(5)

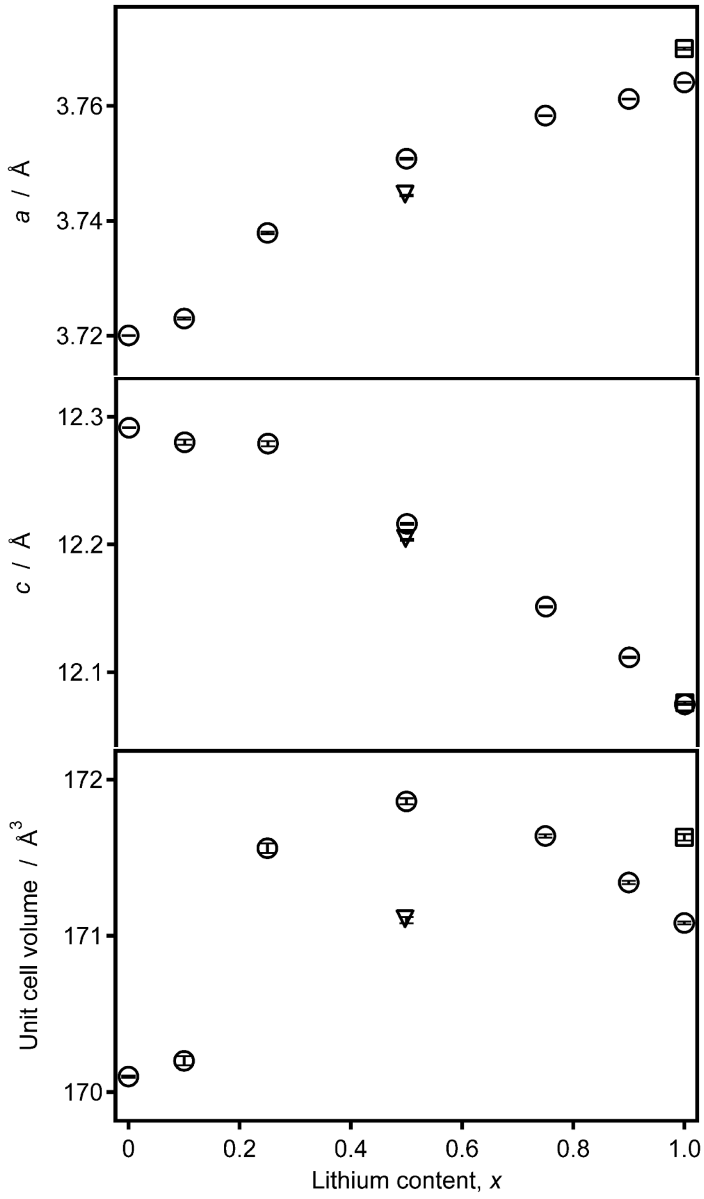

Figure 5.6 Unit cell parameters for the $H_{1-x}Li_xLaTiO_4$ series of compounds derived from least-squares refinement against neutron powder diffraction data collected at room temperature (circles) and 5K (triangle). Additionally shown are literature values for $LiLaTiO_4$ derived from X-ray powder diffraction (squares).[8]

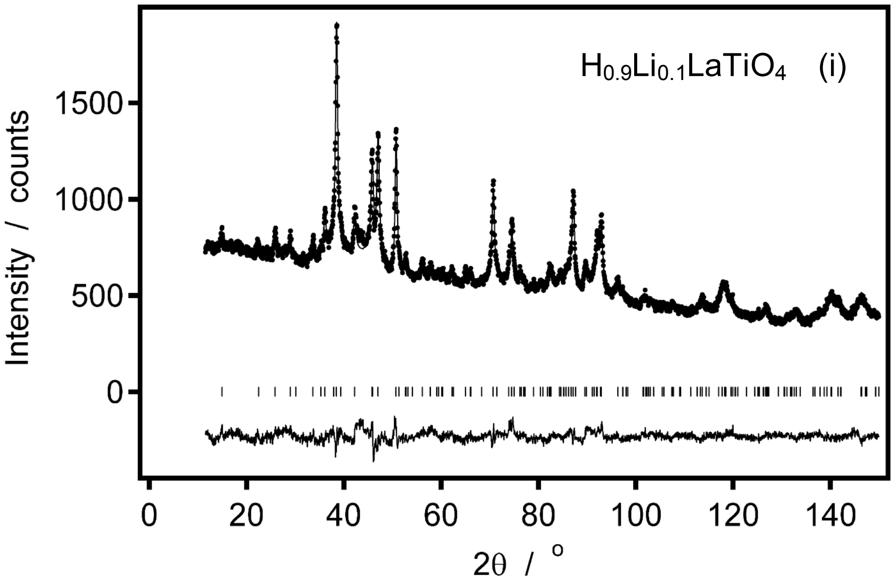

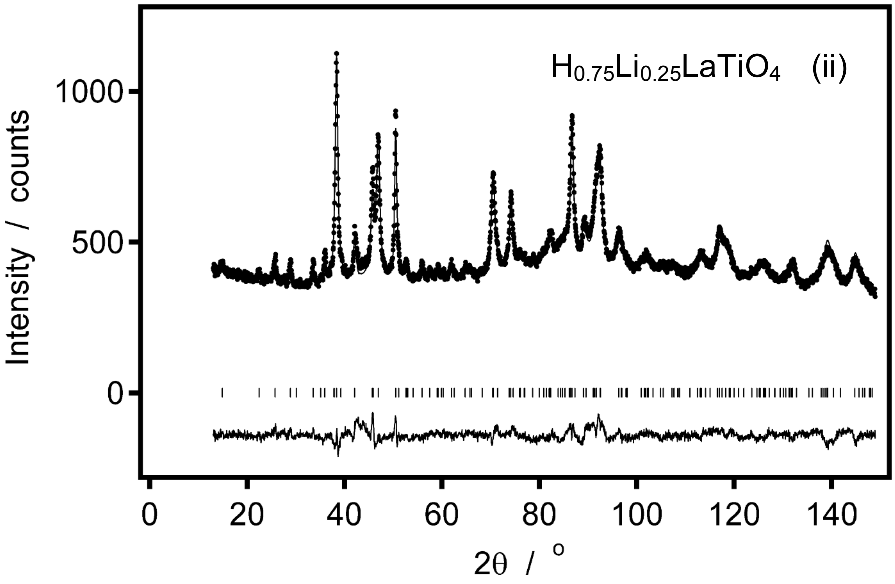

Figures 5.7 Observed (dots), calculated (top line) and difference (bottom line) neutron powder diffraction patterns for (i) $H_{0.9}Li_{0.1}LaTiO_4$ and (ii) $H_{0.75}Li_{0.25}LaTiO_4$. The vertical bars indicate the allowed Bragg reflection positions for these phases.

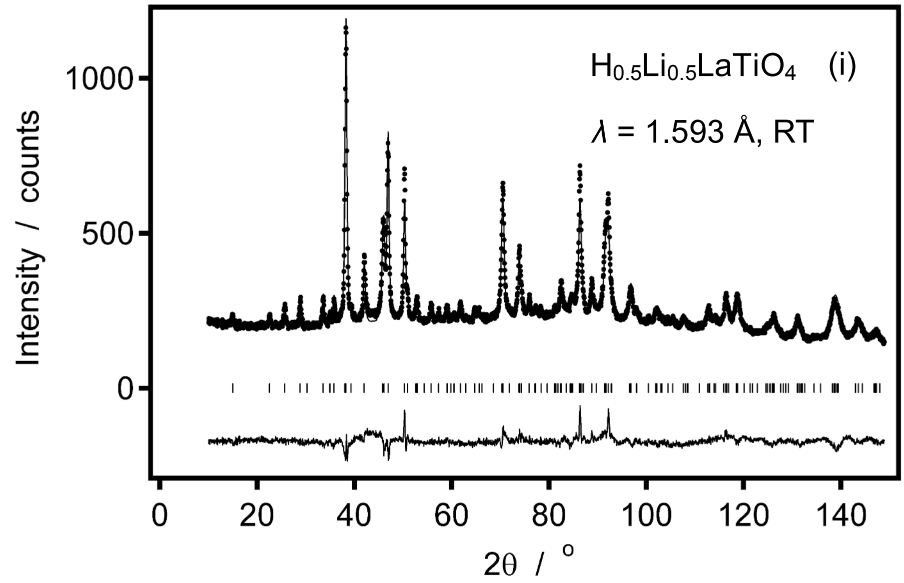

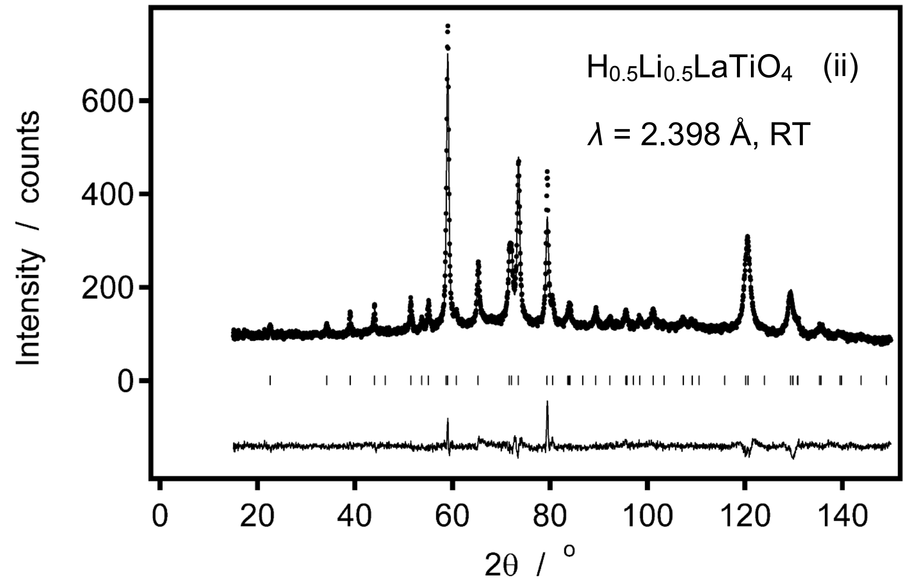

Figures 5.8 Observed (dots), calculated (top line) and difference (bottom line) neutron powder diffraction patterns for $H_{0.5}Li_{0.5}LaTiO_4$ collected at room temperature using (i) 1.593 Å and (ii) 2.398 Å wavelength radiation. The vertical bars indicate the allowed Bragg reflection positions for $H_{0.5}Li_{0.5}LaTiO_4$.

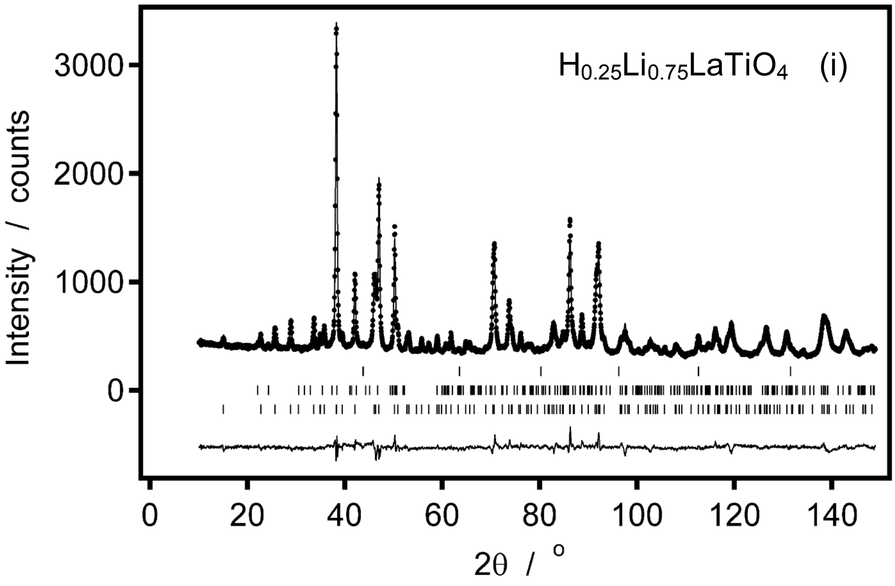

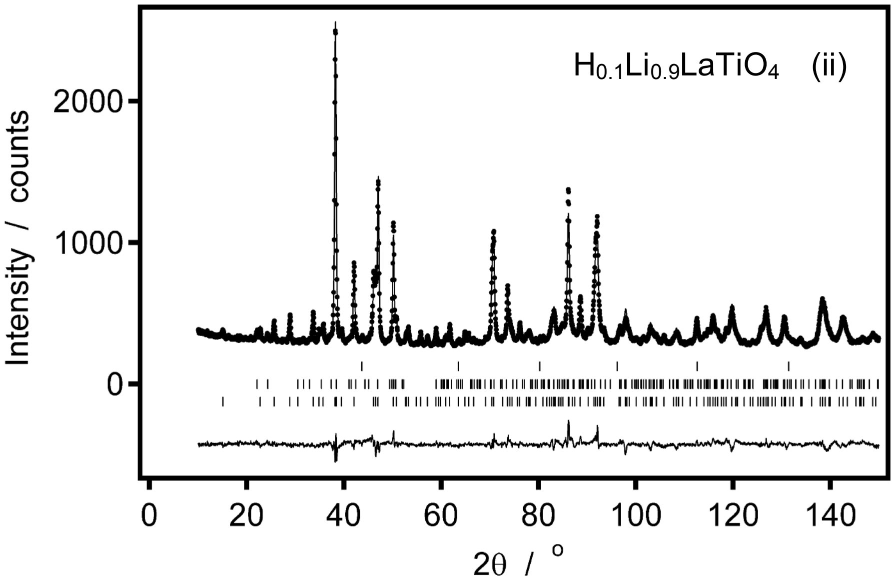

Figures 5.9 Observed (dots), calculated (top line) and difference (bottom line) neutron powder diffraction patterns for (i) $H_{0.25}Li_{0.75}LaTiO_4$ and (ii) $H_{0.1}Li_{0.9}LaTiO_4$. The upper, middle and lower sets of vertical bars indicate the allowed Bragg reflection positions for vanadium (sample holder), Li_2CO_3 and the layered perovskite phase, respectively. In these samples, Li_2CO_3 is present as (i) a 0.0055(8) wt. % minority phase and (ii) a 0.0135(8) wt. % minority phase.

The rapidity of the reaction between $HLaTiO_4$ and $LiOH{\cdot}H_2O$ was assessed for an equimolar mixture of these reagents. These reagents were ground together for 20 min and underwent a temporary reduction in friability. The mass of the resulting sample was then recorded, which revealed that a loss of *ca.* 5 wt. % had occurred. This mass loss is commensurate with the evaporation of *ca.* 60 wt. % of the water produced by reaction (5.1), suggesting that this reaction had commenced during grinding. X-ray powder diffraction data collected over a 23 min period, following a preparation period of 30 min, are shown in Figure 5.10, and indicate that the lattice parameters of $HLaTiO_4$ had undergone a significant change to the values reported for $LiLaTiO_4$.[13]

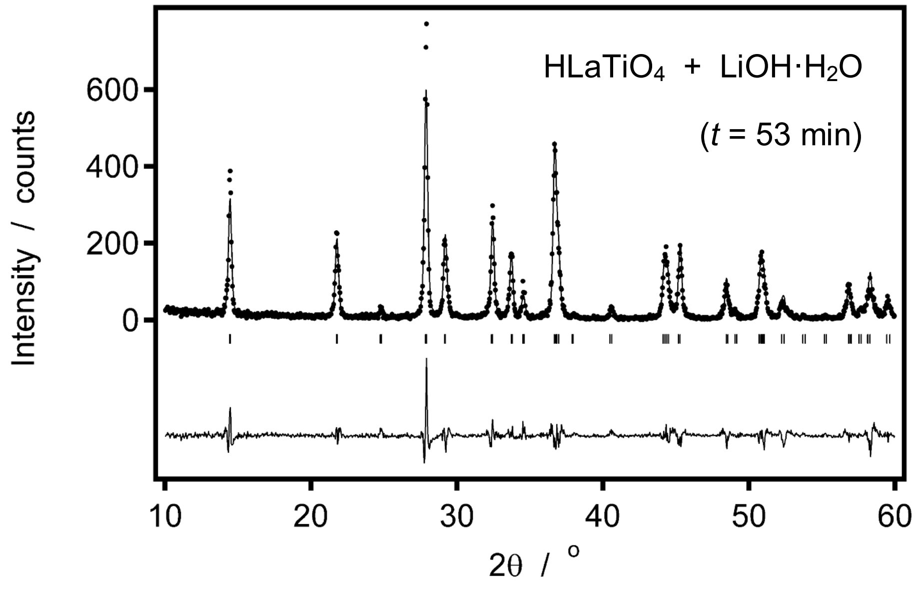

Figure 5.10 Observed (dots) X-ray powder diffraction pattern collected from a 1:1 mixture of $HLaTiO_4$ and $LiOH{\cdot}H_2O$ after it had been ground. The observed data were collected over a 23 min period after the mixture had been ground and prepared for analysis over a 30 min period, which gives a total time of reaction, *t*, of 53 min. The calculated (top line) and difference (bottom line) diffraction patterns were derived from LeBail analysis. The vertical bars indicate the allowed Bragg reflection positions for a tetragonal cell in the space group *P*4/*nmm*.

The ground sample was then monitored intermittently over the next 5 weeks. The lattice parameters derived from these diffraction patterns are plotted in Figure 5.11, and can be seen to evolve smoothly as a function of time. The rate of change of these lattice parameters decreases significantly after 5 d, but there is no obvious or definitive point at which the ion exchange can be described as complete. The latter prevents the kinetics of the reaction from being quantified from these measurements. It should be noted that the lithium-exchanged samples used in the neutron powder diffraction study were prepared at least one week prior to the allocated beamtime.

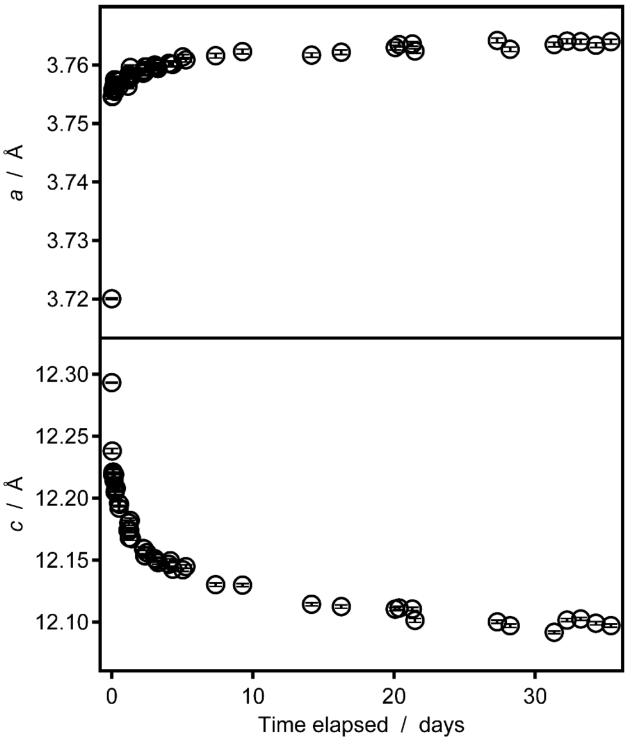

Figure 5.11 Lattice parameters derived from X-ray powder diffraction patterns collected from a 1:1 mixture of $HLaTiO_4$ and $LiOH{\cdot}H_2O$ after the mixture had been ground for 20 min. The diffraction patterns were collected intermittently over the course of 5 weeks, with each data set collected over a 10 min a period.

In order to evaluate the affect that this approach to Li^+ ion exchange has on the particle morphology of the layered perovskite, scanning electron micrographs were collected from $NaLaTiO_4$, $HLaTiO_4$, and the lithium-exchanged materials, $H_{0.5}Li_{0.5}LaTiO_4$ and $LiLaTiO_4$. These micrographs are shown together in Figure 5.12, and show that both $HLaTiO_4$ and the lithium-exchanged samples exhibit the same particle morphology as the $NaLaTiO_4$ high-temperature precursor. In addition, the micrographs collected from the lithium-exchanged samples show no evidence that delamination of the perovskite layers had occurred as a result of grinding.

The affect that Li^+ ion exchange has on the crystallinity of the $[LaTiO_4]^-$ host lattice was examined, on a more local scale, using transmission electron microscopy, as shown in Figure 5.13. High-resolution images recorded from a sample of $H_{0.5}Li_{0.5}LaTiO_4$ show grains that are predominantly characterised by ordered and regularly spaced lattice fringes, but it is noted that regions with little or no obvious order are also observed. These observations indicate that the crystallinity of these materials is largely unaffected by the presence of a disordered mixture of protons and lithium cations in the interlayer region. This retention of crystallinity is supported by selected area electron diffraction patterns, which show regular arrays of sharp peaks. These peaks are often accompanied by a significant degree of streaking as well as weaker satellite peaks, which is commensurate with a multi-crystallite composition. However, the interpretation of these images and electron diffraction patterns, especially the disorder that is encountered, is complicated by evidence of beam-

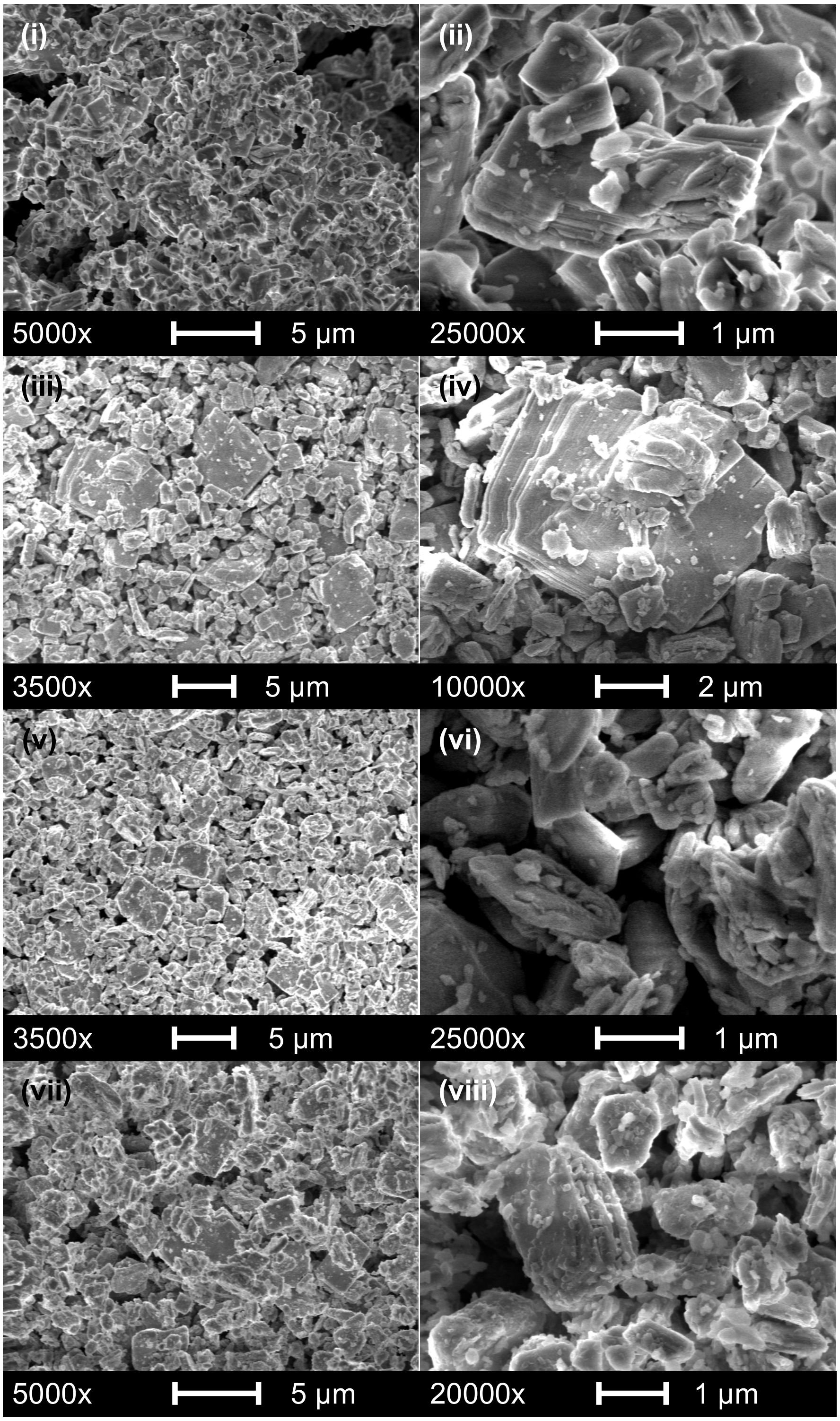

Figure 5.12 Scanning electron micrographs recorded from (i) and (ii) $NaLaTiO_4$, (iii) and (iv) $HLaTiO_4$, (v) and (vi) $H_{0.5}Li_{0.5}LaTiO_4$, and (vii) and (viii) $LiLaTiO_4$ (*via* $LiOH{\cdot}H_2O$).

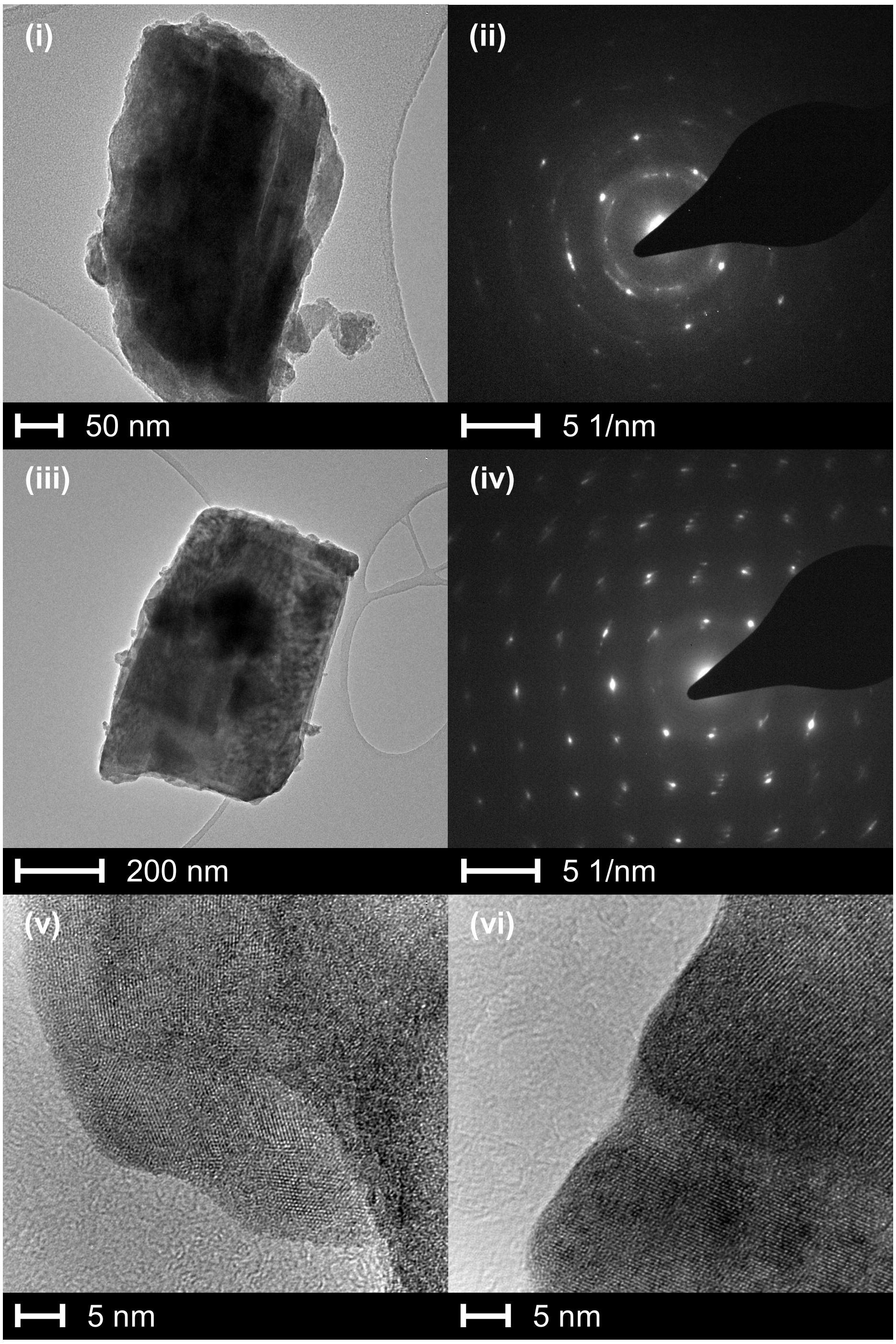

Figure 5.13 (i) to (iv) Transmission electron microscopy images of typical grains of $H_{0.5}Li_{0.5}LaTiO_4$ and their corresponding selected area electron diffraction patterns. (v) and (vi) High-resolution transmission electron microscopy images showing details of the local structure of $H_{0.5}Li_{0.5}LaTiO_4$.

induced structural changes. These changes represent gross modifications on the atomic scale, and so, no further insight can be gained about the local structure from these measurements.

The proton content of these phases was also evaluated from their dehydration behaviours between 120 °C and 800 °C using thermogravimetric measurements. Thermogravimetric data collected from each of the samples in the $H_{1-x}Li_xLaTiO_4$ series indicate a mass loss ranging from 3.7 wt. %, for $HLaTiO_4$, to 1.4 wt. %, for $LiLaTiO_4$, in the temperature range $160 \leq T \leq 720$ °C; data collected from $H_{0.5}Li_{0.5}LaTiO_4$ are shown in Figure 5.14. Figure 5.15 represents these mass losses as the number of moles of water lost per formula unit, and shows a trend in water loss that suggests that reaction (5.2) had occurred.

$$H_{1-x}Li_xLaTiO_4 \rightarrow \square_{1-x}Li_xLaTiO_{4-[(1-x)/2]} + \tfrac{1}{2}(1-x)H_2O \qquad (5.2)$$

Therefore, it can be seen that the dehydration of these lithium-exchanged phases is approximately consistent with the formula stoichiometries derived from the neutron powder diffraction study. The differences between the derived and anticipated losses of water could arise from the evaporation of extra-framework moisture.

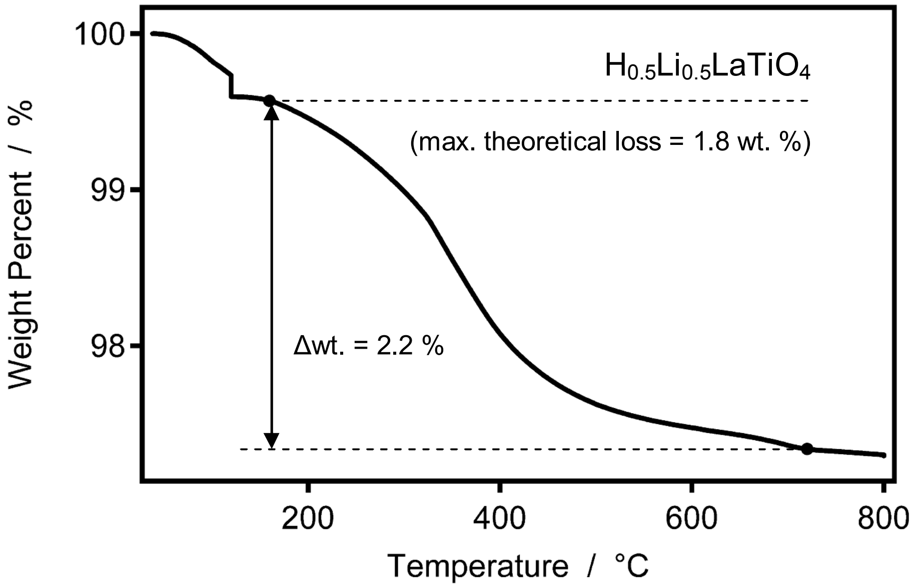

Figure 5.14 Thermogravimetric data collected on heating $H_{0.5}Li_{0.5}LaTiO_4$ from room temperature to 800 °C under a dynamic atmosphere of dry helium. The limits of the mass loss, Δwt., are defined by a significant change in gradient on heating above 120 °C and approaching 800 °C. The maximum loss in mass anticipated from the topochemical dehydration of $H_{0.5}Li_{0.5}LaTiO_4$ is 1.8 wt. %.

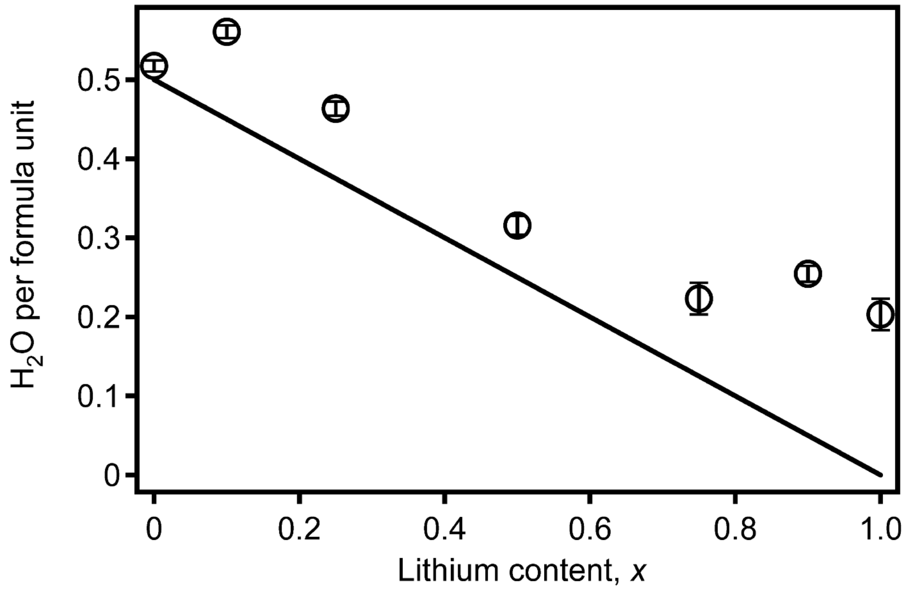

Figure 5.15 Plot of water loss per formula unit derived from thermogravimetric data collected from the $H_{1-x}Li_xLaTiO_4$ series of compounds. The solid line represents the losses of water anticipated from the dehydration in reaction (5.2).

5.3.2 Dehydration of $H_{1-x}Li_xLaTiO_4$ ($0.5 \leq x \leq 0.9$) and AC Impedance Spectroscopy

It has previously been shown by Thangadurai *et al.* that topotactic dehydration of the $HLaTiO_4$ parent phase can be achieved by heating the material at 480 °C for 15 min, and results in the formation of a defective $n = 2$ Ruddlesden-Popper phase, $La_2\square Ti_2O_7$.[15] This double-layered perovskite could be indexed by the authors in a tetragonal cell of dimensions $a = 3.725(3)$ Å and $c = 21.68(5)$ Å. However, this can be contrasted with the behaviour of the intermediate members of the $H_{1-x}Li_xLaTiO_4$ series, over the range $0.5 \leq x \leq 0.9$, which, following a similar heat treatment, gives rise to X-ray powder diffraction data that could be indexed, instead, on the basis of the $[LaTiO_4]^-$ host lattice, but with a considerable reduction in the *c* parameter, as illustrated in Figure 5.16. The fits to each of these X-ray data sets are shown in Figures 5.17 - 5.18. It is noted that X-ray diffraction data collected from the $x = 0.75$ and 0.9 samples could additionally be fitted on the basis of the $[LaTiO_4]^-$ host lattice. However, the anticipated loss of apical oxide anions from the interlayer region could not be verified or disproved in either of these data sets; attempts to refine the site occupancies of the oxide anions yielded unstable refinements. Nevertheless, by taking the observations accumulated from both the X-ray and the TGA experiments together, it can be seen that the lithium-exchanged phases over the range $0.5 \leq x \leq 0.9$ lose water, but retain a structure and composition that can probably be described as $\square_{1-x}Li_xLaTiO_{4-[(1-x)/2]}$. It is also noted that heating the $x = 1$ sample at 480 °C for

30 min results in a negligible change of cell volume, as also illustrated in Figure 5.16, indicating that only lithium cations were present in the interlayer region. This lends weight to the assignment that the mass loss from this sample, as determined from thermogravimetric measurements, arises from loss of extra-framework moisture.

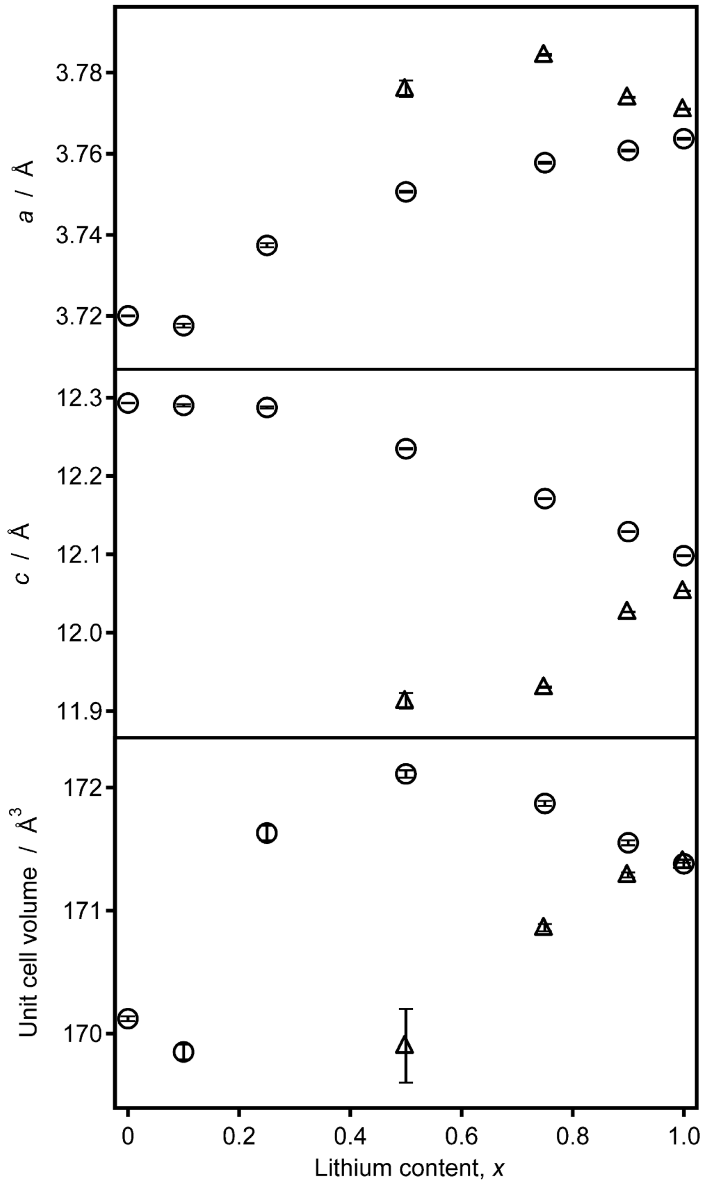

Figure 5.16 Unit cell parameters of the dehydrated $_{1-x}Li_xLaTiO_{4-[(1-x)/2]}$ phases (triangles), over the range $0.5 \leq x \leq 0.9$, and $LiLaTiO_4$ heated up to 480 °C (triangle), derived from X-ray powder diffraction data. Additionally shown are unit cell parameters of the $H_{1-x}Li_xLaTiO_4$ parent phases (circles) derived from X-ray powder diffraction data.

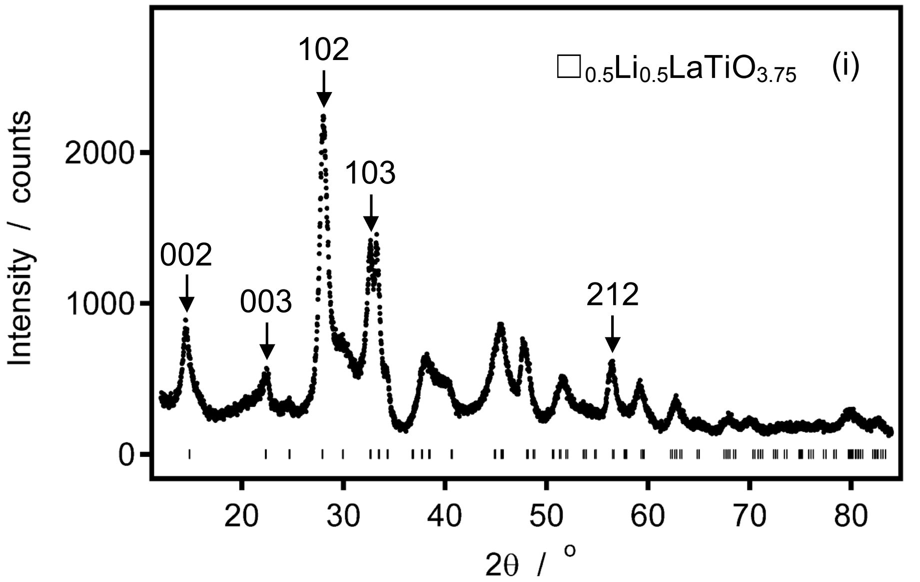

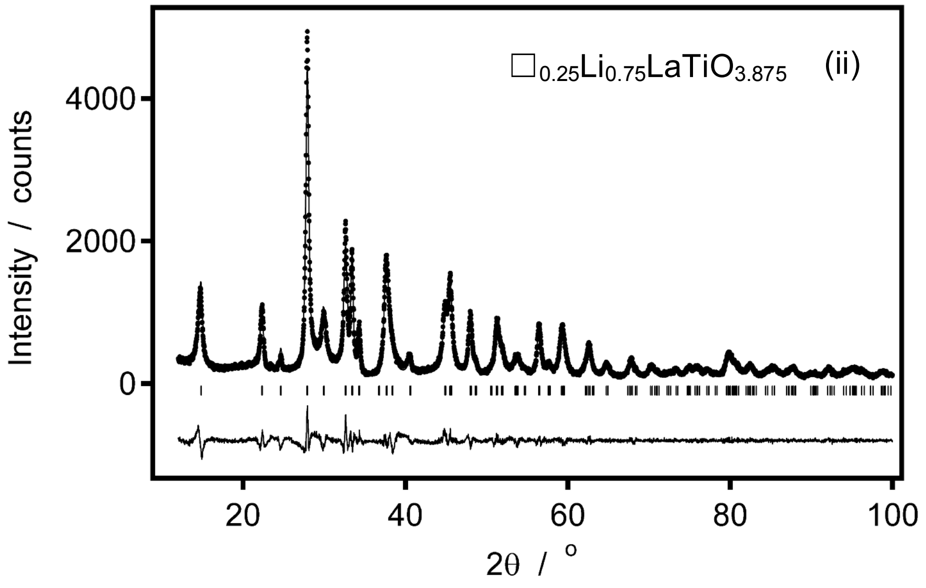

Figure 5.17 Observed (dots) X-ray powder diffraction patterns collected from (i) $\square_{0.5}Li_{0.5}LaTiO_{3.75}$ and (ii) $\square_{0.25}Li_{0.75}LaTiO_{3.875}$. For $\square_{0.25}Li_{0.75}LaTiO_{3.875}$, the calculated (top line) and difference (bottom line) diffraction patterns are derived from LeBail analysis. The vertical bars indicate the allowed Bragg reflection positions for a tetragonal cell in the space group *P*4/*nmm*.

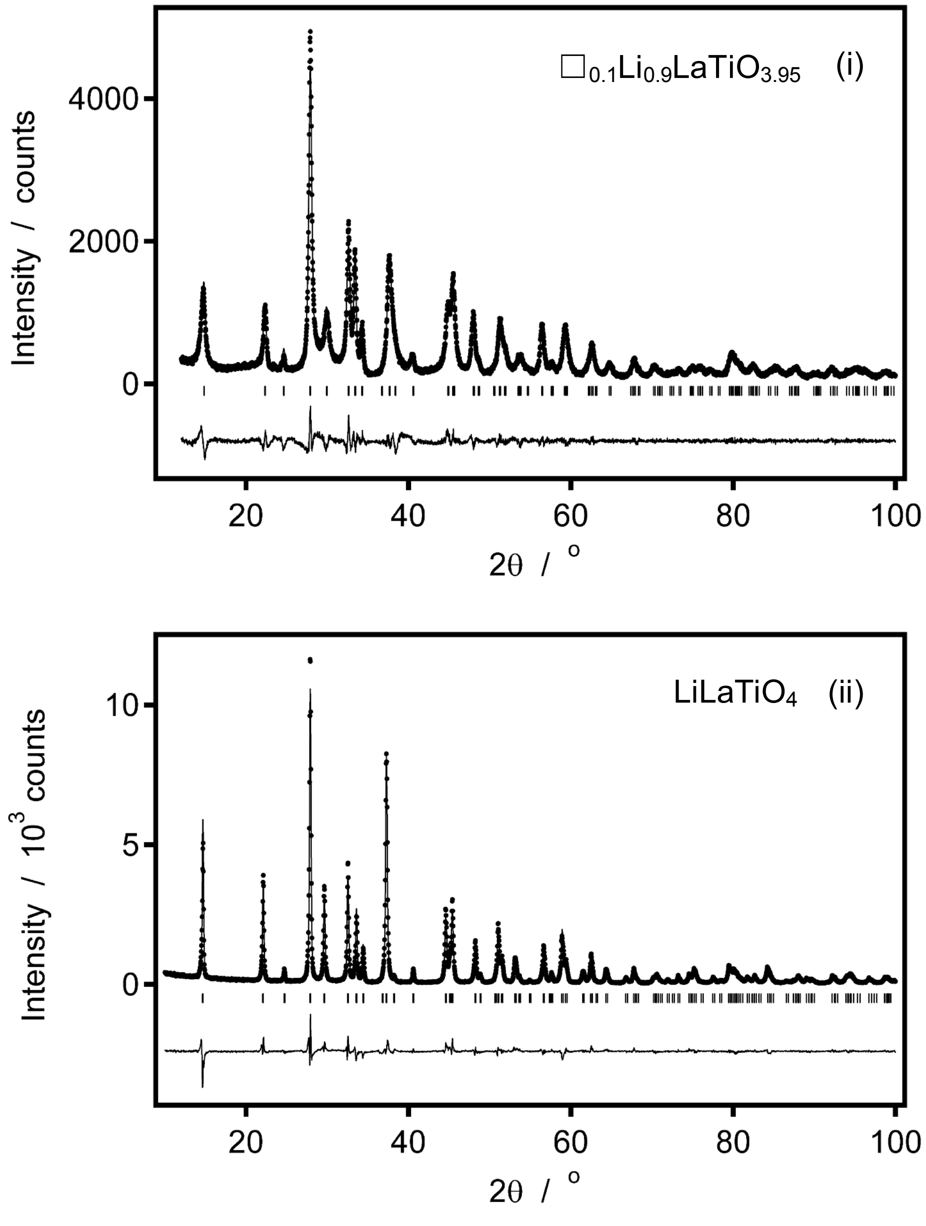

Figure 5.18 Observed (dots) X-ray powder diffraction patterns collected from (i) $\square_{0.1}Li_{0.9}LaTiO_{3.95}$ and (ii) $LiLaTiO_4$ (after heat treatment at 480 °C). Calculated (top line) and difference (bottom line) diffraction patterns are derived from (i) LeBail analysis and (ii) Rietveld analysis. The vertical bars indicate the allowed Bragg reflection positions for a tetragonal cell in the space group *P*4/*nmm*.

Heating the dehydrated samples to 600 °C leads to minimal further mass loss, and resulted in a considerable loss of crystallinity, as shown Figure 5.19. In order to evaluate the potential for fast-ion conduction in the defective phases $\square_{0.5}Li_{0.5}LaTiO_{3.75}$ and $\square_{0.25}Li_{0.75}LaTiO_{3.875}$, AC impedance data were collected from these materials in air. These experiments involved heating a pellet of the $H_{0.5}Li_{0.5}LaTiO_4$ and $H_{0.25}Li_{0.75}LaTiO_4$ parent compounds at either 480 °C, to give the $\square_{1-x}Li_xLaTiO_{4-[(1-x)/2]}$ dehydrated materials, or at 600 °C, to give the unknown structures responsible for the diffraction data in Figure 5.19. The materials formed on heat treatment at 600 °C shall be referred to as $\square_{1-x}Li_xLaTiO_{4-[(1-x)/2]}$ (HT).

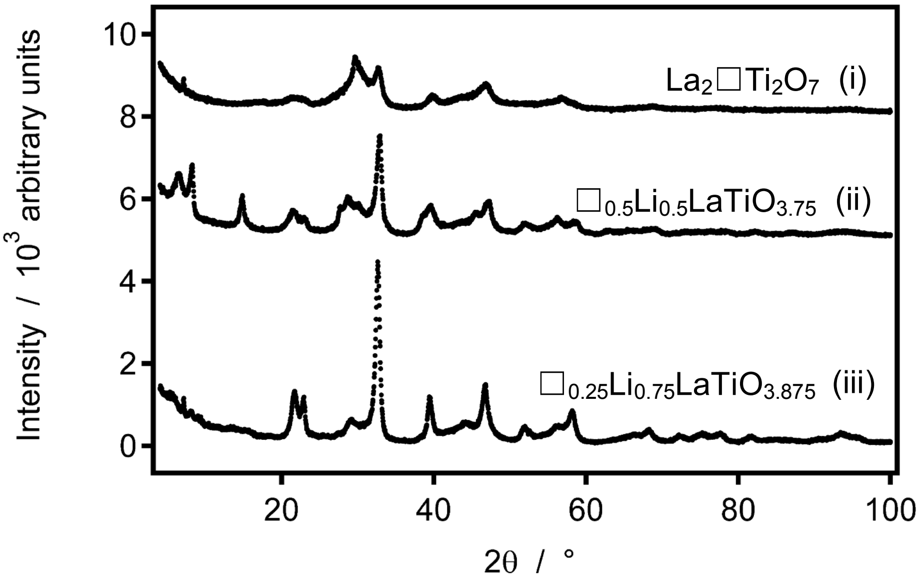

Figure 5.19 X-ray powder diffraction patterns collected from (i) $La_2\square Ti_2O_7$, (ii) $\square_{0.5}Li_{0.5}LaTiO_{3.75}$ (HT) and (iii) $\square_{0.25}Li_{0.75}LaTiO_{3.875}$ (HT).

Impedance data collected from $\square_{0.5}Li_{0.5}LaTiO_{3.75}$ (HT) showed up to three overlapping arcs in the complex plane in the temperature range 300 ≤ T ≤ 600 °C. Below 300 °C, the impedance was immeasurably large. The resistances associated with these arcs were estimated by fitting the data using an equivalent model consisting of up to three parallel combinations of a resistor (R) and a constant phase element (CPE), as illustrated in Figure 5.20. These resistances were added together to provide an estimate of the total conductivity of the pellet.

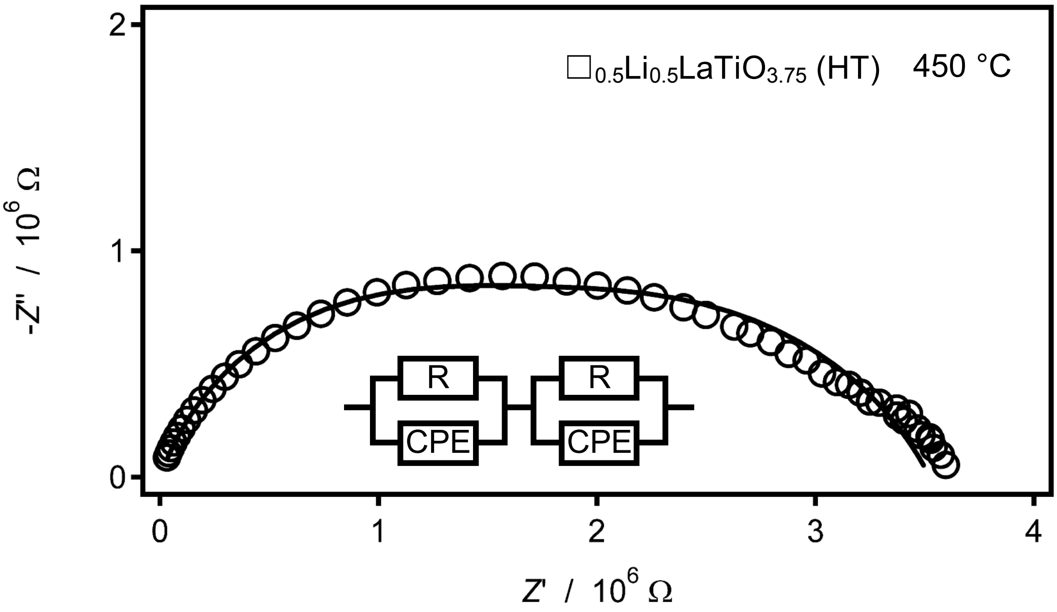

Figure 5.20 A complex-plane representation of AC impedance data collected from $\square_{0.5}Li_{0.5}LaTiO_{3.75}$ (HT) at 450 °C in air. The conductivity was derived from these data on the basis of the equivalent circuit shown.

The temperature dependence of this conductivity behaviour was fitted using a modified Arrhenius equation, and indicated an activation energy of 0.8(2) eV over the temperature range $300 \leq T \leq 600$ °C, as illustrated in Figure 5.21. The total conductivity remains low over the temperature range studied, with a typical value of 1.3×10^{-7} S cm^{-1} at 450 °C. Performing the same experiments under dynamic atmospheres of dry N_2, wet N_2 and dry O_2 showed that the conductivity of $\square_{0.5}Li_{0.5}LaTiO_{3.75}$ (HT) is insensitive to atmosphere.

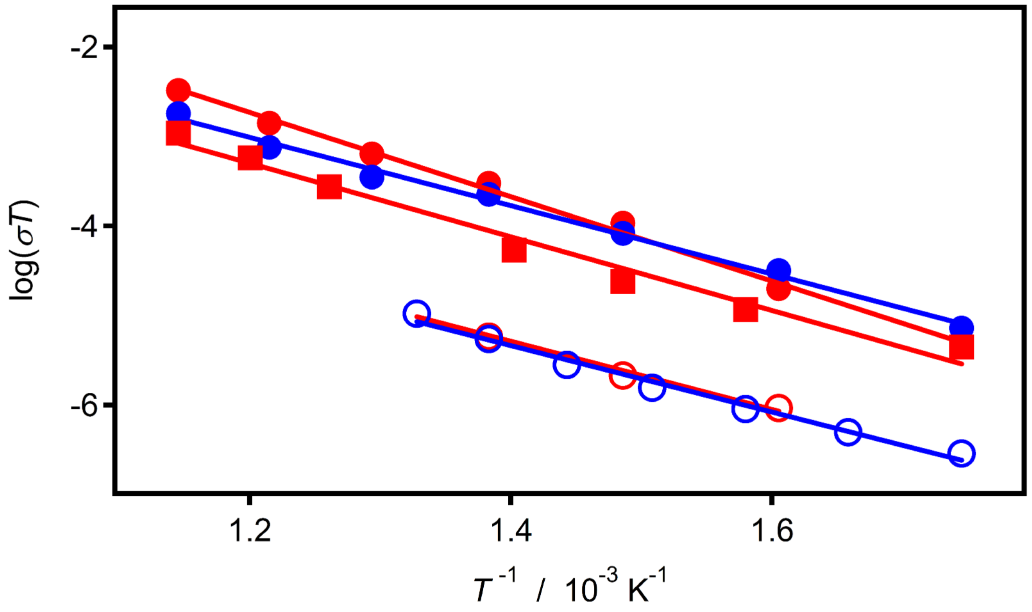

Figure 5.21 Plots of conductivity as a function of temperature for $\square_{0.5}Li_{0.5}LaTiO_{3.75}$ (HT) (squares), $\square_{0.25}Li_{0.75}LaTiO_{3.875}$ (open circles) and $\square_{0.25}Li_{0.75}LaTiO_{3.875}$ (HT) (filled circles), on heating (red) and cooling (blue). These conductivities were derived from AC impedance data collected in air. The solid lines indicate an Arrhenius fit to each data set.

By comparison, impedance data collected from $\square_{0.25}Li_{0.75}LaTiO_{3.875}$ in the temperature range 350 ≤ T ≤ 480 °C, showed only a single arc, as illustrated in Figure 5.22. The resistance associated with this arc was similarly estimated using a resistor and a constant phase element. This indicated that the conductivity of $\square_{0.25}Li_{0.75}LaTiO_{3.875}$ is similarly activated (0.8(2) eV) over the temperature range studied, as illustrated in Figure 5.21, but is approximately an order of magnitude lower than that of $\square_{0.5}Li_{0.5}LaTiO_{3.75}$ (HT), with a typical value of 8.0×10^{-9} S cm^{-1} at 450 °C.

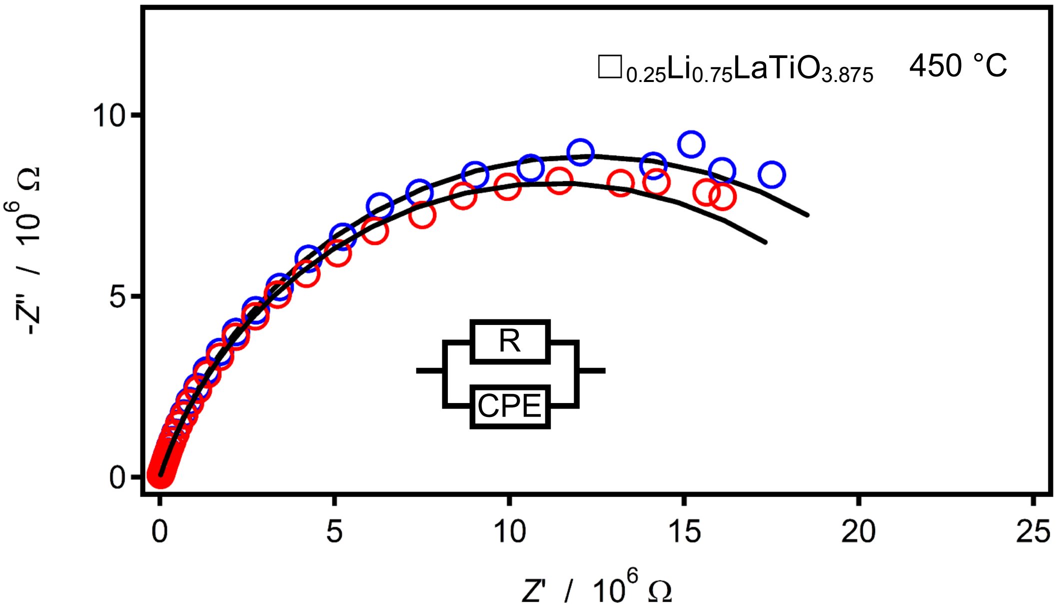

Figure 5.22 A complex-plane representation of AC impedance data collected from $\square_{0.25}Li_{0.75}LaTiO_{3.875}$ at 450 °C in air. Data were collected on both heating (red) and cooling (blue). The conductivities were derived from these data using the equivalent circuit shown.

The pellet of $\square_{0.25}Li_{0.75}LaTiO_{3.875}$ resulting from the above experiment was subsequently heated at 600 °C in N_2 atmosphere for 1 d to give the material $\square_{0.25}Li_{0.75}LaTiO_{3.875}$ (HT). Impedance data collected from this pellet show up to two overlapping arcs in the temperature range $300 \leq T \leq 600$ °C, and were therefore fitted using up to two parallel combinations of a resistor and a constant phase element. The resistances derived from these fits were also added together to provide an estimate of the total conductivity of the pellet. After heating this pellet up to 600 °C in air for the first time, the impedance data additionally showed a tail-like contribution at low frequency, as illustrated in Figure 5.23. This tail-like contribution could be modelled by adding a constant phase element in series to the equivalent circuit, and is attributable to ion-blocking at the electrode interface. The total conductivities derived from these fits indicate that $\square_{0.25}Li_{0.75}LaTiO_{3.875}$ (HT) exhibits similar conductivity behaviour to $\square_{0.5}Li_{0.5}LaTiO_{3.75}$ (HT), with an activation energy of 0.94(5) eV over the temperature range $300 \leq T \leq 600$ °C, and a typical conductivity of 4.1×10^{-7} S cm^{-1} at 450 °C.

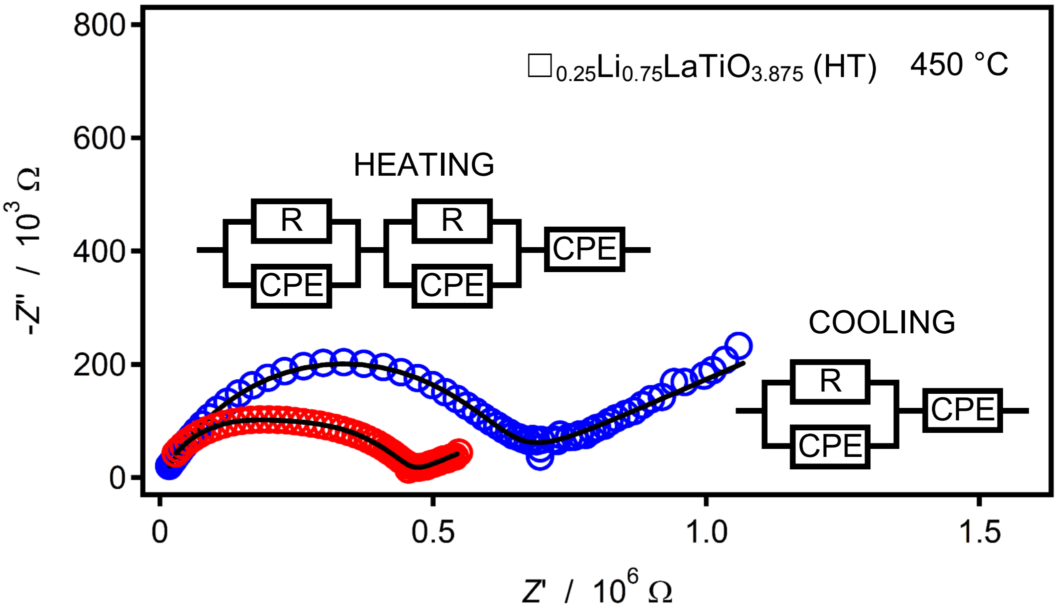

Figure 5.23 A complex-plane representation of AC impedance data collected from $\square_{0.25}Li_{0.75}LaTiO_{3.875}$ (HT) at 450 °C in air. Data were collected on both heating (red) and cooling (blue). The conductivities were derived from these data using the equivalent circuits shown.

5.4 Discussion

The neutron powder diffraction study indicates that the room-temperature mixing of crystalline $LiOH·H_2O$ with the layered perovskite $HLaTiO_4$ gives rise to an ion-exchange reaction, where protons are quantitatively replaced with lithium cations to give the new solid-solution series $H_{1-x}Li_xLaTiO_4$. It is surprising to note that this mixture remains friable throughout the reaction, despite the production of two equivalents of water for each equivalent of proton replaced. This direct room-temperature approach can be contrasted with other methods of ion exchange of layered materials, which typically employ an excess of cations in either aqueous solution[7, 13] or molten salt[9, 16] to drive the exchange. These conventional approaches offer little or no control over the extent of exchange, and typically lead to the fully exchanged material. However, here, we have instead exploited the gain in entropy associated with the liberation of water from the lattice of $LiOH·H_2O$ to drive the exchange of a controlled quantity of lithium cations, in what is otherwise an acid-base reaction. This has allowed stoichiometric control over ion exchange to be demonstrated for the first time in this series of compounds.

The samples that result from these ion-exchange reactions show the same particle morphology as the $HLaTiO_4$ parent as well as that of the $NaLaTiO_4$ precursor. These observations suggest that protons had been replaced with lithium cations without dissolution of the $[LaTiO_4]^-$ host lattice. It is also noted that this reaction proceeds without delamination of the perovskite layers, which can potentially occur during ion exchange[17] and could be anticipated to occur whilst grinding the reagents. These observations are supported by X-ray powder diffraction data collected from an equimolar mixture of the reagents over the course of several weeks. This study indicates the presence of a single phase that is crystalline, and shows a time-evolved change in the lattice parameters rather than a transition *via* an amorphous intermediate.

The structures of the partially exchanged phases are very similar to those of the $HLaTiO_4$ and $LiLaTiO_4$ end members; both the staggering of adjacent perovskite layers and the ordered arrangement of La^{3+} and H^+/Li^+ cations are maintained. The positions adopted by hydrogen and lithium are also consistent with those identified in the end-member phases. In the structure of $HLaTiO_4$, protons are statistically distributed over eight equivalent sites about the apical oxide position, O2, at a distance of 0.997(14) Å that is typical for hydroxide.[18] A longer proton-oxide separation of 1.984(13) Å that spans the interlayer region with an O2-H···O2 angle of 116.8° is typical of hydrogen-bond geometry.[19] The relatively large atomic displacement parameters of O2 and H suggest that the oxide is displaced by the presence of the proton, *i.e.* the hydroxide group is locally ordered, but shows, on average, static disorder. This interpretation of the atomic displacement behaviour is supported by the neutron power diffraction study of $H_{0.5}Li_{0.5}LaTiO_4$, conducted at 5 K; the atomic displacement parameters of O1 and O3 decrease to one third of their room-temperature values, whilst those of O2 and H show no significant change.

In contrast to the proton coordination in $HLaTiO_4$, the lithium cations in $LiLaTiO_4$ coordinate to a pair of oxide anions on both sides of the interlayer region, at a distance of 2.0108(9) Å. These LiO_4 units form an O-Li-O angle of *ca.* 139° between pairs of apical oxide parallel to the (001) plane, which is intermediate between tetrahedral and square planar geometries. This distortion, whilst unusual, is characteristic of a number of lithium-containing layered perovskite phases,[20] although it should be noted that in only a few of these cases have the lithium cations been explicitly located by neutron powder diffraction.[21-24] The distortion of a square planar coordination towards a tetrahedral arrangement can be quantified using the angle between the plane and a Li-O bond, α, as illustrated in Figure 5.24. This angle can vary from 0°, for a square plane (*SP*), to 35.26°, for a regular tetrahedron (*T*), and for the materials studied, ranged from 21.30(10)°, for the $x = 0.5$ member, to 20.62(7)°, for the $x = 1.0$ member. This angle can be normalised using equation (5.1), as defined by Tassel *et al.*,[25] to give a measure of the distortion or square planar character, φ(T-SP).

$$\varphi(T-SP) = \left(1 - \frac{\alpha}{35.26^\circ}\right) \times 100 \qquad (5.1)$$

Evaluating the distortion of the LiO_4 tetrahedra in this manner indicates that this distortion does not vary significantly with lithium content, with values of φ(T-SP) ranging between 40 and 42 %.

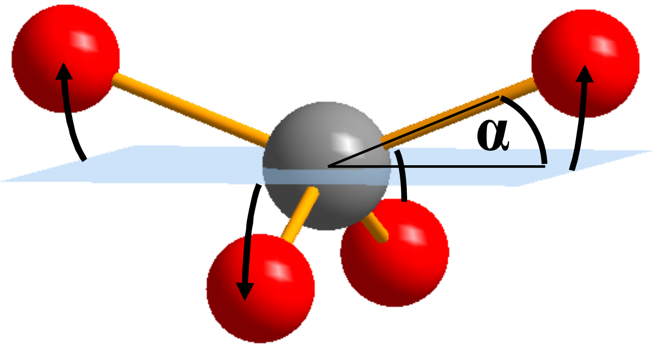

Figure 5.24 Distortion of a square planar coordination towards a tetrahedral arrangement. *α* indicates the angle that is made between the plane and a Li-O bond.

An examination of the crystal structures derived from the neutron powder diffraction study indicates that the replacement of protons with lithium cations results in a reduction in the *c* lattice parameter, despite the ionic radius of Li^+ being larger than that of H^+. In the case of full-exchange to give $LiLaTiO_4$, this amounts to a decrease of 0.2167(5) Å. However, with the exception of the $x = 0.1$ sample, the interlayer distance was found to have increased by an average 0.066 Å in each of the lithium-exchanged samples, as illustrated in Figure 5.25. It follows that the net reduction in the *c* parameter must, instead, arise from the impact of lithium coordination on the neighbouring perovskite layers. Indeed, Li^+ ion exchange also leads to a decrease in the axial O2-Ti-O3 distance, which ranges from 0.07(2) Å, for the $x = 0.25$ member, to 0.135(11) Å, for the $x = 1.0$ member. This is accompanied by an increase in the equatorial Ti-O1 bond distance, which is, on average, 0.024 Å longer, as illustrated in Figure 5.26; this distortion of the TiO_6 octahedron occurs

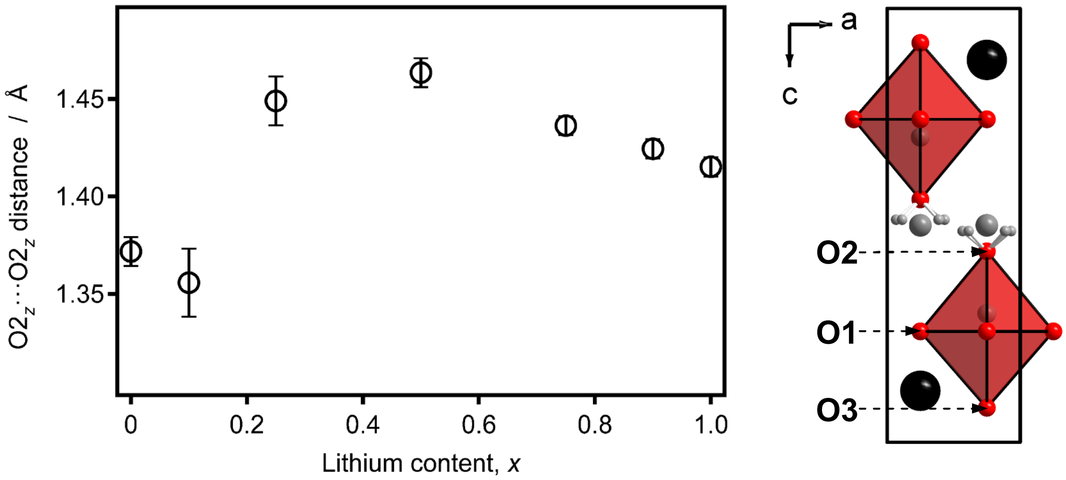

Figure 5.25 Variation in the interlayer distance, O2$_z$···O2$_z$, across the $H_{1-x}Li_xLaTiO_4$ series of compounds derived from least-squares refinement against neutron powder diffraction data. This distance is defined as the z-component of the distance between two apical oxide anions. The positions of the crystallographically distinct O^{2-} anions are indicated in the crystal structure of $H_{0.5}Li_{0.5}LaTiO_4$, where the H^+, Li^+ and La^{3+} cations are represented by small grey, large grey and black spheres, respectively, whilst TiO_6 octahedra are indicated by red units.

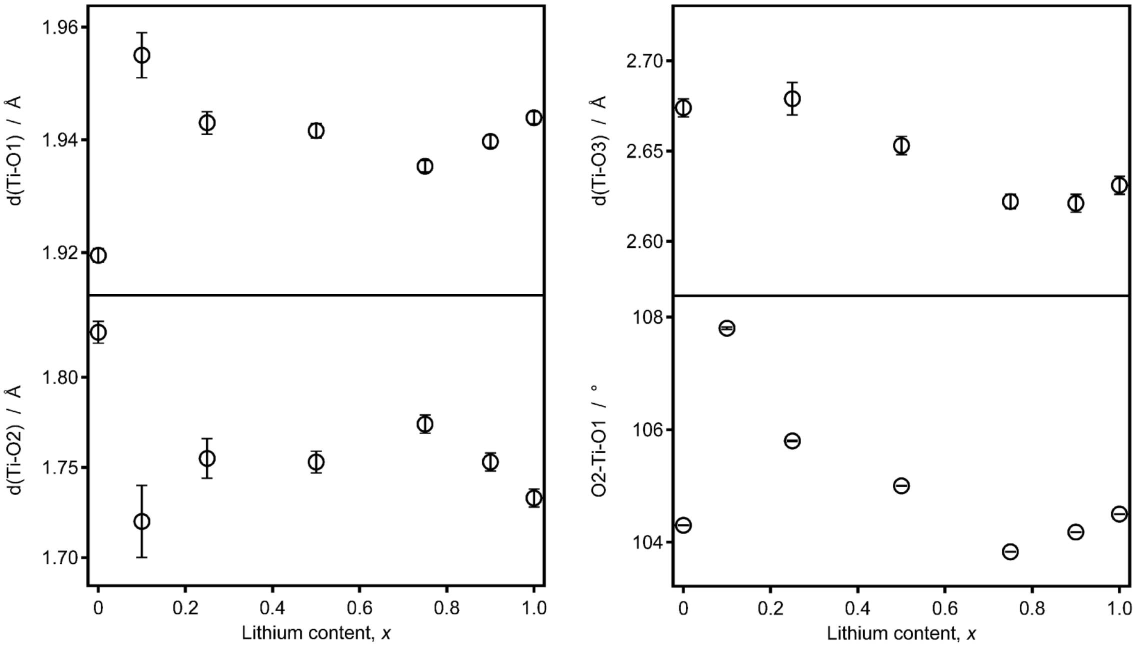

Figure 5.26 Variation in selected Ti-O bond distances and bond angles across the $H_{1-x}Li_xLaTiO_4$ series of compounds derived from least-squares refinement against neutron powder diffraction data. An outlying Ti-O3 bond distance of 2.83(2) Å, derived from the model of the x = 0.1 data set, has been omitted for ease of comparison.

with the relative position of the titanium cation remaining largely unperturbed. When the reduction in the thickness of each of the two perovskite layers is taken together with the increase in the interlayer distance, this difference accounts for the observed reduction in the *c* parameter. Therefore, the distortion of the TiO_6 octahedron does not significantly affect the thickness of the lanthanum-containing rock-salt layer, but it does necessarily give rise to an increase in the longer of the two La-O3 bond distances, as illustrated in Figure 5.27; this is due to the large *x*- and *y*-components in the orientation of this bond. It should be noted that some of the bond distances and bond angles derived from the model of the $x = 0.1$ data set represent outlying values, which arise as a result of refinement against poorer quality data. This model has been included in the structural analysis for completeness only.

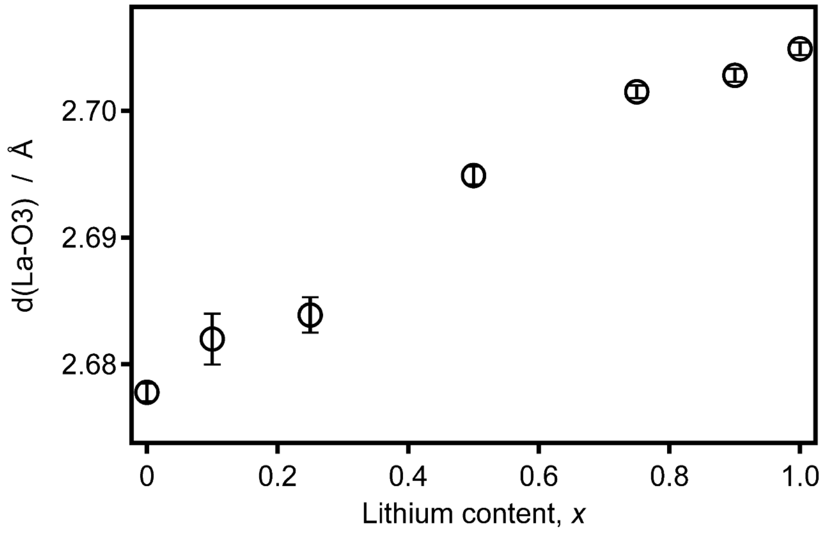

Figure 5.27 Variation in La-O3 bond distances across the $H_{1-x}Li_xLaTiO_4$ series of compounds derived from least-squares refinement against neutron powder diffraction data.

The Li-O bond distance shows no significant variation across the series, with a typical value of 2.0108(9) Å indicated by the $LiLaTiO_4$ end member. A bond valence sum analysis of this distance resulted in a calculated valence of 0.916(4), suggesting that the distorted tetrahedral site of lithium is slightly larger than the optimum size. However, it is interesting to note that the calculation of the bond-valence sum for a fictitious lithium cation on the vacant 2*b* site of $HLaTiO_4$ resulted in a valence of 0.992(4); this valence is significantly closer to that derived from a typical Li-O bond distance. In order to investigate the significance of these results, a review of bond valence sums for similarly distorted LiO_4 tetrahedra in related systems[21-23] was carried out, as summarised in Table 5.6. This indicated a range of calculated valences between 0.64(2) v.u. and 0.82(4) v.u., suggesting that there is a preference for lithium to be under-bonded in Ruddlesden-Popper related structures. Therefore, if similar behaviour is anticipated in the host lattice of $HLaTiO_4$, this apparent over-bonding to lithium provides a possible driving force for the distortion of the TiO_6 octahedron. Furthermore, a comparison of the calculated valences of the titanium cations in $HLaTiO_4$ (4.09(3) v.u.) and $LiLaTiO_4$ (4.18(3) v.u.) suggests that this distortion occurs in a manner that fully compensates for the bonding to the titanium metal centre.

Table 5.6 Bond valence sum analyses of layered Ruddlesden-Popper phases containing distorted LiO_4 tetrahedra

	Li-O / Å		**Calculated valence / v.u.**
$Li_2La_{2/3}Ta_2O_7$[21]			
2 × Li1-O3	1.98(1)		0.243
2 × Li1-O1	2.149(7)		0.155
		BVS =	0.81(2)
$Li_2SrTa_2O_7$[22]			
2 × Li1-O2	2.0320(2)		0.217
2 × Li1-O2	2.1023(3)		0.179
		BVS =	0.792(2)
$HLiSrTa_2O_7$[23]			
2 × Li1-O2	2.10(1)		0.18
2 × Li1-O3	2.193(9)		0.14
		BVS =	0.64(2)
2 × Li2-O2	1.99(1)		0.243
2 × Li2-O3	2.13(3)		0.166
		BVS =	0.82(4)

The X-ray powder diffraction study of the $\square_{1-x}Li_xLaTiO_{4-[(1-x)/2]}$ series of dehydrated materials indicated that the basic structure of the Ruddlesden-Popper phase is retained after the lithium-containing members of the $H_{1-x}Li_xLaTiO_4$ parent series are heated at 480 °C; presumably as a consequence of Li-O bonds bridging between the perovskite layers. However, it is noteworthy that the dehydration of $H_{0.5}Li_{0.5}LaTiO_4$ was accompanied by a considerable loss of crystallinity that was not apparent for the lithium-rich phases. It is important to note that a lithium cation in the interlayer region with a coordination number of greater than two will always lead to bridging of the defective perovskite layers. Therefore, it is likely that the layers will remain more rigidly held together in the lithium-rich samples, whilst those in $\square_{0.5}Li_{0.5}LaTiO_{3.75}$ will be more susceptible to loss of registry between layers. For this reason, increasing the quantity of protons that are replaced with lithium cations in the $HLaTiO_4$ parent phase will lead to an increase in the mean oxide coordination of lithium after dehydration. Fitting the X-ray powder diffraction data using a model based on the structure of $LiLaTiO_4$ suggested that the lithium-oxide units had become considerably more distorted, with a square-planar character of *ca.* 72 %. However, these analyses were unable to indentify the anticipated oxide deficiency of the interlayer region.

Although the structures of these dehydrated phases are not well understood, they presumably must contain a mixture of lithium and vacant sites, and thus bear strong similarities to the fast lithium-conducting perovskite $Li_{3x}La_{2/3-x}TiO_3$.[10, 11] Despite these similarities, the transport measurements of $\square_{0.25}Li_{0.75}LaTiO_{3.875}$ indicated that the conductivity of this material (*ca.* 8.0×10^{-9} S cm^{-1} at 450 °C) is many orders of magnitude lower than that of $Li_{3x}La_{2/3-x}TiO_3$ (*ca.* 10^{-3} S cm^{-1} at 25 °C).[26] Given that the impedance of $\square_{0.25}Li_{0.75}LaTiO_{3.875}$ becomes immeasurably large at lower frequencies, it may be that the grain boundaries are providing the limit to ion mobility. An examination of the particles of $NaLaTiO_4$ after stirring in acid and subsequent grinding with $LiOH{\cdot}H_2O$ showed that each of these processes had a negligible impact on particle size. However, the dehydration reaction could be anticipated to lead to fragmentation of these particles. Indeed, the X-ray powder diffraction study of $H_{0.25}Li_{0.75}LaTiO_4$ showed a general broadening of the peak shape after dehydration, which is commensurate with a reduction in particle size. By contrast, $LiLaTiO_4$ cannot be similarly subjected to such changes in microstructure. Therefore, a comparison of the transport properties of these two materials should establish whether a significant increase in the grain boundary resistance is incurred following the dehydration of $H_{0.25}Li_{0.75}LaTiO_4$. The $LiLaTiO_4$ end member has previously been shown to exhibit a conductivity of *ca.* 3×10^{-6} S cm^{-1} at 450 °C,[8] although no detail was provided regarding its derivation or its relation to the microstructure. Despite these ambiguities, it can be seen that the conductivity of $LiLaTiO_4$ is at least two orders of magnitude higher than that of $\square_{0.25}Li_{0.75}LaTiO_{3.875}$, suggesting that the presence of lithium vacancies does not significantly enhance the intragrain conductivity of these materials. Moreover, it follows that this considerable difference in conductivity arises from a dominant grain boundary contribution to the total resistance.

X-ray powder diffraction patterns collected from $\square_{0.5}Li_{0.5}LaTiO_{3.75}$ (HT) and $\square_{0.25}Li_{0.75}LaTiO_{3.875}$ (HT) indicated the destruction of the layered Ruddlesden-Popper arrangement. By comparison, the defective phase $\square LaTiO_{3.5}$ has been shown by Thangadurai *et al.* to form a <110> terminated layered perovskite, $La_2Ti_2O_7$,[15] on heating to 750-900 °C. It could therefore be anticipated that a similar heat treatment of the dehydrated lithium-containing phases would lead to an equivalent transformation; where the lithium cations would presumably occupy the four-coordinate vacant sites of the perovskite layer. However, the indexing of these diffraction patterns remains far from straightforward.

Although the structures of $\square_{0.5}Li_{0.5}LaTiO_{3.75}$ (HT) and $\square_{0.25}Li_{0.75}LaTiO_{3.875}$ (HT) are not known, it can be seen that these samples afford an order of magnitude enhancement in conductivity over that of $\square_{0.25}Li_{0.75}LaTiO_{3.875}$. The transport measurements of these 600 °C heated samples indicated similar total conductivities (*ca.* 3×10^{-7} S cm^{-1} at 450 °C) and activation energies (*ca.* 0.9 eV), but only the lithium-rich sample, $\square_{0.25}Li_{0.75}LaTiO_{3.875}$ (HT), shows evidence of ion-blocking. A further evaluation of the impedance of $\square_{0.5}Li_{0.5}LaTiO_{3.75}$ (HT) under different atmospheres indicated that the conductivity behaviour of this material shows no dependency on moisture or oxygen, and thus provides some support for lithium-ion mobility in this phase. However, the behaviour of this material often requires the assignment of an extra resistive component that is in addition to the conventional assignments of an intragrain and an intergrain contribution to the conductivity of a polycrystalline sample. This additional resistive component could arise from anisotropic conduction in the sample, *i.e.* where conduction occurs between two adjacent crystallites that are oriented with their stacking vectors perpendicular to one another.

5.5 Conclusions

The mixing of crystalline lithium hydroxide monohydrate with the layered perovskite $HLaTiO_4$ at room temperature gives rise to an ion-exchange reaction, where protons are quantitatively replaced with lithium cations to give the new solid-solution series $H_{1-x}Li_xLaTiO_4$. This exchange represents an acid-base reaction that is driven not by a stoichiometric excess of lithium cations, but instead by the gain in entropy associated with the liberation of water from the lattice of lithium hydroxide monohydrate. In this way, stoichiometric control over ion exchange has been demonstrated for the first time in this series of compounds. Additionally, the water that is formed is the only side-product of this reaction, and so, no purification steps, other than drying in air, are required. This reaction should be sufficiently general to allow it to be extended to other protonated layered perovskites. Layered perovskites constitute a class of materials with a wide range of stoichiometries and structure types,[20] and so the facility to carry out Li^+ ion exchange in a quantitative manner could potentially provide access to a huge range of new compositions that are inaccessible *via* existing synthetic routes.

For the lithium-rich members of the $H_{1-x}Li_xLaTiO_4$ series, dehydration of the interlayer leads to the formation of a new series of defective layered perovskites, $\square_{1-x}Li_xLaTiO_{4-[(1-x)/2]}$, where some of the lithium and interlayer oxygen sites are vacant. However, despite containing a mixture of lithium cations and vacant sites, $\square_{0.25}Li_{0.75}LaTiO_{3.875}$ demonstrates a conductivity several orders of magnitude lower than that of the lithium end member. Given the manner in which these vacancies were formed, it may be that any reduction in the intragrain resistance afforded by these vacancies is masked by an increased grain-boundary contribution. A small enhancement in the conductivity can be achieved by heating the dehydrated material at 600 °C; this results in an irreversible structural transformation that gives rise to an order of magnitude increase in the conductivity.

5.6 Publications

Some of the work described in this chapter has been published as T. W. S. Yip, E. J. Cussen and D. A. MacLaren, *Chem Comm.*, 2010, **46**, 698-700, DOI: 10.1039/b920837b.

5.7 References

1. M. Armand and J.-M. Tarascon, *Nature*, 2008, **451**, 652-657.
2. B. C. H. Steele and A. Heinzel, *Nature*, 2001, **414**, 345-352.
3. C. N. R. Rao and J. Gopalakrishnan, *New Directions in Solid State Chemistry*, 2nd edn., Cambridge University Press, Cambridge, 1997.
4. M. S. Whittingham, *J. Electrochem. Soc.*, 1976, **123**, 315-320.
5. R. E. Schaak and T. E. Mallouk, *Chem. Mater.*, 2002, **14**, 1455-1471.
6. S. N. Ruddlesden and P. Popper, *Acta Cryst.*, 1957, **10**, 538-539.
7. S.-H. Byeon, J.-J. Yoon and S.-O. Lee, *J. Solid State Chem.*, 1996, **127**, 119-122.
8. V. Thangadurai, A. K. Shukla, J. Gopalakrishnan, O. Joubert, L. Brohan and M. Tournoux, *Mater. Sci. Forum*, 2000, **321-324**, 965-970.
9. S. Y. Kim, J.-M. Oh, J.-C. Park and S.-H. Byeon, *Chem. Mater.*, 2002, **14**, 1643-1648.
10. J. A. Alonso, J. Sanz, J. Santamaria, C. Leon, A. Varez and M. T. Fernandez-Diaz, *Angew. Chem. Int. Ed.*, 2000, **39**, 619-621.
11. M. Yashima, M. Itoh, Y. Inaguma and Y. Morii, *J. Am. Chem. Soc.*, 2005, **127**, 3491-3495.
12. E. Suard and A. Hewat, *Neutron News*, 2001, **12**, 30-33.
13. K. Toda, S. Kurita and M. Sato, *J. Ceram. Soc. Jpn.*, 1996, **104**, 140-142.
14. S. Nishimoto, M. Matsuda, S. Harjo, A. Hoshikawa, T. Kamiyama, T. Ishigaki and M. Miyake, *J. Eur. Ceram. Soc.*, 2006, **26**, 725-729.

15. V. Thangadurai, G. N. Subbanna and J. Gopalakrishnan, *Chem. Commun.*, 1998, 1299-1300.

16. D. Neiner, V. Golub and J. B. Wiley, *Mater. Res. Bull.*, 2004, **39**, 1385–1392.

17. S. Ida, C. Ogata, M. Eguchi, W. J. Youngblood, T. E. Mallouk and Y. Matsumoto, *J. Am. Chem. Soc.*, 2008, **130**, 7052-7059.

18. G. Ferraris and G. Ivaldi, *Acta Cryst.*, 1984, **B40**, 1-6.

19. I. D. Brown, *Acta Cryst.*, 1975, **A32**, 24-31.

20. R. H. Mitchell, *Perovskites: Modern and Ancient*, Almaz Press Inc., Thunder Bay, 2002.

21. F. L. Berre, M.-P. Crosnier-Lopez, Y. Laligant, E. Suard, O. Bohnke, J. Emery and J.-L. Fourquet, *J. Mater. Chem.*, 2004, **14**, 3558-3565.

22. T. Pagnier, N. Rosman, C. Galven, E. Suard, J.-L. Fourquet, F. L. Berre and M.-P. Crosnier-Lopez, *J. Solid State Chem.*, 2009, **182**, 317–326.

23. C. Galven, J.-L. Fourquet, E. Suard, M.-P. Crosnier-Lopez and F. L. Berre, *Dalton Trans.*, 2010, **39**, 3212-3218.

24. C. Galven, J.-L. Fourquet, E. Suard, M.-P. Crosnier-Lopez and F. L. Berre, *Dalton Trans.*, 2010, **39**, 4191-4197.

25. C. Tassel, J. M. Pruneda, N. Hayashi, T. Watanabe, A. Kitada, Y. Tsujimoto, H. Kageyama, K. Yoshimura, M. Takano, M. Nishi, K. Ohoyama, M. Mizumaki, N. Kawamura, J. Iñiguez and E. Canadell, *J. Am. Chem. Soc.*, 2009, **131**, 221–229.

26. Y. Inaguma, C. Liquan, M. Itoh, T. Nakamura, T. Uchida, H. Ikuta and M. Wakihara, *Solid State Commun.*, 1993, **86**, 689-693.

6 Li^+ Ion Exchange of $H_2SrTa_2O_7$ and $H_2La_2Ti_3O_{10}$ at Room Temperature using Crystalline $LiOH{\cdot}H_2O$

6.1 Introduction

The mixing of crystalline $LiOH{\cdot}H_2O$ with the layered perovskite $HLaTiO_4$ at room temperature was shown in Chapter 5 to give rise to an ion-exchange reaction, where protons are quantitatively replaced with lithium cations to give the solid-solution series $H_{1-x}Li_xLaTiO_4$. This reaction is driven not by a stoichiometric excess of lithium cations, but instead by the gain in entropy associated with the liberation of water from the lattice of $LiOH{\cdot}H_2O$, and is the first example of Li^+ ion exchange proceeding quantitatively in a Ruddlesden-Popper type layered perovskite.

It is anticipated that this reaction is sufficiently general to allow it to be extended to other protonated layered perovskites. Layered perovskites constitute a class of materials with a wide range of stoichiometries and structure types,[2] and so the facility to carry out Li^+ ion exchange in a quantitative manner could potentially provide access to a huge range of new compositions that are inaccessible *via* existing synthetic routes. Therefore, in order to evaluate such a prospect, this chapter investigates the applicability of the reaction between $LiOH{\cdot}H_2O$ and $HLaTiO_4$ to the higher-order homologues $H_2SrTa_2O_7$ and $H_2La_2Ti_3O_{10}$.

The structure of $H_2SrTa_2O_7$ has been extensively studied by the group of Crosnier-Lopez.[3, 4] They have shown that the perovskite slabs comprising the framework of this material are not regularly offset by ½**a**+½**b**, as is typically observed in the Ruddlesden-Popper family of compounds,[2] but that they can instead be more accurately described by an average of a number of different offsets that are intermediate between eclipsed and staggered arrangements. This variable arrangement between adjacent slabs of perovskite is illustrated schematically in Figure 6.1, and can be evidenced by X-ray powder diffraction, whereby some peaks appear significantly broader than others. These stacking defects have been ascribed to the elasticity of the hydrogen bonds across the interlayer region,[4] and have prevented a conventional and complete structural characterisation of this material. The structure of $H_2La_2Ti_3O_{10}$ has also been investigated,[5] and similarly gives rise to X-ray diffraction data in which some peaks appear significantly broader than others. However, the authors were able to index these data in a tetragonal cell of dimensions a = 3.820(9) Å and c = 27.66(7) Å, from which an interlayer distance of approximately 1.6 Å was estimated.

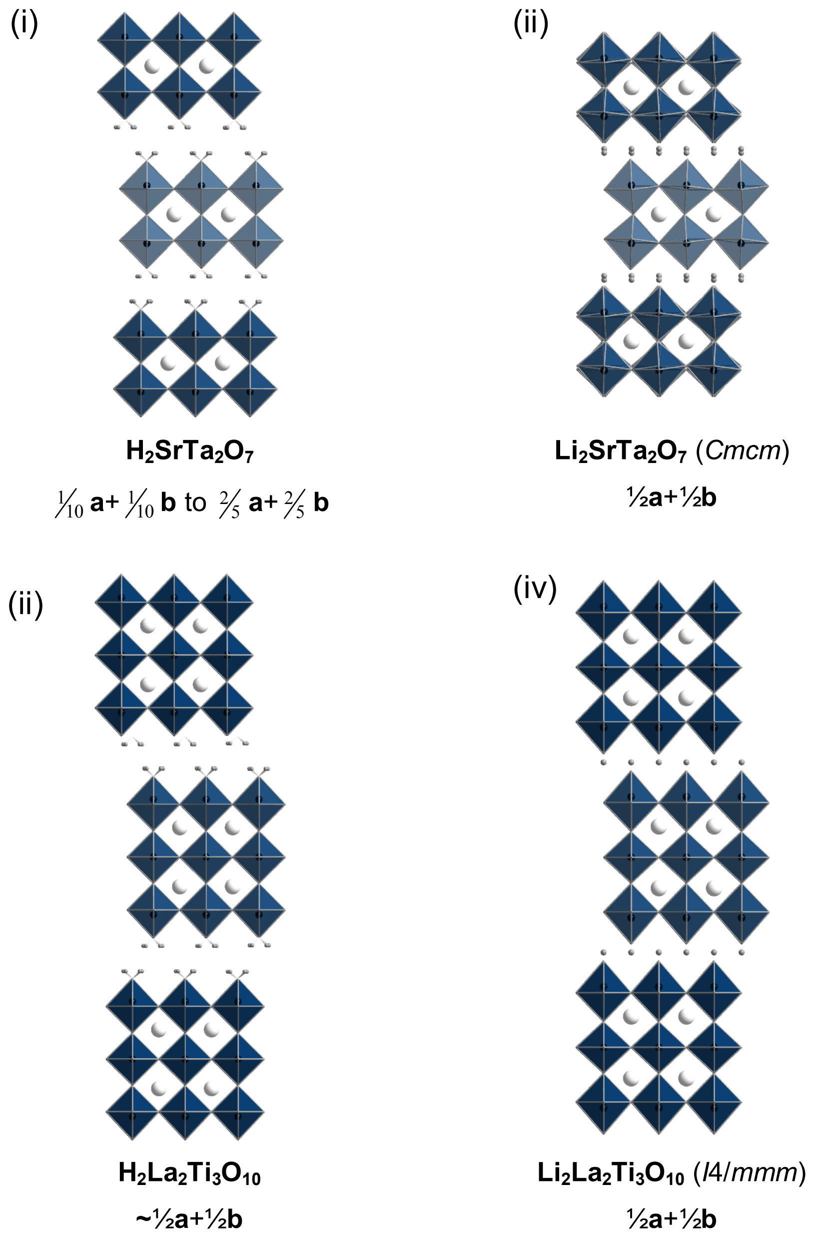

$H_2SrTa_2O_7$
$\frac{1}{10}$**a**+ $\frac{1}{10}$**b** to $\frac{2}{5}$**a**+ $\frac{2}{5}$**b**

$Li_2SrTa_2O_7$ (*Cmcm*)
½a+½b

$H_2La_2Ti_3O_{10}$
~½a+½b

$Li_2La_2Ti_3O_{10}$ (*I*4/*mmm*)
½a+½b

Figure 6.1 Schematic diagrams of the proposed structures of (i) $H_2SrTa_2O_7$ and (ii) $H_2La_2Ti_3O_{10}$, which have been estimated from (i) stacking fault simulations[4] and (ii) the indexing of X-ray powder diffraction data in which some peaks appear significantly broader than others.[5] Additionally shown are the crystal structures of the lithium analogues (iii) $Li_2SrTa_2O_7$[6] and (iv) $Li_2La_2Ti_3O_{10}$.[1] Interlayer and *A*-site cations are represented by grey and white spheres respectively, whilst *B*-site octahedra are indicated by blue units. The lateral offset between adjacent perovskite layers is indicated below each structure.

In contrast to these protonated phases, structural investigations into the lithium-containing analogues have revealed arrangements of perovskite slabs that are significantly more regular, as also illustrated in Figure 6.1, leading to diffraction data that are amenable to full Rietveld analysis. For example, the structures of $Li_2SrTa_2O_7$ and $HLiSrTa_2O_7$ have been determined in the space groups *Cmcm*[6] and *Ama*2[7] respectively, and provide almost equivalent descriptions of the $[SrTa_2O_7]^{2-}$ sublattice, whereby rows of TaO_6 octahedra along each of the cell axes parallel to the perovskite layer exhibit an equal tilt in opposite directions, relative to the non-tilted octahedra in a compound such as $K_2La_{2/3}Ta_2O_7$.[8] This tilting reduces the symmetry of the structure from body-centred to *Cmcm*. However, ordering of the protons and the lithium cations in the structure of $HLiSrTa_2O_7$, induces an additional distortion of the unit cell that is acentric in nature. It should also be noted that the descriptions of these orthorhombic cells differ because the transformation of the space group *Ama*2 to *Cmcm* leads to a change in the relative orientation of the unit cell axes, whereby the orthorhombic super cell transforms from ($a_p\sqrt{2} \times a_p\sqrt{2} \times c$) to ($c \times a_p\sqrt{2} \times a_p\sqrt{2}$), as illustrated in Figure 6.2.

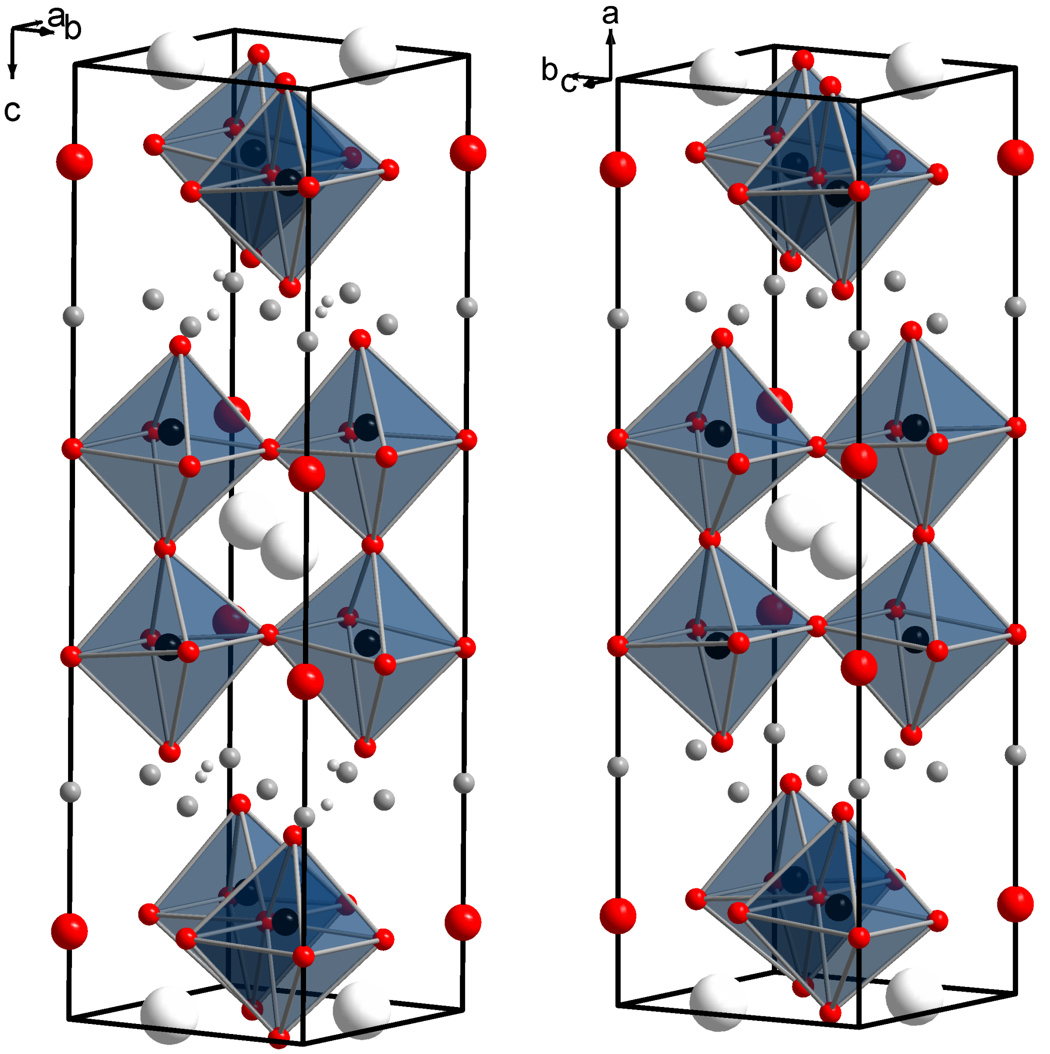

$HLiSrTa_2O_7$

*Ama*2

Orthorhombic super cell: $a_p\sqrt{2} \times a_p\sqrt{2} \times c$

(i)

$Li_2SrTa_2O_7$

Cmcm

Orthorhombic super cell: $c \times a_p\sqrt{2} \times a_p\sqrt{2}$

(ii)

Figure 6.2 Crystal structures of (i) $HLiSrTa_2O_7$[7] and (ii) $Li_2SrTa_2O_7$[6] described in the space groups *Ama*2 and *Cmcm* respectively. Interlayer and *A*-site cations are represented by grey and white spheres respectively, whilst TaO_6 octahedra are indicated by blue units. Note that in the *A*-centred cell the perovskite layers are stacked along the [001] direction, whereas in the *C*-centred cell the perovskite layers are stacked along the [100] direction.

By comparison, only the fully exchanged phase of the triple-layered perovskite, $Li_2La_2Ti_3O_{10}$, has been reported.[1] This structure was characterised by the authors on the basis of X-ray powder diffraction data, and was determined in the archetypal space group *I*4/*mmm*, with lithium located on a special position (0, ½, ¼).

The Li^+ ion exchange of the solid acids $H_2SrTa_2O_7$ and $H_2La_2Ti_3O_{10}$ has been studied by X-ray powder diffraction in order to elucidate changes in the unit cell dimensions that would indicate the exchange of interlayer cations. These materials have also been examined for their thermal stability, to similarly ascertain whether lithium exchange had occurred and to what extent that this could be achieved and controlled. The phases that can be modified as a result of dehydration presumably contain a mixture of lithium cations and vacant sites. In order to evaluate their potential as fast-ion conductors, the transport properties of these defective phases have been analysed by AC impedance spectroscopy.

6.2 Experimental

The layered perovskites $Li_2SrTa_2O_7$ and $K_2La_2Ti_3O_{10}$ were prepared by conventional ceramic methods using suitable mixtures of metal carbonates [Li_2CO_3 (0.6425 g, 8.695 mmol), K_2CO_3 (1.382 g, 10.00 mmol) and $SrCO_3$ (1.284 g, 8.695 mmol)] and metal oxides [La_2O_3 (3.258 g, 10.00 mmol), Ta_2O_5 (3.843 g, 8.695 mmol) and Ti_2O_3 (2.156 g, 10.00 mmol)]. A 10 wt. % excess of lithium carbonate and a 30 wt. % excess of potassium carbonate were added to the reagent mixtures in order to compensate for the volatilisation of these components at high temperature. In the case of $Li_2SrTa_2O_7$, these reagents were heated in a furnace from room temperature to 500 °C at 1 °C min^{-1}, where they were held for 6 hr. This sample was then subjected to two additional firings at 1250 °C for 12 hr, *via* a 2.5 °C min^{-1} ramp from room temperature. The preparation of the potassium precursor was carried out in a similar manner, and involved two direct firings: the first was carried out at 600 °C for 12 hr, and the second at 1100 °C for 6 hr. As a precautionary step, the high-temperature sample was subsequently washed with up to 350 mL of water in order to remove any potassium carbonate that may have formed as a result of post-synthetic reaction of potassium oxide with atmospheric carbon dioxide.

The solid acids $H_2SrTa_2O_7$ and $H_2La_2Ti_3O_{10}$ were prepared by suspending $Li_2SrTa_2O_7$ and $K_2La_2Ti_3O_{10}\cdot xH_2O$ ($x \sim 2$), respectively, in nitric acid. In the case of $Li_2SrTa_2O_7$, 4.800 g (8.342 mmol) of this material was stirred in 480 mL of nitric acid (*ca.* 2 mol dm^{-3}, H^+ in 58-fold excess) at 60 °C for 5 d. The exchanged product was then washed with 200 mL of water and recovered by vacuum filtration. The washed product was allowed to dry at room temperature in air. By contrast, $K_2La_2Ti_3O_{10}$ has been reported to spontaneously hydrate under ambient conditions to give $K_2La_2Ti_3O_{10}\cdot xH_2O$, where $x \sim 2$.[1] Therefore, both the washing of $K_2La_2Ti_3O_{10}$ and the introduction of this material to dilute acid will lead to the formation of the hydrated phase. In order to minimise the damage anticipated from repeated hydration and dehydration of the $K_2La_2Ti_3O_{10}$ structure, the high-temperature sample was washed, and the resulting hydrated phase $K_2La_2Ti_3O_{10}\cdot xH_2O$ ($x \sim 2$) used towards the preparation of the solid acid. Therefore, 2.000 g (2.875 mmol) of $K_2La_2Ti_3O_{10}\cdot xH_2O$ ($x \sim 2$) was stirred in 200 mL of nitric acid (*ca.* 0.1 mol dm^{-3}, H^+ in 3.4-fold excess) at 60 °C for 2 d, followed by an additional day at room temperature without stirring in order to allow the exchanged product to settle. The aqueous solution was then decanted, and the exchanged product washed with water and recovered by centrifugation. The washed product was dried at 200 °C in air for 4 hr.

The replacement of protons with lithium cations in both $H_2SrTa_2O_7$ and $H_2La_2Ti_3O_{10}$ was carried out by grinding these solids with stoichiometric quantities of $LiOH\cdot H_2O$ under ambient conditions. The reagents (0.1 - 1 g) were ground together for 30 min using a pestle and mortar. The resulting sample was then left to stand in an open-top vial in ambient atmosphere for the reaction to complete. The structures of the protonated and lithium-exchanged phases were analysed by X-ray powder diffraction using a Siemens 500 diffractometer in Bragg-Brentano geometry.

The thermal stabilities of $H_2SrTa_2O_7$, $H_2La_2Ti_3O_{10}$ and the lithium-exchanged samples were evaluated using a Perkin Elmer TGA 7 thermal gravimetric analyser. These measurements were carried out under a dynamic atmosphere of dry helium, whereby approximately 30 mg of sample was equilibrated at 40 °C for 5 min before being heated to temperatures of up to 900 °C. Additional experiments involving both the protonated and the lithium-exchanged phases being heated in air and then analysed by X-ray powder diffraction were also employed; these experiments were used to correlate the losses in mass to changes in structure.

The transport properties of the 1:1 lithium-exchanged samples were assessed by AC impedance spectroscopy using a Solartron SI 1260 frequency response analyser. These experiments were carried out by pressing approximately 0.2 g of the as made lithium-exchanged sample under a load of 3 tonnes to give a 10 mm diameter cylindrical pellet approximately 0.7 mm thick. This pellet was attached to two platinum electrodes and heated from room temperature to temperatures of up to 650 °C in air. AC impedance data were collected from this pellet over the range $0.2 \leq f \leq 10^6$ Hz on heating over this temperature range.

6.3 Results

6.3.1 Reaction between $H_2SrTa_2O_7$ and $LiOH \cdot H_2O$

X-ray powder diffraction data collected from a sample of $H_2SrTa_2O_7$ 5 d after grinding with one equivalent of $LiOH \cdot H_2O$ showed that a number of the sharp peaks arising from $H_2SrTa_2O_7$ appear to have undergone significant shifts in angle, as illustrated in Figure 6.3. This is accompanied by the disappearance of a number of broad peaks in the range 25-40° 2θ, such that the diffraction pattern could be fully indexed using an orthorhombic cell (a = 5.537(2) Å, b = 5.549(2) Å, c = 18.7607(13) Å) that is of similar dimensions to that reported for $HLiSrTa_2O_7$.[7]

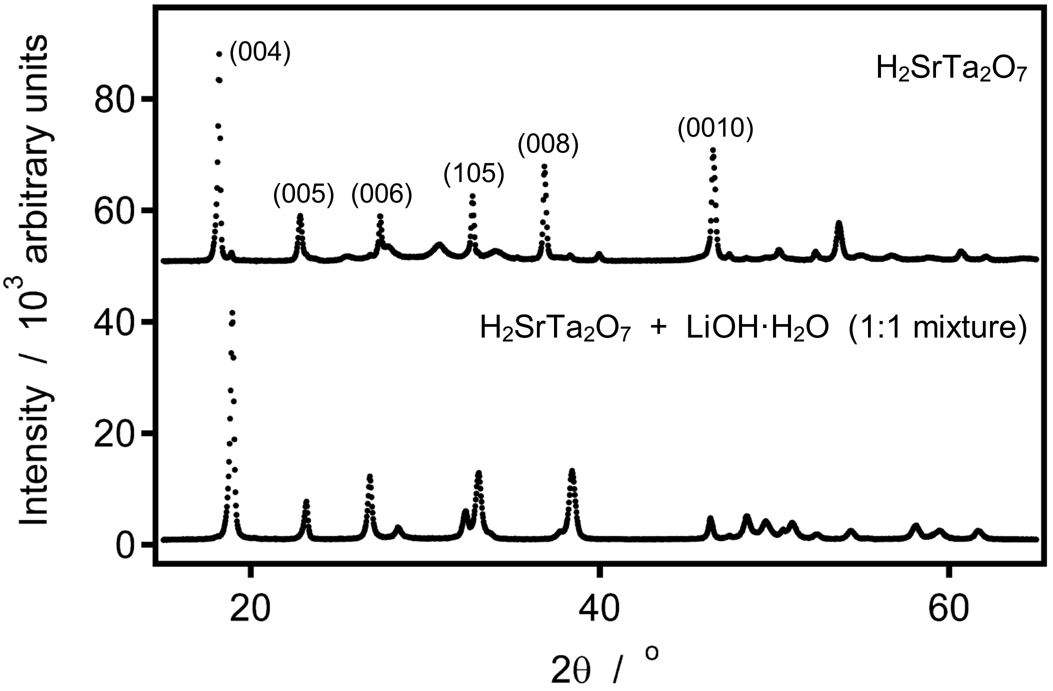

Figure 6.3 Observed X-ray diffraction patterns collected from a sample of (i) $H_2SrTa_2O_7$ starting material and (ii) $H_2SrTa_2O_7$ ground with one equivalent of $LiOH \cdot H_2O$ after 5 d.

This diffraction pattern could be fitted using a structural model based on the $[SrTa_2O_7]^{2-}$ host lattice of $HLiSrTa_2O_7$, as described in the space group *Ama*2,[7] with a total of 18 parameters refined, including background terms, a histogram scale factor, a preferred orientation parameter, a diffractometer zero point error, lattice parameters and profile coefficients. A trial refinement that allowed the atomic parameters to vary would converge only when the refinement of the atom positions was dampened and did not significantly improve the quality of the fit. The refinement subsequently became unstable when these dampening terms were removed, and so the final refinement used both the atomic coordinates reported for $HLiSrTa_2O_7$ and isotropic atomic displacement parameters that were fixed at a physically reasonable value of 0.012 Å^2 for all atoms. The final fit obtained to this diffraction pattern is shown in Figure 6.4.

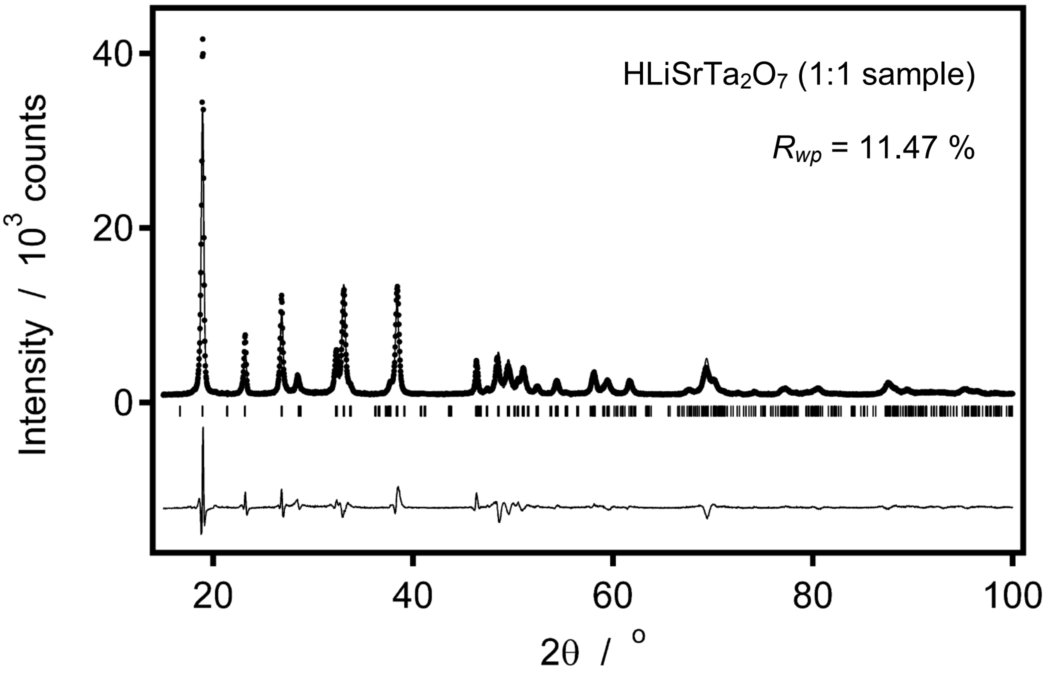

Figure 6.4 Observed (dots), calculated (top line) and difference (bottom line) X-ray powder diffraction patterns for the 1:1 sample. The vertical bars indicate the allowed Bragg reflection positions for $HLiSrTa_2O_7$. Data collected at angles below 15° 2θ were excluded from the refinement due to systematic experimental problems in the peak shape and intensity.

By contrast, X-ray powder diffraction data collected from the sample of $H_2SrTa_2O_7$ at room temperature could not be fully indexed, as similarly encountered by Crosnier-Lopez *et al.*[4] However, on the basis of the sharpest and most intense peaks in the range $5 \leq 2\theta \leq 50°$, this diffraction pattern could be partially indexed using a tetragonal cell of dimensions $a = 3.84$ Å and $c = 19.48$ Å. This indicates that grinding $H_2SrTa_2O_7$ with $LiOH \cdot H_2O$ leads to a significant contraction along the stacking direction of the layered perovskite structure. The mass of the ground sample was also recorded after 5 d, which indicated a loss in mass of *ca.* 5.2 wt. % that is commensurate with the loss of 1.7 moles of water per formula unit. This loss in mass together with the contraction of the c lattice parameter suggests that reaction (6.1) had occurred.

$$H_2SrTa_2O_7 + LiOH \cdot H_2O \rightarrow HLiSrTa_2O_7 + 2H_2O \qquad (6.1)$$

In an attempt to prepare the fully exchanged compound $Li_2SrTa_2O_7$, a sample of $H_2SrTa_2O_7$ was also ground with two equivalents of $LiOH \cdot H_2O$. X-ray powder diffraction data were collected from this mixture 5 d later, and could be fitted in a similar manner to the 1:1 data set, as shown in Figure 6.5. This refinement indicated the presence of an orthorhombic cell ($a = 5.536(3)$ Å, $b = 5.546(3)$ Å, $c = 18.7686(13)$ Å) that is, at the 3 esd level, indistinguishable from that of $HLiSrTa_2O_7$ prepared using a 1:1 mixture of reagents, suggesting that reaction (6.2) had occurred instead.

$$H_2SrTa_2O_7 + 2LiOH \cdot H_2O \rightarrow HLiSrTa_2O_7 + LiOH \cdot H_2O + 2H_2O \qquad (6.2)$$

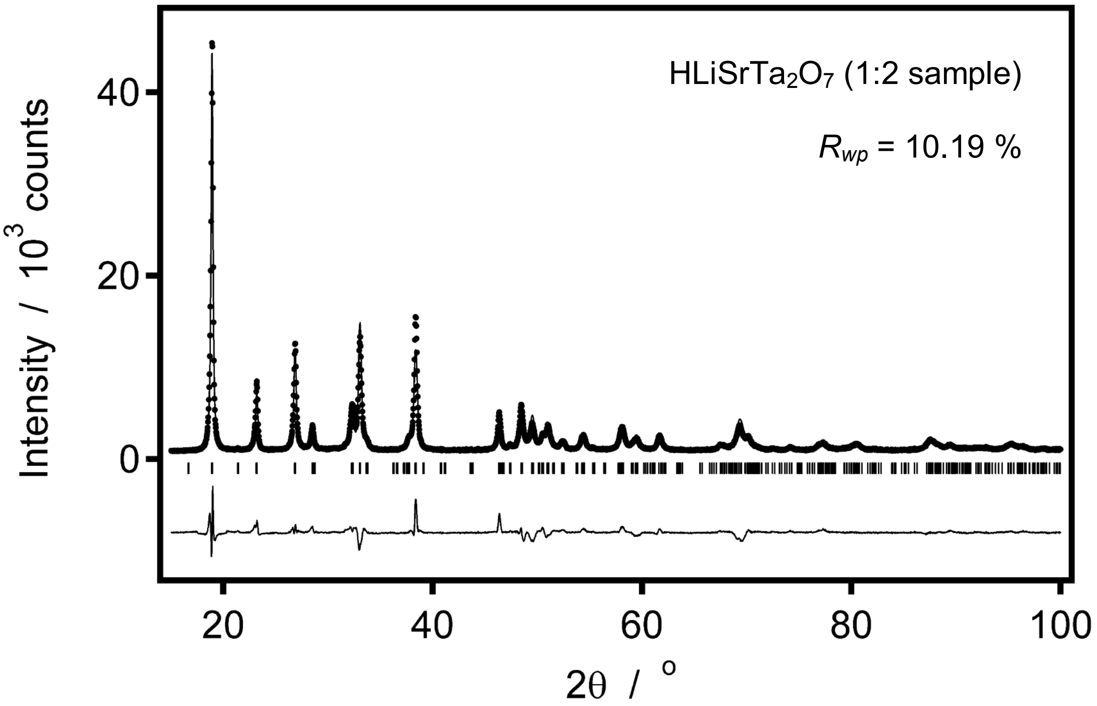

Figure 6.5 Observed (dots), calculated (top line) and difference (bottom line) X-ray powder diffraction patterns for the 1:2 sample. The vertical bars indicate the allowed Bragg reflection positions for $HLiSrTa_2O_7$.

For comparison, the reaction between $H_2SrTa_2O_7$ and half an equivalent of $LiOH{\cdot}H_2O$ was also carried out. X-ray powder diffraction data were collected from this sample 12 d later, and showed an approximately 1:1 mixture of the $H_2SrTa_2O_7$ starting material and the $HLiSrTa_2O_7$ exchanged product, as illustrated in Figure 6.6, suggesting that reaction (6.3) had occurred.

$$H_2SrTa_2O_7 + \tfrac{1}{2}LiOH{\cdot}H_2O \rightarrow \tfrac{1}{2}HLiSrTa_2O_7 + \tfrac{1}{2}H_2SrTa_2O_7 + H_2O \qquad (6.3)$$

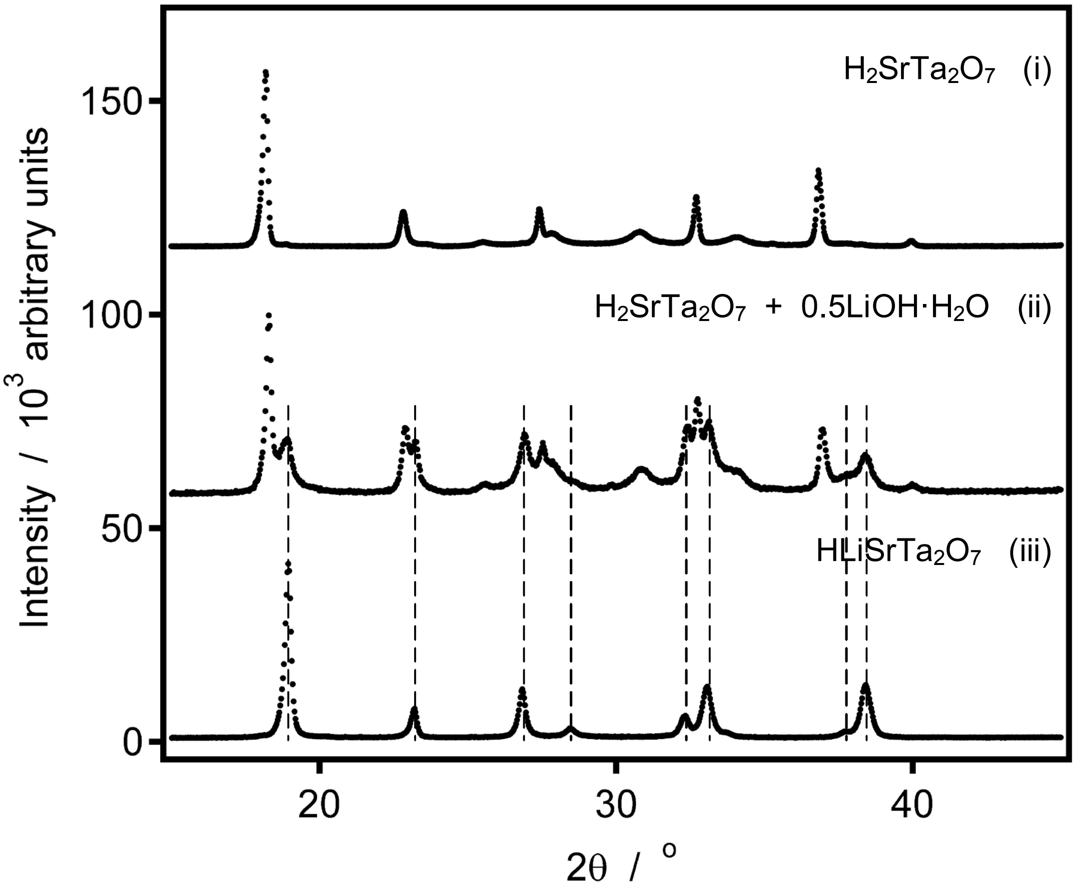

Figure 6.6 (ii) Observed X-ray powder diffraction pattern collected from a sample of $H_2SrTa_2O_7$ 12 d after it had been ground with half an equivalent of LiOH·H_2O. Diffraction patterns for (i) the $H_2SrTa_2O_7$ starting material and (iii) the $HLiSrTa_2O_7$ exchanged product are also shown for comparison.

These trial reactions suggest that the $[SrTa_2O_7]^{2-}$ host lattice can only be stabilised by a mixture of protons and lithium cations when they are present in equimolar quantities. However, it was noted that some of the 1:2 samples also gave rise to a number of low intensity peaks that could be indexed as (00*l*) reflections using the smaller orthorhombic cell of $Li_2SrTa_2O_7$.[6] X-ray powder diffraction data were collected from such a sample after it had been left in ambient atmosphere for a further 5 d, and showed that the intensities of the peaks arising from $Li_2SrTa_2O_7$ had significantly increased, as illustrated in Figure 6.7. Therefore, in an attempt to form a monophasic sample of $Li_2SrTa_2O_7$, this mixture was heated at 120 °C in air for a total of 8 d. The resulting sample gave rise to diffraction data that could be fully indexed using the orthorhombic cell of $Li_2SrTa_2O_7$, suggesting that $HLiSrTa_2O_7$ had undergone ion exchange with the remainder of the lithium in the sample. These diffraction data could be fitted using the structural model reported for $Li_2SrTa_2O_7$ in the space group *Cmcm*,[6] as illustrated in Figure 6.8. The atom positions described by this model could not be refined against the observed data, as similarly encountered

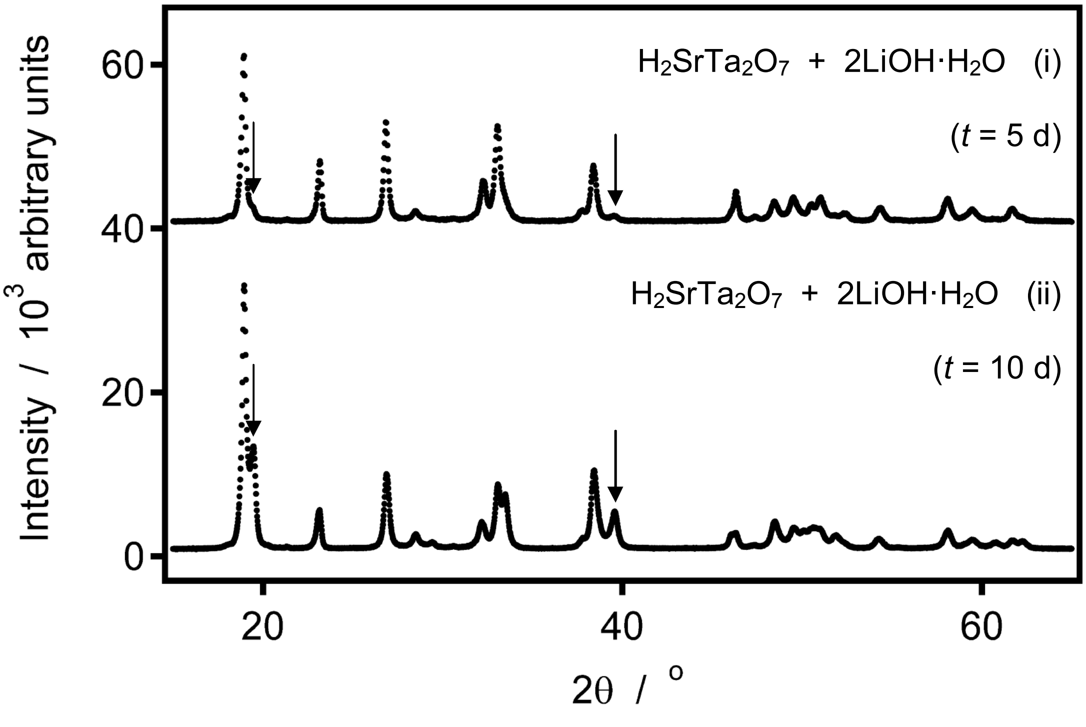

Figure 6.7 Observed X-ray powder diffraction patterns collected from a 1:2 mixture of $H_2SrTa_2O_7$ and $LiOH{\cdot}H_2O$ (i) 5 d and (ii) 10 d after the reagents were ground together. A minority phase of the fully exchanged compound $Li_2SrTa_2O_7$ is indicated by peaks labelled with an arrow.

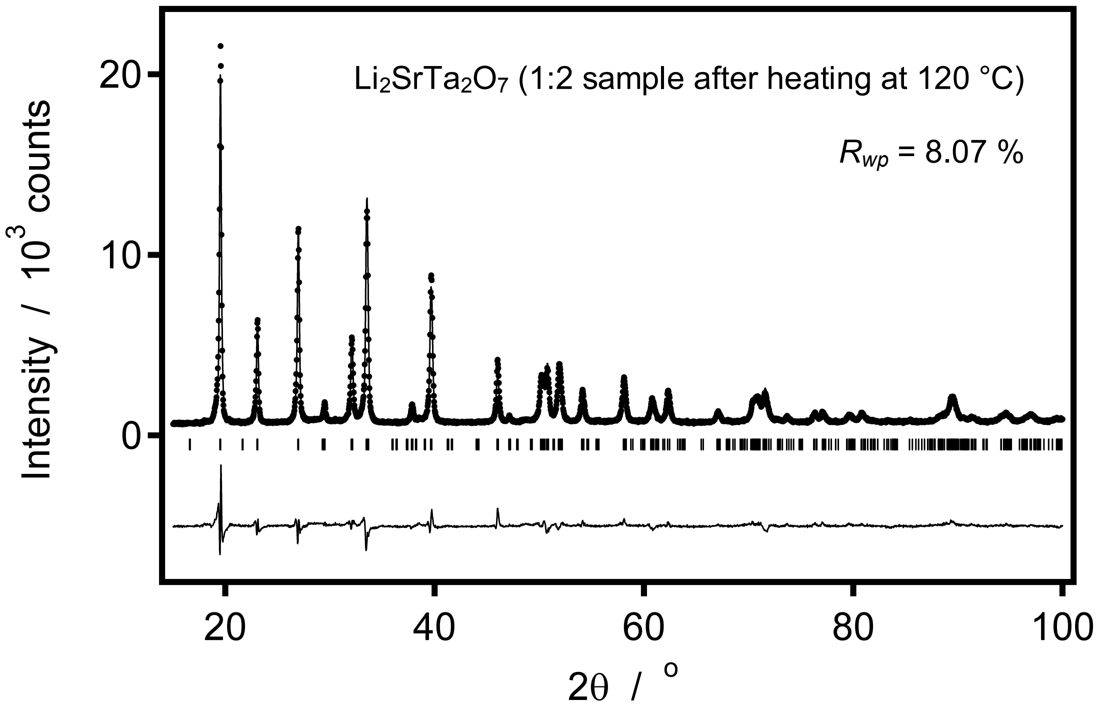

Figure 6.8 Observed (dots), calculated (top line) and difference (bottom line) X-ray powder diffraction patterns for a 1:2 sample after heat treatment at 120 °C in air for a total of 8 d. The vertical bars indicate the allowed Bragg reflection positions for $Li_2SrTa_2O_7$.

when the $[SrTa_2O_7]^{2-}$ model was fitted against the 1:1 data set, but nevertheless provide a reasonable fit to the observed data. Consequently, the atomic coordinates were constrained at the literature values, with the atomic displacement parameters modelled isotropically and fixed at a value of 0.012 Å^2 for all atoms.

In order to provide additional evidence with which to support the reaction schemes proposed, the thermal stabilities of the protonated and lithium-exchanged samples were evaluated. It has previously been shown by Bhuvanesh *et al.* that heating $H_2SrTa_2O_7$ in the temperature range 350-700 °C results in topochemical dehydration of this material to give a defective three-dimensional perovskite, $Sr_{0.5}TaO_3$,[3] as described by reaction (6.4).

$$H_2SrTa_2O_7 \rightarrow 2Sr_{0.5}TaO_3 + H_2O \qquad (6.4)$$

Therefore, a sample of $H_2SrTa_2O_7$ was heated at 360 °C in air for 2 d. X-ray powder diffraction data collected from the resulting sample could be largely indexed using a tetragonal cell (a = 3.925(2) Å and c = 3.983(2) Å) of similar dimensions to that reported for $Sr_{0.5}TaO_3$, as illustrated in Figure 6.9. The broad peak at approximately 10° 2θ can be indexed by doubling the c lattice parameter, which suggests that a small quantity of the perovskite with strontium site ordering is still present, as also reported by Bhuvanesh *et al.* The mass of $H_2SrTa_2O_7$ was also monitored during this transformation; thermogravimetric data were collected on heating a sample of

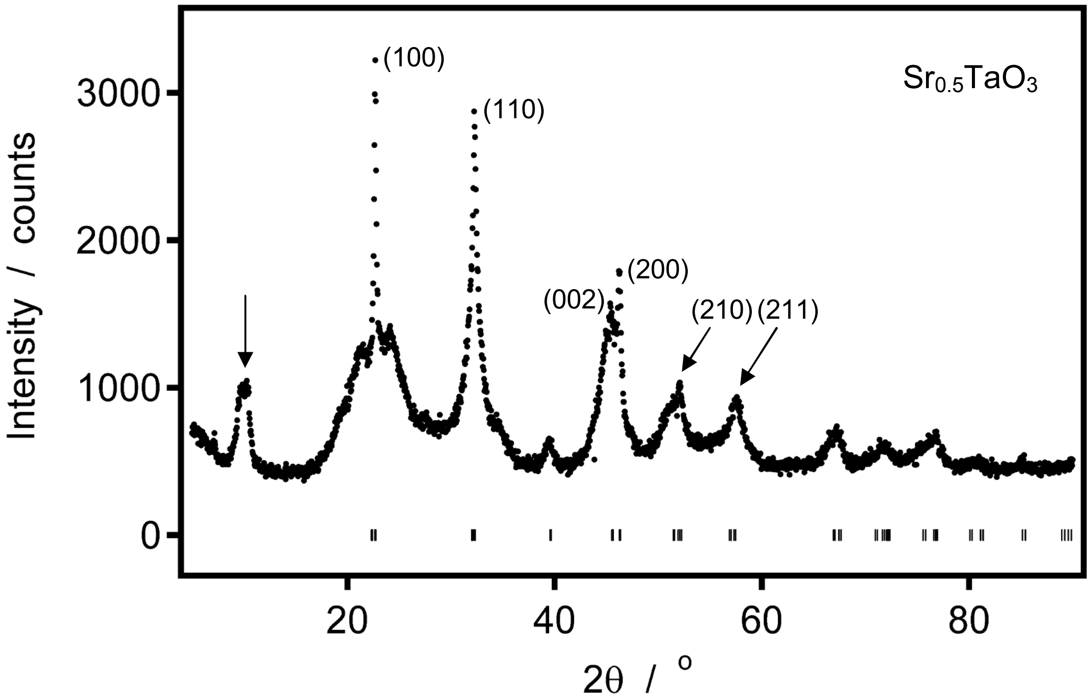

Figure 6.9 Observed X-ray powder diffraction pattern collected from a sample of $H_2SrTa_2O_7$ following heat treatment at 360 °C in air for 2 d. The vertical bars indicate the allowed Bragg reflection positions for a tetragonal unit cell of dimensions a = 3.925(2) Å and c = 3.983(2). A broad peak indicative of a doubling of the c lattice parameter is marked with an arrow.

$H_2SrTa_2O_7$ at 360 °C under a dynamic atmosphere of dry helium for 2 d, *via* a 10 °C min^{-1} ramp from room temperature, and showed a loss in mass of 2.8 wt. %, as illustrated in Figure 6.10. This mass loss is commensurate with the evaporation of 0.87 moles of water per formula unit, which accounts for the majority of the water produced by reaction (6.4). Additional thermogravimetric data were collected on heating a sample of $H_2SrTa_2O_7$ from room temperature up to 800 °C at 10 °C min^{-1}, under a dynamic atmosphere of dry helium. This experiment was repeated for a number of separately prepared samples of $H_2SrTa_2O_7$, and, in all cases, indicated a complex mass loss ranging from 3.9 wt. % to 6.8 wt. %, as illustrated in Figure 6.11. This mass loss both varies from sample-to-sample, and is in excess of that anticipated from reaction (6.4). However, all the samples of $H_2SrTa_2O_7$ gave rise to identical looking diffraction patterns. Therefore, although the mass loss recorded on holding a sample of $H_2SrTa_2O_7$ at 360 °C is in agreement with reaction (6.4), this reaction is not compatible with data recorded over a broad temperature range. This prevents the interpretation of thermogravimetric data collected from the lithium-exchanged samples, which show a more complex mass loss.

By comparison, the heat treatment of the 1:1 sample at 360 °C in air for 2 d led to X-ray diffraction data that could be indexed instead using a combination of an orthorhombic cell (a = 18.327(2) Å, b = 5.5562(6) Å and c = 5.5659(7) Å) and a tetragonal cell (a = 3.9321(3) Å and c = 3.9188(7) Å), as illustrated by the LeBail fit in Figure 6.12(i). The indexing of the orthorhombic cell was performed in the same

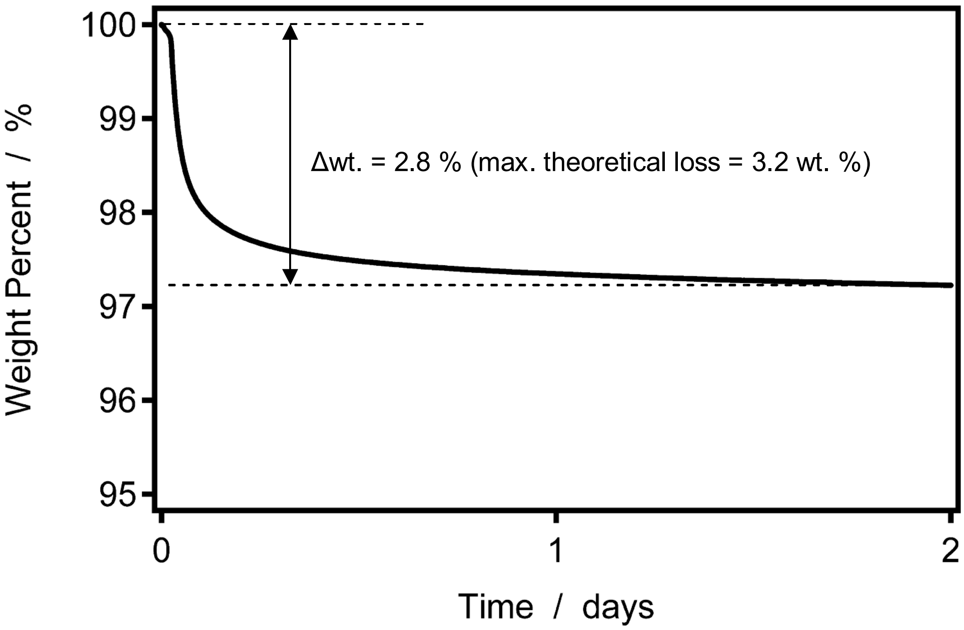

Figure 6.10 Thermogravimetric data collected on heating a sample of $H_2SrTa_2O_7$ at 360 °C under a dynamic atmosphere of dry helium for 2 d, *via* a 10 °C min^{-1} ramp from room temperature. The maximum loss in mass anticipated from the topochemical dehydration of $H_2SrTa_2O_7$ is 3.2 wt. %.

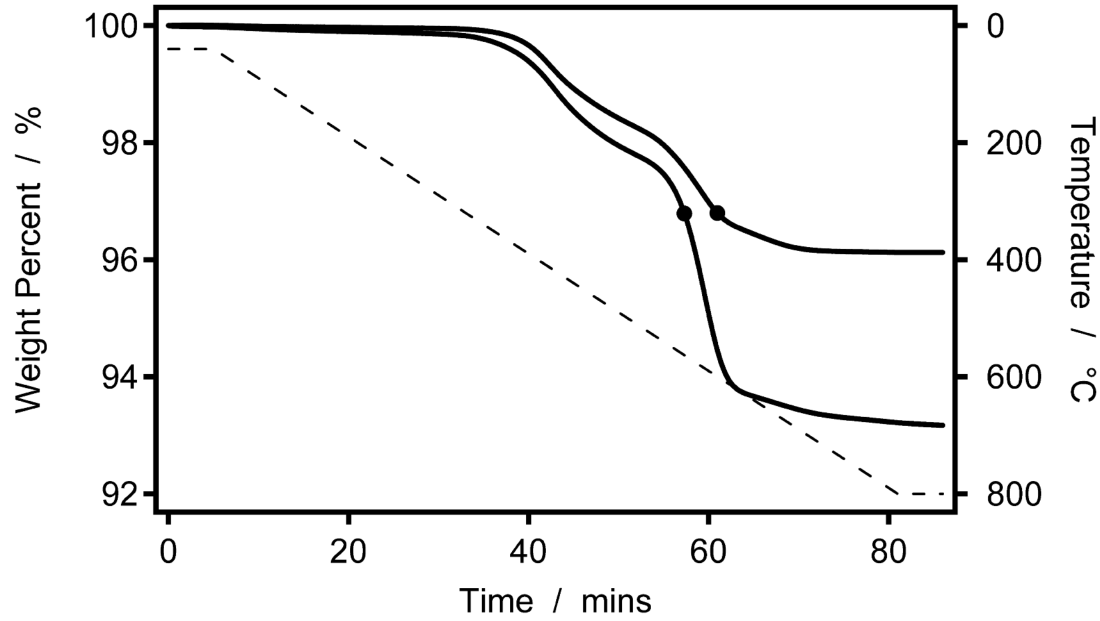

Figure 6.11 Thermogravimetric data (solid lines) collected on heating samples of $H_2SrTa_2O_7$ from room temperature up to 800 °C at 10 °C min^{-1}, under a dynamic atmosphere of dry helium. The circles indicate the maximum loss in mass anticipated from each sample, *i.e.* 3.2 wt. %, which is commensurate with the loss of one mole of water per formula unit. The temperature is indicated by a dashed line.

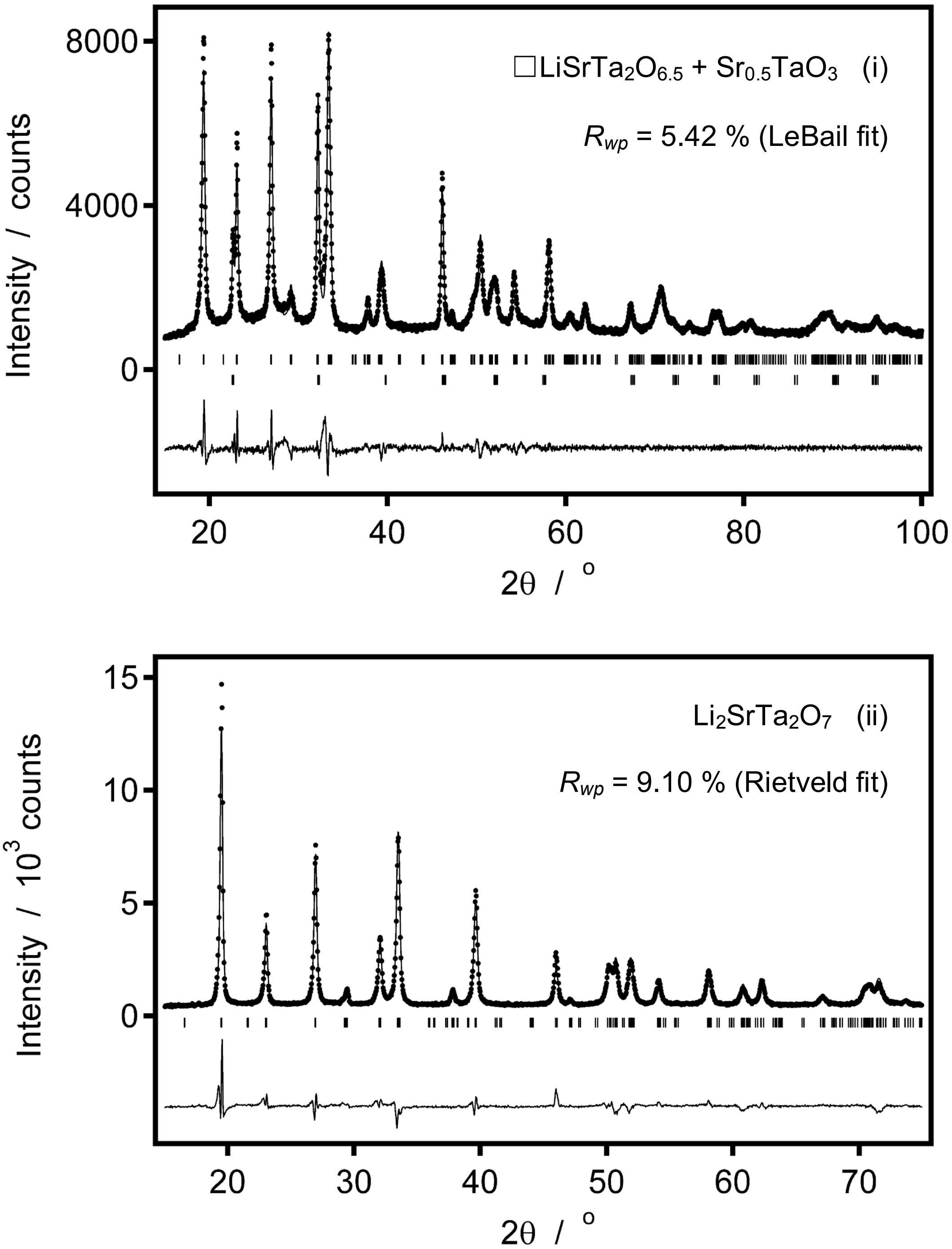

Figure 6.12 Observed (dots), calculated (top line) and difference (bottom line) X-ray powder diffraction patterns for (i) a 1:1 sample and (ii) a 1:2 sample after heat treatment at 360 °C. The vertical bars indicate the allowed Bragg reflection positions for an orthorhombic cell in the space group *Cmcm*, whilst a lower set indicates those allowed for a tetragonal cell in the space group *I*4/*mmm*.

space group, *Cmcm*, as used to describe the structure of $Li_2SrTa_2O_7$, rather than that of *Ama*2, which is used to describe the structure of the $HLiSrTa_2O_7$ parent phase. These models provide an almost equivalent description of the $[SrTa_2O_7]^{2-}$ sublattice. However, by using neutrons instead of X-rays, an acentric distortion of the $HLiSrTa_2O_7$ structure becomes apparent, as determined by Galven *et al.*[7] The authors suggest that this distortion is driven by the ordering of the deuterium and lithium cations. Therefore, although these diffraction data are from X-rays, which are poorly scattered by these elements, the choice of the space group *Cmcm* over *Ama*2 is based on the anticipated absence of protons. In addition, the descriptions of these orthorhombic cells differ because the transformation of *Ama*2 to *Cmcm* leads to a reorientation of the unit cell axes, whereby the super cell transforms from ($a_p\sqrt{2} \times a_p\sqrt{2} \times c$) to ($c \times a_p\sqrt{2} \times a_p\sqrt{2}$). Therefore, the LeBail fit indicated the presence of an orthorhombic cell with an a parameter (18.327(2) Å) that is equivalent to, and significantly shorter than, the c parameter (18.7607(13) Å) derived from the $HLiSrTa_2O_7$ parent compound. The tetragonal cell that is additionally indexed is of similar dimensions to that of the defective perovskite $Sr_{0.5}TaO_3$. These observations suggest that on heating the 1:1 sample at 360 °C, $HLiSrTa_2O_7$ undergoes topochemical dehydration to give a mixture of the defective compounds $\square LiSrTa_2O_{6.5}$ and $Sr_{0.5}TaO_3$, as described by reaction (6.5).

$$HLiSrTa_2O_7 \rightarrow (1\text{-}x)\square LiSrTa_2O_{6.5} + (\tfrac{x}{2})\,Li_2O + (2x)Sr_{0.5}TaO_3 + \tfrac{1}{2}H_2O \quad (6.5)$$

In contrast to the dehydration behaviour of $HLiSrTa_2O_7$, the heat treatment of the 1:2 sample under the same conditions led to X-ray diffraction data which could be fully indexed using the orthorhombic cell of $Li_2SrTa_2O_7$. This suggests that the remainder of the protons in the $HLiSrTa_2O_7$ lattice can be replaced with lithium cations when heated at temperatures as low as 120 °C. Additionally, diffraction data collected from the sample heated at 360 °C could be fitted using the structural model of $Li_2SrTa_2O_7$, in a similar manner to data collected from the sample heated at 120 °C, as illustrated in Figure 6.12(ii). The cell and fit parameters derived from each of the lithium-exchanged phases studied, both as made and after heat treatment at 360 °C, are summarised in Tables 6.1 and 6.2, whilst the changes in the lattice parameters are illustrated in Figure 6.13.

Table 6.1 Cell parameters for the $H_{2-2x}Li_{2x}SrTa_2O_7$ series of compounds derived from least-squares refinement against X-ray powder diffraction data

Compound	Space group	*a* / Å	*b* / Å	*c* / Å	V / Å^3
$HLiSr_2Ta_2O_7$ (1:1 sample)	*Ama*2	5.537(2)	5.549(2)	18.7607(13)	576.46(11)
□$LiSr_2Ta_2O_{6.5}$ $^{*\#}$	*Cmcm*	18.327(2)	5.5562(6)	5.5659(7)	566.77(10)
$HLiSr_2Ta_2O_7$ (2:1 sample)	*Ama*2	5.536(3)	5.546(3)	18.7686(13)	576.27(11)
$Li_2Sr_2Ta_2O_7$ $^{\neq}$	*Cmcm*	18.1744(8)	5.581(2)	5.575(2)	565.52(7)
$Li_2Sr_2Ta_2O_7$ $^{\#}$	*Cmcm*	18.1744(14)	5.581(2)	5.571(2)	565.02(11)

* LeBail fit
$^{\neq}$ heat treated at 120 °C in air for a total of 8 d
$^{\#}$ heat treated at 360 °C in air for 2 d

Table 6.2 Fit and preferred orientation parameters for the $H_{2-2x}Li_{2x}SrTa_2O_7$ series of compounds derived from least-squares refinement against X-ray powder diffraction data

Compound	R_{wp} / %	χ^2	Variables	P.O.$^{¥}$
$HLiSr_2Ta_2O_7$ (1:1 sample)	11.47	22.02	11	0.6110(14)
□$LiSr_2Ta_2O_{6.5}$ $^{*\#}$	5.42	3.973	10	n/a
$HLiSr_2Ta_2O_7$ (2:1 sample)	10.19	17.98	18	0.6070(13)
$Li_2Sr_2Ta_2O_7$ $^{\neq}$	8.07	7.704	12	0.6840(13)
$Li_2Sr_2Ta_2O_7$ $^{\#}$	9.10	7.472	12	0.683(2)

* LeBail fit
$^{\neq}$ heat treated at 120 °C in air for a total of 8 d
$^{\#}$ heat treated at 360 °C in air for 2 d
$^{¥}$ preferred orientation modelled along the stacking direction using the March-Dollase model

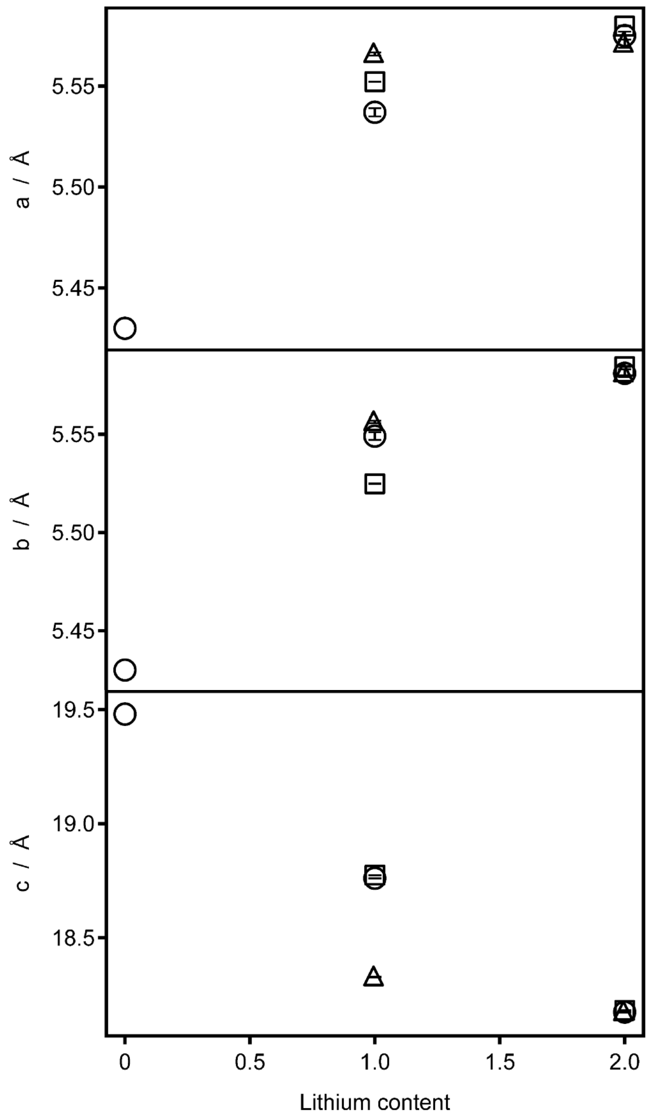

Figure 6.13 Lattice parameters of $H_2SrTa_2O_7$* and those of the lithium-exchanged samples $HLiSrTa_2O_7$ and $Li_2SrTa_2O_7$ (circles) derived from least-squares refinement against X-ray powder diffraction data. Additionally shown are data collected from the lithium-exchanged samples after heat treatment at 360 °C (triangles), and literature values (squares) for $HLiSrTa_2O_7$[7] and $Li_2SrTa_2O_7$[6]. Lattice parameters derived from fits in the space group *Cmcm* were reoriented from ($c \times a_p\sqrt{2} \times a_p\sqrt{2}$) to ($a_p\sqrt{2} \times a_p\sqrt{2} \times c$) for ease of comparison. * Lattice parameters derived from partial indexing using a tetragonal cell of dimensions $a = 3.84$ Å and $c = 19.48$ Å; the a parameter has been multiplied by $\sqrt{2}$ for ease of comparison.

6.3.2 Reaction between $H_2La_2Ti_3O_{10}$ and $LiOH\cdot H_2O$

X-ray powder diffraction data collected from a sample of $H_2La_2Ti_3O_{10}$ 1 d after it had been ground with two equivalents of $LiOH\cdot H_2O$ also showed peaks that appear to have undergone significant shifts in angle, as well as peaks that appear considerably narrower, as illustrated in Figure 6.14. These diffraction data could be indexed on the basis of a tetragonal cell (a = 3.8367(3) Å and c = 25.538(3) Å), which is of similar dimensions to that reported for $Li_2La_2Ti_3O_{10}$,[1] and a few additional weak Bragg peaks, which correspond to an unidentified impurity phase that was formed at high temperature. Therefore, a trial refinement was carried out

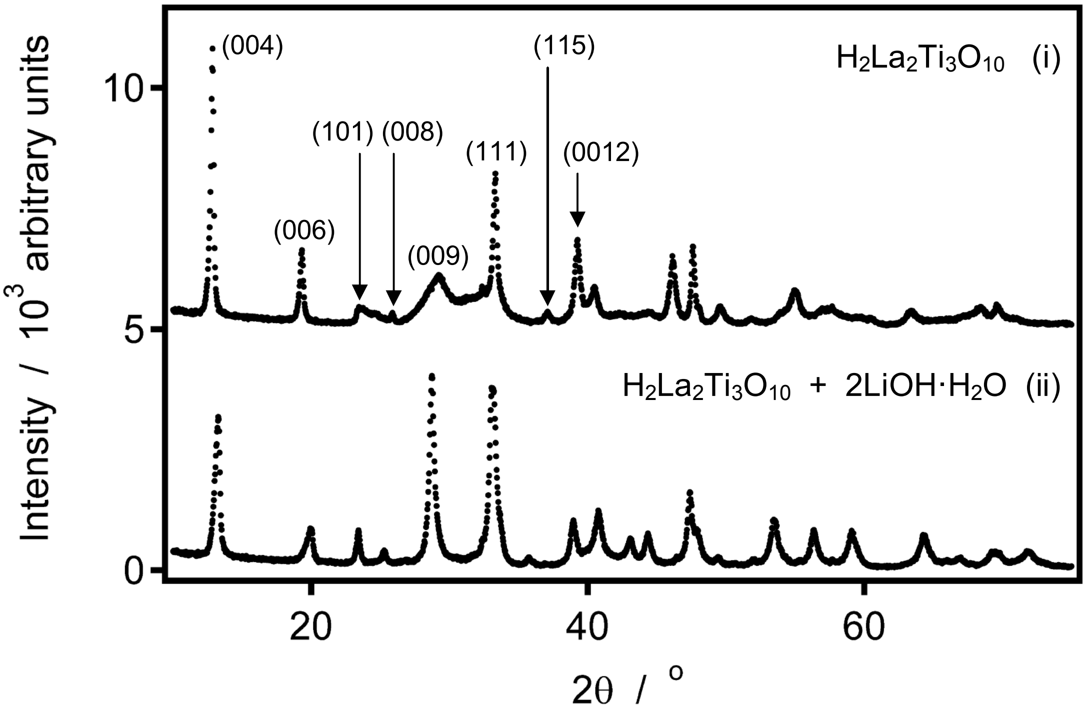

Figure 6.14 Observed X-ray powder diffraction pattern collected from a sample of (i) $H_2La_2Ti_3O_{10}$ starting material and (ii) $H_2La_2Ti_3O_{10}$ ground with two equivalents of $LiOH\cdot H_2O$ after 5 d.

using the structural model reported for $Li_2La_2Ti_3O_{10}$, as described in the space group *I*4/*mmm*. The atom positions within this model were allowed to vary, whilst the atomic displacement parameters for all non-lithium atoms were modelled isotropically and constrained to be equal for like elements. Additionally, a correction for preferred orientation along the stacking direction was applied. The final refinement provided a reasonable fit to the observed data, as illustrated in Figure 6.15, suggesting that the protons in the $H_2La_2Ti_3O_{10}$ lattice had been replaced with lithium cations. By comparison, X-ray powder diffraction data collected from the parent compound, $H_2La_2Ti_3O_{10}$, showed some peaks that were considerably

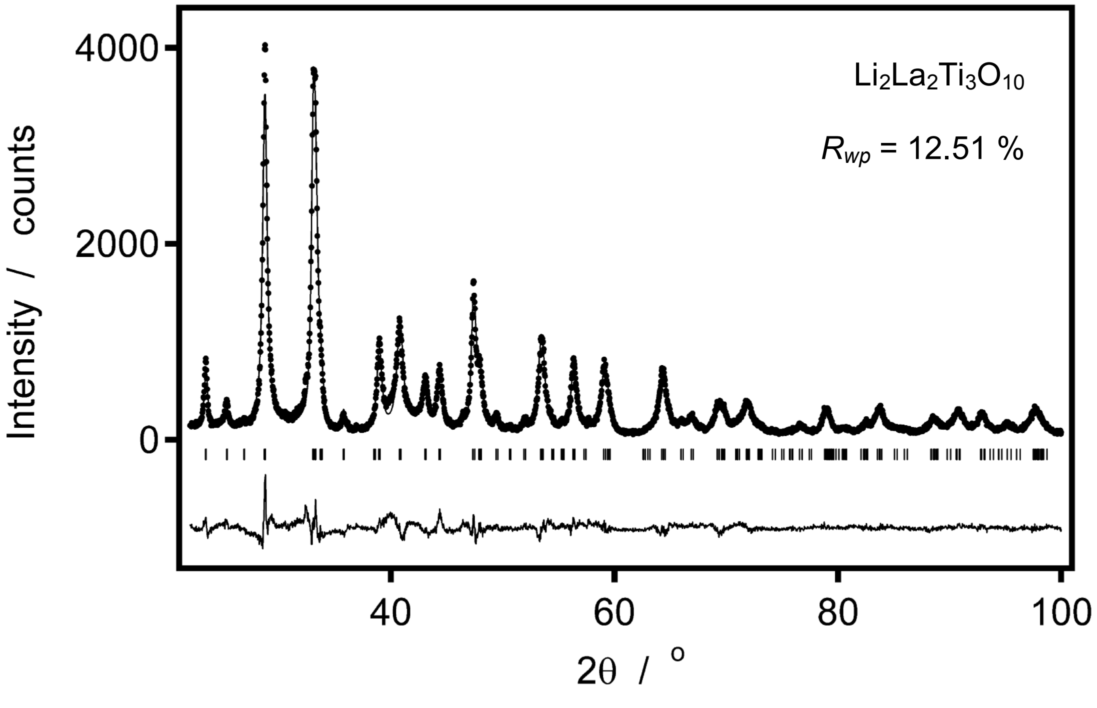

Figure 6.15 Observed (dots), calculated (top line) and difference (bottom line) X-ray powder diffraction patterns for a sample of $H_2La_2Ti_3O_{10}$ ground with two equivalents of $LiOH{\cdot}H_2O$. The vertical bars indicate the allowed Bragg reflection positions for $Li_2La_2Ti_3O_{10}$. Data collected at angles below 22° 2θ were excluded from the refinement due to systematic experimental problems in the peak shape and intensity.

broader than the others. It was also noted that this broadening is significantly more pronounced than that published by Gopalakrishnan *et al.*[5] Nevertheless, diffraction data collected from $H_2La_2Ti_3O_{10}$ could be indexed using a tetragonal cell of dimensions a = 3.819(8) Å and c = 27.54(6) Å; these are consistent with the cell parameters reported by these authors.

In an attempt to form members of the solid-solution series $H_{2-2x}Li_{2x}La_2Ti_3O_{10}$, samples of $H_2La_2Ti_3O_{10}$ were also ground with sub-stoichiometric quantities of $LiOH{\cdot}H_2O$ ($x = 0.125, 0.25, 0.5, 0.75$), as described by reaction (6.6).

$$H_2La_2Ti_3O_{10} + (2x)LiOH{\cdot}H_2O \rightarrow H_{2-2x}Li_{2x}La_2Ti_3O_{10} + (4x)H_2O \qquad (6.6)$$

X-ray powder diffraction data collected from each of these samples could be indexed on the basis of the same space group and impurity peaks as those used in indexing the data collected from the lithium end member. The unit cell parameters derived from each of these data sets show an almost linear evolution with lithium content, and indicate that the transition from $H_2La_2Ti_3O_{10}$ to a lithium-exchanged sample occurs discontinuously with respect to the stacking direction, as illustrated in Figure 6.16. The mass of each of the lithium-containing samples was also recorded after grinding, which indicated a mass loss ranging from 1.6 wt. %, for the $x = 0.125$ sample, to 9.2 wt. %, for the $x = 1.0$ sample. These mass losses are commensurate with the loss of the majority (average of 73 %) of the water product proposed by reaction (6.6). This loss in mass together with the evolution of the unit cell parameters suggests that protons had been quantitatively replaced with lithium cations.

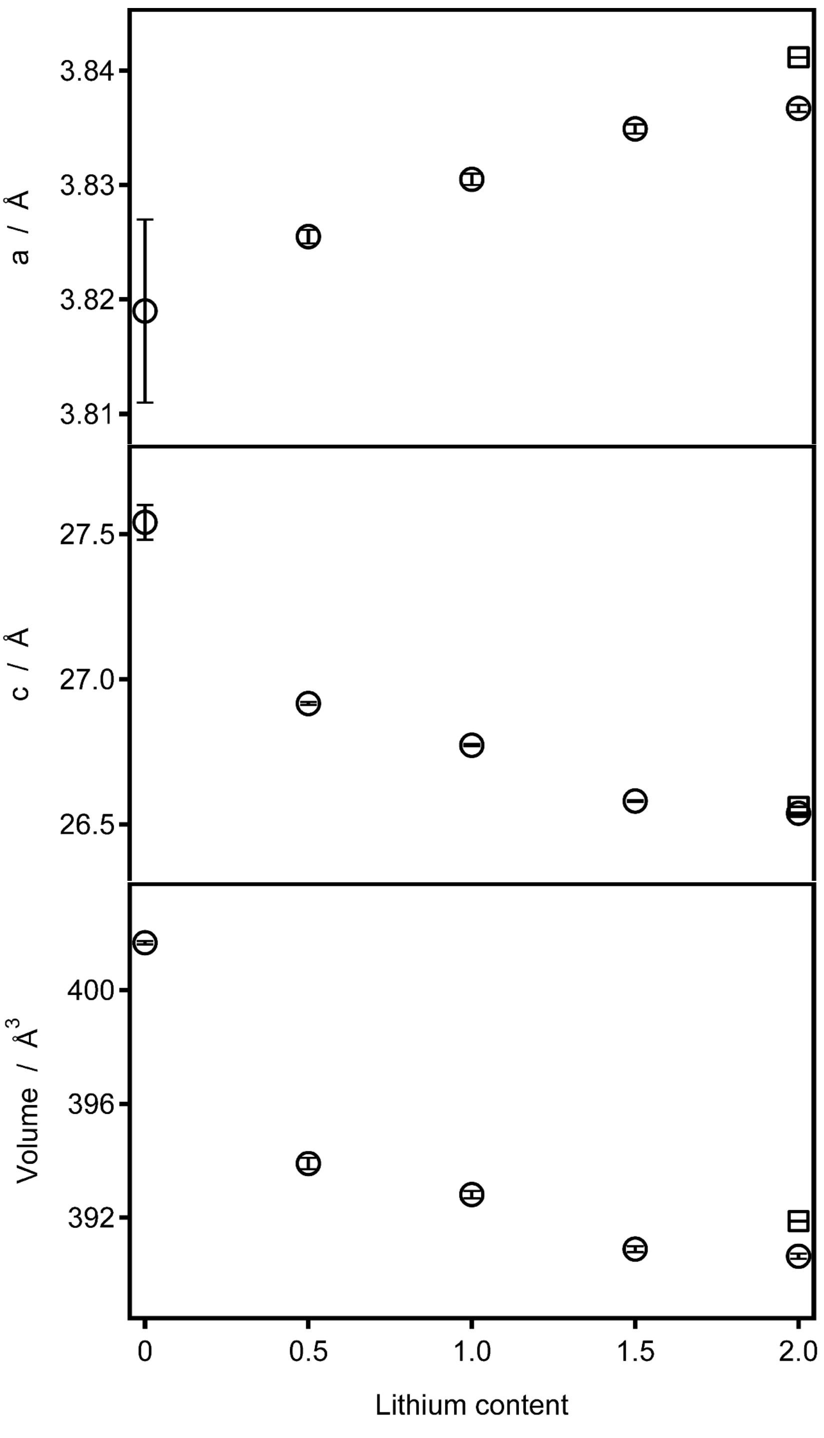

Figure 6.16 Unit cell parameters for the $H_{2-2x}Li_{2x}La_2Ti_3O_{10}$ series of compounds derived from least-squares refinement against X-ray powder diffraction data (circles). Additionally shown are literature values for $Li_2La_2Ti_3O_{10}$ derived from X-ray powder diffraction data (squares).[1]

The diffraction patterns collected from the sub-stoichiometric samples, with the exception of the $x = 0.125$ sample, could all be fitted on the basis of the $[La_2Ti_3O_{10}]^{2-}$ host lattice reported for $Li_2La_2Ti_3O_{10}$,[1] in a similar manner to the data collected from the lithium end member. Lithium was also included in these models at the special position (0, ½, ¼) reported for $Li_2La_2Ti_3O_{10}$,[1] with the fractional occupancy of this site adjusted to the stoichiometry anticipated for each series member. In the case of data collected from the $x = 0.125$ sample, these data exhibit peaks that are significantly broader than those that arise from the other lithium-exchanged samples. Furthermore, the background in the region of 25-35° 2θ is maintained at the same elevated level as observed in the parent compound. Attempts to refine the $[La_2Ti_3O_{10}]^{2-}$ model against these data showed that this model is unable to provide a satisfactory match to the intensity or position of a number of peaks. It was therefore necessary to perform a LeBail extraction to obtain a reasonable fit to the $x = 0.125$ data set. This was performed in the same space group, *I*4/*mmm*, as used to describe the structure of the other lithium-exchanged phases. The fits to all these data sets are shown in Figures 6.17 - 6.18, whilst the fit and structural parameters are presented in Tables 6.3 - 6.5. Selected bond distances and interlayer distances are presented in Tables 6.6 - 6.7.

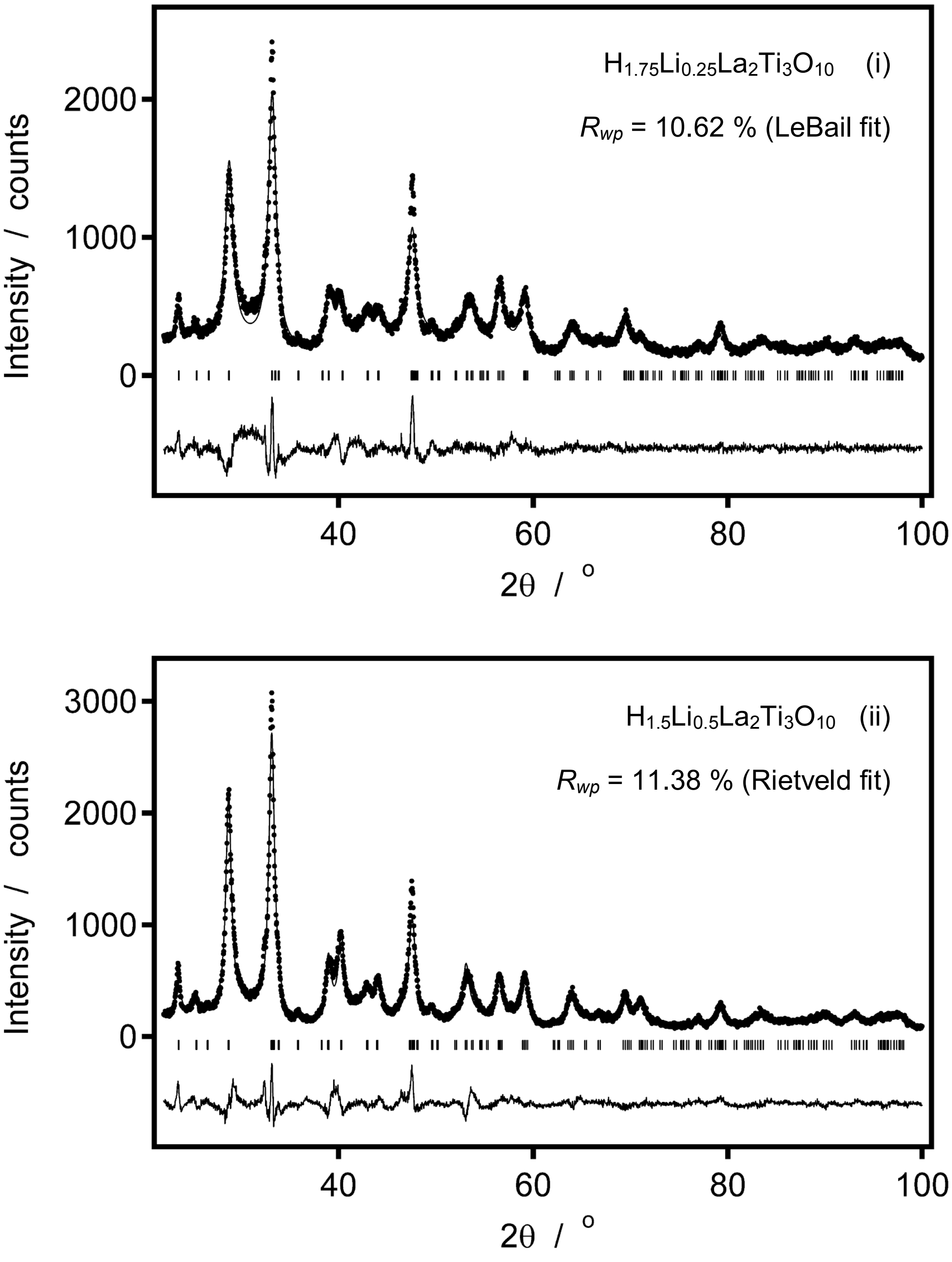

Figures 6.17 Observed (dots), calculated (top line) and difference (bottom line) X-ray powder diffraction patterns for (i) $H_{1.75}Li_{0.25}La_2Ti_3O_{10}$ and (ii) $H_{1.5}Li_{0.5}La_2Ti_3O_{10}$. The vertical bars indicate the allowed Bragg reflection positions for a tetragonal cell in the space group *I*4/*mmm*.

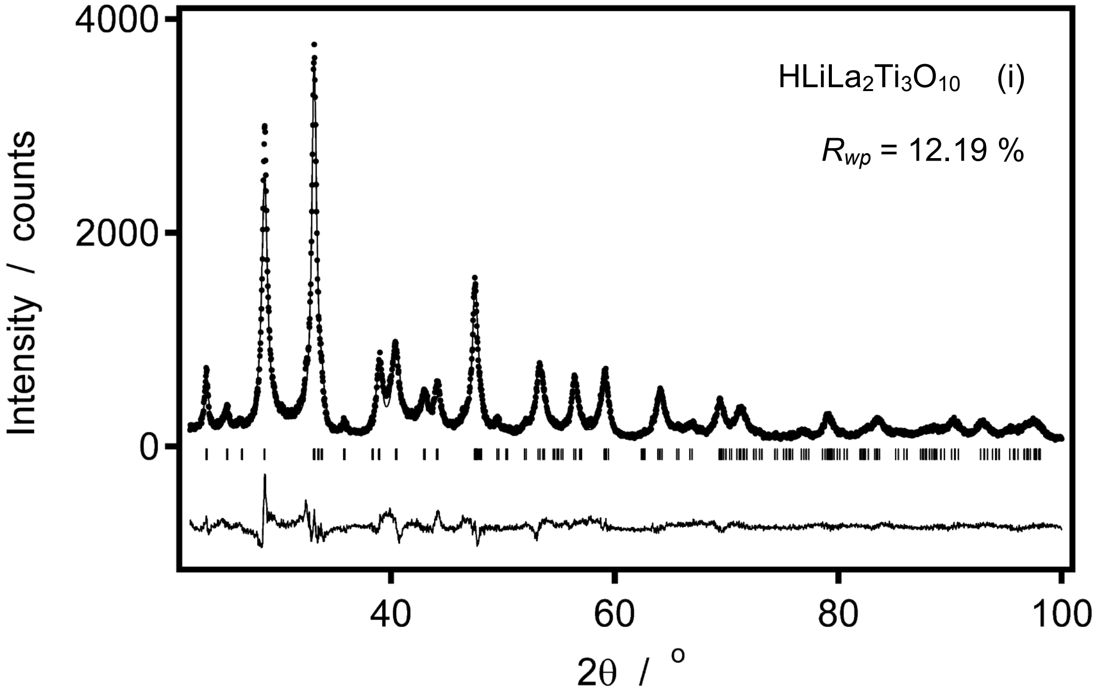

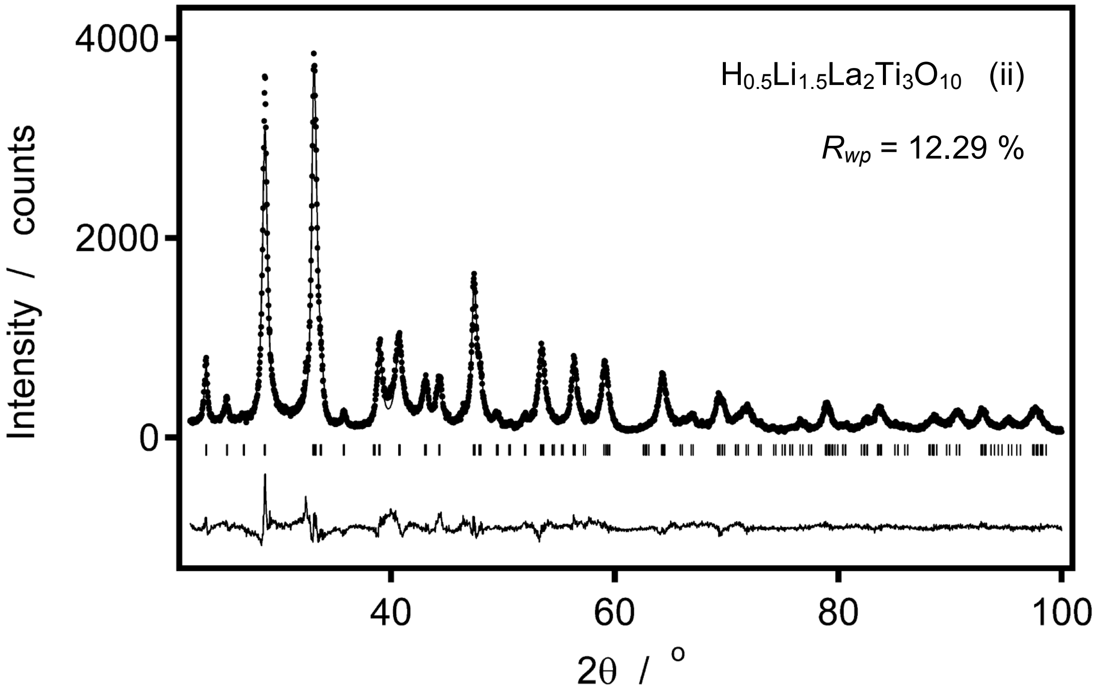

Figures 6.18 Observed (dots), calculated (top line) and difference (bottom line) X-ray powder diffraction patterns for (i) $HLiLa_2Ti_3O_{10}$ and (ii) $H_{0.5}Li_{1.5}La_2Ti_3O_{10}$. The vertical bars indicate the allowed Bragg reflection positions for a tetragonal cell in the space group *I*4/*mmm*.

Table 6.3 Fit parameters for the $H_{2-2x}Li_{2x}La_2Ti_3O_{10}$ series of compounds derived from least-squares refinement against X-ray powder diffraction data

Compound	**a / Å**	**c / Å**	**V / Å^3**	**R_{wp} / %**	**χ^2**	**Variables**
$H_{1.75}Li_{0.25}La_2Ti_3O_{10}$ *	3.8303(8)	26.936(10)	395.2(2)	10.62	3.977	4
$H_{1.5}Li_{0.5}La_2Ti_3O_{10}$	3.8255(6)	26.916(5)	393.9(2)	11.38	3.948	33
$HLiLa_2Ti_3O_{10}$	3.8305(5)	26.772(4)	392.81(13)	12.19	4.499	32
$\square LiLa_2Ti_3O_{9.5}$ $^{\neq}$*	3.8413(4)	26.489(4)	390.86(11)	11.23	3.749	5
$H_{0.5}Li_{1.5}La_2Ti_3O_{10}$	3.8349(4)	26.580(3)	390.89(10)	12.29	4.538	32
$Li_2La_2Ti_3O_{10}$	3.8367(3)	26.538(3)	390.64(9)	12.51	4.713	32
$Li_2La_2Ti_3O_{10}$ $^{\#}$	3.8409(3)	26.447(2)	390.17(8)	12.80	5.037	22

* LeBail fit

$^{\neq}$ $HLiLa_2Ti_3O_{10}$ heat treated at 500 °C in air for 2 d

$^{\#}$ $Li_2La_2Ti_3O_{10}$ heat treated at 500 °C in air for 2 d

Table 6.4 Structural parameters for the $H_{2-2x}Li_{2x}La_2Ti_3O_{10}$ series of compounds derived from least-squares refinement against X-ray powder diffraction data

Compound	**La 4*e* (0,0,*z*)**	**Ti2 4*e* (0,0,*z*)**	**O2 4*e* (0,0,*z*)**	**O3 8*g* (0,½,*z*)**	**O4 4*e* (0,0,*z*)**
$H_{1.5}Li_{0.5}La_2Ti_3O_{10}$	0.4187(2)	0.1569(3)	0.0860(12)	0.1469(5)	0.2259(8)
$HLiLa_2Ti_3O_{10}$	0.41888(11)	0.1588(2)	0.0811(13)	0.1438(5)	0.2279(8)
$H_{0.5}Li_{1.5}La_2Ti_3O_{10}$	0.41841(10)	0.1594(2)	0.0791(11)	0.1438(4)	0.2297(7)
$Li_2La_2Ti_3O_{10}$	0.41819(9)	0.1594(2)	0.0744(9)	0.1422(5)	0.2300(7)
$Li_2La_2Ti_3O_{10}$ $^{\#}$	0.41803(7)	0.15930(13)	0.0717(6)	0.1440(4)	0.2285(5)

$^{\#}$ $Li_2La_2Ti_3O_{10}$ heat treated at 500 °C in air for 2 d

Atomic coordinates of proton have not been defined

Atoms in special positions: Li 4*d* (0, ½, ¼), Ti1 2*a* (0, 0, 0), O1 4*c* (0, ½, 0)

Table 6.5 Atomic displacement parameters, $100U_{iso}$ (Å^2), and preferred orientation parameters, P.O., for the $H_{2-2x}Li_{2x}La_2Ti_3O_{10}$ series of compounds derived from least-squares refinement against X-ray powder diffraction data

Compound	**Li**	**La**	**Ti(1-2)$^{\$}$**	**O(1-4)$^{\$}$**	**P.O.$^{¥}$**
$H_{1.5}Li_{0.5}La_2Ti_3O_{10}$	1.2	3.7(2)	0.7(2)	0.9(3)	0.856(6)
$HLiLa_2Ti_3O_{10}$	1.2	1.58(11)	0.9(2)	1.9(3)	0.803(5)
$H_{0.5}Li_{1.5}La_2Ti_3O_{10}$	1.2	1.29(9)	0.4(2)	0.7(2)	0.843(5)
$Li_2La_2Ti_3O_{10}$	1.2	1.11(8)	0.60(15)	1.4(2)	0.808(4)
$Li_2La_2Ti_3O_{10}$ $^{\#}$	1.2	1.59(7)	0.31(12)	1.4(2)	0.719(2)

$^{\#}$ $Li_2La_2Ti_3O_{10}$ heat treated at 500 °C in air for 2 d

$^{\$}$ constrained atomic displacement parameters of like-elements to be equal

$^{¥}$ preferred orientation modelled along the [001] direction using the March-Dollase model

Table 6.6 Selected bond distances (Å) and interlayer distances (Å) derived from least-squares refinement against X-ray powder diffraction data

Compound	**4 × Li-O4**	**4 × La-O1**	**4 × La-O2**	**4 × La-O3**	**$O4_z \cdots O4_z$**
$H_{1.5}Li_{0.5}La_2Ti_3O_{10}$	2.020(7)	2.906(3)	2.708(2)	2.603(11)	1.30(3)
$HLiLa_2Ti_3O_{10}$	2.005(6)	2.896(2)	2.7086(3)	2.546(10)	1.18(3)
$H_{0.5}Li_{1.5}La_2Ti_3O_{10}$	1.992(5)	2.895(2)	2.7125(7)	2.533(8)	1.08(3)
$Li_2La_2Ti_3O_{10}$	1.990(5)	2.897(2)	2.720(2)	2.499(8)	1.06(3)
$Li_2La_2Ti_3O_{10}$ #					1.17(4)

$Li_2La_2Ti_3O_{10}$ heat treated at 500 °C in air for 2 d

Table 6.7 Selected bond distances (Å) for the titanium oxide sublattice derived from least-squares refinement against X-ray powder diffraction data

Compound	**4 × Ti1-O1**	**2 × Ti1-O2**	**4 × Ti2-O3**	**1 × Ti2-O2**	**1 × Ti2-O4**
$H_{1.5}Li_{0.5}La_2Ti_3O_{10}$	1.9128(3)	2.32(3)	1.932(2)	1.91(3)	1.86(2)
$HLiLa_2Ti_3O_{10}$	1.9152(2)	2.17(4)	1.957(3)	2.08(3)	1.85(2)
$H_{0.5}Li_{1.5}La_2Ti_3O_{10}$	1.9174(2)	2.10(3)	1.962(3)	2.13(3)	1.87(2)
$Li_2La_2Ti_3O_{10}$	1.9183(2)	1.98(3)	1.972(3)	2.26(2)	1.87(2)
$Li_2La_2Ti_3O_{10}$ #					

$Li_2La_2Ti_3O_{10}$ heat treated at 500 °C in air for 2 d

In order to evaluate the rapidity of reaction (6.6), a sample of $H_2La_2Ti_3O_{10}$ was ground with two equivalents of $LiOH{\cdot}H_2O$ for 30 min, and the progress of this reaction then monitored by X-ray powder diffraction. Diffraction data collected over a 23 min period, following a preparation period of 45 min, could be fitted using the structural model reported for $Li_2La_2Ti_3O_{10}$, as illustrated in Figure 6.19. This sample was subsequently monitored over the next several months, during which time, no significant change in either of the lattice parameters was observed. These observations indicate that the replacement of protons with lithium cations occurs rapidly, leading to a product that remains stable at room temperature.

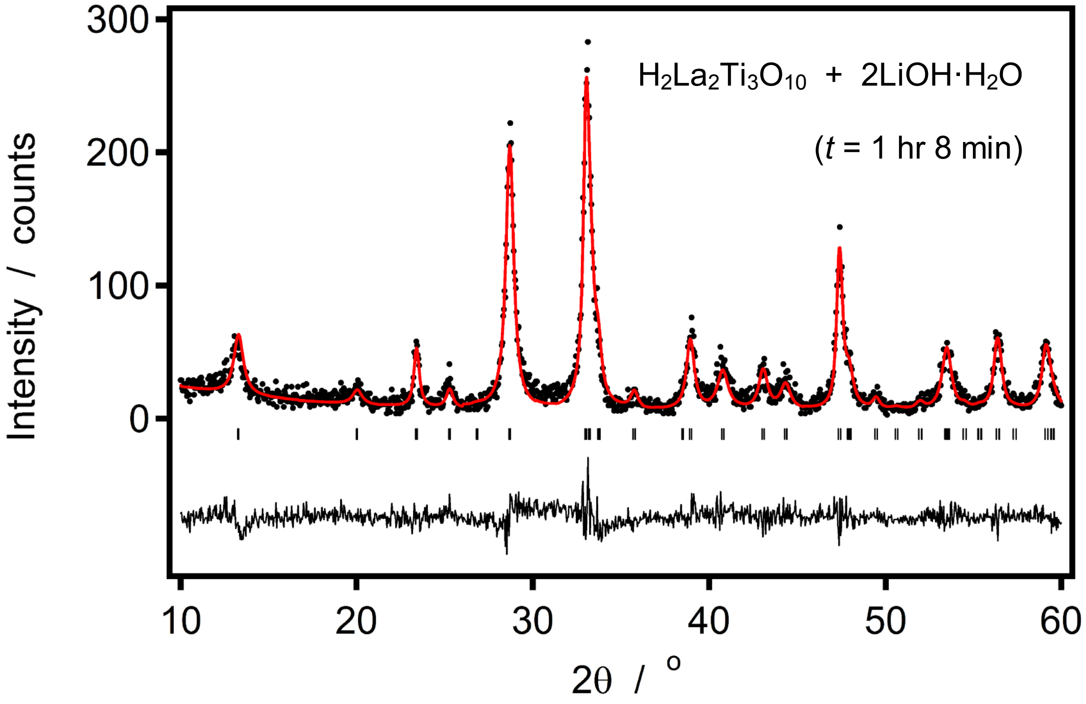

Figure 6.19 Observed (dots), calculated (red line) and difference (black line) X-ray powder diffraction patterns for a 1:2 mixture of $H_2La_2Ti_3O_{10}$ and $LiOH{\cdot}H_2O$ after it had been ground. The observed data were collected over a 23 min period after the mixture had been ground and prepared for analysis over a 45 min period, which gives a total time of reaction, t, of 1 hr 8 min. The vertical bars indicate the allowed Bragg reflection positions for a tetragonal cell in the space group $I4/mmm$.

In order to provide additional evidence with which to support the series of ion-exchange reactions proposed, the thermal stabilities of the protonated and lithium-exchanged samples were evaluated. The compound $H_2La_2Ti_3O_{10}$ has previously been proposed by Gönen *et al.* to topochemically dehydrate at 250 °C under reduced pressure to give a defective layered perovskite, $\square_2La_2Ti_3O_9$,[9] as described by reaction (6.7).

$$H_2La_2Ti_3O_{10} \rightarrow \square_2La_2Ti_3O_9 + H_2O \qquad (6.7)$$

The proposed structural model of $\square_2La_2Ti_3O_9$ can be derived from the $[La_2Ti_3O_{10}]^{2-}$ sublattice by introducing a suitable number of vacancies in the oxygen sites, in addition to approximately halving the interlayer distance. To investigate this, a sample of $H_2La_2Ti_3O_{10}$ was similarly heated at 250 °C, but under ambient pressure and for 2 d. X-ray powder diffraction data collected from the resulting sample could not be satisfactorily fitted using the model reported for $\square_2La_2Ti_3O_9$, but could instead be largely indexed using a tetragonal cell ($a = 3.8595(4)$ Å and $c = 24.852(4)$ Å) that is of similar dimensions to this defective phase, as illustrated by the LeBail fit in Figure 6.20.

The heat treatment of the $x = 0.5$ ($HLiLa_2Ti_3O_{10}$) and $x = 1.0$ ($Li_2La_2Ti_3O_{10}$) lithium-exchanged samples at 500 °C in air for 2 d led to X-ray powder diffraction data that could be indexed, instead, on the basis of the $[La_2Ti_3O_{10}]^{2-}$ host lattice. In the case of data collected from the heat-treated sample of $Li_2La_2Ti_3O_{10}$, these data could additionally be fitted using the model reported for $Li_2La_2Ti_3O_{10}$,[1] as illustrated in

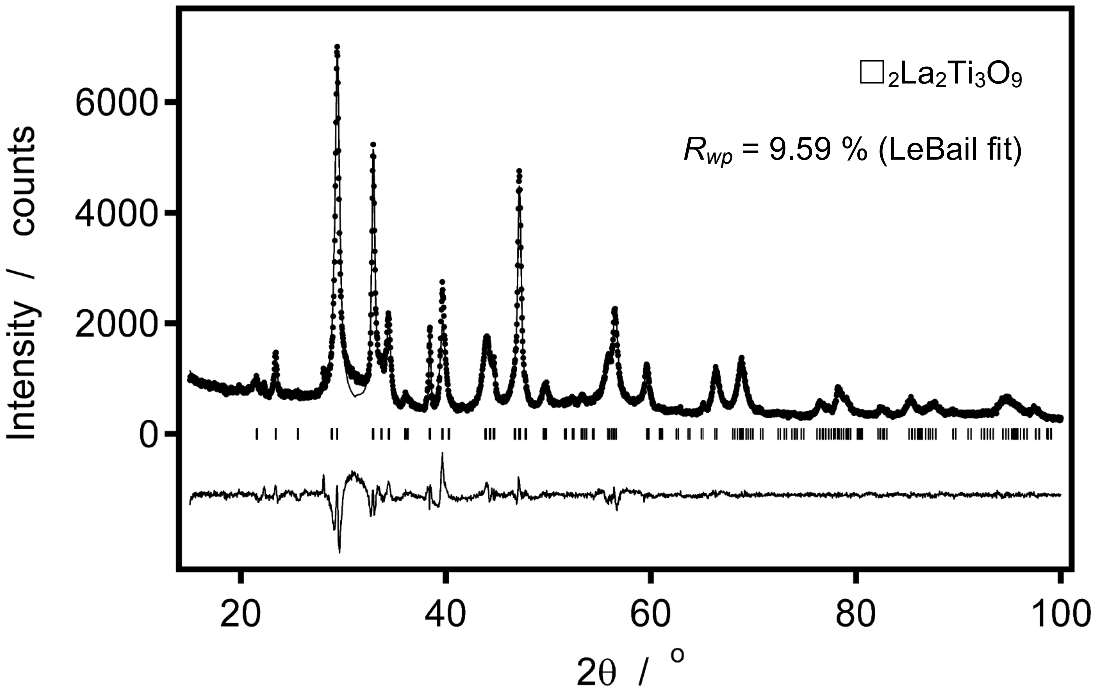

Figure 6.20 Observed (dots), calculated (top line) and difference (bottom line) X-ray powder diffraction patterns for a sample of $H_2La_2Ti_3O_{10}$ after heat treatment at 250 °C in air for 2 d. The calculated diffraction pattern was derived from a LeBail extraction of the observed intensities. The vertical bars indicate the allowed Bragg reflection positions for a tetragonal cell in the space group *I*4/*mmm*.

Figure 6.21(i), in a similar manner to data collected from the as made sample. This refinement showed that $Li_2La_2Ti_3O_{10}$ undergoes a negligible change in cell volume after heat treatment at 500 °C, indicating that only lithium cations were present in the interlayer region.

By comparison, data collected from a heat-treated sample of $HLiLa_2Ti_3O_{10}$ were not amenable to full Rietveld analysis. Consequently, these data were fitted instead by LeBail extraction, as illustrated in Figure 6.21(ii). This indicated that the tetragonal cell of $HLiLa_2Ti_3O_{10}$ had undergone an overall contraction to give a cell of

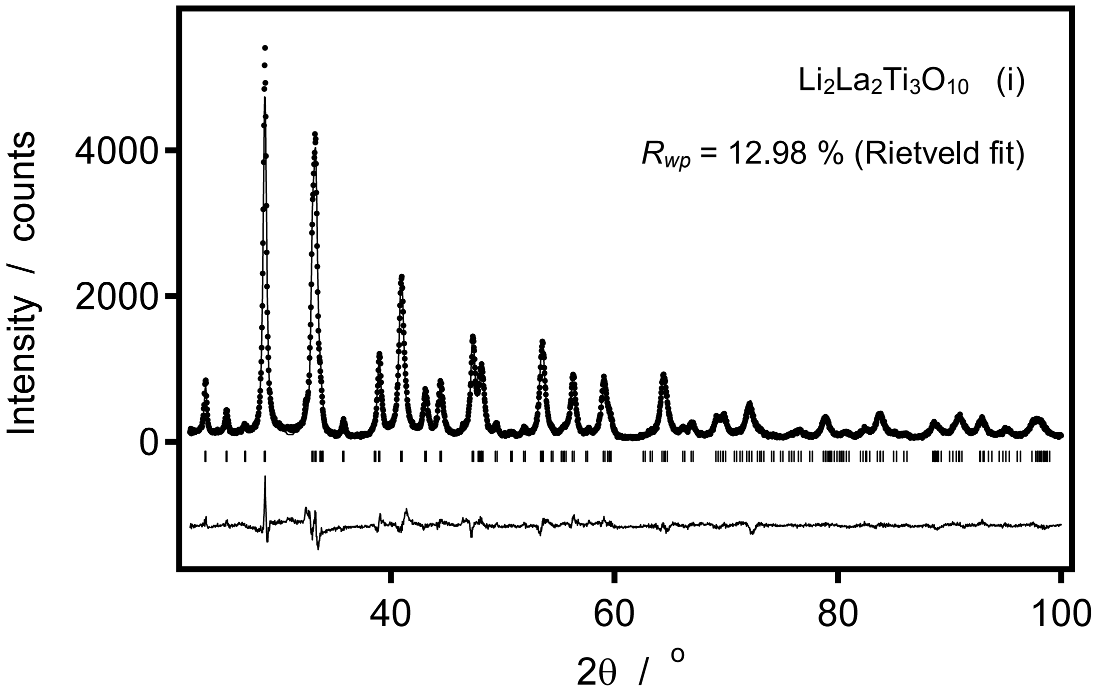

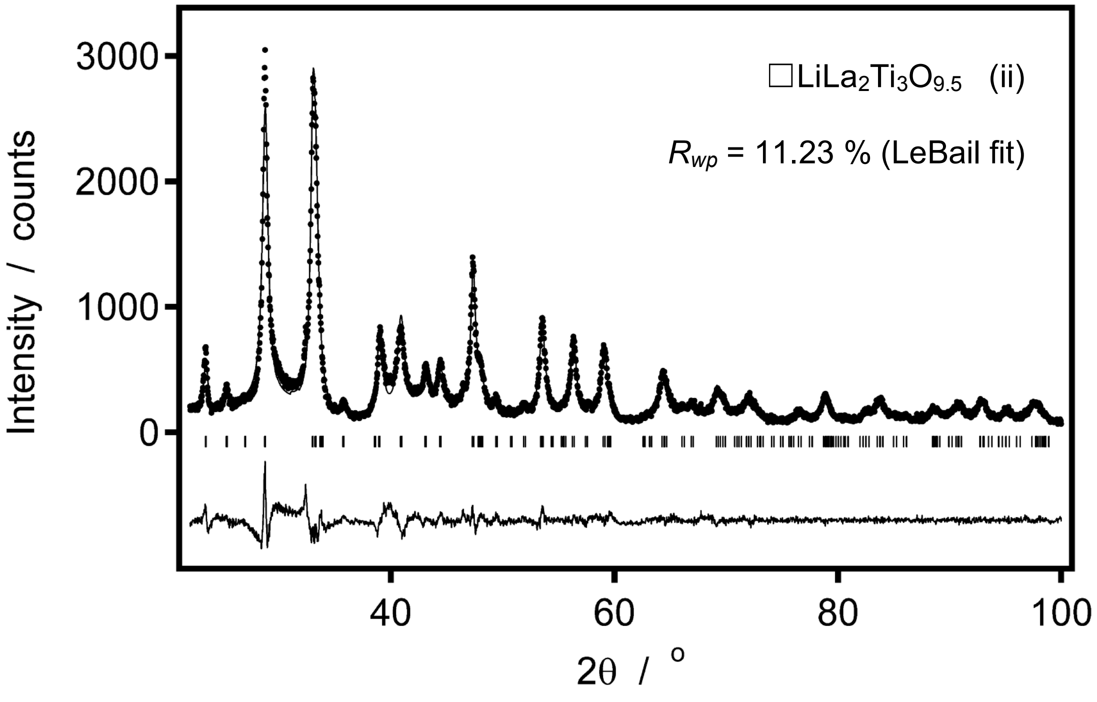

Figure 6.21 Observed (dots), calculated (top line) and difference (bottom line) X-ray powder diffraction patterns for a sample of (i) $Li_2La_2Ti_3O_{10}$ and (ii) $HLiLa_2Ti_3O_{10}$, after heat treatment at 500 °C in air for 2 d. The vertical bars indicate the allowed Bragg reflection positions for a tetragonal cell in the space group *I*4/*mmm*.

dimensions a = 3.8413(4) Å and c = 26.489(4) Å; these lattice parameters are comparable to the values derived from the heat-treated sample of $Li_2La_2Ti_3O_{10}$ (a = 3.8409(3) Å and c = 26.447(2) Å). The magnitude of this c parameter contraction suggests that on heating a sample of $HLiLa_2Ti_3O_{10}$ to 500 °C, $HLiLa_2Ti_3O_{10}$ undergoes topochemical dehydration to give a defective layered perovskite, $\square LiLa_2Ti_3O_{9.5}$, as described by reaction (6.8). This proposed structure differs from that of $\square_2La_2Ti_3O_9$ in that the dehydration of $HLiLa_2Ti_3O_{10}$ leads only to half the number of defects, and so the perovskite layers should still be interleaved with lithium cations.

$$H_{2-2x}Li_{2x}La_2Ti_3O_{10} \rightarrow \square_{2-2x}Li_{2x}La_2Ti_3O_{10-(1-x)} + (1-x)H_2O \qquad (6.8)$$

Thermogravimetric data were also collected from the protonated and lithium-exchanged samples, in a similar manner to the double layer compounds, and all show a complex mass loss. In the case of $H_2La_2Ti_3O_{10}$, two distinct mass losses are observed; the first corresponding to a small loss of 0.32 wt. % on heating from room temperature up to 200 °C, and the second to a more significant loss of 3.3 wt. % over the temperature 200 °C to 900 °C, as illustrated in Figure 6.22(i). The latter is commensurate with the evaporation of 1.1 moles of water per formula unit, which is in good agreement with the amount of water product proposed by reaction (6.7), and so the mass loss occurring below 200 °C is likely to arise from the evaporation of extra-framework moisture. Thermogravimetric data collected from $HLiLa_2Ti_3O_{10}$ and $Li_2La_2Ti_3O_{10}$ are less straightforward than $H_2La_2Ti_3O_{10}$, as illustrated in Figure 6.22(ii), and in each case show a total mass loss that is greater than can be anticipated from the dehydration in reaction (6.8). These additional mass losses could arise from either

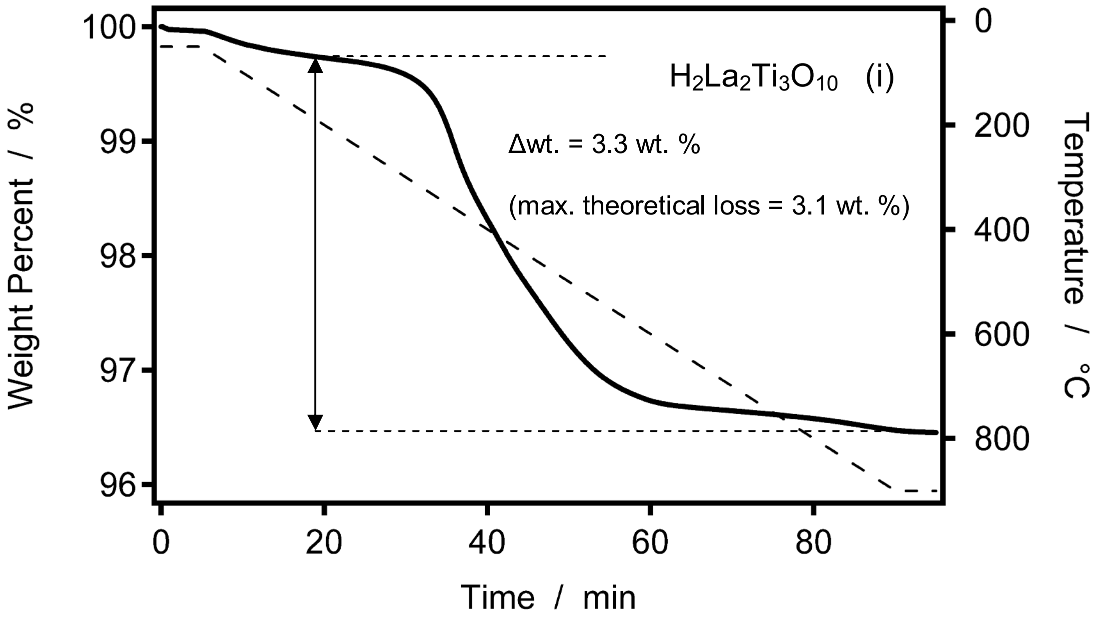

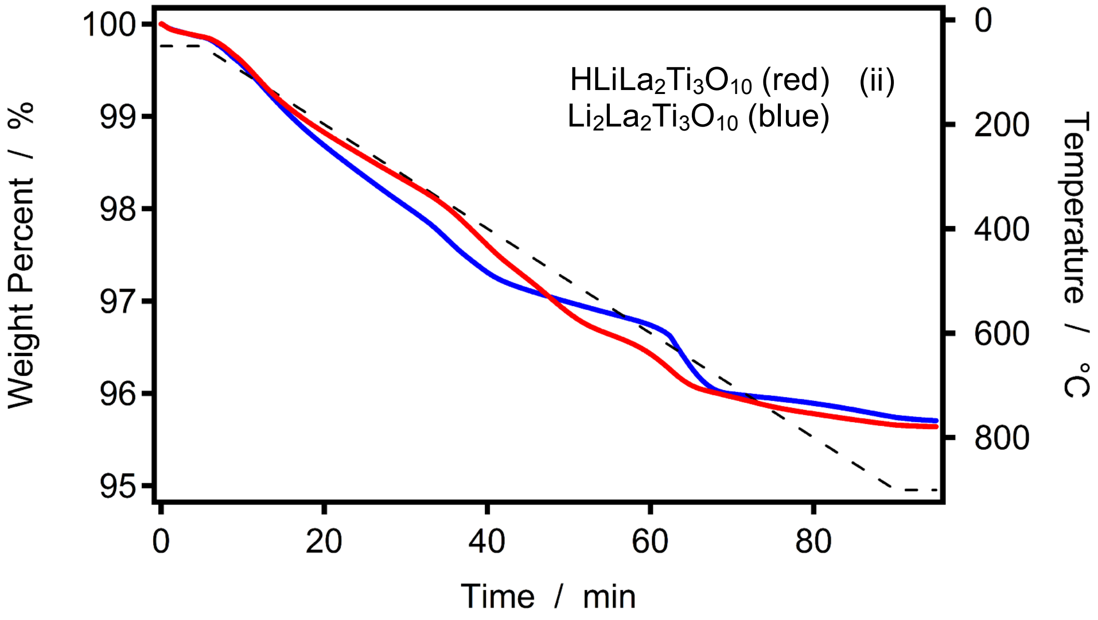

Figure 6.22 Thermogravimetric data collected on heating (i) $H_2La_2Ti_3O_{10}$ (black line) and (ii) the $HLiLa_2Ti_3O_{10}$ (red line) and $Li_2La_2Ti_3O_{10}$ (blue line) lithium-exchanged samples from room temperature up to 900 °C at 10 °C min^{-1}, under a dynamic atmosphere of dry helium. In (i), the maximum loss in mass anticipated from the topochemical dehydration of $H_2La_2Ti_3O_{10}$ is 3.1 wt. %. In (ii), a total mass loss of *ca.* 4.3 wt. % is observed from both $HLiLa_2Ti_3O_{10}$ (max. theoretical loss = 1.5 wt. %) and $Li_2La_2Ti_3O_{10}$ (max. theoretical loss = 0 wt. %).

evaporation of extra-framework moisture, volatilisation of lithium as Li_2O from the layered perovskite, or a combination of both. However, analyses of the multi-stage mass losses do not reveal a clear correlation with the H/Li ratio in these samples.

X-ray powder diffraction data were subsequently collected from the x = 1.0 residue obtained from the thermogravimetric study. These data could be indexed on the basis of a tetragonal cell (a = 3.83913(12) Å and c = 26.4580(11) Å), as illustrated in Figure 6.23, which is indistinguishable from that of $Li_2La_2Ti_3O_{10}$ after heat treatment at 500 °C. This observation indicates that no detectable loss of Li_2O, and accompanying formation of $\square_{2-2x}Li_{2x}La_2Ti_3O_{10-(1-x)}$, has occurred. Therefore, the mass losses shown in Figure 6.22(ii) presumably arise almost exclusively from the evaporation of moisture.

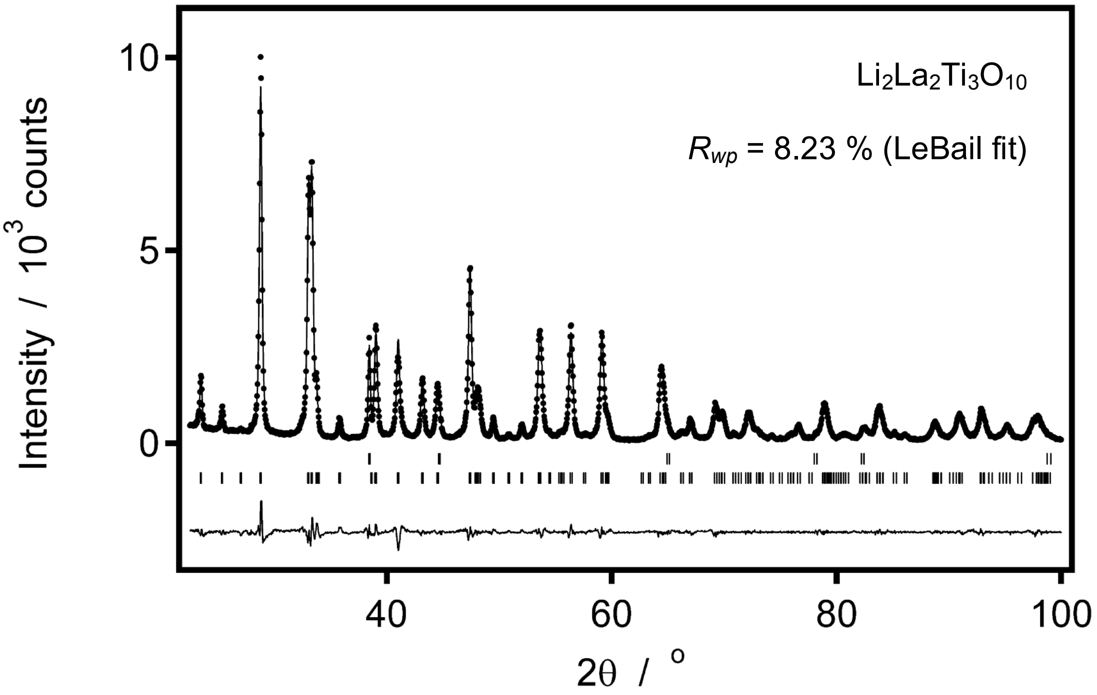

Figure 6.23 Observed (dots), calculated (top line) and difference (bottom line) X-ray powder diffraction patterns for a sample of $Li_2La_2Ti_3O_{10}$ obtained as the residue from a thermogravimetric experiment in which the sample was heated up to 900 °C in a dynamic atmosphere of dry helium. The upper and lower vertical bars indicate the allowed Bragg reflection positions for Al (sample holder) and $Li_2La_2Ti_3O_{10}$ respectively.

6.3.3 AC Impedance Spectroscopy

In order to evaluate the potential for fast-ion conduction in the defective layered perovskites $\square LiSrTa_2O_{6.5}$ and $\square LiLa_2Ti_3O_{9.5}$, AC impedance data were collected from a pellet of each of these materials in air. These experiments initially involved heating a pellet of the $HLiSrTa_2O_7$ or $HLiLa_2Ti_3O_{10}$ parent compound at 360 °C and 450 °C, respectively, in air for 2 d, to give the dehydrated material. Impedance data were then collected from the resulting pellet at temperatures of up to 650 °C. Data collected from a heat-treated sample of the double-layered perovskite show a pair of overlapping arcs in the temperature range $360 \leq T \leq 550$ °C, as illustrated in Figure 6.24(i). The resistances associated with these arcs were estimated by fitting the data using an equivalent circuit model consisting of two parallel combinations of a resistor (R) and a constant phase element (CPE). The arc at lower frequency becomes increasingly less arched with temperature, and at 600 °C can be described, instead, as a tail-like contribution. This tail-like contribution could be modelled using a constant phase element, and is attributable to ion-blocking at the electrode interface.

By comparison, data collected from a heat-treated sample of the triple-layered perovskite also show an arc, but these data become immeasurably large at lower frequencies, as illustrated in Figure 6.24(ii). The resistance associated with this arc was similarly estimated using a resistor and a constant phase element. For both the pellets studied, the resistance derived from the first or only arc was used to provide an estimate of the total conductivity of each pellet.

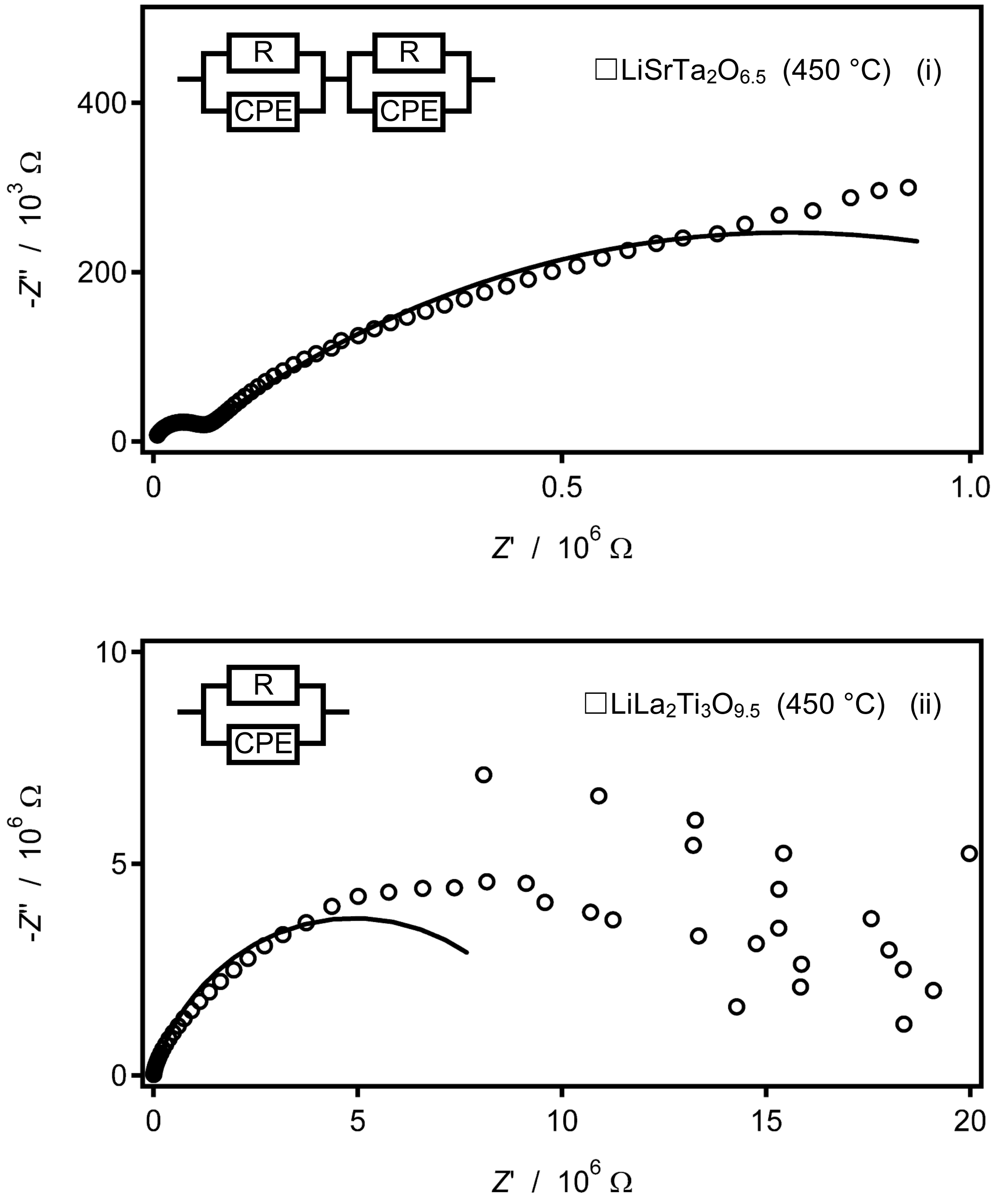

Figure 6.24 Complex plane representations of AC impedance data collected from (i) □$LiSrTa_2O_{6.5}$ and (ii) □$LiLa_2Ti_3O_{9.5}$ at 450 °C in air. The conductivities were derived from these data on the basis of the equivalent circuits shown.

The temperature dependence of the total conductivity behaviour exhibited by □$LiSrTa_2O_{6.5}$ and □$LiLa_2Ti_3O_{9.5}$ could each be fitted using a modified Arrhenius equation, as illustrated in Figure 6.25, and indicated activation energies of 0.90(10) eV and 0.8(2) eV, respectively, over the temperature range studied. The conductivity of each of these samples remains low over this temperature range, with typical values of 2.1 × 10^{-6} S cm^{-1} (□$LiSrTa_2O_{6.5}$) and 8.8 × 10^{-9} S cm^{-1} (□$LiLa_2Ti_3O_{9.5}$) determined at 450 °C.

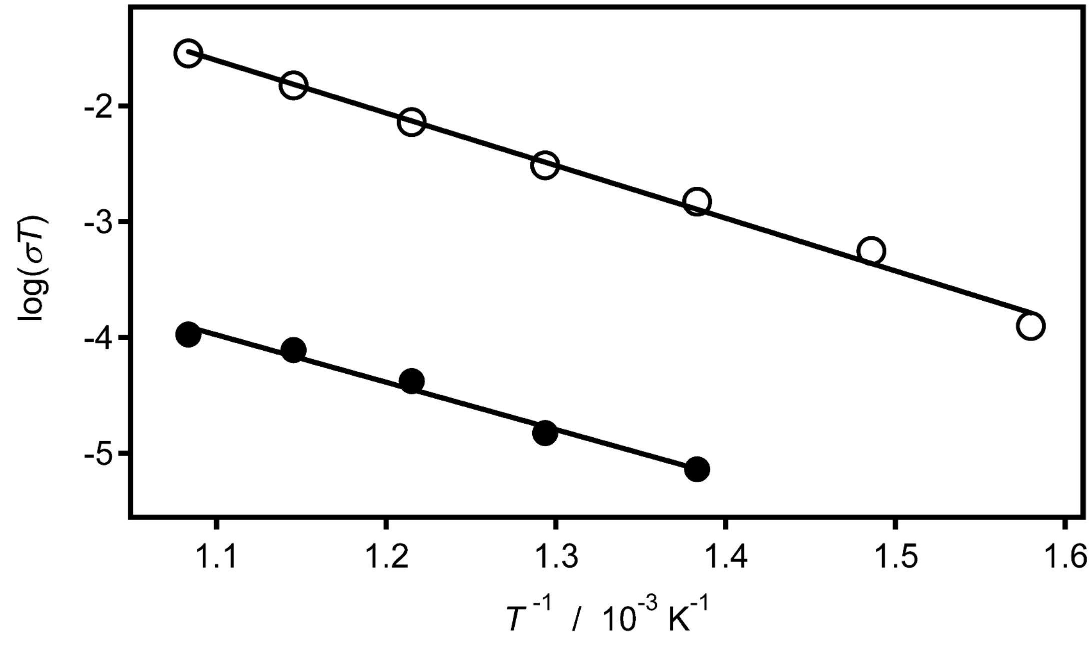

Figure 6.25 Plots of total conductivity as a function of temperature for □$LiSrTa_2O_{6.5}$ (open circles) and □$LiLa_2Ti_3O_{9.5}$ (filled circles). These total conductivities were derived from AC impedance data collected in air. The solid line indicates an Arrhenius fit to each data set.
]

6.4 Discussion

The X-ray powder diffraction studies indicate that the room-temperature mixing of crystalline $LiOH{\cdot}H_2O$ with the layered perovskites $H_2SrTa_2O_7$ and $H_2La_2Ti_3O_{10}$ gives rise to an ion-exchange reaction, where protons are replaced with lithium cations to give $HLiSrTa_2O_7$ and the new solid-solution series $H_{2-2x}Li_{2x}La_2Ti_3O_{10}$, respectively. It has been noted in the literature that stacking defects are prevalent in a number of protonated layered perovskites,[4, 10] which lead to the broadening and shifting of some Bragg peaks, and prevent a complete indexing of the diffraction patterns. This can be contrasted with the structures of the lithium-exchanged compounds, which give rise to peak widths that are considerably more uniform and diffraction patterns that can be fully indexed. Therefore, the mixing of crystalline $LiOH{\cdot}H_2O$ with these solid acids can be considered to affect the crystallinity of these layered materials in a considerably more dramatic manner than is observed for the $H_{1-x}Li_xLaTiO_4$ series of compounds.

In the case of the double-layered perovskite, this direct, room-temperature approach can be compared with the low-temperature route reported by Galven *et al.*,[7] in which one equivalent of lithium cations in the structure of $Li_2SrTa_2O_7$ is replaced with protons to similarly give $HLiSrTa_2O_7$. This molten-salt approach involved heating a 1:25 mixture of $Li_2SrTa_2O_7$ and NH_4Cl at 225 °C under flowing argon for 20 hr. It was noted by the authors that in spite of the excess of NH_4Cl used, only the 1:1 product, $HLiSrTa_2O_7$, could be produced in this manner. This can be contrasted with the approach employed in this thesis, which proceeds, instead, to replace the protons in a relatively less crystalline material, $H_2SrTa_2O_7$, with lithium cations, and so, give a more crystalline product. In this way, $HLiSrTa_2O_7$ (1:1 sample) and mixtures of $H_2SrTa_2O_7$ and $HLiSrTa_2O_7$ (2:1 sample) and $HLiSrTa_2O_7$ and $Li_2SrTa_2O_7$ (1:2 sample) could be prepared at room temperature. Additionally, it is surprising to note that complete exchange to give a monophasic sample of $Li_2SrTa_2O_7$ could be achieved by heating a 1:2 sample at temperatures as low as 120 °C. This suggests that the barrier to complete exchange is not thermodynamic in nature, but is, instead, driven by kinetic considerations. It was noted by Galven *et al.* that $HLiSrTa_2O_7$ could also be prepared by suspending $Li_2SrTa_2O_7$ in a stoichiometric solution of nitric acid at 60 °C.[7] However, it was not explicitly reported whether the use of an excess of protons would lead to complete exchange.

The X-ray powder diffraction study of the $H_{2-2x}Li_{2x}La_2Ti_3O_{10}$ series additionally indicates that the interlayer distance, as defined by the z-component of the distance between two apical oxide anions, contracts from 1.30(3) Å, for the $x = 0.25$ member, to 1.06(3) Å, for the $x = 1.0$ member, as illustrated in Figure 6.26. There is a negligible increase in the thickness of the perovskite layer of 0.05(4) Å with lithium content, and so the contraction in the interlayer distance of 0.24(4) Å dominates, leading to a large reduction in the c lattice parameter. This behaviour can be contrasted with that exhibited by the single-layered $H_{1-x}Li_xLaTiO_4$ series of compounds described in Chapter 4, which exhibits an average elongation in the interlayer distance of 0.066 Å and a contraction in the thickness of the perovskite layer of up to 0.135(11) Å. Other

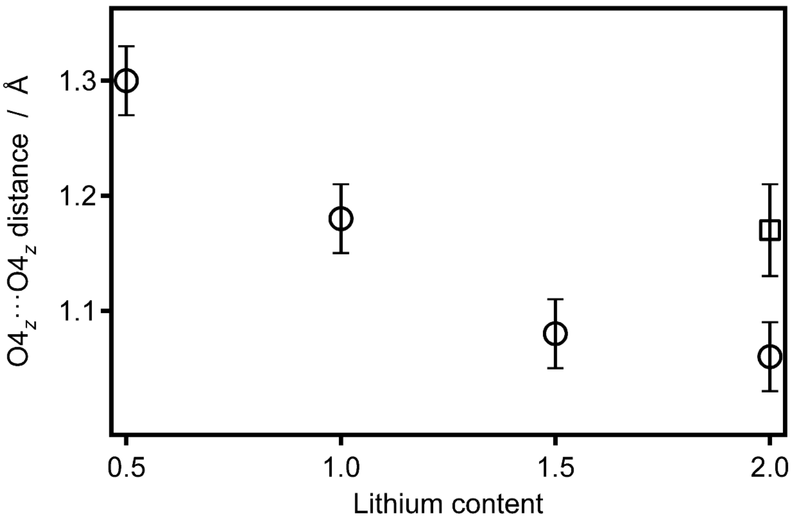

Figure 6.26 Variation in the interlayer distance (circles) across the $H_{2-2x}Li_{2x}La_2Ti_3O_{10}$ series of compounds derived from least-squares refinement against X-ray powder diffraction data. Additionally shown is a literature value (square) derived from the lithium end-member structure[1]

notable differences between these two series include the manner in which the TiO_6 octahedra distort with increasing lithium content. In the single-layer series, the Ti-O bond closest to the alkali interlayer region contracts by up to 0.092(8) Å, whilst the opposing bond contracts by 0.043(7) Å. By comparison, the triple-layer series is characterised by two TiO_6 environments; one on either edge of the perovskite layer, $Ti2O_6$, and a second, $Ti1O_6$, that is in the central layer of the perovskite slab. In the first of these environments, the axial Ti-O bond closest to the interlayer region shows a negligible elongation of 0.01(3) Å with lithium content, whilst the opposing bond elongates by a distance of up to 0.35(4) Å, as illustrated in Figure 6.27. The two equivalent axial Ti-O bond distances in the second octahedral environment, Ti1-O2, each undergo a contraction of up to 0.34(4) Å, and so the elongation of the two Ti2-O2 distances (2 × 0.36(5) Å) is fully compensated. Furthermore, a comparison of the

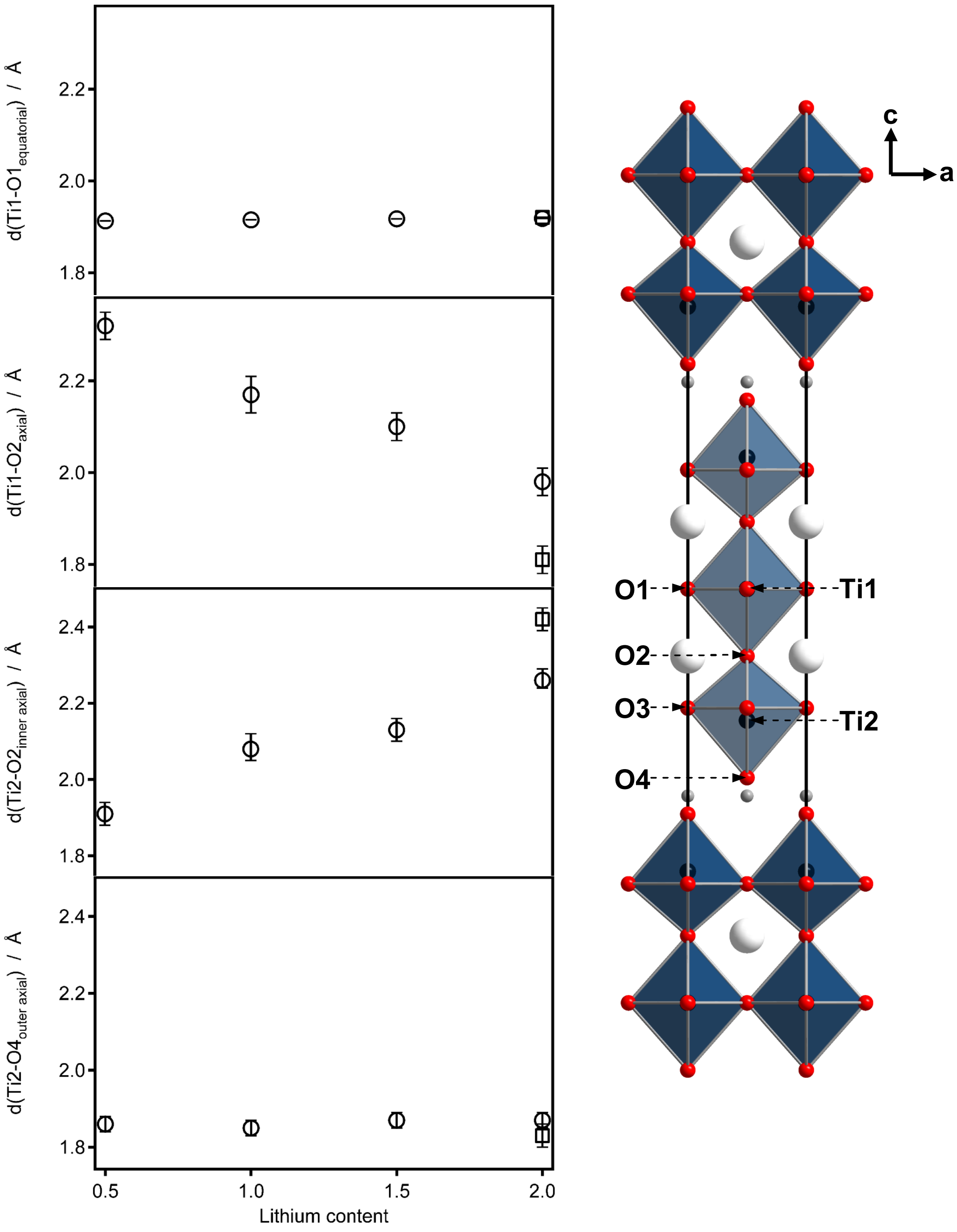

Figure 6.27 Variation in selected Ti-O bond distances (circles) across the $H_{2-2x}Li_{2x}La_2Ti_3O_{10}$ series of compounds derived from least-squares refinement against X-ray powder diffraction data. Additionally shown are literature values (squares) derived from the lithium end-member structure.[1] The positions of the crystallographically distinct Ti^{4+} and O^{2-} ions are indicated in the crystal structure of $Li_2La_2Ti_3O_{10}$, where the Li^+ and La^{3+} cations are represented by grey and white spheres, respectively.

elongation of the Ti2-O2 bond distance with the increase in the distance between titanium and the equatorial plane in the Ti2O_6 octahedron, as illustrated in Figure 6.28, indicates that Li^+ ion exchange results in the displacement of both the O2 and O3 positions towards the centre of perovskite layer, whilst leaving both the Ti2-O4 bond distance and the overall thickness of the perovskite layer unperturbed. However, there is no obvious explanation as to why an increase in lithium content should lead to these distortions of the TiO_6 octahedra. By comparison, the lanthanum oxide environment remains relatively unperturbed with lithium content.

An examination of the Li-O bond distances across the series showed that these are comparable with the Li-O distances derived from the neutron diffraction study of the $H_{1-x}Li_xLaTiO_4$ series of compounds in Chapter 4, and can be described by a typical distance of 2.00(5) Å.

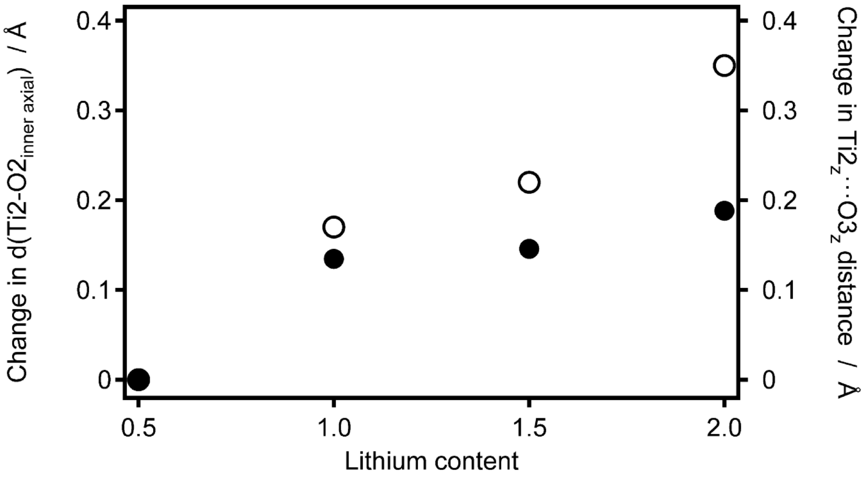

Figure 6.28 A comparison between the elongation of the Ti2-O2 bond distance (open circles) and the increase in the distance between titanium and the equatorial plane of the Ti2O_6 octahedron (filled circles), $Ti2_z \cdots O3_z$, both with respect to values determined for $HLiLa_2Ti_3O_{10}$. These distances were derived from least-squares refinement against X-ray powder diffraction data

The transport measurements of the defective layered perovskite $\Box LiSrTa_2O_{6.5}$ showed evidence of ion blocking at temperatures of 600 °C and above, and indicate that the total conductivity of this material (2.1×10^{-6} S cm^{-1} at 450 °C) is almost an order of magnitude lower than that reported for the lithium end member, $Li_2SrTa_2O_7$ (1×10^{-5} S cm^{-1} at 450 °C).[11] However, it should be noted that the magnitude of this conductivity may be attenuated by the presence of $Sr_{0.5}TaO_3$, which is formed in a significant quantity on dehydration of the $HLiSrTa_2O_7$ parent phase. By comparison, the total conductivity of $\Box LiLa_2Ti_3O_{9.5}$ (8.8×10^{-9} S cm^{-1} at 450 °C) is only slightly lower than the conductivity reported for $Li_2La_2Ti_3O_{10}$ (2.8×10^{-8} S cm^{-1} at 450 °C).[12] Additionally, the impedance of $\Box LiLa_2Ti_3O_{9.5}$ becomes immeasurably large at lower frequencies; this behaviour is also exhibited in the impedance response of the single-layered analogue $\Box_{0.25}Li_{0.75}LaTiO_{3.875}$, as described in Chapter 4, and may be attributed to the grain boundaries providing the limit to ion mobility. Indeed, scanning electron micrographs published by Gönen *et al.* show that topochemical dehydration of $H_2La_2Ti_3O_{10}$ results in considerable fragmentation of the particles,[9] which both destroys the original platelet morphology and reduces the size of these particles by an order of magnitude. The destructive nature of this approach to vacancy formation should similarly apply to the dehydration of $HLiSrTa_2O_7$, and may therefore account for the formation of $Sr_{0.5}TaO_3$ as a minority product.

6.5 Conclusions

The mixing of crystalline lithium hydroxide monohydrate with the layered perovskite $H_2La_2Ti_3O_{10}$ at room temperature gives rise to an ion-exchange reaction, where protons are quantitatively replaced with lithium cations to give a new solid-solution series. This demonstrates that Li^+ ion exchange can proceed quantitatively in a protonated layered perovskite other than $HLaTiO_4$. The reaction between lithium hydroxide monohydrate and $H_2SrTa_2O_7$ shows a different but related behaviour in that the exchange is limited by the preferential stabilisation of the 1:1 product. However, the fully exchanged product can be formed from a 1:2 mixture when heated at a modest temperature of 120 °C. This suggests that the barrier to complete exchange is not thermodynamic in nature, but is instead driven by kinetic considerations. These studies suggest that other protonated Ruddlesden-Popper type layered perovskites should be amenable to Li^+ ion exchange when ground with crystalline lithium hydroxide monohydrate. Therefore, the case for this reaction serving as a general route to the Li^+ ion exchange of protonated layered perovskites is made more compelling. A synthetic route such as this would complement, as well as be a valuable addition to, the set of reactions by which layered perovskites can be topochemically transformed,[13] *i.e.* at low temperature and in a step-wise manner, to give new materials that are metastable or thermodynamically stable at low temperature.

For the intermediate members of each of these series, dehydration of the interlayer leads to the formation of new defective layered perovskites, where some of the lithium and interlayer oxygen sites are vacant. However, despite containing a mixture of lithium cations and vacant sites, each of these compounds demonstrated poorer conductivity than that of the respective lithium end members. Given the manner in which these vacancies were formed, it may be that the reduction in the intragrain resistance afforded by these vacancies is masked by the grain-boundary contribution. In the case of the double-layered perovskite, it was also found that this approach to vacancy formation led a proportion of the sample to topochemically dehydrate to give a three-dimensional perovskite; this is in spite of the layers being interleaved with half an equivalent of lithium cations, and attests to the destructive nature of this approach.

6.6 References

1. K. Toda, J. Watanabe and M. Sato, *Mater. Res. Bull.*, 1996, **31**, 1427-1435.
2. R. H. Mitchell, *Perovskites: Modern and Ancient*, Almaz Press Inc., Thunder Bay, 2002.
3. N. S. P. Bhuvanesh, M.-P. Crosnier-Lopez, H. Duroy and J.-L. Fourquet, *J. Mater. Chem.*, 2000, **10**, 1685-1692.
4. M.-P. Crosnier-Lopez and J.-L. Fourquet, *Solid State Sci.*, 2005, **7**, 530-538.
5. J. Gopalakrishnan and V. Bhat, *Inorg. Chem.*, 1987, **26**, 4299-4301.
6. T. Pagnier, N. Rosman, C. Galven, E. Suard, J.-L. Fourquet, F. L. Berre and M.-P. Crosnier-Lopez, *J. Solid State Chem.*, 2009, **182**, 317–326.
7. C. Galven, J.-L. Fourquet, E. Suard, M.-P. Crosnier-Lopez and F. L. Berre, *Dalton Trans.*, 2010, **39**, 3212-3218.
8. M. P. Crosnier-Lopez, F. Le Berre and J. L. Fourquet, *Z. Anorg. Allg. Chem.*, 2002, **628**, 2049-2056.
9. Z. S. Gönen, D. Paluchowski, P. Zavalij, B. W. Eichhorn and J. Gopalakrishnan, *Inorg. Chem.*, 2006, **45**, 8736-8742.
10. N. S. P. Bhuvanesh, M. P. Crosnier-Lopez, H. Duroy and J. L. Fourquet, *J. Mater. Chem.*, 1999, **9**, 3093-3100.
11. T. Fukushima, S. Suzuki and M. Miyayama, *Key Eng. Mater.*, 2009, **388**, 69-72.
12. V. Thangadurai, A. K. Shukla, J. Gopalakrishnan, O. Joubert, L. Brohan and M. Tournoux, *Mater. Sci. Forum*, 2000, **321-324**, 965-970.
13. R. E. Schaak and T. E. Mallouk, *Chem. Mater.*, 2002, **14**, 1455-1471.

7 Conclusions

The reactions presented in this thesis represent unusual room-temperature chemistry that involves the direct reaction of crystalline lithium hydroxide monohydrate with various metal oxides. The first of these examples relates to the reaction between lithium hydroxide monohydrate and molybdenum trioxide, which proceeds to completion within minutes to give a crystalline sample of lithium molybdate. Calorimetric studies have revealed that this reaction proceeds spontaneously, and is driven by the gain in entropy associated with the liberation of water from the lattice of lithium hydroxide monohydrate. The morphology and size of the particles produced show that this reaction is not topotactic in nature, but instead involves localised dissolution of the reagents. A different reactivity is exhibited when either starting material is substituted with a larger metal cation analogue, leading to reactions that proceed, in one or more steps, to give hydrated products.

This reaction has been developed further to provide an unusual method for replacing the protons in a series of Ruddlesden-Popper layered perovskites, of different thicknesses, with lithium cations. The Li^+ ion exchange of these materials exploits similar considerations to drive an acid-base reaction, but since the host lattices remain in the solid state, these reactions instead represent a topotactic approach that exploits room-temperature ionic conduction. These reactions also represent the first examples of Li^+ ion exchange proceeding quantitatively in Ruddlesden-Popper type layered perovskites, where each has given access to a series of compounds with a controlled proton and lithium content.

For the intermediate members of each of these series, dehydration of the interlayer leads to the formation of new defective layered perovskites, where some of the lithium and interlayer oxygen sites are vacant. However, despite containing a mixture of lithium cations and vacant sites, each of these compounds demonstrate a lower total conductivity than that of the respective lithium end member. This suggests that topochemical dehydration is a destructive approach to vacancy formation, and is unlikely to lead to an enhancement in the total conductivity of this family of materials.

To summarise, the reaction of crystalline lithium hydroxide monohydrate with various metal oxides can proceed under ambient conditions, and, in almost all of the cases investigated, employs reagents in stoichiometric quantities. The water that is formed in these reactions is the only side-product, and so, no purification steps, other than drying in air, are required. There is also evidence to suggest that these reactions are sufficiently general to offer both an environmentally and economically sound route to other mixed-metal oxides with interesting particle morphologies, or new compositions of layered perovskites. The latter, in particular, could potentially provide access to layered perovskites with a controlled lithium and sodium content, *via* a two-step reaction involving lithium hydroxide monohydrate and sodium hydroxide monohydrate. It would also be interesting to see whether this approach to ion exchange could be applied to three-dimensional solid acids such as the garnets

$Li_{2.25}H_{4.75}La_3Sn_2O_{12}$ and $Li_{5-x}H_xLa_3Nb_2O_{12}$;[1] the former has recently been prepared *via* the exchange of $Li_7La_2Sn_2O_{12}$ in acidic ethanolic solution at 60 °C, but it was noted by the authors that the replacement of lithium cations with protons proceeds spontaneously in this structure under ambient conditions.

7.1 Reference

1. C. Galven, J.-L. Fourquet, M.-P. Crosnier-Lopez and F. Le Berre, *Chem. Mater.*, 2011, **23**, 1892-1900.